METHODS IN ENZYMOLOGY

Editors-in-Chief

JOHN N. ABELSON and MELVIN I. SIMON
Division of Biology
California Institute of Technology
Pasadena, California

Founding Editors

SIDNEY P. COLOWICK and NATHAN O. KAPLAN

Academic Press is an imprint of Elsevier
525 B Street, Suite 1800, San Diego, CA 92101-4495, USA
225 Wyman Street, Waltham, MA 02451, USA
Radarweg 29, PO Box 211, 1000 AE Amsterdam, The Netherlands
The Boulevard, Langford Lane, Kidlington, Oxford, OX5 1GB, UK
32 Jamestown Road, London NW1 7BY, UK

First edition 2013

Copyright © 2013, Elsevier Inc. All Rights Reserved.

No part of this publication may be reproduced, stored in a retrieval system or transmitted in any form or by any means electronic, mechanical, photocopying, recording or otherwise without the prior written permission of the publisher

Permissions may be sought directly from Elsevier's Science & Technology Rights Department in Oxford, UK: phone (+44) (0) 1865 843830; fax (+44) (0) 1865 853333; email: permissions@elsevier.com. Alternatively you can submit your request online by visiting the Elsevier web site at http://elsevier.com/locate/permissions, and selecting *Obtaining permission to use Elsevier material*

Notice
No responsibility is assumed by the publisher for any injury and/or damage to persons or property as a matter of products liability, negligence or otherwise, or from any use or operation of any methods, products, instructions or ideas contained in the material herein. Because of rapid advances in the medical sciences, in particular, independent verification of diagnoses and drug dosages should be made

For information on all Academic Press publications visit our website at store.elsevier.com

ISBN: 978-0-12-405883-5
ISSN: 0076-6879

Printed and bound in United States of America
13 14 15 16 11 10 9 8 7 6 5 4 3 2 1

CONTRIBUTORS

Fernando Antunes
Departamento de Química e Bioquímica and Centro de Química e Bioquímica, Faculdade de Ciências, Universidade de Lisboa, Lisboa, Portugal

Ana G. Barata
Division of Redox Regulation, German Cancer Research Center (DKFZ), DKFZ-ZMBH Alliance, Heidelberg, Germany

Vsevolod V. Belousov
Shemyakin-Ovchinnikov Institute of Bioorganic Chemistry, RAS, Moscow, and Nizhny Novgorod State Medical Academy, Nizhny Novgorod, Russia

Dmitry S. Bilan
Shemyakin-Ovchinnikov Institute of Bioorganic Chemistry, RAS, Moscow, and Nizhny Novgorod State Medical Academy, Nizhny Novgorod, Russia

Martin D. Brand
The Buck Institute for Research on Aging, Novato, California, USA

Enrique Cadenas
Pharmacology & Pharmaceutical Sciences, School of Pharmacy, University of Southern California, Los Angeles, California, USA

Christopher J. Chang
Department of Chemistry; Department of Molecular and Cell Biology, University of California, Berkeley, California, and Howard Hughes Medical Institute, Chevy Chase, Maryland, USA

Luísa Cyrne
Departamento de Química e Bioquímica and Centro de Química e Bioquímica, Faculdade de Ciências, Universidade de Lisboa, Lisboa, Portugal

Bryan C. Dickinson
Department of Chemistry and Chemical Biology, Harvard University, Cambridge, Massachusetts, USA

Tobias P. Dick
Division of Redox Regulation, German Cancer Research Center (DKFZ), DKFZ-ZMBH Alliance, Heidelberg, Germany

James Enomoto
Department of Biomedical Engineering, University of California, Davis, California, USA

Arkady F. Fradkov
Shemyakin-Ovchinnikov Institute of Bioorganic Chemistry, RAS, Moscow, Russia

Douglas Ganini
Laboratory of Toxicology and Pharmacology, National Institute of Environmental Health Sciences, NIH, Research Triangle Park, North Carolina, USA

Marco Giorgio
Department of Experimental Oncology, European Institute of Oncology, Milan, Italy

Renata L.S. Goncalves
The Buck Institute for Research on Aging, Novato, California, USA

Longwei He
State Key Laboratory of Chemo/Biosensing and Chemometrics, College of Chemistry and Chemical Engineering, Hunan University, Changsha, PR China

Martin Hey-Mogensen
The Buck Institute for Research on Aging, Novato, California, USA, and Center for Healthy Aging, Department of Biomedical Sciences, Copenhagen University, Copenhagen, Denmark

Etsuro Ito
Kagawa School of Pharmaceutical Sciences, Tokushima Bunri University, Sanuki, Japan

Dean P. Jones
Division of Pulmonary, Allergy and Critical Care Medicine, Clinical Biomarkers Laboratory, Department of Medicine, Emory University School of Medicine, Atlanta, Georgia, USA

Joy Joseph
Department of Biophysics and Free Radical Research Center, Medical College of Wisconsin, Milwaukee, Wisconsin, USA

Balaraman Kalyanaraman
Department of Biophysics and Free Radical Research Center, Medical College of Wisconsin, Milwaukee, Wisconsin, USA

Randal J. Kaufman
Center for Neuroscience, Aging, and Stem Cell Research, Sanford-Burnham Medical Research Institute, La Jolla, California, USA

Melissa L. Kemp
The Wallace H. Coulter Department of Biomedical Engineering, Georgia Institute of Technology and Emory University, Atlanta, Georgia, USA

Ariel Kniss
The Wallace H. Coulter Department of Biomedical Engineering, Georgia Institute of Technology and Emory University, Atlanta, Georgia, USA

Vamsi K. Kodali
Center for Neuroscience, Aging, and Stem Cell Research, Sanford-Burnham Medical Research Institute, La Jolla, California, USA

Hiromi Kodama
Kagawa School of Pharmaceutical Sciences, Tokushima Bunri University, Sanuki, Japan

Guy Landau
Center for Neuroscience, Aging, and Stem Cell Research, Sanford-Burnham Medical Research Institute, La Jolla, California, USA

David Liebl
Institute for Molecular Bioscience, The University of Queensland, St. Lucia, Queensland, Australia

Vivian S. Lin
Department of Chemistry, University of California, Berkeley, California, USA

Weiying Lin
State Key Laboratory of Chemo/Biosensing and Chemometrics, College of Chemistry and Chemical Engineering, Hunan University, Changsha, PR China

Hang Lu
School of Chemical & Biomolecular Engineering, Georgia Institute of Technology, Atlanta, Georgia, USA

Sergey Lukyanov
Shemyakin-Ovchinnikov Institute of Bioorganic Chemistry, RAS, Moscow, and Nizhny Novgorod State Medical Academy, Nizhny Novgorod, Russia

Jyoti D. Malhotra
Proteostasis Therapeutics, Cambridge, Massachusetts, USA

Raluca Marcu*
Department of Experimental Oncology, European Institute of Oncology, Milan, Italy

H. Susana Marinho
Departamento de Química e Bioquímica and Centro de Química e Bioquímica, Faculdade de Ciências, Universidade de Lisboa, Lisboa, Portugal

Kseniya N. Markvicheva
Shemyakin-Ovchinnikov Institute of Bioorganic Chemistry, RAS, Moscow, Russia

Ronald P. Mason
Laboratory of Toxicology and Pharmacology, National Institute of Environmental Health Sciences, NIH, Research Triangle Park, North Carolina, USA

Zimple Matharu
Department of Biomedical Engineering, University of California, Davis, California, USA

Mikhail E. Matlashov
Shemyakin-Ovchinnikov Institute of Bioorganic Chemistry, RAS, Moscow, Russia

Nataliya M. Mishina
Shemyakin-Ovchinnikov Institute of Bioorganic Chemistry, RAS, Moscow, and Nizhny Novgorod State Medical Academy, Nizhny Novgorod, Russia

Toshiaki Miura
Graduate School of Pharmaceutical Sciences, Hokkaido University, Sapporo, Japan

Mika Morikawa
Kagawa School of Pharmaceutical Sciences, Tokushima Bunri University, Sanuki, Japan

Ryuichi Okada
Kagawa School of Pharmaceutical Sciences, Tokushima Bunri University, Sanuki, Japan

Francesco Paolucci
Department of Chemistry, University of Bologna, "G. Ciamician", Bologna, Italy

*Present address: Mitochondria and Metabolism Center, Seattle, Washington, USA

Irina V. Perevoschikova
The Buck Institute for Research on Aging, Novato, California, USA

Casey L. Quinlan
The Buck Institute for Research on Aging, Novato, California, USA

Stefania Rapino
Department of Experimental Oncology, European Institute of Oncology, Milan, Italy

Alexander Revzin
Department of Biomedical Engineering, University of California, Davis, California, USA

Carsten Schultz
EMBL Heidelberg, Heidelberg, Germany

Marina V. Shirmanova
Nizhny Novgorod State Medical Academy, Nizhny Novgorod, Russia

Adam Sikora
Department of Biophysics and Free Radical Research Center, Medical College of Wisconsin, Milwaukee, Wisconsin, USA, and Institute of Applied Radiation Chemistry, Lodz University of Technology, Lodz, Poland

Fiona A. Summers
Laboratory of Toxicology and Pharmacology, National Institute of Environmental Health Sciences, NIH, Research Triangle Park, North Carolina, USA

Satoshi Watabe
BL Co., Ltd., Numazu, Japan

Lin Yuan
State Key Laboratory of Chemo/Biosensing and Chemometrics, College of Chemistry and Chemical Engineering, Hunan University, Changsha, PR China

Elena V. Zagaynova
Nizhny Novgorod State Medical Academy, Nizhny Novgorod, Russia

Baozhong Zhao
Section of Dermatology, Department of Medicine, University of Chicago, Chicago, Illinois, USA

Kaibo Zheng
State Key Laboratory of Chemo/Biosensing and Chemometrics, College of Chemistry and Chemical Engineering, Hunan University, Changsha, PR China

Sasa Zhu
State Key Laboratory of Chemo/Biosensing and Chemometrics, College of Chemistry and Chemical Engineering, Hunan University, Changsha, PR China

Jacek Zielonka
Department of Biophysics and Free Radical Research Center, Medical College of Wisconsin, Milwaukee, Wisconsin, USA

PREFACE

The identification of hydrogen peroxide in regulation of cell signaling and gene expression was a significant breakthrough in oxygen biology. Hydrogen peroxide is probably the most important redox signaling molecule that, among others, can activate NFκB, Nrf2, and other universal transcription factors and is involved in the regulation of insulin and MAPK signaling. These pleiotropic effects of hydrogen peroxide are largely accounted for by changes in the thiol/disulfide status of the cell, an important determinant of the cell's redox status. Moreover, disruption of redox signaling and control recognizes the occurrence of compartmentalized cell redox circuits.

Hydrogen peroxide signaling has been of central importance in cell research for some time, and some previous volumes of *Methods in Enzymology* have covered in part some aspects of the physiological roles of hydrogen peroxide. However, there have been new developments and techniques that warrant these three volumes of *Methods in Enzymology*, which were designed to be the premier place for a compendium of hydrogen peroxide detection and delivery methods, microdomain imaging, and determinants of hydrogen peroxide steady-state levels; in addition, the role of hydrogen peroxide in cellular processes entailing redox regulation of cell signaling and transcription was covered by experts in mammalian and plant biochemistry and physiology.

In bringing this volume to fruition, credit must be given to the experts in various aspects of hydrogen peroxide signaling research, whose thorough and innovative work is the basis of these three *Methods in Enzymology* volumes. Special thanks to the Advisory Board Members—Christopher J. Chang, So Goo Rhee, and Balyanaraman Kalyanaram—who provided guidance in the selection of topics and contributors. We hope that these volumes would be of help to both new and established investigators in this field.

Enrique Cadenas
Lester Packer
May 2013

METHODS IN ENZYMOLOGY

VOLUME I. Preparation and Assay of Enzymes
Edited by SIDNEY P. COLOWICK AND NATHAN O. KAPLAN

VOLUME II. Preparation and Assay of Enzymes
Edited by SIDNEY P. COLOWICK AND NATHAN O. KAPLAN

VOLUME III. Preparation and Assay of Substrates
Edited by SIDNEY P. COLOWICK AND NATHAN O. KAPLAN

VOLUME IV. Special Techniques for the Enzymologist
Edited by SIDNEY P. COLOWICK AND NATHAN O. KAPLAN

VOLUME V. Preparation and Assay of Enzymes
Edited by SIDNEY P. COLOWICK AND NATHAN O. KAPLAN

VOLUME VI. Preparation and Assay of Enzymes (*Continued*)
Preparation and Assay of Substrates
Special Techniques
Edited by SIDNEY P. COLOWICK AND NATHAN O. KAPLAN

VOLUME VII. Cumulative Subject Index
Edited by SIDNEY P. COLOWICK AND NATHAN O. KAPLAN

VOLUME VIII. Complex Carbohydrates
Edited by ELIZABETH F. NEUFELD AND VICTOR GINSBURG

VOLUME IX. Carbohydrate Metabolism
Edited by WILLIS A. WOOD

VOLUME X. Oxidation and Phosphorylation
Edited by RONALD W. ESTABROOK AND MAYNARD E. PULLMAN

VOLUME XI. Enzyme Structure
Edited by C. H. W. HIRS

VOLUME XII. Nucleic Acids (Parts A and B)
Edited by LAWRENCE GROSSMAN AND KIVIE MOLDAVE

VOLUME XIII. Citric Acid Cycle
Edited by J. M. LOWENSTEIN

VOLUME XIV. Lipids
Edited by J. M. LOWENSTEIN

VOLUME XV. Steroids and Terpenoids
Edited by RAYMOND B. CLAYTON

VOLUME XVI. Fast Reactions
Edited by KENNETH KUSTIN

VOLUME XVII. Metabolism of Amino Acids and Amines (Parts A and B)
Edited by HERBERT TABOR AND CELIA WHITE TABOR

VOLUME XVIII. Vitamins and Coenzymes (Parts A, B, and C)
Edited by DONALD B. MCCORMICK AND LEMUEL D. WRIGHT

VOLUME XIX. Proteolytic Enzymes
Edited by GERTRUDE E. PERLMANN AND LASZLO LORAND

VOLUME XX. Nucleic Acids and Protein Synthesis (Part C)
Edited by KIVIE MOLDAVE AND LAWRENCE GROSSMAN

VOLUME XXI. Nucleic Acids (Part D)
Edited by LAWRENCE GROSSMAN AND KIVIE MOLDAVE

VOLUME XXII. Enzyme Purification and Related Techniques
Edited by WILLIAM B. JAKOBY

VOLUME XXIII. Photosynthesis (Part A)
Edited by ANTHONY SAN PIETRO

VOLUME XXIV. Photosynthesis and Nitrogen Fixation (Part B)
Edited by ANTHONY SAN PIETRO

VOLUME XXV. Enzyme Structure (Part B)
Edited by C. H. W. HIRS AND SERGE N. TIMASHEFF

VOLUME XXVI. Enzyme Structure (Part C)
Edited by C. H. W. HIRS AND SERGE N. TIMASHEFF

VOLUME XXVII. Enzyme Structure (Part D)
Edited by C. H. W. HIRS AND SERGE N. TIMASHEFF

VOLUME XXVIII. Complex Carbohydrates (Part B)
Edited by VICTOR GINSBURG

VOLUME XXIX. Nucleic Acids and Protein Synthesis (Part E)
Edited by LAWRENCE GROSSMAN AND KIVIE MOLDAVE

VOLUME XXX. Nucleic Acids and Protein Synthesis (Part F)
Edited by KIVIE MOLDAVE AND LAWRENCE GROSSMAN

VOLUME XXXI. Biomembranes (Part A)
Edited by SIDNEY FLEISCHER AND LESTER PACKER

VOLUME XXXII. Biomembranes (Part B)
Edited by SIDNEY FLEISCHER AND LESTER PACKER

VOLUME XXXIII. Cumulative Subject Index Volumes I-XXX
Edited by MARTHA G. DENNIS AND EDWARD A. DENNIS

VOLUME XXXIV. Affinity Techniques (Enzyme Purification: Part B)
Edited by WILLIAM B. JAKOBY AND MEIR WILCHEK

VOLUME XXXV. Lipids (Part B)
Edited by JOHN M. LOWENSTEIN

VOLUME XXXVI. Hormone Action (Part A: Steroid Hormones)
Edited by BERT W. O'MALLEY AND JOEL G. HARDMAN

VOLUME XXXVII. Hormone Action (Part B: Peptide Hormones)
Edited by BERT W. O'MALLEY AND JOEL G. HARDMAN

VOLUME XXXVIII. Hormone Action (Part C: Cyclic Nucleotides)
Edited by JOEL G. HARDMAN AND BERT W. O'MALLEY

VOLUME XXXIX. Hormone Action (Part D: Isolated Cells, Tissues, and Organ Systems)
Edited by JOEL G. HARDMAN AND BERT W. O'MALLEY

VOLUME XL. Hormone Action (Part E: Nuclear Structure and Function)
Edited by BERT W. O'MALLEY AND JOEL G. HARDMAN

VOLUME XLI. Carbohydrate Metabolism (Part B)
Edited by W. A. WOOD

VOLUME XLII. Carbohydrate Metabolism (Part C)
Edited by W. A. WOOD

VOLUME XLIII. Antibiotics
Edited by JOHN H. HASH

VOLUME XLIV. Immobilized Enzymes
Edited by KLAUS MOSBACH

VOLUME XLV. Proteolytic Enzymes (Part B)
Edited by LASZLO LORAND

VOLUME XLVI. Affinity Labeling
Edited by WILLIAM B. JAKOBY AND MEIR WILCHEK

VOLUME XLVII. Enzyme Structure (Part E)
Edited by C. H. W. HIRS AND SERGE N. TIMASHEFF

VOLUME XLVIII. Enzyme Structure (Part F)
Edited by C. H. W. HIRS AND SERGE N. TIMASHEFF

VOLUME XLIX. Enzyme Structure (Part G)
Edited by C. H. W. HIRS AND SERGE N. TIMASHEFF

VOLUME L. Complex Carbohydrates (Part C)
Edited by VICTOR GINSBURG

VOLUME LI. Purine and Pyrimidine Nucleotide Metabolism
Edited by PATRICIA A. HOFFEE AND MARY ELLEN JONES

VOLUME LII. Biomembranes (Part C: Biological Oxidations)
Edited by SIDNEY FLEISCHER AND LESTER PACKER

VOLUME LIII. Biomembranes (Part D: Biological Oxidations)
Edited by SIDNEY FLEISCHER AND LESTER PACKER

VOLUME LIV. Biomembranes (Part E: Biological Oxidations)
Edited by SIDNEY FLEISCHER AND LESTER PACKER

VOLUME LV. Biomembranes (Part F: Bioenergetics)
Edited by SIDNEY FLEISCHER AND LESTER PACKER

VOLUME LVI. Biomembranes (Part G: Bioenergetics)
Edited by SIDNEY FLEISCHER AND LESTER PACKER

VOLUME LVII. Bioluminescence and Chemiluminescence
Edited by MARLENE A. DELUCA

VOLUME LVIII. Cell Culture
Edited by WILLIAM B. JAKOBY AND IRA PASTAN

VOLUME LIX. Nucleic Acids and Protein Synthesis (Part G)
Edited by KIVIE MOLDAVE AND LAWRENCE GROSSMAN

VOLUME LX. Nucleic Acids and Protein Synthesis (Part H)
Edited by KIVIE MOLDAVE AND LAWRENCE GROSSMAN

VOLUME 61. Enzyme Structure (Part H)
Edited by C. H. W. HIRS AND SERGE N. TIMASHEFF

VOLUME 62. Vitamins and Coenzymes (Part D)
Edited by DONALD B. MCCORMICK AND LEMUEL D. WRIGHT

VOLUME 63. Enzyme Kinetics and Mechanism (Part A: Initial Rate and Inhibitor Methods)
Edited by DANIEL L. PURICH

Volume 64. Enzyme Kinetics and Mechanism
(Part B: Isotopic Probes and Complex Enzyme Systems)
Edited by Daniel L. Purich

Volume 65. Nucleic Acids (Part I)
Edited by Lawrence Grossman and Kivie Moldave

Volume 66. Vitamins and Coenzymes (Part E)
Edited by Donald B. McCormick and Lemuel D. Wright

Volume 67. Vitamins and Coenzymes (Part F)
Edited by Donald B. McCormick and Lemuel D. Wright

Volume 68. Recombinant DNA
Edited by Ray Wu

Volume 69. Photosynthesis and Nitrogen Fixation (Part C)
Edited by Anthony San Pietro

Volume 70. Immunochemical Techniques (Part A)
Edited by Helen Van Vunakis and John J. Langone

Volume 71. Lipids (Part C)
Edited by John M. Lowenstein

Volume 72. Lipids (Part D)
Edited by John M. Lowenstein

Volume 73. Immunochemical Techniques (Part B)
Edited by John J. Langone and Helen Van Vunakis

Volume 74. Immunochemical Techniques (Part C)
Edited by John J. Langone and Helen Van Vunakis

Volume 75. Cumulative Subject Index Volumes XXXI, XXXII, XXXIV–LX
Edited by Edward A. Dennis and Martha G. Dennis

Volume 76. Hemoglobins
Edited by Eraldo Antonini, Luigi Rossi-Bernardi, and Emilia Chiancone

Volume 77. Detoxication and Drug Metabolism
Edited by William B. Jakoby

Volume 78. Interferons (Part A)
Edited by Sidney Pestka

VOLUME 79. Interferons (Part B)
Edited by SIDNEY PESTKA

VOLUME 80. Proteolytic Enzymes (Part C)
Edited by LASZLO LORAND

VOLUME 81. Biomembranes (Part H: Visual Pigments and Purple Membranes, I)
Edited by LESTER PACKER

VOLUME 82. Structural and Contractile Proteins (Part A: Extracellular Matrix)
Edited by LEON W. CUNNINGHAM AND DIXIE W. FREDERIKSEN

VOLUME 83. Complex Carbohydrates (Part D)
Edited by VICTOR GINSBURG

VOLUME 84. Immunochemical Techniques (Part D: Selected Immunoassays)
Edited by JOHN J. LANGONE AND HELEN VAN VUNAKIS

VOLUME 85. Structural and Contractile Proteins (Part B: The Contractile Apparatus and the Cytoskeleton)
Edited by DIXIE W. FREDERIKSEN AND LEON W. CUNNINGHAM

VOLUME 86. Prostaglandins and Arachidonate Metabolites
Edited by WILLIAM E. M. LANDS AND WILLIAM L. SMITH

VOLUME 87. Enzyme Kinetics and Mechanism (Part C: Intermediates, Stereo-chemistry, and Rate Studies)
Edited by DANIEL L. PURICH

VOLUME 88. Biomembranes (Part I: Visual Pigments and Purple Membranes, II)
Edited by LESTER PACKER

VOLUME 89. Carbohydrate Metabolism (Part D)
Edited by WILLIS A. WOOD

VOLUME 90. Carbohydrate Metabolism (Part E)
Edited by WILLIS A. WOOD

VOLUME 91. Enzyme Structure (Part I)
Edited by C. H. W. HIRS AND SERGE N. TIMASHEFF

VOLUME 92. Immunochemical Techniques (Part E: Monoclonal Antibodies and General Immunoassay Methods)
Edited by JOHN J. LANGONE AND HELEN VAN VUNAKIS

Volume 93. Immunochemical Techniques (Part F: Conventional Antibodies, Fc Receptors, and Cytotoxicity)
Edited by John J. Langone and Helen Van Vunakis

Volume 94. Polyamines
Edited by Herbert Tabor and Celia White Tabor

Volume 95. Cumulative Subject Index Volumes 61–74, 76–80
Edited by Edward A. Dennis and Martha G. Dennis

Volume 96. Biomembranes [Part J: Membrane Biogenesis: Assembly and Targeting (General Methods; Eukaryotes)]
Edited by Sidney Fleischer and Becca Fleischer

Volume 97. Biomembranes [Part K: Membrane Biogenesis: Assembly and Targeting (Prokaryotes, Mitochondria, and Chloroplasts)]
Edited by Sidney Fleischer and Becca Fleischer

Volume 98. Biomembranes (Part L: Membrane Biogenesis: Processing and Recycling)
Edited by Sidney Fleischer and Becca Fleischer

Volume 99. Hormone Action (Part F: Protein Kinases)
Edited by Jackie D. Corbin and Joel G. Hardman

Volume 100. Recombinant DNA (Part B)
Edited by Ray Wu, Lawrence Grossman, and Kivie Moldave

Volume 101. Recombinant DNA (Part C)
Edited by Ray Wu, Lawrence Grossman, and Kivie Moldave

Volume 102. Hormone Action (Part G: Calmodulin and Calcium-Binding Proteins)
Edited by Anthony R. Means and Bert W. O'Malley

Volume 103. Hormone Action (Part H: Neuroendocrine Peptides)
Edited by P. Michael Conn

Volume 104. Enzyme Purification and Related Techniques (Part C)
Edited by William B. Jakoby

Volume 105. Oxygen Radicals in Biological Systems
Edited by Lester Packer

Volume 106. Posttranslational Modifications (Part A)
Edited by Finn Wold and Kivie Moldave

VOLUME 107. Posttranslational Modifications (Part B)
Edited by FINN WOLD AND KIVIE MOLDAVE

VOLUME 108. Immunochemical Techniques (Part G: Separation and Characterization of Lymphoid Cells)
Edited by GIOVANNI DI SABATO, JOHN J. LANGONE, AND HELEN VAN VUNAKIS

VOLUME 109. Hormone Action (Part I: Peptide Hormones)
Edited by LUTZ BIRNBAUMER AND BERT W. O'MALLEY

VOLUME 110. Steroids and Isoprenoids (Part A)
Edited by JOHN H. LAW AND HANS C. RILLING

VOLUME 111. Steroids and Isoprenoids (Part B)
Edited by JOHN H. LAW AND HANS C. RILLING

VOLUME 112. Drug and Enzyme Targeting (Part A)
Edited by KENNETH J. WIDDER AND RALPH GREEN

VOLUME 113. Glutamate, Glutamine, Glutathione, and Related Compounds
Edited by ALTON MEISTER

VOLUME 114. Diffraction Methods for Biological Macromolecules (Part A)
Edited by HAROLD W. WYCKOFF, C. H. W. HIRS, AND SERGE N. TIMASHEFF

VOLUME 115. Diffraction Methods for Biological Macromolecules (Part B)
Edited by HAROLD W. WYCKOFF, C. H. W. HIRS, AND SERGE N. TIMASHEFF

VOLUME 116. Immunochemical Techniques
(Part H: Effectors and Mediators of Lymphoid Cell Functions)
Edited by GIOVANNI DI SABATO, JOHN J. LANGONE, AND HELEN VAN VUNAKIS

VOLUME 117. Enzyme Structure (Part J)
Edited by C. H. W. HIRS AND SERGE N. TIMASHEFF

VOLUME 118. Plant Molecular Biology
Edited by ARTHUR WEISSBACH AND HERBERT WEISSBACH

VOLUME 119. Interferons (Part C)
Edited by SIDNEY PESTKA

VOLUME 120. Cumulative Subject Index Volumes 81–94, 96–101

VOLUME 121. Immunochemical Techniques (Part I: Hybridoma Technology and Monoclonal Antibodies)
Edited by JOHN J. LANGONE AND HELEN VAN VUNAKIS

Volume 122. Vitamins and Coenzymes (Part G)
Edited by Frank Chytil and Donald B. McCormick

Volume 123. Vitamins and Coenzymes (Part H)
Edited by Frank Chytil and Donald B. McCormick

Volume 124. Hormone Action (Part J: Neuroendocrine Peptides)
Edited by P. Michael Conn

Volume 125. Biomembranes (Part M: Transport in Bacteria, Mitochondria, and Chloroplasts: General Approaches and Transport Systems)
Edited by Sidney Fleischer and Becca Fleischer

Volume 126. Biomembranes (Part N: Transport in Bacteria, Mitochondria, and Chloroplasts: Protonmotive Force)
Edited by Sidney Fleischer and Becca Fleischer

Volume 127. Biomembranes (Part O: Protons and Water: Structure and Translocation)
Edited by Lester Packer

Volume 128. Plasma Lipoproteins (Part A: Preparation, Structure, and Molecular Biology)
Edited by Jere P. Segrest and John J. Albers

Volume 129. Plasma Lipoproteins (Part B: Characterization, Cell Biology, and Metabolism)
Edited by John J. Albers and Jere P. Segrest

Volume 130. Enzyme Structure (Part K)
Edited by C. H. W. Hirs and Serge N. Timasheff

Volume 131. Enzyme Structure (Part L)
Edited by C. H. W. Hirs and Serge N. Timasheff

Volume 132. Immunochemical Techniques (Part J: Phagocytosis and Cell-Mediated Cytotoxicity)
Edited by Giovanni Di Sabato and Johannes Everse

Volume 133. Bioluminescence and Chemiluminescence (Part B)
Edited by Marlene DeLuca and William D. McElroy

Volume 134. Structural and Contractile Proteins (Part C: The Contractile Apparatus and the Cytoskeleton)
Edited by Richard B. Vallee

Volume 135. Immobilized Enzymes and Cells (Part B)
Edited by Klaus Mosbach

VOLUME 136. Immobilized Enzymes and Cells (Part C)
Edited by KLAUS MOSBACH

VOLUME 137. Immobilized Enzymes and Cells (Part D)
Edited by KLAUS MOSBACH

VOLUME 138. Complex Carbohydrates (Part E)
Edited by VICTOR GINSBURG

VOLUME 139. Cellular Regulators (Part A: Calcium- and Calmodulin-Binding Proteins)
Edited by ANTHONY R. MEANS AND P. MICHAEL CONN

VOLUME 140. Cumulative Subject Index Volumes 102–119, 121–134

VOLUME 141. Cellular Regulators (Part B: Calcium and Lipids)
Edited by P. MICHAEL CONN AND ANTHONY R. MEANS

VOLUME 142. Metabolism of Aromatic Amino Acids and Amines
Edited by SEYMOUR KAUFMAN

VOLUME 143. Sulfur and Sulfur Amino Acids
Edited by WILLIAM B. JAKOBY AND OWEN GRIFFITH

VOLUME 144. Structural and Contractile Proteins (Part D: Extracellular Matrix)
Edited by LEON W. CUNNINGHAM

VOLUME 145. Structural and Contractile Proteins (Part E: Extracellular Matrix)
Edited by LEON W. CUNNINGHAM

VOLUME 146. Peptide Growth Factors (Part A)
Edited by DAVID BARNES AND DAVID A. SIRBASKU

VOLUME 147. Peptide Growth Factors (Part B)
Edited by DAVID BARNES AND DAVID A. SIRBASKU

VOLUME 148. Plant Cell Membranes
Edited by LESTER PACKER AND ROLAND DOUCE

VOLUME 149. Drug and Enzyme Targeting (Part B)
Edited by RALPH GREEN AND KENNETH J. WIDDER

VOLUME 150. Immunochemical Techniques (Part K: *In Vitro* Models of B and T Cell Functions and Lymphoid Cell Receptors)
Edited by GIOVANNI DI SABATO

VOLUME 151. Molecular Genetics of Mammalian Cells
Edited by MICHAEL M. GOTTESMAN

VOLUME 152. Guide to Molecular Cloning Techniques
Edited by SHELBY L. BERGER AND ALAN R. KIMMEL

VOLUME 153. Recombinant DNA (Part D)
Edited by RAY WU AND LAWRENCE GROSSMAN

VOLUME 154. Recombinant DNA (Part E)
Edited by RAY WU AND LAWRENCE GROSSMAN

VOLUME 155. Recombinant DNA (Part F)
Edited by RAY WU

VOLUME 156. Biomembranes (Part P: ATP-Driven Pumps and Related Transport: The Na, K-Pump)
Edited by SIDNEY FLEISCHER AND BECCA FLEISCHER

VOLUME 157. Biomembranes (Part Q: ATP-Driven Pumps and Related Transport: Calcium, Proton, and Potassium Pumps)
Edited by SIDNEY FLEISCHER AND BECCA FLEISCHER

VOLUME 158. Metalloproteins (Part A)
Edited by JAMES F. RIORDAN AND BERT L. VALLEE

VOLUME 159. Initiation and Termination of Cyclic Nucleotide Action
Edited by JACKIE D. CORBIN AND ROGER A. JOHNSON

VOLUME 160. Biomass (Part A: Cellulose and Hemicellulose)
Edited by WILLIS A. WOOD AND SCOTT T. KELLOGG

VOLUME 161. Biomass (Part B: Lignin, Pectin, and Chitin)
Edited by WILLIS A. WOOD AND SCOTT T. KELLOGG

VOLUME 162. Immunochemical Techniques (Part L: Chemotaxis and Inflammation)
Edited by GIOVANNI DI SABATO

VOLUME 163. Immunochemical Techniques (Part M: Chemotaxis and Inflammation)
Edited by GIOVANNI DI SABATO

VOLUME 164. Ribosomes
Edited by HARRY F. NOLLER, JR., AND KIVIE MOLDAVE

VOLUME 165. Microbial Toxins: Tools for Enzymology
Edited by SIDNEY HARSHMAN

VOLUME 166. Branched-Chain Amino Acids
Edited by ROBERT HARRIS AND JOHN R. SOKATCH

VOLUME 167. Cyanobacteria
Edited by LESTER PACKER AND ALEXANDER N. GLAZER

VOLUME 168. Hormone Action (Part K: Neuroendocrine Peptides)
Edited by P. MICHAEL CONN

VOLUME 169. Platelets: Receptors, Adhesion, Secretion (Part A)
Edited by JACEK HAWIGER

VOLUME 170. Nucleosomes
Edited by PAUL M. WASSARMAN AND ROGER D. KORNBERG

VOLUME 171. Biomembranes (Part R: Transport Theory: Cells and Model Membranes)
Edited by SIDNEY FLEISCHER AND BECCA FLEISCHER

VOLUME 172. Biomembranes (Part S: Transport: Membrane Isolation and Characterization)
Edited by SIDNEY FLEISCHER AND BECCA FLEISCHER

VOLUME 173. Biomembranes [Part T: Cellular and Subcellular Transport: Eukaryotic (Nonepithelial) Cells]
Edited by SIDNEY FLEISCHER AND BECCA FLEISCHER

VOLUME 174. Biomembranes [Part U: Cellular and Subcellular Transport: Eukaryotic (Nonepithelial) Cells]
Edited by SIDNEY FLEISCHER AND BECCA FLEISCHER

VOLUME 175. Cumulative Subject Index Volumes 135–139, 141–167

VOLUME 176. Nuclear Magnetic Resonance (Part A: Spectral Techniques and Dynamics)
Edited by NORMAN J. OPPENHEIMER AND THOMAS L. JAMES

VOLUME 177. Nuclear Magnetic Resonance (Part B: Structure and Mechanism)
Edited by NORMAN J. OPPENHEIMER AND THOMAS L. JAMES

VOLUME 178. Antibodies, Antigens, and Molecular Mimicry
Edited by JOHN J. LANGONE

VOLUME 179. Complex Carbohydrates (Part F)
Edited by VICTOR GINSBURG

VOLUME 180. RNA Processing (Part A: General Methods)
Edited by JAMES E. DAHLBERG AND JOHN N. ABELSON

VOLUME 181. RNA Processing (Part B: Specific Methods)
Edited by JAMES E. DAHLBERG AND JOHN N. ABELSON

VOLUME 182. Guide to Protein Purification
Edited by MURRAY P. DEUTSCHER

VOLUME 183. Molecular Evolution: Computer Analysis of Protein and Nucleic Acid Sequences
Edited by RUSSELL F. DOOLITTLE

VOLUME 184. Avidin-Biotin Technology
Edited by MEIR WILCHEK AND EDWARD A. BAYER

VOLUME 185. Gene Expression Technology
Edited by DAVID V. GOEDDEL

VOLUME 186. Oxygen Radicals in Biological Systems (Part B: Oxygen Radicals and Antioxidants)
Edited by LESTER PACKER AND ALEXANDER N. GLAZER

VOLUME 187. Arachidonate Related Lipid Mediators
Edited by ROBERT C. MURPHY AND FRANK A. FITZPATRICK

VOLUME 188. Hydrocarbons and Methylotrophy
Edited by MARY E. LIDSTROM

VOLUME 189. Retinoids (Part A: Molecular and Metabolic Aspects)
Edited by LESTER PACKER

VOLUME 190. Retinoids (Part B: Cell Differentiation and Clinical Applications)
Edited by LESTER PACKER

VOLUME 191. Biomembranes (Part V: Cellular and Subcellular Transport: Epithelial Cells)
Edited by SIDNEY FLEISCHER AND BECCA FLEISCHER

VOLUME 192. Biomembranes (Part W: Cellular and Subcellular Transport: Epithelial Cells)
Edited by SIDNEY FLEISCHER AND BECCA FLEISCHER

VOLUME 193. Mass Spectrometry
Edited by JAMES A. MCCLOSKEY

VOLUME 194. Guide to Yeast Genetics and Molecular Biology
Edited by CHRISTINE GUTHRIE AND GERALD R. FINK

VOLUME 195. Adenylyl Cyclase, G Proteins, and Guanylyl Cyclase
Edited by ROGER A. JOHNSON AND JACKIE D. CORBIN

VOLUME 196. Molecular Motors and the Cytoskeleton
Edited by RICHARD B. VALLEE

VOLUME 197. Phospholipases
Edited by EDWARD A. DENNIS

VOLUME 198. Peptide Growth Factors (Part C)
Edited by DAVID BARNES, J. P. MATHER, AND GORDON H. SATO

VOLUME 199. Cumulative Subject Index Volumes 168–174, 176–194

VOLUME 200. Protein Phosphorylation (Part A: Protein Kinases: Assays, Purification, Antibodies, Functional Analysis, Cloning, and Expression)
Edited by TONY HUNTER AND BARTHOLOMEW M. SEFTON

VOLUME 201. Protein Phosphorylation (Part B: Analysis of Protein Phosphorylation, Protein Kinase Inhibitors, and Protein Phosphatases)
Edited by TONY HUNTER AND BARTHOLOMEW M. SEFTON

VOLUME 202. Molecular Design and Modeling: Concepts and Applications (Part A: Proteins, Peptides, and Enzymes)
Edited by JOHN J. LANGONE

VOLUME 203. Molecular Design and Modeling: Concepts and Applications (Part B: Antibodies and Antigens, Nucleic Acids, Polysaccharides, and Drugs)
Edited by JOHN J. LANGONE

VOLUME 204. Bacterial Genetic Systems
Edited by JEFFREY H. MILLER

VOLUME 205. Metallobiochemistry (Part B: Metallothionein and Related Molecules)
Edited by JAMES F. RIORDAN AND BERT L. VALLEE

VOLUME 206. Cytochrome P450
Edited by MICHAEL R. WATERMAN AND ERIC F. JOHNSON

VOLUME 207. Ion Channels
Edited by BERNARDO RUDY AND LINDA E. IVERSON

VOLUME 208. Protein–DNA Interactions
Edited by ROBERT T. SAUER

VOLUME 209. Phospholipid Biosynthesis
Edited by EDWARD A. DENNIS AND DENNIS E. VANCE

VOLUME 210. Numerical Computer Methods
Edited by LUDWIG BRAND AND MICHAEL L. JOHNSON

VOLUME 211. DNA Structures (Part A: Synthesis and Physical Analysis of DNA)
Edited by DAVID M. J. LILLEY AND JAMES E. DAHLBERG

VOLUME 212. DNA Structures (Part B: Chemical and Electrophoretic Analysis of DNA)
Edited by DAVID M. J. LILLEY AND JAMES E. DAHLBERG

VOLUME 213. Carotenoids (Part A: Chemistry, Separation, Quantitation, and Antioxidation)
Edited by LESTER PACKER

VOLUME 214. Carotenoids (Part B: Metabolism, Genetics, and Biosynthesis)
Edited by LESTER PACKER

VOLUME 215. Platelets: Receptors, Adhesion, Secretion (Part B)
Edited by JACEK J. HAWIGER

VOLUME 216. Recombinant DNA (Part G)
Edited by RAY WU

VOLUME 217. Recombinant DNA (Part H)
Edited by RAY WU

VOLUME 218. Recombinant DNA (Part I)
Edited by RAY WU

VOLUME 219. Reconstitution of Intracellular Transport
Edited by JAMES E. ROTHMAN

VOLUME 220. Membrane Fusion Techniques (Part A)
Edited by NEJAT DÜZGÜNEŞ

VOLUME 221. Membrane Fusion Techniques (Part B)
Edited by NEJAT DÜZGÜNEŞ

VOLUME 222. Proteolytic Enzymes in Coagulation, Fibrinolysis, and Complement Activation (Part A: Mammalian Blood Coagulation

Factors and Inhibitors)
Edited by Laszlo Lorand and Kenneth G. Mann

Volume 223. Proteolytic Enzymes in Coagulation, Fibrinolysis, and Complement Activation (Part B: Complement Activation, Fibrinolysis, and Nonmammalian Blood Coagulation Factors)
Edited by Laszlo Lorand and Kenneth G. Mann

Volume 224. Molecular Evolution: Producing the Biochemical Data
Edited by Elizabeth Anne Zimmer, Thomas J. White, Rebecca L. Cann, and Allan C. Wilson

Volume 225. Guide to Techniques in Mouse Development
Edited by Paul M. Wassarman and Melvin L. DePamphilis

Volume 226. Metallobiochemistry (Part C: Spectroscopic and Physical Methods for Probing Metal Ion Environments in Metalloenzymes and Metalloproteins)
Edited by James F. Riordan and Bert L. Vallee

Volume 227. Metallobiochemistry (Part D: Physical and Spectroscopic Methods for Probing Metal Ion Environments in Metalloproteins)
Edited by James F. Riordan and Bert L. Vallee

Volume 228. Aqueous Two-Phase Systems
Edited by Harry Walter and Göte Johansson

Volume 229. Cumulative Subject Index Volumes 195–198, 200–227

Volume 230. Guide to Techniques in Glycobiology
Edited by William J. Lennarz and Gerald W. Hart

Volume 231. Hemoglobins (Part B: Biochemical and Analytical Methods)
Edited by Johannes Everse, Kim D. Vandegriff, and Robert M. Winslow

Volume 232. Hemoglobins (Part C: Biophysical Methods)
Edited by Johannes Everse, Kim D. Vandegriff, and Robert M. Winslow

Volume 233. Oxygen Radicals in Biological Systems (Part C)
Edited by Lester Packer

Volume 234. Oxygen Radicals in Biological Systems (Part D)
Edited by Lester Packer

Volume 235. Bacterial Pathogenesis (Part A: Identification and Regulation of Virulence Factors)
Edited by Virginia L. Clark and Patrik M. Bavoil

Volume 236. Bacterial Pathogenesis (Part B: Integration of Pathogenic Bacteria with Host Cells)
Edited by Virginia L. Clark and Patrik M. Bavoil

Volume 237. Heterotrimeric G Proteins
Edited by Ravi Iyengar

Volume 238. Heterotrimeric G-Protein Effectors
Edited by Ravi Iyengar

Volume 239. Nuclear Magnetic Resonance (Part C)
Edited by Thomas L. James and Norman J. Oppenheimer

Volume 240. Numerical Computer Methods (Part B)
Edited by Michael L. Johnson and Ludwig Brand

Volume 241. Retroviral Proteases
Edited by Lawrence C. Kuo and Jules A. Shafer

Volume 242. Neoglycoconjugates (Part A)
Edited by Y. C. Lee and Reiko T. Lee

Volume 243. Inorganic Microbial Sulfur Metabolism
Edited by Harry D. Peck, Jr., and Jean LeGall

Volume 244. Proteolytic Enzymes: Serine and Cysteine Peptidases
Edited by Alan J. Barrett

Volume 245. Extracellular Matrix Components
Edited by E. Ruoslahti and E. Engvall

Volume 246. Biochemical Spectroscopy
Edited by Kenneth Sauer

Volume 247. Neoglycoconjugates (Part B: Biomedical Applications)
Edited by Y. C. Lee and Reiko T. Lee

Volume 248. Proteolytic Enzymes: Aspartic and Metallo Peptidases
Edited by Alan J. Barrett

Volume 249. Enzyme Kinetics and Mechanism (Part D: Developments in Enzyme Dynamics)
Edited by Daniel L. Purich

Volume 250. Lipid Modifications of Proteins
Edited by Patrick J. Casey and Janice E. Buss

VOLUME 251. Biothiols (Part A: Monothiols and Dithiols, Protein Thiols, and Thiyl Radicals)
Edited by LESTER PACKER

VOLUME 252. Biothiols (Part B: Glutathione and Thioredoxin; Thiols in Signal Transduction and Gene Regulation)
Edited by LESTER PACKER

VOLUME 253. Adhesion of Microbial Pathogens
Edited by RON J. DOYLE AND ITZHAK OFEK

VOLUME 254. Oncogene Techniques
Edited by PETER K. VOGT AND INDER M. VERMA

VOLUME 255. Small GTPases and Their Regulators (Part A: Ras Family)
Edited by W. E. BALCH, CHANNING J. DER, AND ALAN HALL

VOLUME 256. Small GTPases and Their Regulators (Part B: Rho Family)
Edited by W. E. BALCH, CHANNING J. DER, AND ALAN HALL

VOLUME 257. Small GTPases and Their Regulators (Part C: Proteins Involved in Transport)
Edited by W. E. BALCH, CHANNING J. DER, AND ALAN HALL

VOLUME 258. Redox-Active Amino Acids in Biology
Edited by JUDITH P. KLINMAN

VOLUME 259. Energetics of Biological Macromolecules
Edited by MICHAEL L. JOHNSON AND GARY K. ACKERS

VOLUME 260. Mitochondrial Biogenesis and Genetics (Part A)
Edited by GIUSEPPE M. ATTARDI AND ANNE CHOMYN

VOLUME 261. Nuclear Magnetic Resonance and Nucleic Acids
Edited by THOMAS L. JAMES

VOLUME 262. DNA Replication
Edited by JUDITH L. CAMPBELL

VOLUME 263. Plasma Lipoproteins (Part C: Quantitation)
Edited by WILLIAM A. BRADLEY, SANDRA H. GIANTURCO, AND JERE P. SEGREST

VOLUME 264. Mitochondrial Biogenesis and Genetics (Part B)
Edited by GIUSEPPE M. ATTARDI AND ANNE CHOMYN

VOLUME 265. Cumulative Subject Index Volumes 228, 230–262

Volume 266. Computer Methods for Macromolecular Sequence Analysis
Edited by Russell F. Doolittle

Volume 267. Combinatorial Chemistry
Edited by John N. Abelson

Volume 268. Nitric Oxide (Part A: Sources and Detection of NO; NO Synthase)
Edited by Lester Packer

Volume 269. Nitric Oxide (Part B: Physiological and Pathological Processes)
Edited by Lester Packer

Volume 270. High Resolution Separation and Analysis of Biological Macromolecules (Part A: Fundamentals)
Edited by Barry L. Karger and William S. Hancock

Volume 271. High Resolution Separation and Analysis of Biological Macromolecules (Part B: Applications)
Edited by Barry L. Karger and William S. Hancock

Volume 272. Cytochrome P450 (Part B)
Edited by Eric F. Johnson and Michael R. Waterman

Volume 273. RNA Polymerase and Associated Factors (Part A)
Edited by Sankar Adhya

Volume 274. RNA Polymerase and Associated Factors (Part B)
Edited by Sankar Adhya

Volume 275. Viral Polymerases and Related Proteins
Edited by Lawrence C. Kuo, David B. Olsen, and Steven S. Carroll

Volume 276. Macromolecular Crystallography (Part A)
Edited by Charles W. Carter, Jr., and Robert M. Sweet

Volume 277. Macromolecular Crystallography (Part B)
Edited by Charles W. Carter, Jr., and Robert M. Sweet

Volume 278. Fluorescence Spectroscopy
Edited by Ludwig Brand and Michael L. Johnson

Volume 279. Vitamins and Coenzymes (Part I)
Edited by Donald B. McCormick, John W. Suttie, and Conrad Wagner

Volume 280. Vitamins and Coenzymes (Part J)
Edited by Donald B. McCormick, John W. Suttie, and Conrad Wagner

VOLUME 281. Vitamins and Coenzymes (Part K)
Edited by DONALD B. MCCORMICK, JOHN W. SUTTIE, AND CONRAD WAGNER

VOLUME 282. Vitamins and Coenzymes (Part L)
Edited by DONALD B. MCCORMICK, JOHN W. SUTTIE, AND CONRAD WAGNER

VOLUME 283. Cell Cycle Control
Edited by WILLIAM G. DUNPHY

VOLUME 284. Lipases (Part A: Biotechnology)
Edited by BYRON RUBIN AND EDWARD A. DENNIS

VOLUME 285. Cumulative Subject Index Volumes 263, 264, 266–284, 286–289

VOLUME 286. Lipases (Part B: Enzyme Characterization and Utilization)
Edited by BYRON RUBIN AND EDWARD A. DENNIS

VOLUME 287. Chemokines
Edited by RICHARD HORUK

VOLUME 288. Chemokine Receptors
Edited by RICHARD HORUK

VOLUME 289. Solid Phase Peptide Synthesis
Edited by GREGG B. FIELDS

VOLUME 290. Molecular Chaperones
Edited by GEORGE H. LORIMER AND THOMAS BALDWIN

VOLUME 291. Caged Compounds
Edited by GERARD MARRIOTT

VOLUME 292. ABC Transporters: Biochemical, Cellular, and Molecular Aspects
Edited by SURESH V. AMBUDKAR AND MICHAEL M. GOTTESMAN

VOLUME 293. Ion Channels (Part B)
Edited by P. MICHAEL CONN

VOLUME 294. Ion Channels (Part C)
Edited by P. MICHAEL CONN

VOLUME 295. Energetics of Biological Macromolecules (Part B)
Edited by GARY K. ACKERS AND MICHAEL L. JOHNSON

VOLUME 296. Neurotransmitter Transporters
Edited by SUSAN G. AMARA

VOLUME 297. Photosynthesis: Molecular Biology of Energy Capture
Edited by LEE MCINTOSH

VOLUME 298. Molecular Motors and the Cytoskeleton (Part B)
Edited by RICHARD B. VALLEE

VOLUME 299. Oxidants and Antioxidants (Part A)
Edited by LESTER PACKER

VOLUME 300. Oxidants and Antioxidants (Part B)
Edited by LESTER PACKER

VOLUME 301. Nitric Oxide: Biological and Antioxidant Activities (Part C)
Edited by LESTER PACKER

VOLUME 302. Green Fluorescent Protein
Edited by P. MICHAEL CONN

VOLUME 303. cDNA Preparation and Display
Edited by SHERMAN M. WEISSMAN

VOLUME 304. Chromatin
Edited by PAUL M. WASSARMAN AND ALAN P. WOLFFE

VOLUME 305. Bioluminescence and Chemiluminescence (Part C)
Edited by THOMAS O. BALDWIN AND MIRIAM M. ZIEGLER

VOLUME 306. Expression of Recombinant Genes in Eukaryotic Systems
Edited by JOSEPH C. GLORIOSO AND MARTIN C. SCHMIDT

VOLUME 307. Confocal Microscopy
Edited by P. MICHAEL CONN

VOLUME 308. Enzyme Kinetics and Mechanism (Part E: Energetics of Enzyme Catalysis)
Edited by DANIEL L. PURICH AND VERN L. SCHRAMM

VOLUME 309. Amyloid, Prions, and Other Protein Aggregates
Edited by RONALD WETZEL

VOLUME 310. Biofilms
Edited by RON J. DOYLE

VOLUME 311. Sphingolipid Metabolism and Cell Signaling (Part A)
Edited by ALFRED H. MERRILL, JR., AND YUSUF A. HANNUN

VOLUME 312. Sphingolipid Metabolism and Cell Signaling (Part B)
Edited by ALFRED H. MERRILL, JR., AND YUSUF A. HANNUN

VOLUME 313. Antisense Technology
(Part A: General Methods, Methods of Delivery, and RNA Studies)
Edited by M. IAN PHILLIPS

VOLUME 314. Antisense Technology (Part B: Applications)
Edited by M. IAN PHILLIPS

VOLUME 315. Vertebrate Phototransduction and the Visual Cycle
(Part A)
Edited by KRZYSZTOF PALCZEWSKI

VOLUME 316. Vertebrate Phototransduction and the Visual Cycle (Part B)
Edited by KRZYSZTOF PALCZEWSKI

VOLUME 317. RNA–Ligand Interactions (Part A: Structural Biology Methods)
Edited by DANIEL W. CELANDER AND JOHN N. ABELSON

VOLUME 318. RNA–Ligand Interactions (Part B: Molecular Biology Methods)
Edited by DANIEL W. CELANDER AND JOHN N. ABELSON

VOLUME 319. Singlet Oxygen, UV-A, and Ozone
Edited by LESTER PACKER AND HELMUT SIES

VOLUME 320. Cumulative Subject Index Volumes 290–319

VOLUME 321. Numerical Computer Methods (Part C)
Edited by MICHAEL L. JOHNSON AND LUDWIG BRAND

VOLUME 322. Apoptosis
Edited by JOHN C. REED

VOLUME 323. Energetics of Biological Macromolecules (Part C)
Edited by MICHAEL L. JOHNSON AND GARY K. ACKERS

VOLUME 324. Branched-Chain Amino Acids (Part B)
Edited by ROBERT A. HARRIS AND JOHN R. SOKATCH

VOLUME 325. Regulators and Effectors of Small GTPases
(Part D: Rho Family)
Edited by W. E. BALCH, CHANNING J. DER, AND ALAN HALL

VOLUME 326. Applications of Chimeric Genes and Hybrid Proteins
(Part A: Gene Expression and Protein Purification)
Edited by JEREMY THORNER, SCOTT D. EMR, AND JOHN N. ABELSON

VOLUME 327. Applications of Chimeric Genes and Hybrid Proteins (Part B: Cell Biology and Physiology)
Edited by JEREMY THORNER, SCOTT D. EMR, AND JOHN N. ABELSON

VOLUME 328. Applications of Chimeric Genes and Hybrid Proteins (Part C: Protein–Protein Interactions and Genomics)
Edited by JEREMY THORNER, SCOTT D. EMR, AND JOHN N. ABELSON

VOLUME 329. Regulators and Effectors of Small GTPases (Part E: GTPases Involved in Vesicular Traffic)
Edited by W. E. BALCH, CHANNING J. DER, AND ALAN HALL

VOLUME 330. Hyperthermophilic Enzymes (Part A)
Edited by MICHAEL W. W. ADAMS AND ROBERT M. KELLY

VOLUME 331. Hyperthermophilic Enzymes (Part B)
Edited by MICHAEL W. W. ADAMS AND ROBERT M. KELLY

VOLUME 332. Regulators and Effectors of Small GTPases (Part F: Ras Family I)
Edited by W. E. BALCH, CHANNING J. DER, AND ALAN HALL

VOLUME 333. Regulators and Effectors of Small GTPases (Part G: Ras Family II)
Edited by W. E. BALCH, CHANNING J. DER, AND ALAN HALL

VOLUME 334. Hyperthermophilic Enzymes (Part C)
Edited by MICHAEL W. W. ADAMS AND ROBERT M. KELLY

VOLUME 335. Flavonoids and Other Polyphenols
Edited by LESTER PACKER

VOLUME 336. Microbial Growth in Biofilms (Part A: Developmental and Molecular Biological Aspects)
Edited by RON J. DOYLE

VOLUME 337. Microbial Growth in Biofilms (Part B: Special Environments and Physicochemical Aspects)
Edited by RON J. DOYLE

VOLUME 338. Nuclear Magnetic Resonance of Biological Macromolecules (Part A)
Edited by THOMAS L. JAMES, VOLKER DÖTSCH, AND ULI SCHMITZ

VOLUME 339. Nuclear Magnetic Resonance of Biological Macromolecules (Part B)
Edited by THOMAS L. JAMES, VOLKER DÖTSCH, AND ULI SCHMITZ

Volume 340. Drug–Nucleic Acid Interactions
Edited by Jonathan B. Chaires and Michael J. Waring

Volume 341. Ribonucleases (Part A)
Edited by Allen W. Nicholson

Volume 342. Ribonucleases (Part B)
Edited by Allen W. Nicholson

Volume 343. G Protein Pathways (Part A: Receptors)
Edited by Ravi Iyengar and John D. Hildebrandt

Volume 344. G Protein Pathways (Part B: G Proteins and Their Regulators)
Edited by Ravi Iyengar and John D. Hildebrandt

Volume 345. G Protein Pathways (Part C: Effector Mechanisms)
Edited by Ravi Iyengar and John D. Hildebrandt

Volume 346. Gene Therapy Methods
Edited by M. Ian Phillips

Volume 347. Protein Sensors and Reactive Oxygen Species (Part A: Selenoproteins and Thioredoxin)
Edited by Helmut Sies and Lester Packer

Volume 348. Protein Sensors and Reactive Oxygen Species (Part B: Thiol Enzymes and Proteins)
Edited by Helmut Sies and Lester Packer

Volume 349. Superoxide Dismutase
Edited by Lester Packer

Volume 350. Guide to Yeast Genetics and Molecular and Cell Biology (Part B)
Edited by Christine Guthrie and Gerald R. Fink

Volume 351. Guide to Yeast Genetics and Molecular and Cell Biology (Part C)
Edited by Christine Guthrie and Gerald R. Fink

Volume 352. Redox Cell Biology and Genetics (Part A)
Edited by Chandan K. Sen and Lester Packer

Volume 353. Redox Cell Biology and Genetics (Part B)
Edited by Chandan K. Sen and Lester Packer

Volume 354. Enzyme Kinetics and Mechanisms (Part F: Detection and Characterization of Enzyme Reaction Intermediates)
Edited by Daniel L. Purich

Volume 355. Cumulative Subject Index Volumes 321–354

Volume 356. Laser Capture Microscopy and Microdissection
Edited by P. Michael Conn

Volume 357. Cytochrome P450, Part C
Edited by Eric F. Johnson and Michael R. Waterman

Volume 358. Bacterial Pathogenesis (Part C: Identification, Regulation, and Function of Virulence Factors)
Edited by Virginia L. Clark and Patrik M. Bavoil

Volume 359. Nitric Oxide (Part D)
Edited by Enrique Cadenas and Lester Packer

Volume 360. Biophotonics (Part A)
Edited by Gerard Marriott and Ian Parker

Volume 361. Biophotonics (Part B)
Edited by Gerard Marriott and Ian Parker

Volume 362. Recognition of Carbohydrates in Biological Systems (Part A)
Edited by Yuan C. Lee and Reiko T. Lee

Volume 363. Recognition of Carbohydrates in Biological Systems (Part B)
Edited by Yuan C. Lee and Reiko T. Lee

Volume 364. Nuclear Receptors
Edited by David W. Russell and David J. Mangelsdorf

Volume 365. Differentiation of Embryonic Stem Cells
Edited by Paul M. Wassauman and Gordon M. Keller

Volume 366. Protein Phosphatases
Edited by Susanne Klumpp and Josef Krieglstein

Volume 367. Liposomes (Part A)
Edited by Nejat Düzgüneş

Volume 368. Macromolecular Crystallography (Part C)
Edited by Charles W. Carter, Jr., and Robert M. Sweet

Volume 369. Combinational Chemistry (Part B)
Edited by Guillermo A. Morales and Barry A. Bunin

Volume 370. RNA Polymerases and Associated Factors (Part C)
Edited by Sankar L. Adhya and Susan Garges

Volume 371. RNA Polymerases and Associated Factors (Part D)
Edited by Sankar L. Adhya and Susan Garges

Volume 372. Liposomes (Part B)
Edited by Nejat Düzgüneş

Volume 373. Liposomes (Part C)
Edited by Nejat Düzgüneş

Volume 374. Macromolecular Crystallography (Part D)
Edited by Charles W. Carter, Jr., and Robert W. Sweet

Volume 375. Chromatin and Chromatin Remodeling Enzymes (Part A)
Edited by C. David Allis and Carl Wu

Volume 376. Chromatin and Chromatin Remodeling Enzymes (Part B)
Edited by C. David Allis and Carl Wu

Volume 377. Chromatin and Chromatin Remodeling Enzymes (Part C)
Edited by C. David Allis and Carl Wu

Volume 378. Quinones and Quinone Enzymes (Part A)
Edited by Helmut Sies and Lester Packer

Volume 379. Energetics of Biological Macromolecules (Part D)
Edited by Jo M. Holt, Michael L. Johnson, and Gary K. Ackers

Volume 380. Energetics of Biological Macromolecules (Part E)
Edited by Jo M. Holt, Michael L. Johnson, and Gary K. Ackers

Volume 381. Oxygen Sensing
Edited by Chandan K. Sen and Gregg L. Semenza

Volume 382. Quinones and Quinone Enzymes (Part B)
Edited by Helmut Sies and Lester Packer

Volume 383. Numerical Computer Methods (Part D)
Edited by Ludwig Brand and Michael L. Johnson

Volume 384. Numerical Computer Methods (Part E)
Edited by Ludwig Brand and Michael L. Johnson

Volume 385. Imaging in Biological Research (Part A)
Edited by P. Michael Conn

Volume 386. Imaging in Biological Research (Part B)
Edited by P. Michael Conn

VOLUME 387. Liposomes (Part D)
Edited by NEJAT DÜZGÜNEŞ

VOLUME 388. Protein Engineering
Edited by DAN E. ROBERTSON AND JOSEPH P. NOEL

VOLUME 389. Regulators of G-Protein Signaling (Part A)
Edited by DAVID P. SIDEROVSKI

VOLUME 390. Regulators of G-Protein Signaling (Part B)
Edited by DAVID P. SIDEROVSKI

VOLUME 391. Liposomes (Part E)
Edited by NEJAT DÜZGÜNEŞ

VOLUME 392. RNA Interference
Edited by ENGELKE ROSSI

VOLUME 393. Circadian Rhythms
Edited by MICHAEL W. YOUNG

VOLUME 394. Nuclear Magnetic Resonance of Biological Macromolecules (Part C)
Edited by THOMAS L. JAMES

VOLUME 395. Producing the Biochemical Data (Part B)
Edited by ELIZABETH A. ZIMMER AND ERIC H. ROALSON

VOLUME 396. Nitric Oxide (Part E)
Edited by LESTER PACKER AND ENRIQUE CADENAS

VOLUME 397. Environmental Microbiology
Edited by JARED R. LEADBETTER

VOLUME 398. Ubiquitin and Protein Degradation (Part A)
Edited by RAYMOND J. DESHAIES

VOLUME 399. Ubiquitin and Protein Degradation (Part B)
Edited by RAYMOND J. DESHAIES

VOLUME 400. Phase II Conjugation Enzymes and Transport Systems
Edited by HELMUT SIES AND LESTER PACKER

VOLUME 401. Glutathione Transferases and Gamma Glutamyl Transpeptidases
Edited by HELMUT SIES AND LESTER PACKER

VOLUME 402. Biological Mass Spectrometry
Edited by A. L. BURLINGAME

Volume 403. GTPases Regulating Membrane Targeting and Fusion
Edited by William E. Balch, Channing J. Der, and Alan Hall

Volume 404. GTPases Regulating Membrane Dynamics
Edited by William E. Balch, Channing J. Der, and Alan Hall

Volume 405. Mass Spectrometry: Modified Proteins and Glycoconjugates
Edited by A. L. Burlingame

Volume 406. Regulators and Effectors of Small GTPases: Rho Family
Edited by William E. Balch, Channing J. Der, and Alan Hall

Volume 407. Regulators and Effectors of Small GTPases: Ras Family
Edited by William E. Balch, Channing J. Der, and Alan Hall

Volume 408. DNA Repair (Part A)
Edited by Judith L. Campbell and Paul Modrich

Volume 409. DNA Repair (Part B)
Edited by Judith L. Campbell and Paul Modrich

Volume 410. DNA Microarrays (Part A: Array Platforms and Web-Bench Protocols)
Edited by Alan Kimmel and Brian Oliver

Volume 411. DNA Microarrays (Part B: Databases and Statistics)
Edited by Alan Kimmel and Brian Oliver

Volume 412. Amyloid, Prions, and Other Protein Aggregates (Part B)
Edited by Indu Kheterpal and Ronald Wetzel

Volume 413. Amyloid, Prions, and Other Protein Aggregates (Part C)
Edited by Indu Kheterpal and Ronald Wetzel

Volume 414. Measuring Biological Responses with Automated Microscopy
Edited by James Inglese

Volume 415. Glycobiology
Edited by Minoru Fukuda

Volume 416. Glycomics
Edited by Minoru Fukuda

Volume 417. Functional Glycomics
Edited by Minoru Fukuda

Volume 418. Embryonic Stem Cells
Edited by Irina Klimanskaya and Robert Lanza

VOLUME 419. Adult Stem Cells
Edited by IRINA KLIMANSKAYA AND ROBERT LANZA

VOLUME 420. Stem Cell Tools and Other Experimental Protocols
Edited by IRINA KLIMANSKAYA AND ROBERT LANZA

VOLUME 421. Advanced Bacterial Genetics: Use of Transposons and Phage for Genomic Engineering
Edited by KELLY T. HUGHES

VOLUME 422. Two-Component Signaling Systems, Part A
Edited by MELVIN I. SIMON, BRIAN R. CRANE, AND ALEXANDRINE CRANE

VOLUME 423. Two-Component Signaling Systems, Part B
Edited by MELVIN I. SIMON, BRIAN R. CRANE, AND ALEXANDRINE CRANE

VOLUME 424. RNA Editing
Edited by JONATHA M. GOTT

VOLUME 425. RNA Modification
Edited by JONATHA M. GOTT

VOLUME 426. Integrins
Edited by DAVID CHERESH

VOLUME 427. MicroRNA Methods
Edited by JOHN J. ROSSI

VOLUME 428. Osmosensing and Osmosignaling
Edited by HELMUT SIES AND DIETER HAUSSINGER

VOLUME 429. Translation Initiation: Extract Systems and Molecular Genetics
Edited by JON LORSCH

VOLUME 430. Translation Initiation: Reconstituted Systems and Biophysical Methods
Edited by JON LORSCH

VOLUME 431. Translation Initiation: Cell Biology, High-Throughput and Chemical-Based Approaches
Edited by JON LORSCH

VOLUME 432. Lipidomics and Bioactive Lipids: Mass-Spectrometry–Based Lipid Analysis
Edited by H. ALEX BROWN

VOLUME 433. Lipidomics and Bioactive Lipids: Specialized Analytical Methods and Lipids in Disease
Edited by H. ALEX BROWN

VOLUME 434. Lipidomics and Bioactive Lipids: Lipids and Cell Signaling
Edited by H. ALEX BROWN

VOLUME 435. Oxygen Biology and Hypoxia
Edited by HELMUT SIES AND BERNHARD BRÜNE

VOLUME 436. Globins and Other Nitric Oxide-Reactive Protiens (Part A)
Edited by ROBERT K. POOLE

VOLUME 437. Globins and Other Nitric Oxide-Reactive Protiens (Part B)
Edited by ROBERT K. POOLE

VOLUME 438. Small GTPases in Disease (Part A)
Edited by WILLIAM E. BALCH, CHANNING J. DER, AND ALAN HALL

VOLUME 439. Small GTPases in Disease (Part B)
Edited by WILLIAM E. BALCH, CHANNING J. DER, AND ALAN HALL

VOLUME 440. Nitric Oxide, Part F Oxidative and Nitrosative Stress in Redox Regulation of Cell Signaling
Edited by ENRIQUE CADENAS AND LESTER PACKER

VOLUME 441. Nitric Oxide, Part G Oxidative and Nitrosative Stress in Redox Regulation of Cell Signaling
Edited by ENRIQUE CADENAS AND LESTER PACKER

VOLUME 442. Programmed Cell Death, General Principles for Studying Cell Death (Part A)
Edited by ROYA KHOSRAVI-FAR, ZAHRA ZAKERI, RICHARD A. LOCKSHIN, AND MAURO PIACENTINI

VOLUME 443. Angiogenesis: *In Vitro* Systems
Edited by DAVID A. CHERESH

VOLUME 444. Angiogenesis: *In Vivo* Systems (Part A)
Edited by DAVID A. CHERESH

VOLUME 445. Angiogenesis: *In Vivo* Systems (Part B)
Edited by DAVID A. CHERESH

VOLUME 446. Programmed Cell Death, The Biology and Therapeutic Implications of Cell Death (Part B)
Edited by ROYA KHOSRAVI-FAR, ZAHRA ZAKERI, RICHARD A. LOCKSHIN, AND MAURO PIACENTINI

Volume 447. RNA Turnover in Bacteria, Archaea and Organelles
Edited by Lynne E. Maquat and Cecilia M. Arraiano

Volume 448. RNA Turnover in Eukaryotes: Nucleases, Pathways and Analysis of mRNA Decay
Edited by Lynne E. Maquat and Megerditch Kiledjian

Volume 449. RNA Turnover in Eukaryotes: Analysis of Specialized and Quality Control RNA Decay Pathways
Edited by Lynne E. Maquat and Megerditch Kiledjian

Volume 450. Fluorescence Spectroscopy
Edited by Ludwig Brand and Michael L. Johnson

Volume 451. Autophagy: Lower Eukaryotes and Non-Mammalian Systems (Part A)
Edited by Daniel J. Klionsky

Volume 452. Autophagy in Mammalian Systems (Part B)
Edited by Daniel J. Klionsky

Volume 453. Autophagy in Disease and Clinical Applications (Part C)
Edited by Daniel J. Klionsky

Volume 454. Computer Methods (Part A)
Edited by Michael L. Johnson and Ludwig Brand

Volume 455. Biothermodynamics (Part A)
Edited by Michael L. Johnson, Jo M. Holt, and Gary K. Ackers (Retired)

Volume 456. Mitochondrial Function, Part A: Mitochondrial Electron Transport Complexes and Reactive Oxygen Species
Edited by William S. Allison and Immo E. Scheffler

Volume 457. Mitochondrial Function, Part B: Mitochondrial Protein Kinases, Protein Phosphatases and Mitochondrial Diseases
Edited by William S. Allison and Anne N. Murphy

Volume 458. Complex Enzymes in Microbial Natural Product Biosynthesis, Part A: Overview Articles and Peptides
Edited by David A. Hopwood

Volume 459. Complex Enzymes in Microbial Natural Product Biosynthesis, Part B: Polyketides, Aminocoumarins and Carbohydrates
Edited by David A. Hopwood

Volume 460. Chemokines, Part A
Edited by Tracy M. Handel and Damon J. Hamel

Volume 461. Chemokines, Part B
Edited by Tracy M. Handel and Damon J. Hamel

Volume 462. Non-Natural Amino Acids
Edited by Tom W. Muir and John N. Abelson

Volume 463. Guide to Protein Purification, 2nd Edition
Edited by Richard R. Burgess and Murray P. Deutscher

Volume 464. Liposomes, Part F
Edited by Nejat Düzgüneş

Volume 465. Liposomes, Part G
Edited by Nejat Düzgüneş

Volume 466. Biothermodynamics, Part B
Edited by Michael L. Johnson, Gary K. Ackers, and Jo M. Holt

Volume 467. Computer Methods Part B
Edited by Michael L. Johnson and Ludwig Brand

Volume 468. Biophysical, Chemical, and Functional Probes of RNA Structure, Interactions and Folding: Part A
Edited by Daniel Herschlag

Volume 469. Biophysical, Chemical, and Functional Probes of RNA Structure, Interactions and Folding: Part B
Edited by Daniel Herschlag

Volume 470. Guide to Yeast Genetics: Functional Genomics, Proteomics, and Other Systems Analysis, 2nd Edition
Edited by Gerald Fink, Jonathan Weissman, and Christine Guthrie

Volume 471. Two-Component Signaling Systems, Part C
Edited by Melvin I. Simon, Brian R. Crane, and Alexandrine Crane

Volume 472. Single Molecule Tools, Part A: Fluorescence Based Approaches
Edited by Nils G. Walter

Volume 473. Thiol Redox Transitions in Cell Signaling, Part A Chemistry and Biochemistry of Low Molecular Weight and Protein Thiols
Edited by Enrique Cadenas and Lester Packer

VOLUME 474. Thiol Redox Transitions in Cell Signaling, Part B Cellular Localization and Signaling
Edited by ENRIQUE CADENAS AND LESTER PACKER

VOLUME 475. Single Molecule Tools, Part B: Super-Resolution, Particle Tracking, Multiparameter, and Force Based Methods
Edited by NILS G. WALTER

VOLUME 476. Guide to Techniques in Mouse Development, Part A Mice, Embryos, and Cells, 2nd Edition
Edited by PAUL M. WASSARMAN AND PHILIPPE M. SORIANO

VOLUME 477. Guide to Techniques in Mouse Development, Part B Mouse Molecular Genetics, 2nd Edition
Edited by PAUL M. WASSARMAN AND PHILIPPE M. SORIANO

VOLUME 478. Glycomics
Edited by MINORU FUKUDA

VOLUME 479. Functional Glycomics
Edited by MINORU FUKUDA

VOLUME 480. Glycobiology
Edited by MINORU FUKUDA

VOLUME 481. Cryo-EM, Part A: Sample Preparation and Data Collection
Edited by GRANT J. JENSEN

VOLUME 482. Cryo-EM, Part B: 3-D Reconstruction
Edited by GRANT J. JENSEN

VOLUME 483. Cryo-EM, Part C: Analyses, Interpretation, and Case Studies
Edited by GRANT J. JENSEN

VOLUME 484. Constitutive Activity in Receptors and Other Proteins, Part A
Edited by P. MICHAEL CONN

VOLUME 485. Constitutive Activity in Receptors and Other Proteins, Part B
Edited by P. MICHAEL CONN

VOLUME 486. Research on Nitrification and Related Processes, Part A
Edited by MARTIN G. KLOTZ

VOLUME 487. Computer Methods, Part C
Edited by MICHAEL L. JOHNSON AND LUDWIG BRAND

VOLUME 488. Biothermodynamics, Part C
Edited by MICHAEL L. JOHNSON, JO M. HOLT, AND GARY K. ACKERS

VOLUME 489. The Unfolded Protein Response and Cellular Stress, Part A
Edited by P. MICHAEL CONN

VOLUME 490. The Unfolded Protein Response and Cellular Stress, Part B
Edited by P. MICHAEL CONN

VOLUME 491. The Unfolded Protein Response and Cellular Stress, Part C
Edited by P. MICHAEL CONN

VOLUME 492. Biothermodynamics, Part D
Edited by MICHAEL L. JOHNSON, JO M. HOLT, AND GARY K. ACKERS

VOLUME 493. Fragment-Based Drug Design Tools,
Practical Approaches, and Examples
Edited by LAWRENCE C. KUO

VOLUME 494. Methods in Methane Metabolism, Part A
Methanogenesis
Edited by AMY C. ROSENZWEIG AND STEPHEN W. RAGSDALE

VOLUME 495. Methods in Methane Metabolism, Part B
Methanotrophy
Edited by AMY C. ROSENZWEIG AND STEPHEN W. RAGSDALE

VOLUME 496. Research on Nitrification and Related Processes, Part B
Edited by MARTIN G. KLOTZ AND LISA Y. STEIN

VOLUME 497. Synthetic Biology, Part A
Methods for Part/Device Characterization and Chassis Engineering
Edited by CHRISTOPHER VOIGT

VOLUME 498. Synthetic Biology, Part B
Computer Aided Design and DNA Assembly
Edited by CHRISTOPHER VOIGT

VOLUME 499. Biology of Serpins
Edited by JAMES C. WHISSTOCK AND PHILLIP I. BIRD

VOLUME 500. Methods in Systems Biology
Edited by DANIEL JAMESON, MALKHEY VERMA, AND HANS V. WESTERHOFF

VOLUME 501. Serpin Structure and Evolution
Edited by JAMES C. WHISSTOCK AND PHILLIP I. BIRD

VOLUME 502. Protein Engineering for Therapeutics, Part A
Edited by K. DANE WITTRUP AND GREGORY L. VERDINE

VOLUME 503. Protein Engineering for Therapeutics, Part B
Edited by K. DANE WITTRUP AND GREGORY L. VERDINE

VOLUME 504. Imaging and Spectroscopic Analysis of Living Cells
Optical and Spectroscopic Techniques
Edited by P. MICHAEL CONN

VOLUME 505. Imaging and Spectroscopic Analysis of Living Cells
Live Cell Imaging of Cellular Elements and Functions
Edited by P. MICHAEL CONN

VOLUME 506. Imaging and Spectroscopic Analysis of Living Cells
Imaging Live Cells in Health and Disease
Edited by P. MICHAEL CONN

VOLUME 507. Gene Transfer Vectors for Clinical Application
Edited by THEODORE FRIEDMANN

VOLUME 508. Nanomedicine
Cancer, Diabetes, and Cardiovascular, Central Nervous System, Pulmonary and Inflammatory Diseases
Edited by NEJAT DÜZGÜNEŞ

VOLUME 509. Nanomedicine
Infectious Diseases, Immunotherapy, Diagnostics, Antifibrotics, Toxicology and Gene Medicine
Edited by NEJAT DÜZGÜNEŞ

VOLUME 510. Cellulases
Edited by HARRY J. GILBERT

VOLUME 511. RNA Helicases
Edited by ECKHARD JANKOWSKY

VOLUME 512. Nucleosomes, Histones & Chromatin, Part A
Edited by CARL WU AND C. DAVID ALLIS

VOLUME 513. Nucleosomes, Histones & Chromatin, Part B
Edited by CARL WU AND C. DAVID ALLIS

VOLUME 514. Ghrelin
Edited by MASAYASU KOJIMA AND KENJI KANGAWA

VOLUME 515. Natural Product Biosynthesis by Microorganisms and Plants, Part A
Edited by DAVID A. HOPWOOD

VOLUME 516. Natural Product Biosynthesis by Microorganisms and Plants, Part B
Edited by DAVID A. HOPWOOD

VOLUME 517. Natural Product Biosynthesis by Microorganisms and Plants, Part C
Edited by DAVID A. HOPWOOD

VOLUME 518. Fluorescence Fluctuation Spectroscopy (FFS), Part A
Edited by SERGEY Y. TETIN

VOLUME 519. Fluorescence Fluctuation Spectroscopy (FFS), Part B
Edited by SERGEY Y. TETIN

VOLUME 520. G Protein Couple Receptors
Structure
Edited by P. MICHAEL CONN

VOLUME 521. G Protein Couple Receptors
Trafficking and Oligomerization
Edited by P. MICHAEL CONN

VOLUME 522. G Protein Couple Receptors
Modeling, Activation, Interactions and Virtual Screening
Edited by P. MICHAEL CONN

VOLUME 523. Methods in Protein Design
Edited by AMY E. KEATING

VOLUME 524. Cilia, Part A
Edited by WALLACE F. MARSHALL

VOLUME 525. Cilia, Part B
Edited by WALLACE F. MARSHALL

VOLUME 526. Hydrogen Peroxide and Cell Signaling, Part A
Edited by ENRIQUE CADENAS AND LESTER PACKER

CHAPTER ONE

Photooxidation of Amplex Red to Resorufin: Implications of Exposing the Amplex Red Assay to Light

Fiona A. Summers*, Baozhong Zhao†, Douglas Ganini*, Ronald P. Mason*,1

*Laboratory of Toxicology and Pharmacology, National Institute of Environmental Health Sciences, NIH, Research Triangle Park, North Carolina, USA
†Section of Dermatology, Department of Medicine, University of Chicago, Chicago, Illinois, USA
1Corresponding author: e-mail address: mason4@niehs.nih.gov

Contents

1. Introduction 2
2. Amplex Red Assay and Its Possible Artifacts due to Light Exposure 3
   2.1 Light, resorufin, and oxygen are involved in the artifactual formation of resorufin in Amplex Red exposed to light 3
   2.2 Amplex Red exposed to room light in the presence of HRP and H_2O_2 6
   2.3 Artifactual measurement of H_2O_2 released by cells exposed to UV light using the Amplex Red assay 9
   2.4 Controversy over the characterization of MnSOD as a peroxidase 10
3. Experimental Considerations 12
Acknowledgments 16
References 16

Abstract

The Amplex Red assay, a fluorescent assay for the detection of H_2O_2, relies on the reaction of H_2O_2, which, in the presence of horseradish peroxidase, oxidizes the colorless, nonfluorescent, Amplex Red with a 1:1 stoichiometry to form the colored, fluorescent resorufin. We have found that resorufin is artifactually formed when Amplex Red is exposed to light. This photochemistry is initiated by trace amounts of resorufin present in Amplex Red stock solutions. ESR spin-trapping studies have demonstrated that superoxide radical is an intermediate in this process. Oxygen consumption measurements further confirmed that superoxide and H_2O_2 were artifactually produced by the photooxidation of Amplex Red. The artifactual formation of resorufin was also significantly increased by the presence of superoxide dismutase or HRP. This photooxidation process leads to a less sensitive assay for H_2O_2 under ambient light exposure and potentially invalid measurements under high energy exposure such as UVA irradiation. In general,

Methods in Enzymology, Volume 526
ISSN 0076-6879
http://dx.doi.org/10.1016/B978-0-12-405883-5.00001-6

© 2013 Elsevier Inc.
All rights reserved.

precautions should be taken to minimize exposure to light, including that from instrumental light, during measurement of oxidative stress with Amplex Red.

ABBREVIATIONS

AR Amplex Red
DMPO 5,5-dimethy-1-pyrroline *N*-oxide
ESR electron spin resonance
HRP horseradish peroxidase
ROS reactive oxygen species
RSF resorufin
SOD superoxide dismutase

1. INTRODUCTION

Amplex Red is a colorless and nonfluorescent compound used as a probe to measure extracellular H_2O_2, but because H_2O_2 is freely diffusible, this measurement is an indication of cellular H_2O_2 production. Catalyzed by horseradish peroxidase (HRP), H_2O_2 reacts with Amplex Red at 1:1 stoichiometric ratios to form the colored and fluorescent compound resorufin (Zhou, Diwu, Panchuk-Voloshina, & Haugland, 1997). The high fluorescence properties of resorufin (fluorescence quantum yield, $\Phi_F = 0.74$, Bueno et al., 2002) confer the high sensitivity of this assay, which can be used to detect as little as 19 n*M* H_2O_2 (Zhao, Summers, & Mason, 2012). However, at high H_2O_2 concentrations, the concentration of Amplex Red becomes limiting and resorufin can be further oxidized by HRP to colorless, nonfluorescent product(s) (Mohanty, Jaffe, Schulman, & Raible, 1997; Reszka, Wagner, Burns, & Britigan, 2005; Towne, Will, Oswald, & Zhao, 2004). In addition, the concentration of H_2O_2 can be underestimated if a biological sample contains high levels of other peroxidase substrates. Endogenous or exogenous compounds such as drugs and other small molecules could compete with Amplex Red for the oxidation by H_2O_2/HRP, resulting in less resorufin formation, which ultimately would lead to erroneously low estimations of H_2O_2 concentration (Reszka et al., 2005).

Recently, we have investigated the effect of exposing Amplex Red to light in the presence and absence of HRP and H_2O_2 (Zhao, Ranguelova, Jiang, & Mason, 2011; Zhao et al., 2012). Our results clearly show that resorufin is formed by exposing Amplex Red to light and that this photochemistry is initiated by trace amounts of resorufin present in Amplex Red

stock solutions. This effect is dependent on the duration and intensity of exposure to light and the presence of oxygen in the solution. We also investigated the potential problems arising from this photochemistry by assessing the efficacy of the Amplex Red assay in measuring H_2O_2 under room light exposure, under exposure to instrumental light of a UV–visible spectrophotometer and a spectrofluorometer, and finally under UVA irradiation. This review shows the major findings about the limitations and the precautions that should be considered when the Amplex Red assay is exposed to light, even the instrumental light of a spectrophotometer or spectrofluorometer.

2. AMPLEX RED ASSAY AND ITS POSSIBLE ARTIFACTS DUE TO LIGHT EXPOSURE

2.1. Light, resorufin, and oxygen are involved in the artifactual formation of resorufin in Amplex Red exposed to light

The accuracy of H_2O_2 measurement by the Amplex Red assay relies on the reaction of colorless and nonfluorescent Amplex Red with H_2O_2 in the presence of HRP to form the colored and fluorescent product resorufin. However, in the absence of H_2O_2 and HRP, resorufin was also generated when Amplex Red was exposed to a 450-W xenon-mercury light (Fig. 1.1A), as shown by the increase in absorbance at 572 nm. The Amplex Red exposed to unfiltered light showed the fastest generation of resorufin (Fig. 1.1B, line 2), while resorufin was not formed if the Amplex Red was kept in the dark (Fig. 1.1B, line 1). When long-pass filters cutting off at different wavelengths of light were used, the generation of resorufin was approximately proportional to the light absorption of Amplex Red (Fig. 1.1B, line 3–5).

In each case, the absorbance at 572 nm attributed to resorufin increased and then declined with the longer exposure times, suggesting the formation of a photobleached oxidation product; this decline also occurs when Amplex Red is largely consumed and resorufin acts as a peroxidase substrate (Mohanty et al., 1997; Reszka et al., 2005; Towne et al., 2004).

When Amplex Red was continuously exposed to instrumental light of 520 nm (with a 10-nm slit width for excitation) in a spectrofluorometer (450-W lamp) in the absence of HRP and H_2O_2, the fluorescence at 585 nm increased, indicating the formation of resorufin (Fig. 1.2, solid line). There was no increase in fluorescence when Amplex Red was kept in the dark, except for a measurement at the start and end time points (Fig. 1.2,

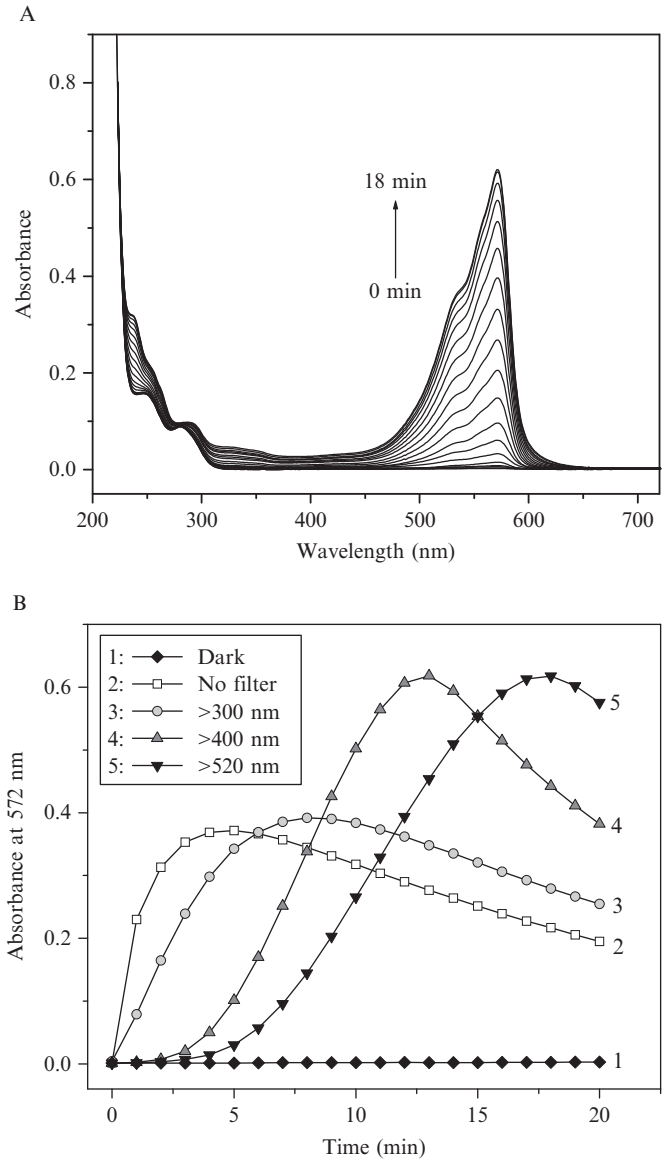

Figure 1.1 Photo-induced oxidation of Amplex Red with production of resorufin during irradiation as measured by UV–vis absorption. (A) Absorption spectra of 10 μ*M* AR solution at pH 7.4 after irradiation (>520 nm) for every minute from 0 to 18 min. The arrow indicates direction of the changes. (B) Plot of peak absorbance of RSF at 572 nm against irradiation time (1, dark; 2, no filter; 3, >300 nm; 4, >400 nm; and 5, >520 nm). The fluence rate (from 250 to 850 nm) was 0, 0.392, 0.329, 0.322, and 0.271 W/cm^2 as measured with a SPR-4001 Spectroradiometer (Luzchem Research Inc., Ottawa, Ontario, Canada). *From Zhao et al. (2012).*

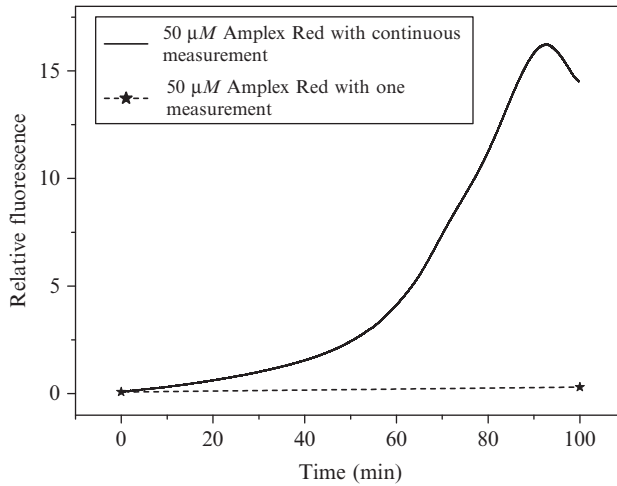

Figure 1.2 The effect of instrumental light from a spectrofluorometer (450-W lamp) on the formation of resorufin in Amplex Red samples. Fluorescence intensity at 585 nm of 50 μ*M* Amplex Red solution during continuous measurement (solid line) and one measurement at 100 min (dotted line) with an excitation wavelength of 520 nm. *From Zhao et al. (2012).*

dashed line). Therefore, resorufin, measured by light absorption (Fig. 1.1) or fluorescence spectroscopy (Fig. 1.2), was formed when Amplex Red was continuously exposed to a 450-W xenon-mercury lamp or to a spectrofluorometer instrumental light (450-W lamp), respectively. The rate of this resorufin formation was exponential, suggesting that this process was autocatalytic.

Trace amounts of resorufin catalyze the conversion of Amplex Red to resorufin upon exposure to light. The addition of as little as 0.1 μ*M* resorufin increased the rate of Amplex Red photooxidation (Zhao et al., 2012). Amplex Red mixed with resorufin but kept in the dark with one measurement at the end time point did not generate more resorufin, indicating that the oxidation of Amplex Red is dependent on the presence of light and the presence of resorufin (Zhao et al., 2012).

To investigate the role of oxygen in air-saturated solutions in the photooxidation of Amplex Red, we purged the Amplex Red solution with nitrogen and exposed it to light. The removal of oxygen suppressed Amplex Red autooxidation. Adding azide, a classical singlet oxygen quencher, to air-saturated solutions of Amplex Red had no effect on the rate of resorufin formation. Adding superoxide dismutase (SOD), which catalyzes the

conversion of $O_2^{\cdot-}$ to H_2O_2, dramatically increased the oxidation of Amplex Red, and the increase was dependent on the concentration of SOD. Taken together, these results suggest that $O_2^{\cdot-}$ formed from dissolved oxygen is an intermediate product during the oxidation of Amplex Red (Zhao et al., 2012).

Using ESR and DMPO as a spin trap, we further confirmed that $O_2^{\cdot-}$ is formed during the photooxidation of Amplex Red. When Amplex Red, resorufin, and DMPO were exposed to light, the spectrum was characteristic of the DMPO/$^{\cdot}$OOH radical adduct (Zhao et al., 2012). This adduct was not detected when samples were prepared in the presence of SOD (Zhao et al., 2012), but adding catalase did not alter the formation of this adduct. This adduct was not detected if resorufin was omitted from the mixture or if the mixture was kept in the dark. This indicates that the same conditions necessary for the formation of $O_2^{\cdot-}$ are necessary for the photooxidation of Amplex Red, which is consistent with $O_2^{\cdot-}$ being an intermediate in this process.

2.2. Amplex Red exposed to room light in the presence of HRP and H_2O_2

The light-induced formation of resorufin from Amplex Red in the absence of H_2O_2 and HRP represents a potential confounding factor in the use of the Amplex Red assay. As the Amplex Red assay also contains HRP and H_2O_2, the effect of light was investigated under these conditions.

Since ESR and oxygen consumption experiments showed that the photooxidation of Amplex Red resulted in the formation of $O_2^{\cdot-}$ (Zhao et al., 2012), this raised the possibility that $O_2^{\cdot-}$, dismutated to H_2O_2, could serve as a substrate for HRP when Amplex Red was exposed to light in the presence of HRP. To test this possibility, Amplex Red was incubated with HRP in the absence of H_2O_2 and exposed to ambient room light (Fig. 1.3A). The presence of HRP greatly increased the fluorescence compared to Amplex Red alone, which indicated that the photooxidation of Amplex Red in the context of an Amplex Red assay is more problematic than that which occurs with Amplex Red alone. Adding catalase to Amplex Red and HRP greatly decreased this increase in fluorescence indicating a dependence on H_2O_2. This suggested that the resorufin resulting from the exposure of Amplex Red and HRP to light was formed in two ways: the photooxidation of Amplex Red and the artifactual generation of H_2O_2 serving as a substrate

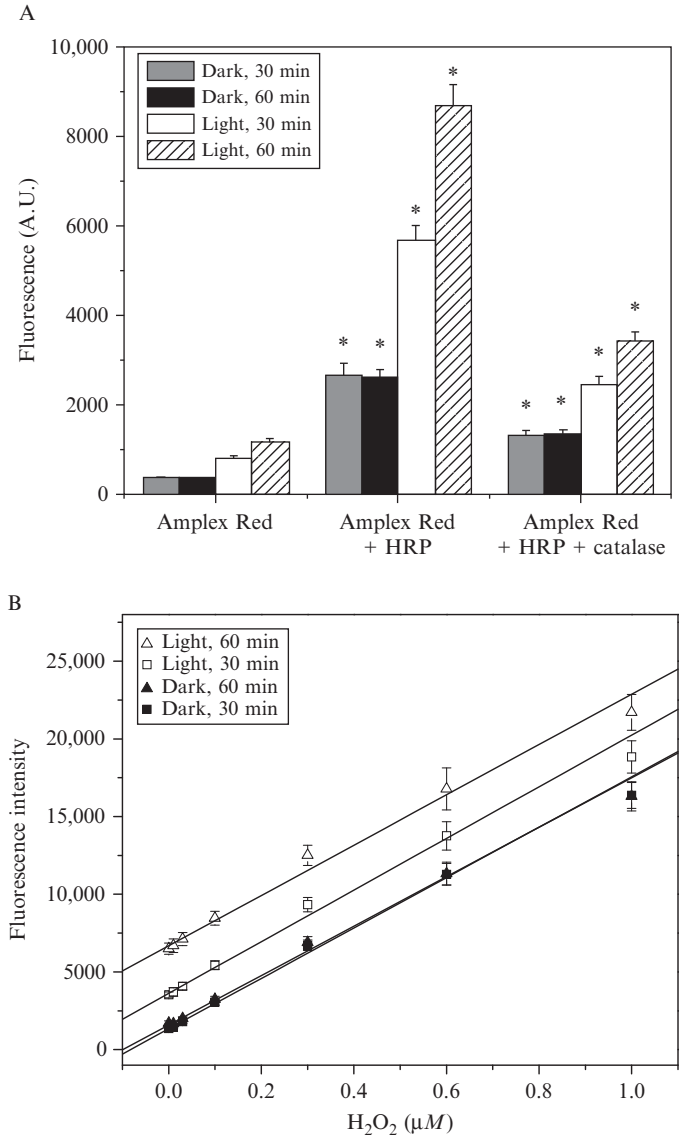

Figure 1.3 The effect of room light on the Amplex Red assay. Reactions containing 50 μ*M* Amplex Red and 0.1 U/mL HRP in 50 m*M* sodium phosphate buffer, pH 7.4, were incubated with and without catalase (A) or with H_2O_2 (B) for 30 and 60 min under ambient laboratory lighting or in the dark. The significance of adding HRP to Amplex Red and the significance of adding catalase to mixtures containing Amplex Red and HRP were assessed using the Student's *t*-test ($^*p < 0.05$). *From Zhao et al. (2012).*

for HRP. Incubated in the dark, Amplex Red and HRP had higher fluorescence than Amplex Red alone although this was far less than that seen with exposure to ambient room lighting (Fig. 1.3A). This might be attributed to the photooxidation of Amplex Red from the use of a red light (>600 nm) in the darkroom during sample preparation.

Therefore, mixtures containing Amplex Red, HRP, and varying concentrations of H_2O_2 were prepared in a darkroom under low-energy red light and then incubated in 96-well plates either in the dark or under normal laboratory lights for 30 or 60 min before the fluorescence was measured with a fluorescence plate reader (Fig. 1.3B). The mixtures incubated in the dark for 30 and 60 min yielded overlapping standard curves, indicating that the Amplex Red assay, when incubated in the dark, is a stable end point assay (i.e., reaches a single, final, and stable measurement). In contrast, the mixtures exposed to the light had consistently higher fluorescence measurements than those incubated in the dark, and the final fluorescence measurement was dependent on the length of exposure to light, indicating that the Amplex Red assay incubated in the light is not an end point assay.

However, the standard curves for the mixtures incubated in the light were parallel to those obtained in the dark, indicating that the generation of resorufin due to photooxidation of Amplex Red is constant over this range of H_2O_2 concentrations despite varying amounts of resorufin being formed from the HRP-catalyzed reaction of Amplex Red and H_2O_2 (Fig. 1.3B). This is different from the experiments done in a spectrofluorometer, where small initial differences in resorufin concentration made a large difference in the amount of resorufin formed from the photooxidation of Amplex Red (Zhao et al., 2012). This difference was attributed to the lower intensity of laboratory lighting compared to the light from the spectrofluorometer.

The limit of detection of H_2O_2 was calculated for each standard curve and was 19 n*M* for the samples incubated for 30 min in the dark and 30 n*M* for samples incubated for 60 min in the dark (Zhao et al., 2012). The higher limit of detection for the 60-min dark samples, despite overlapping standard curves, was due to the larger standard deviation (error bars) for the 60-min dark standard curve compared to the 30-min dark standard curve. The limit of detection was 31 n*M* for the 30-min light standard curve and 61 n*M* for the 60-min light standard curve, with the larger standard deviations (error bars) for increased time and exposure to light. Thus, it can be seen that both exposure to room light and extended incubation times result in a less sensitive and accurate assay for H_2O_2.

2.3. Artifactual measurement of H_2O_2 released by cells exposed to UV light using the Amplex Red assay

The Amplex Red assay has been used previously to measure H_2O_2 released from cells during exposure to UV light (Peus et al., 1999, 1998). To ascertain whether this assay should be used in this system, Amplex Red and HRP were added to cells and then exposed to UVA irradiation (315–400 nm). One control was Amplex Red and HRP added to cells and kept in the dark. Another control was Amplex Red and HRP exposed to UVA irradiation in the absence of cells.

Cells exposed to UVA irradiation in PBS buffer had higher fluorescent measurements than cells kept in the dark, and this fluorescence was dependent on the length of exposure to UVA (Fig. 1.4). However, the same increased fluorescence occurred in the Amplex Red and HRP sample exposed to UVA light in the absence of cells, indicating that the majority of the fluorescence from irradiated cells was due to UVA irradiation of Amplex Red and HRP and not due to H_2O_2 released from the cells (Fig. 1.4). This large artifactual resorufin formation, despite the poor absorption of Amplex Red and resorufin in the UVA region (Fig. 1.1A,

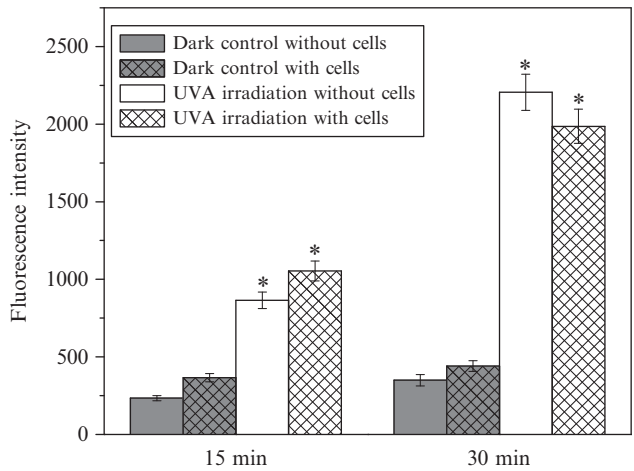

Figure 1.4 Fluorescence of HaCaT keratinocytes exposed to UVA in the presence of 50 μ*M* Amplex Red. Detection of autooxidation of Amplex Red with cells irradiated with 0, 15, and 30 min UVA and control without cells. The significance of the UVA-irradiated sample without cells to its dark control and the significance of the UVA-irradiated sample with cells to its dark control were assessed using the Student's *t*-test ($^*p < 0.05$). *From Zhao et al. (2012).*

315–400 nm), is most likely due to the high energy and intensity of UVA light. This shows that Amplex Red is not useful for measuring H_2O_2 released by cells concomitantly exposed to UV, because the UV irradiation causes a large artifactual resorufin formation *per se*, which leads to an overestimation of H_2O_2 that would be released by the cells.

2.4. Controversy over the characterization of MnSOD as a peroxidase

In the classical Amplex Red assay, the low concentration of H_2O_2 limits the resorufin formation, which is proportional to the concentration of H_2O_2 in a sample. However, to test the peroxidase activity of a protein, saturating concentrations of H_2O_2 are used, and the peroxidase activity is measured by monitoring resorufin formation. Recently, this strategy was used to evidentiate the peroxidase activity of MnSOD.

However, Liochev and Fridovich expressed surprise that MnSOD acted as a peroxidase toward Amplex Red (Liochev & Fridovich, 2013). Part of their explanation relies on the fact that the resorufin formation is exponentially increased by MnSOD (Ansenberger-Fricano et al., 2012). In contrast, Ansenberger-Fricano et al. propose that the exponential formation of resorufin in the presence of MnSOD is due to a high excess of H_2O_2 potentiating the enzyme's peroxidase activity, possibly by oxidatively modifying the structure of MnSOD (Ansenberger-Fricano et al., 2012).

As an important matter for discussion in this review, Liochev and Fridovich further propose that the catalysis by MnSOD is due to the photochemical artifact inherent in Amplex Red assays and that the MnSOD increases the artifactual generation of resorufin by lowering the steady-state level of superoxide via its SOD activity (Liochev & Fridovich, 2013). This photochemical effect theoretically could cause apparent similar autocatalytic accumulation of resorufin, which would cause further photochemical-mediated oxidation of Amplex Red; however, Liochev and Fridovich, during their explanation, compare the findings of two very different experiments (Liochev & Fridovich, 2013). Zhao et al. measured fluorescence using a FL3-22 spectrofluorometer with a xenon 450-W lamp with a 10-nm slit width for excitation (Zhao et al., 2012), whereas Ansenberger-Fricano et al. measured absorption using a Varian Cary spectrophotometer with a 55-W lamp (basically a light bulb) and a 0.5-nm slit width (Ansenberger-Fricano et al., 2012). Nonetheless, as mentioned earlier, Zhao et al. found effects on the Amplex Red assay with 30 min of room light exposure. As noted, these effects raised the background level of resorufin, which

lowered the ultimate sensitivity of the assay, but otherwise did not affect the results (Zhao et al., 2012).

To test the effect of this instrumental light in a spectrophotometer (55-W lamp), control experiments were prepared. The Amplex Red oxidation in the presence of H_2O_2 under the 55-W spectrophotometer light was almost negligible (Fig. 1.5). Note that the dark control with a single measurement of absorbance at the end of the experiment is slightly lower (Fig. 1.5). Clearly, MnSOD shows dependence on H_2O_2 for the oxidation of Amplex Red, and this is the fundamental characteristic of a peroxidase. If Liochev and Fridovich were correct, then the oxidation of Amplex Red would not depend on H_2O_2, which it does (Fig. 1.5). As shown in Fig. 1.5, some artifactual oxidation of Amplex Red by the spectrophotometer 55-W light does occur and it accounts for approximately 20% of the overall response. This is similar to the Amplex Red assay exposed to room light for 30 min, in which exposure to light accounted for approximately 15% of the overall fluorescence at the highest concentration of H_2O_2 compared with the samples kept in the dark (Fig. 1.3B). The results of the MnSOD dark control experiment (Fig. 1.5) do not contradict the conclusions of Ansenberger-Fricano et al.

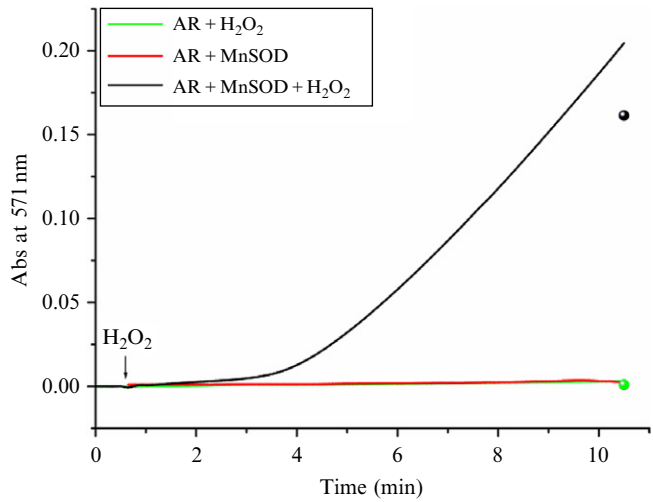

Figure 1.5 Detection of peroxidase activity of MnSOD. Reaction mixtures were prepared with 100 μ*M* Amplex Red, 1 mg/mL MnSOD, and 2 m*M* H_2O_2 in 100 m*M* sodium phosphate buffer, pH 7.4, with 25 μ*M* DTPA. Samples were continuously monitored for the absorbance at 571 nm or incubated in the dark for 10 min. Final absorbances of the dark-incubated samples are shown on the right, with the complete sample (AR + MnSOD + H_2O_2) being the only one with significant absorbance. *From Mason (2013).*

since the oxidation is totally dependent on both MnSOD and H_2O_2. Most critically, the MnSOD-catalyzed oxidation of Amplex Red in the presence of H_2O_2 still occurs in the dark with a simple measurement of the absorbance (Fig. 1.5). Nonetheless, once resorufin is formed, instrumental light will form additional resorufin. In all probability, the light effect is present in all published works with Amplex Red detected with absorption or fluorescence detection. In conclusion, the importance of the photochemical-mediated artifactual Amplex Red oxidation will depend on a case-by-case analysis. The preparation of the "single measurement" control (endpoint assay) where the samples have been protected from light even during sample preparation must be adopted as good practice for this assay.

3. EXPERIMENTAL CONSIDERATIONS

The Amplex Red assay is based on the stoichiometric oxidation of Amplex Red with H_2O_2 to resorufin catalyzed by HRP. Amplex Red itself can also be oxidized to resorufin after exposure to light in the absence of HRP and H_2O_2, and this photochemistry is initiated by trace amounts of resorufin present in Amplex Red stock solutions (Zhao et al., 2012). This effect is dependent on the duration of light exposure, the energy of the light, and the presence of oxygen in the solutions. Superoxide and H_2O_2 were identified as being formed during this process. Based on these results, we propose the following photochemical mechanism (Scheme 1.1). After

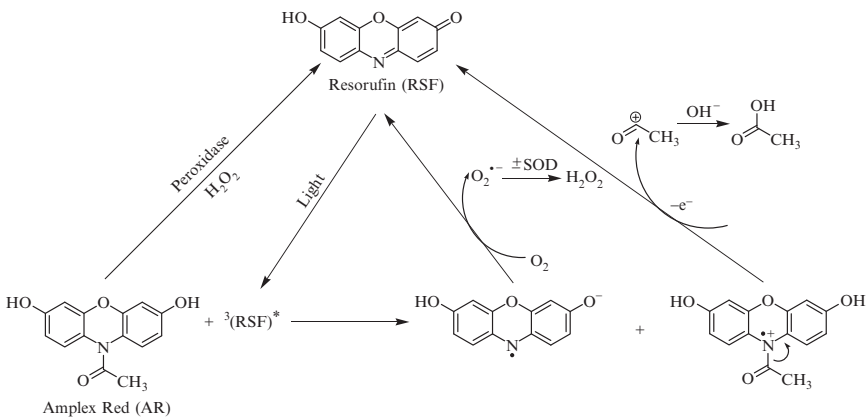

Scheme 1.1 Proposed mechanism of photo-induced oxidation of Amplex Red. *From Zhao et al. (2012).*

exposure to light, resorufin is activated to form a triplet-excited state ($\Phi_T = 0.04$, Bueno et al., 2002). An electron transfer from Amplex Red to the triplet resorufin generates an Amplex Red cation radical and a resorufin anion radical in the classical Type I photochemical pathway. With oxidation, the Amplex Red cation radical can deacetylate to form 1 mol of resorufin. The resorufin anion radical can react with oxygen to produce $O_2^{\cdot -}$, and in the process, resorufin is regenerated. During exposure to light, this redox cycling continuously oxidizes the Amplex Red to resorufin with the formation of $O_2^{\cdot -}$ and, subsequently, H_2O_2.

When Amplex Red is exposed to light in the presence of HRP, $O_2^{\cdot -}$ can spontaneously dismutate to H_2O_2 and serve as a substrate for HRP (Scheme 1.1). The addition of catalase will break down this H_2O_2 and artifactual resorufin formation can be inhibited (Fig. 1.3A). This is noteworthy because catalase can be added to a biological system to confirm that H_2O_2 is the species being produced, so it is important to realize that catalase can not only break down the H_2O_2 being released from a biological sample but also inhibit artifactual resorufin formation, thus mimicking the former situation.

The exposure of Amplex Red to light in media should be absolutely avoided. Media usually contains reducing agents such as NADH or GSH which interact with HRP to produce H_2O_2 via superoxide, which subsequently oxidizes Amplex Red without the need of exogenous H_2O_2 (Votyakova & Reynolds, 2004). This photochemistry with reducing agents is analogous to what happens with Amplex Red (Scheme 1.2). The only difference is that NADH instead of Amplex Red is the electron donor to the excited resorufin in the Type I photoreaction (Zhao et al., 2011).

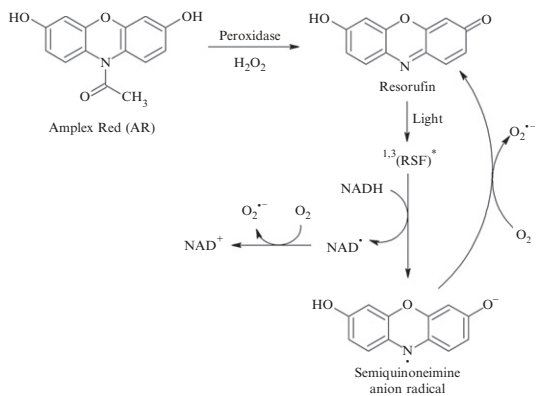

Scheme 1.2 Photo-induced reduction of resorufin by NADH. *Modified from Zhao et al. (2011).*

Thus, our studies provide some cautions and guidelines for the use of the Amplex Red assay. Exposure of Amplex Red to light will result in photooxidation of Amplex Red to form resorufin. The impact of this photochemistry on the experiment varies; for example, in Fig. 1.3, the assay is less sensitive when carried out under room light than when incubated in the dark, which could be problematic if the concentrations of H_2O_2 to be measured are near the limit of detection of the assay. It is noteworthy that this experiment was carried out in a 96-well plate, so all the samples were exposed to the same amount of light. Nonetheless, it would be prudent to minimize exposure to light because, as well as increasing the background fluorescence, the photochemical formation of $O_2^{\cdot -}$ may alter an enzymatic system or biological response under study, which may change the H_2O_2 production by that system. In addition, the amount of photochemistry occurring may not be the same between control samples and treated samples; for instance, the amount of photochemistry in a hypoxia treatment would be expected to be less than in normoxic controls since this photochemistry is dependent on the presence of dissolved oxygen (Zhao et al., 2012). The levels of H_2O_2 in pulmonary and coronary smooth muscle cells have been reported to be lower in hypoxia than in normoxia (Mehta et al., 2008), but there have been conflicting reports from other groups (Korge, Ping, & Weiss, 2008; Michelakis, Thebaud, Weir, & Archer, 2004; Waypa & Schumacker, 2005), underscoring the need to carefully control for potentially confounding variables.

Inappropriate experimental design may result in invalid measurements such as shown in Fig. 1.4 where cells, Amplex Red, and HRP were exposed to UV irradiation to measure H_2O_2 from cells produced in response to UV irradiation. However, the irradiated Amplex Red generated large amounts of artifactual resorufin, and this high background fluorescence obscured any H_2O_2 produced by the cells. Even if the sample containing irradiated cells, Amplex Red, and HRP had shown a final higher fluorescence than that containing irradiated Amplex Red and HRP, subtracting the test fluorescence from the control fluorescence would not be a valid method for determining H_2O_2 released by the cells because Amplex Red photooxidation generates $O_2^{\cdot -}$, which is also likely to interfere with the metabolism of the cells and thus would not be representative of H_2O_2 release from cells exposed to UV. Not only would the H_2O_2 measurements be inaccurate, but they might divert the researcher's attention away from more significant findings.

In general, precautions should be taken to minimize the exposure to light, such as using a darkroom or low-energy red light for lab work and

incubating the samples in the dark in order to minimize any effects resulting from the photooxidation of Amplex Red. Single measurements of fluorescence or even absorption are preferable to continuous measurements as this minimizes exposure to light from the spectrometer or plate reader. The H_2O_2 levels produced by isolated mitochondria are typically measured with continuous measurements using a spectrofluorometer (Bhattacharya et al., 2009; Panov et al., 2005; Starkov et al., 2004). The light from a spectrofluorometer under our conditions was enough to cause photochemical reactions. If continuous measurements are used with Amplex Red, such as in the experiments shown here for the peroxidase activity of MnSOD, single measurements could also be taken as a comparison to check whether the continuous irradiation of the sample by instrumental light would be responsible for the Amplex Red oxidation. It may be more convenient to compare single measurements and continuous measurements by performing the experiments in a 96-well plate (Armstrong & Whiteman, 2007), or a robust alternative approach is to chromatographically separate Amplex Red and resorufin as isolated pure compounds by HPLC before the photometric detection and consequent exposure to instrumental light (Zielonka et al., 2012).

Confocal microscopy of Amplex Red samples has been done previously (DeYulia, Carcamo, Borquez-Ojeda, Shelton, & Golde, 2005). The cells appeared fluorescent against a fluorescent background, but it should be noted that Amplex Red is cell-impermeable and is designed to be used in extracellular assays. Confocal microscopy should be avoided because the laser light source is very powerful and will certainly induce the photochemistry-mediated formation of resorufin. In addition, if attempts are made to develop a cell-permeable version of Amplex Red, the high intracellular concentrations of the biological reducing agents glutathione and NADH (Votyakova & Reynolds, 2004; Zhao et al., 2011) and redox cycling enzymes (Balvers, Boersma, Vervoort, & Rietjens, 1992; Dutton, Reed, & Parkinson, 1989) are likely to result in artifactual production of $O_2^{\cdot -}$ and H_2O_2 with exposure to light, even when instrumental light is kept to a minimum. If the above precautions are taken, the Amplex Red assay is, in general, a very sensitive, specific, and robust assay for the measurement of H_2O_2 and peroxidase activity of enzymes. Although it must be assumed that nearly all published work with Amplex Red has been affected to some degree by the exposure to both room and instrumental light, whether these light-dependent effects change the conclusions of the experiments will need to be determined on a case-by-case basis.

ACKNOWLEDGMENTS

This work was supported by the Intramural Research Program of the National Institutes of Health and the National Institute of Environmental Health Sciences 52 (Z01 ES050139-13). The authors are indebted to Mrs. Mary Mason and Dr. Ann Motten for their critical reading of the manuscript.

REFERENCES

Ansenberger-Fricano, K., Ganini, D., Mao, M., Chatterjee, S., Dallas, S., Mason, R. P., et al. (2012). The peroxidase activity of mitochondrial superoxide dismutase. *Free Radical Biology & Medicine*, *54*, 116–124.

Armstrong, J. S., & Whiteman, M. (2007). Measurement of reactive oxygen species in cells and mitochondria. *Methods in Cell Biology*, *80*, 355–377.

Balvers, W. G., Boersma, M. G., Vervoort, J., & Rietjens, I. M. (1992). Experimental and theoretical study on the redox cycling of resorufin by solubilized and membrane-bound NADPH-cytochrome reductase. *Chemical Research in Toxicology*, *5*(2), 268–273.

Bhattacharya, A., Muller, F. L., Liu, Y., Sabia, M., Liang, H., Song, W., et al. (2009). Denervation induces cytosolic phospholipase A2-mediated fatty acid hydroperoxide generation by muscle mitochondria. *Journal of Biological Chemistry*, *284*(1), 46–55.

Bueno, C., Villegas, M. L., Bertolotti, S. G., Previtali, C. M., Neumann, M. G., & Encinas, M. V. (2002). The excited-state interaction of resazurin and resorufin with amines in aqueous solutions. Photophysics and photochemical reactions. *Photochemistry and Photobiology*, *76*(4), 385–390.

DeYulia, G. J., Jr., Carcamo, J. M., Borquez-Ojeda, O., Shelton, C. C., & Golde, D. W. (2005). Hydrogen peroxide generated extracellularly by receptor-ligand interaction facilitates cell signaling. *Proceedings of the National Academy of Sciences of the United States of America*, *102*(14), 5044–5049.

Dutton, D. R., Reed, G. A., & Parkinson, A. (1989). Redox cycling of resorufin catalyzed by rat liver microsomal NADPH-cytochrome P450 reductase. *Archives of Biochemistry and Biophysics*, *268*(2), 605–616.

Korge, P., Ping, P., & Weiss, J. N. (2008). Reactive oxygen species production in energized cardiac mitochondria during hypoxia/reoxygenation: Modulation by nitric oxide. *Circulation Research*, *103*(8), 873–880.

Liochev, S. I., & Fridovich, I. (2013). Peroxidase activity by MnSOD? *Free Radical Biology & Medicine*. In press.

Mason, R. P. (2013). Two hypotheses for the peroxidase activity of Mn-superoxide dismutase. *Free Radical in Biology & Medicine*. In press.

Mehta, J. P., Campian, J. L., Guardiola, J., Cabrera, J. A., Weir, E. K., & Eaton, J. W. (2008). Generation of oxidants by hypoxic human pulmonary and coronary smooth-muscle cells. *Chest*, *133*(6), 1410–1414.

Michelakis, E. D., Thebaud, B., Weir, E. K., & Archer, S. L. (2004). Hypoxic pulmonary vasoconstriction: Redox regulation of O_2-sensitive K^+ channels by a mitochondrial O_2-sensor in resistance artery smooth muscle cells. *Journal of Molecular and Cellular Cardiology*, *37*(6), 1119–1136.

Mohanty, J. G., Jaffe, J. S., Schulman, E. S., & Raible, D. G. (1997). A highly sensitive fluorescent micro-assay of H_2O_2 release from activated human leukocytes using a dihydroxyphenoxazine derivative. *Journal of Immunological Methods*, *202*(2), 133–141.

Panov, A., Dikalov, S., Shalbuyeva, N., Taylor, G., Sherer, T., & Greenamyre, J. T. (2005). Rotenone model of Parkinson disease: Multiple brain mitochondria dysfunctions after short term systemic rotenone intoxication. *Journal of Biological Chemistry*, *280*(51), 42026–42035.

Peus, D., Meves, A., Vasa, R. A., Beyerle, A., O'Brien, T., & Pittelkow, M. R. (1999). H2O2 is required for UVB-induced EGF receptor and downstream signaling pathway activation. *Free Radical Biology & Medicine*, *27*(11–12), 1197–1202.

Peus, D., Vasa, R. A., Meves, A., Pott, M., Beyerle, A., Squillace, K., et al. (1998). H_2O_2 is an important mediator of UVB-induced EGF-receptor phosphorylation in cultured keratinocytes. *The Journal of Investigative Dermatology*, *110*(6), 966–971.

Reszka, K. J., Wagner, B. A., Burns, C. P., & Britigan, B. E. (2005). Effects of peroxidase substrates on the Amplex red/peroxidase assay: Antioxidant properties of anthracyclines. *Analytical Biochemistry*, *342*(2), 327–337.

Starkov, A. A., Fiskum, G., Chinopoulos, C., Lorenzo, B. J., Browne, S. E., Patel, M. S., et al. (2004). Mitochondrial alpha-ketoglutarate dehydrogenase complex generates reactive oxygen species. *Journal of Neuroscience*, *24*(36), 7779–7788.

Towne, V., Will, M., Oswald, B., & Zhao, Q. (2004). Complexities in horseradish peroxidase-catalyzed oxidation of dihydroxyphenoxazine derivatives: Appropriate ranges for pH values and hydrogen peroxide concentrations in quantitative analysis. *Analytical Biochemistry*, *334*(2), 290–296.

Votyakova, T. V., & Reynolds, I. J. (2004). Detection of hydrogen peroxide with Amplex Red: Interference by NADH and reduced glutathione auto-oxidation. *Archives of Biochemistry and Biophysics*, *431*(1), 138–144.

Waypa, G. B., & Schumacker, P. T. (2005). Hypoxic pulmonary vasoconstriction: Redox events in oxygen sensing. *Journal of Applied Physiology*, *98*(1), 404–414.

Zhao, B., Ranguelova, K., Jiang, J., & Mason, R. P. (2011). Studies on the photosensitized reduction of resorufin and implications for the detection of oxidative stress with Amplex Red. *Free Radical Biology & Medicine*, *51*(1), 153–159.

Zhao, B., Summers, F. A., & Mason, R. P. (2012). Photooxidation of Amplex red to resorufin: Implications of exposing the Amplex red assay to light. *Free Radical Biology & Medicine*, *53*(5), 1080–1087.

Zhou, M., Diwu, Z., Panchuk-Voloshina, N., & Haugland, R. P. (1997). A stable non-fluorescent derivative of resorufin for the fluorometric determination of trace hydrogen peroxide: Applications in detecting the activity of phagocyte NADPH oxidase and other oxidases. *Analytical Biochemistry*, *253*(2), 162–168.

Zielonka, J., Zielonka, M., Sikora, A., Adamus, J., Joseph, J., Hardy, M., et al. (2012). Global profiling of reactive oxygen and nitrogen species in biological systems: High-throughput real-time analyses. *Journal of Biological Chemistry*, *287*(5), 2984–2995.

CHAPTER TWO

Boronate-Based Fluorescent Probes: Imaging Hydrogen Peroxide in Living Systems

Vivian S. Lin[*], **Bryan C. Dickinson**[§], **Christopher J. Chang**[*,†,‡,1]
[*]Department of Chemistry, University of California, Berkeley, California, USA
[†]Department of Molecular and Cell Biology, University of California, Berkeley, California, USA
[‡]Howard Hughes Medical Institute, Chevy Chase, Maryland, USA
[§]Department of Chemistry and Chemical Biology, Harvard University, Cambridge, Massachusetts, USA
[1]Corresponding author: e-mail address: chrischang@berkeley.edu

Contents

1. Introduction 20
2. Fluorescent Boronate-Based Hydrogen Peroxide Probes 22
   2.1 Probe design 22
   2.2 Reactivity 23
   2.3 Selecting a probe 27
   2.4 Use and storage of probes 28
3. Examples of Probes and Their Usage 28
   3.1 PO1 used for fluorometry 28
   3.2 Trappable PF6-AM for use in flow cytometry experiments 30
   3.3 Targeted MitoPY1 for fluorescence microscopy 31
4. Imaging Endogenous H_2O_2 Using Fluorescent Probes 32
   4.1 Imaging hydrogen peroxide and hROS simultaneously in macrophages 34
   4.2 Growth factor stimulation 36
   4.3 Controls utilizing inhibitors of H_2O_2 38
5. Conclusions 39
Acknowledgments 40
References 40

Abstract

Hydrogen peroxide, a reactive oxygen species with unique chemical properties, is produced endogenously in living systems as a destructive oxidant to ward off pathogens or as a finely tuned second messenger in dynamic cellular signaling pathways. In order to understand the complex roles that hydrogen peroxide can play in biological systems, new tools to monitor hydrogen peroxide in its native settings, with high selectivity and sensitivity, are needed. Knowledge of organic synthetic reactivity provides the foundation for the molecular design of selective, functional hydrogen peroxide probes. A palette of fluorescent and luminescent probes that react chemoselectively with

Methods in Enzymology, Volume 526
ISSN 0076-6879
http://dx.doi.org/10.1016/B978-0-12-405883-5.00002-8
© 2013 Elsevier Inc.
All rights reserved.

hydrogen peroxide has been developed, utilizing a boronate oxidation trigger. These indicators offer a variety of colors and *in cellulo* characteristics and have been used to examine hydrogen peroxide in a number of experimental setups, including *in vitro* fluorometry, confocal fluorescence microscopy, and flow cytometry. In this chapter, we provide an overview of the chemical features of these probes and information on their behavior to help researchers select the optimal probe and application.

1. INTRODUCTION

Reactive oxygen species (ROS), including hydrogen peroxide, are products of cellular respiration that can modulate physiology through a variety of homeostatic mechanisms (D'Autréaux & Toledano, 2007; Dickinson & Chang, 2011; Murphy et al., 2011; Rhee, 2006; Stone & Yang, 2006; Veal, Day, & Morgan, 2007; Winterbourn, 2008). On the other hand, aberrant ROS production is implicated in aging (Giorgio, Trinei, Migliaccio, & Pelicci, 2007), as well as illnesses such as Alzheimer's (Huang & Mucke, 2012; Mattson, 2004), Huntington's (Xun et al., 2012), Parkinson's (Exner, Lutz, Haass, & Winklhofer, 2012), and other neurodegenerative diseases (Lin & Beal, 2006). In many cases, high levels of ROS may result in lipid peroxidation, protein modifications leading to loss or gain of function, and DNA and RNA damage (Frisard & Ravussin, 2006). As such, the generation of ROS must be tightly regulated, both spatially and temporally, to protect the cell from oxidative stress, while taking advantage of the unique and powerful reactivity of these small molecules. To control ROS levels, organisms have evolved specialized enzymes such as superoxide dismutase and catalase to transform ROS into less harmful species (Zelko, Mariani, & Folz, 2002).

While ROS were long considered molecules that negatively impact human health, emerging studies have since shown that ROS are also essential to maintaining cellular health. In particular, several NADPH oxidases (Noxs) have been identified in many tissue types and are known to play important roles in cellular defense and the modulation of cellular signaling events via the controlled production of hydrogen peroxide (Bedard & Krause, 2007; Lambeth, 2004). Low levels of endogenous hydrogen peroxide can lead to specific protein modifications such as sulfenic acid or disulfide formation upon cysteine oxidation (Nelson et al., 2010; Paulsen & Carroll, 2010). The dual ability of hydrogen peroxide to act

as a beneficial or detrimental species in biological systems highlights the challenges of disentangling the complex mechanisms of action of this particular ROS.

Owing to the transient nature of hydrogen peroxide, fluorescent probes, which generally display high sensitivity and can be used to determine spatial and temporal distributions in live specimens, are particularly appealing tools for the detection of ROS and related metabolites. Useful peroxide probes for biological applications must possess the following qualities: (1) compatibility with aqueous media at physiological pH, (2) cell permeability and/or subcellular targetability, (3) high selectivity and sensitivity for hydrogen peroxide over other biologically relevant ROS and reactive species, and (4) spectroscopic properties that are suited for commonly used instrumentation.

To meet this need, our laboratory has developed and continues to expand the toolkit of chemoselective hydrogen peroxide probes based on boronate oxidation, a classic chemical transformation that has its origins in organic synthesis (Kuivila & Armour, 1957; Kuivila & Wiles, 1955). Discovering its compatibility with aqueous environments, our group sought to harness this chemical reaction as a trigger for the selective detection of hydrogen peroxide in biological settings (Chang, Pralle, Isacoff, & Chang, 2004; Lippert, Van de Bittner, & Chang, 2011). This strategy has given rise to a palette of boronate-based fluorescent and luminescent probes that give a turn-on (or ratiometric) response upon reaction with hydrogen peroxide in living systems. In general, these probes are weakly fluorescent in their initial form, and upon oxidation by hydrogen peroxide, they are irreversibly converted to a brighter species. Familiarity with the photophysical properties and the behavior of these probes in biological systems will permit the reader to select and use these probes most effectively in their chosen research endeavors.

The remainder of this chapter is organized as follows. An introduction to fluorescent boronate-based hydrogen peroxide probes is presented in Section 2, summarizing the properties of selected probes and offering a basic guide to choosing a probe for different types of applications. In Section 3, we describe representative experiments using these probes, including fluorometry for *in vitro* studies, fluorescent microscopy, and flow cytometry. Section 4 outlines methods for inducing the production of endogenous hydrogen peroxide, as well as reagents that can be used to specifically block increases of hydrogen peroxide levels in living cells.

2. FLUORESCENT BORONATE-BASED HYDROGEN PEROXIDE PROBES

2.1. Probe design

The present classes of boronate-based hydrogen peroxide probes rely primarily upon masked fluoresceins and rhodols (Fig. 2.1); the aniline functionality of the latter provides a synthetic handle that can be modified to alter the emission wavelength of the probe (Dickinson, Huynh, & Chang, 2010) or used for targeting the probe to subcellular locations such as the nucleus or mitochondria (Dickinson & Chang, 2008; Dickinson, Tang, Chang, & Chang, 2011). The introduction of alternative fluorophores can also give rise to different emission colors (Miller, Albers, Pralle, Isacoff, & Chang, 2005; Miller, Tulyathan, Isacoff, & Chang, 2007). Additionally, synthetic modification can be performed on the benzene moiety orthogonal to the xanthene with little effect upon the fluorescent properties of the molecule. Tethering a benzyl guanine of benzyl-2-chloro-6-aminopyrimidin-4-amine to PG1 affords the probes SPG1 and SPG2, which react selectively with SNAP-tag fusion proteins to

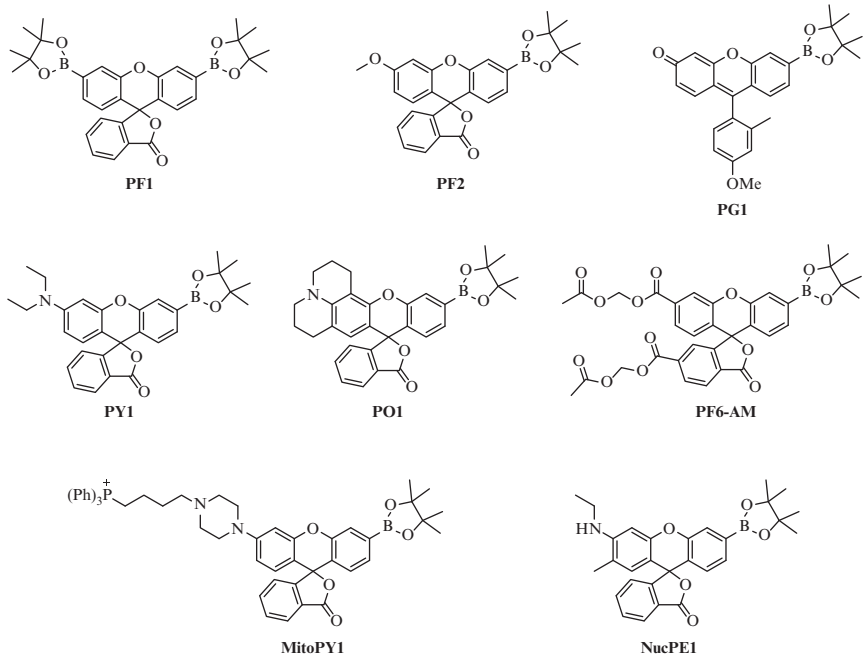

Figure 2.1 Molecular structures of selected boronate-based hydrogen peroxide probes.

deliver the synthetic hydrogen peroxide probes to selected subcellular localizations (Juillerat et al., 2003; Keppler et al., 2004; Srikun, Albers, Nam, Iavarone, & Chang, 2010). Other variants allow for ratiometric imaging by internal charge transfer (Srikun, Miller, Domaille, & Chang, 2008) or fluorescent resonance energy transfer approaches (Albers, Okreglak, & Chang, 2006) as well as dual-analyte versions on dendrimer scaffolds (Srikun, Albers, & Chang, 2011).

A comparison of the spectroscopic properties and applications of commonly used boronate probes reveals a range of excitation and emission wavelengths as well as variations in the fluorescence intensities of these probes (Table 2.1). Background fluorescence, or the brightness of the unreacted probe, varies depending on the structure of the probe and its environment. Boronate probes such as PF1 and PF2, which exist in the "closed" or lactone form, are virtually nonfluorescent before reaction with hydrogen peroxide (Chang et al., 2004; Dickinson, Huynh, & Chang, 2010; Miller et al., 2005). Oxidation of the boronate to the phenol leads to subsequent opening of the lactone ring and tautomerization; the dye in aqueous solution now exists in an equilibrium that lies toward the "open," fluorescent form (Fig. 2.2). While high background fluorescence should be avoided, probes with low background fluorescence may be desirable over a completely dark or nonfluorescent probe to confirm successful uptake of the dye into cells. Probes such as PG1 (Miller et al., 2007), which is based upon the Tokyo Green scaffold, are weakly fluorescent due to quenching via photoinduced electron transfer (PET) from the electron-donating substituents on the benzene group to the xanthene ring (Urano et al., 2005). Conversion to the phenol and deprotonation to the phenolate results in an anionic molecule, which is electronically less susceptible to PET quenching and therefore more fluorescent.

2.2. Reactivity

The boronate-based probes are classified as chemodosimeters, which differ from chemosensors in that an irreversible chemical transformation rather than a reversible binding event gives rise to the observed fluorescence increase (Chan, Dodani, & Chang, 2012; Cho & Sessler, 2009; Czarnik, 1994; Du, Hu, Fan, & Peng, 2012; Jun, Roy, & Ahn, 2011; Quang & Kim, 2010). Due to the short lifetimes of ROS in the biological environment, imaging with chemodosimeters is advantageous, particularly when studying systems involving low levels of ROS flux; the accumulation of

Table 2.1 Spectroscopic properties, localization, and example applications of selected boronate-based hydrogen peroxide probes

Probe	Probe $\lambda_{abs}/\lambda_{em}$ (nm)	Product $\lambda_{abs}/\lambda_{em}$ (nm)	Intracellular localization	Successful applications
Peroxyfluor 1 (PF1)	NA/NA	494/521	Nontargeted, diffuse	Exogenous H_2O_2 detection in cells
Peroxyfluor 2 (PF2)	NA/NA	475/511	Nontargeted, diffuse	Detection of H_2O_2 upon glucose treatment of hematopoietic stem cells *in vivo* in zebrafish
Peroxy green 1 (PG1)	460/510	460/510	Nontargeted, diffuse	Detection of H_2O_2 in EGF signaling in A431 cells
Peroxy yellow 1 (PY1)	494/558	519/548	Nontargeted, diffuse	Detection of H_2O_2 in EGF signaling in A431 cells, multiple colors
Peroxy orange-1 (PO1)	507/574	540/565	Nontargeted, diffuse	Detection of H_2O_2 and HOCl during immune response in RAW264.7 macrophages; detection of H_2O_2 in FLT3/STAT5 signaling in leukemia cells
Peroxyfluor 6 acetoxymethyl ester (PF6-AM)	460/530	492/517	Cytosol	Detection of H_2O_2 in FGF-2 signaling in adult hippocampal progenitor cells, sodium delivery, or angiotensin II stimulation in the medullary thick ascending limb, and during chemotaxis of neutrophils
Mitochondria peroxy yellow 1 (MitoPY1)	489, 510/540	510/528	Mitochondria	Detection of H_2O_2 upon paraquat treatment of HeLa cells, S100β, or APP treatment of DS neural progenitors, and sodium delivery in the medullary thick ascending limb
Nuclear peroxy emerald 1 (NucPE1)	468,490/530	505/530	Nucleus	Detection of H_2O_2 *in vivo* in a long-lived zebrafish model

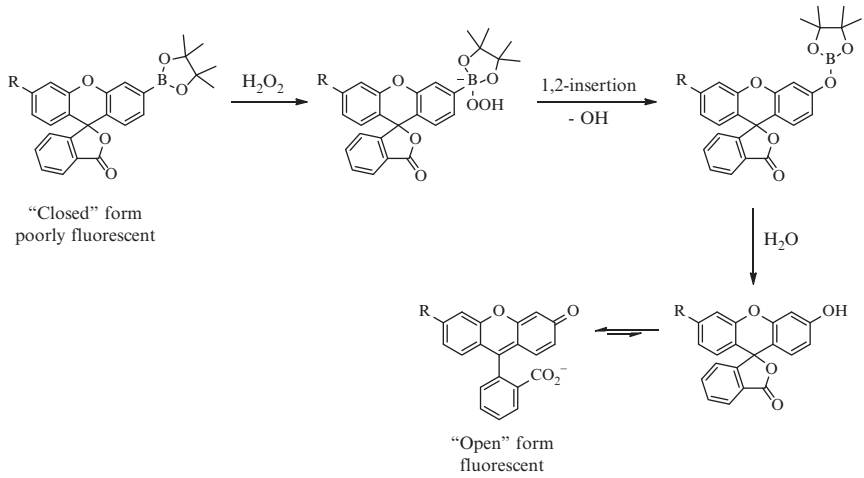

Figure 2.2 Molecular design of fluorescent boronate-based hydrogen peroxide probes.

signal over time can be readily measured via endpoint assays. For real-time detection in intact biological systems, other tools such as genetically encoded hydrogen peroxide sensors of the HyPer family (Belousov et al., 2006; Bilan et al., 2013) and redox-sensitive green fluorescent protein indicators fused to oxidant receptor peroxidase 1 (Albrecht, Barata, Grosshans, Teleman, & Dick, 2011) are available.

In terms of chemical selectivity, incorporation of the boronate functionality into an assortment of dye scaffolds affords a caged fluorophore sensitive to hydrogen peroxide, but not readily oxidized by many other ROS, such as superoxide, hypochlorite, or hydroxyl radical. Selectivity tests have shown negligible turn-on responses of these probes to a wide range of reactive oxygen and nitrogen species (Fig. 2.3B). The boronate oxidation takes advantage of hydrogen peroxide's specific molecular characteristics, particularly its enhanced nucleophilicity due to the α-effect (Jencks & Carriulo, 1960; Ren & Yamataka, 2007), imparted by adjacent nonbonding orbitals on its oxygen atoms, and the weak O—O bond. Nucleophilic addition of hydrogen peroxide to the boron results in a charged tetrahedral boronate complex, which subsequently undergoes a 1,2-insertion in which the C—B bond migrates to one of the now-electrophilic peroxide oxygens (Fig. 2.2). The resulting borate ester is then hydrolyzed by water to the phenol.

While the boronate functionality displays little reactivity toward the majority of biologically relevant oxidizing species, highly reactive oxygen/nitrogen species such as peroxynitrite have been observed to

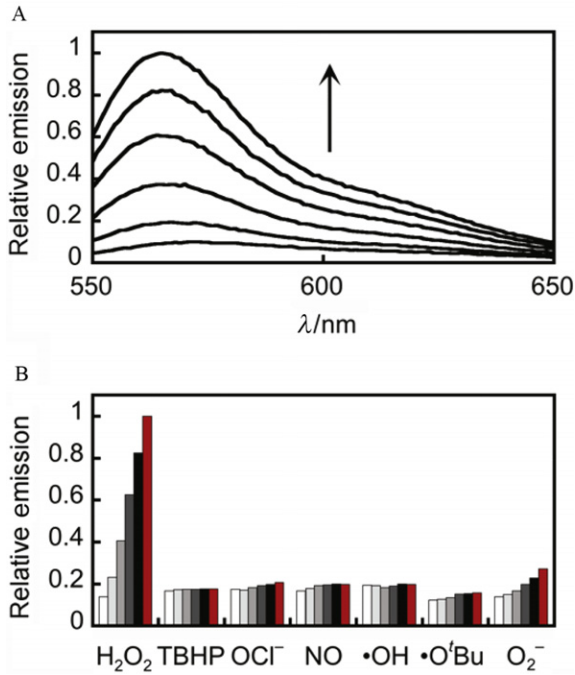

Figure 2.3 Fluorescence turn-on response and selectivity profile of PO1. (A) Fluorescence emission response of 5 μ*M* PO1 after the addition of 100 μ*M* H_2O_2. Time points represent 0, 5, 15, 30, 45, and 60 min. (B) Fluorescence emission response of 5 μ*M* PO1 after the addition of a variety of ROS. Bars represent relative responses at 0, 5, 15, 30, 45, and 60 min after addition of each ROS. Data shown are for 200 μ*M* NO and 100 μ*M* for all other ROS. Data were acquired at 25 °C in 20 m*M* HEPES, pH 7, with excitation at $\lambda = 540$ nm and emission was collected between 545 and 750 nm. Reactions were not complete at these time points. *Reprinted with permission from Dickinson, Huynh, and Chang (2010). Copyright 2010 American Chemical Society.*

react rapidly with aryl boronates (Sikora, Zielonka, Lopez, Joseph, & Kalyanaraman, 2009). However, we note that peroxynitrite and related species are typically generated at much lower concentrations and exhibit markedly shorter biological half-lives compared to hydrogen peroxide, which can offset differences in *in vitro* second-order rate constants. In experiments where these species may be added exogenously or produced endogenously in competition with hydrogen peroxide, use of a boronate-based probe for specific detection of hydrogen peroxide must be accompanied by appropriate control experiments (Section 4.3). These controls generally either reduce

hydrogen peroxide levels with antioxidants or inhibit its direct enzymatic production to confirm the identity of hydrogen peroxide as the major ROS in a given system of interest.

Finally, the performance of these probes, depending on the fluorophore released, can also be affected by variations in local pH, and therefore it is important to employ buffering systems to maintain a stable pH. The oxidation of boronates to phenols by hydrogen peroxide itself is accelerated at higher pH (Kuivila, 1954), and since the final, deprotected form of the probe is a fluorescein or rhodol derivative, any effect of pH upon the behavior and properties of these fluorophores should be considered. Since fluoresceins are quenched at low pH, appropriate control experiments and adjustments to protocols should be made when imaging with these probes in an acidic environment, such as within the macrophage phagosome.

2.3. Selecting a probe

Choosing an appropriate probe for a particular application is critical, since each probe displays different properties that affect its performance, depending on the system of interest. A number of factors will guide probe selection, including the permeability of the probe or ease with which it diffuses through the cellular membrane or throughout an organism, trappability or extent to which the dye is retained within the cell, color of fluorescence, and targeting of the probe to specific subcellular locations. Trappable probes are effective for flow cytometry experiments, monolayer cell culture, and other experiments requiring media exchange with retention of the dye (Dickinson, Peltier, Stone, Schaffer, & Chang, 2011; Miller, Dickinson, & Chang, 2010; Tsien, 1981). Ester functional groups on the probes are cleaved by intracellular esterases, resulting in a charged molecule that cannot readily diffuse across the plasma membrane. Moreover, most of the boronate-based probes are less cell-permeable upon reaction with hydrogen peroxide, as oxidation of the boronate to a phenol increases the hydrophilicity of the dye. Nontrappable, highly permeable probes such as Peroxy Orange-1 (PO1) and PF2 are more suitable for tissue and *in vivo* applications than trappable probes (Harris et al., 2013). Additionally, a set of bioluminescent hydrogen peroxide probes has been developed (Van de Bittner, Bertozzi, & Chang, 2013; Van de Bittner, Dubikovskaya, Bertozzi, & Chang, 2010) that can be used in transgenic mice for whole animal experiments.

2.4. Use and storage of probes

To prepare the probes for imaging use, an aliquot of dry probe is dissolved in the designated amount of dry DMSO to give a stock solution of 5–10 m*M*. This DMSO stock (1–25 μL) is then diluted in 1 mL of an aqueous buffer such as PBS, HEPES, or Tris and mixed thoroughly by pipetting or vortexing to give working concentrations of 1–50 μ*M*. Anhydrous DMSO must be used to dissolve the probe, as high water content may prevent full dissolution of the solid material and interfere with the preparation of a homogenous stock solution.

These probes are most stable in dry, solid form and can be stored for up to 6 months at −20 °C. Solid probe may be dissolved in a small amount of an organic solvent such as chloroform or anhydrous methanol (if soluble) and divided into small portions. The organic solvent can then be removed under reduced pressure in a vacuum desiccator, yielding dried individual aliquots. Once dissolved in anhydrous DMSO, stocks can be stored for 3–4 weeks at −80 °C. Freeze-thaw cycles should be avoided. Any aqueous solutions of boronate-based probes should be freshly prepared and used the same day, as hydrolysis of the boronate reduces permeability and sensitivity of the probe. Furthermore, the probes are sensitive to light and should be protected from photodegradation by storing aliquots and prepared solutions in the dark or covering them with aluminum foil.

3. EXAMPLES OF PROBES AND THEIR USAGE

3.1. PO1 used for fluorometry

3.1.1 Instrumentation and materials

Spectroscopy was performed in 20 m*M* HEPES buffer, pH 7.4. All solutions were prepared using ultrapure water from a purification system such as Barnstead Nanopure or Millipore. Fluorescence spectra were recorded on a Photon Technology International Quanta Master 4 L-format scanning spectrofluorometer (Lawrenceville, NJ) with an LPS-220B 75-W xenon lamp and power supply, A-1010B lamp housing with integrated igniter, switchable 814 photon-counting/analog photomultiplier detection unit, and MD5020 motor driver. Samples for emission measurements were contained in a quartz cuvette with a path length of 1 cm and width of 0.1 cm (1.5 mL volume, Starna, Atascadero, CA). Absorption spectra were recorded using a Varian Cary 50 spectrophotometer (Walnut Creek, CA).

Probe. PO1 stock solution (5 m*M*) in anhydrous DMSO.
H_2O_2. 100 m*M* aqueous stock made freshly by dissolving 11 μL of 30% H_2O_2 (Sigma-Aldrich) in 989 μL H_2O.

3.1.2 In vitro *time course assays*

In order to study the response of a probe to 100 μ*M* hydrogen peroxide over time, the dye was freshly diluted to a concentration of 5 μ*M* in 3 mL of buffer in a 15-mL Falcon tube. The dye was mixed by vortexing to ensure a homogeneous solution. The diluted probe was then distributed by adding 1 mL volume to each of two microcentrifuge tubes, one for studying hydrogen peroxide and the other as a negative control. To one tube, 1 μL of 100 m*M* H_2O_2 solution was added. The solution was vortexed and rapidly transferred to the quartz cuvette, and absorption and fluorescence emission spectra were collected over time. To the second tube, 1 μL of water was added, and spectra were collected as described above.

For all *in vitro* fluorometry experiments, a positive and negative control should be done on each day using the same probe aliquot between samples to account for potential variation in environmental factors, aliquot quality, and reagent preparation. Reactions with hydrogen peroxide and other ROS are usually monitored on an hour or longer time scale, with conversion being incomplete after 1 h at room temperature when using 100 μ*M* hydrogen peroxide. Excessive radiation should be avoided to prevent photobleaching of the dye, and excessive heat or very alkaline environments should be avoided due to risk of boronate hydrolysis.

This protocol yields samples with a final DMSO concentration of 0.1%. In experiments where a minimal volume of organic cosolvent is desired, reduced amounts of stock solution may be used or the concentration of the stock solution may be increased. However, care must be taken to ensure that sufficient organic cosolvent is present to prevent the probe from precipitating out of solution upon addition to aqueous buffer. All solutions should appear optically clear and without particulates.

3.1.3 *Data processing and analysis*

The integrated fluorescence intensity—the area under the fluorescence emission curve—was plotted against time (Fig. 2.3). Fluorescence intensity at a single point, typically the emission maximum, may also be used.

3.2. Trappable PF6-AM for use in flow cytometry experiments

3.2.1 Instrumentation and materials

Instrumentation. We performed flow cytometry experiments on either a Beckman-Coulter EPICS XV-MCL flow cytometer or a LSR Fortessa cell analyzer (BD Biosciences) equipped with a 488-nm laser. The data were analyzed with FlowJo.

Media. (1) Dulbecco's modified Eagle medium (DMEM, Mediatech) with 10% heat-deactivated fetal bovine serum (FBS, HyClone) and 1% penicillin–streptomycin (Mediatech); (2) washing media: Dulbecco's phosphate-buffered saline (DPBS, Invitrogen), DMEM containing no dye, serum, or antibiotics.

Probe. 5 m*M* PF6-AM stock solution in anhydrous DMSO made the day of the experiment.

Exogenous H_2O_2. 100 m*M* aqueous stock made by dissolving 11 μL of 30% H_2O_2 (Sigma-Aldrich) in 989 μL H_2O.

Cell culture supplies. Standard supplies for mammalian cell culture.

3.2.2 Cell culture, dye loading, stimulation, and flow cytometry

Culture HeLa cells in DMEM with high glucose, GlutaMAX™ (Invitrogen, Carlsbad, CA), and 10% FBS in an incubator at 37 °C, 5% CO_2. Passage the cells every 3–4 days at nearly 100% confluence. We typically assay cells with passage numbers of 4–20, both to ensure a stable, exponentially growing culture and to avoid cumulative changes at high passage numbers.

Two days before imaging. Passage the cells and plate in 35-mm tissue culture plates. At the time of the experiment, the confluence level was ca. 70%.

Approximately 1 h before assay. Wash the cells twice with DPBS, detach with 200 μL 0.05% trypsin (Invitrogen), quench the trypsin with 1 mL DMEM with 10% FBS, and collect the cells by centrifugation. Redissolve the cell pellets in 1 mL of 5 μ*M* PF6-AM (from 5 m*M* stock solution in DMSO) in DPBS with calcium chloride and magnesium chloride and incubate the cell solution for 20 min in an incubator at 37 °C, 5% CO_2. Divide the cell solution into two portions, one for treatment conditions and one for control conditions. Treat one cell suspension with 100–300 μ*M* H_2O_2 and the other cell suspension with an equal volume of water. Incubate the cell solutions for 40 min in an incubator at 37 °C, 5% CO_2. Analyze each cell solution by flow cytometry using excitation by a 488-nm laser and collection by a 525-mm band pass filter.

Collect data for at least 10,000 cells for each condition using identical instrument settings.

3.2.3 Data processing and results

In order to exclude dead cells and debris from the final quantification, the forward scatter (FS) and side scatter (SS) results should be used to gate only on the live cell population in each dataset. It is critical to use an identical gate for each condition, and note any significant changes in cell morphology as indicated by FS/SS results upon any condition as these changes may indicate toxicity issues. Using the gate on the live cell population, a histogram should be generated for PF6-AM intensity. The average fluorescence intensity of each population can then be quantified and compared between conditions. This experiment can be performed in multiple biological replicates to generate statistics for the average fluorescence intensity of each condition. When detecting endogenous H_2O_2, control experiments coadministering antioxidants, inhibitors, or RNA interference (RNAi; Section 4.3) are particularly important in identifying the source of fluorescence turn-on.

3.3. Targeted MitoPY1 for fluorescence microscopy

3.3.1 Instrumentation and materials

Confocal microscope. Fluorescence microscopy studies were performed with a LSM 710 laser scanning confocal microscope (Carl Zeiss) with a 63 × oil objective lens, with Zen 2009 software (Carl Zeiss). MitoPY1 was excited using a 488-nm Ar laser, and emission was collected using a META detector between 527 and 580 nm. Hoechst 33342 was excited with a 405-nm diode laser, and emission was collected using a META detector between 450 and 500 nm. The cells were imaged at 37 °C throughout the course of the experiment. Data processing and analysis were conducted using ImageJ (National Institute of Health) or Zen 2009 software (Carl Zeiss).

Probe. MitoPY1 stock solution (5 m*M*) in anhydrous DMSO.

Mitochrondria marker. MitoTracker Deep Red (Invitrogen) stock solution (50 μ*M*) in DMSO.

Nuclear stain. Hoechst 33342 (Sigma-Aldrich) stock solution (1 m*M*) in DMSO.

Exogenous H_2O_2. 100 m*M* aqueous stock made by dissolving 11 μL of 30% H_2O_2 (Sigma-Aldrich) in 989 μL H_2O.

3.3.2 Cell culture

HeLa cells were maintained and passaged using standard protocols. For imaging by fluorescence microscopy, cells were plated at 70–90% confluency in 0.5 mL DMEM supplemented with 10% FBS and 2 m*M* glutamine without phenol red in glass 4-well chamber slides or in a 24-well plate with 18-mm glass coverslips 1–2 days prior to imaging. HeLa cells will grow on uncoated glass. An appropriate coating should be used for plating other adherent cell lines to facilitate growth on glass.

3.3.3 Dye loading, imaging, and data analysis

A dry aliquot of MitoPY1 was allowed to reach room temperature, and then it was diluted in an appropriate volume of anhydrous DMSO to yield a 5 m*M* stock solution. An aqueous solution of 5 μ*M* MitoPY1 in DPBS was prepared by adding 2 μL of the stock solution to 2 mL warm DPBS and mixing thoroughly by vortexing. The cell media was exchanged for the MitoPY1 solution and the cells incubated for 45 min at 37 °C. The probe solution was then removed and buffer replaced with warm DPBS containing 1 μ*M* Hoechst and 25 n*M* MitoTracker Deep Red. At this point, H_2O (control) or 100 μ*M* H_2O_2 was added. The HeLa cells were then incubated for an additional 60 min at 37 °C before imaging.

Image analysis was performed in ImageJ or Zen 2009 software. Z-stacks and maximum intensity projections should be acquired for cells with variation in topology to ensure reproducible quantification of fluorescence. As seen in Fig. 2.4, hydrogen peroxide triggers a robust mitochondrial fluorescent enhancement in the MitoPY1 channel, without change in the MitoTracker Deep Red channel. Only images acquired under the same parameters can be compared during analysis, and analysis should be performed using a standardized method. This type of experiment allows for colocalization studies using a targeted fluorescent hydrogen peroxide probe (Dickinson, Lin, & Chang, in press).

4. IMAGING ENDOGENOUS H_2O_2 USING FLUORESCENT PROBES

In this section, we provide examples to illustrate how H_2O_2 fluorescent probes allow for imaging endogenous H_2O_2 in two representative experimental systems. To demonstrate the simultaneous detection of two separate classes of ROS, dual-imaging experiments with macrophages were carried out using PO1, a red-shifted probe, and aminophenyl fluorescein

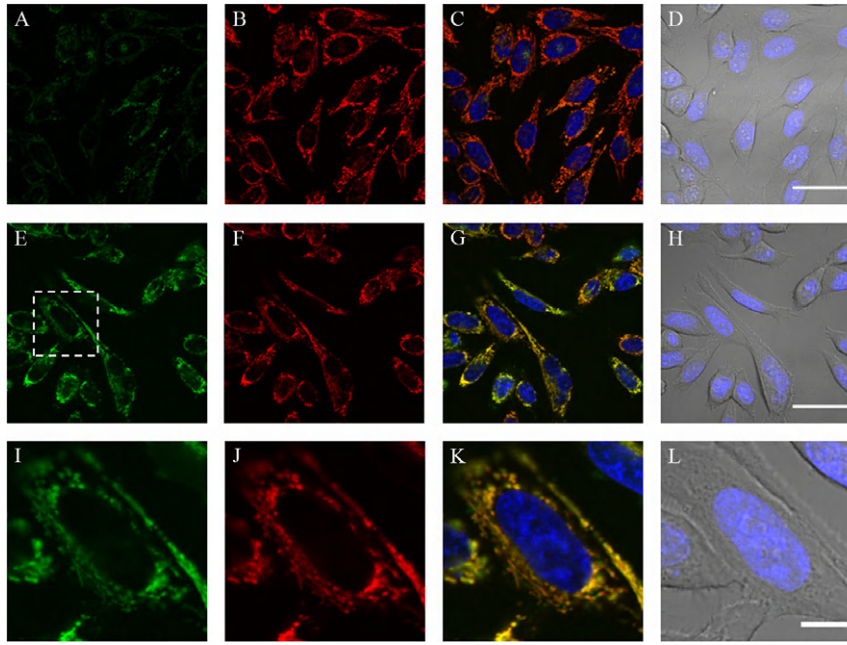

Figure 2.4 Confocal fluorescence images of exogenous H_2O_2 added to live HeLa cells with mitochondrial-targeted H_2O_2 probe MitoPY1. HeLa cells were loaded with 10 μ*M* MitoPY1 in DPBS for 45 min at 37 °C. The media was then exchanged for fresh DPBS containing 25 n*M* Mitotracker Deep Red and 1 μ*M* Hoechst. After the addition of either H_2O (control) or 100 μ*M* H_2O_2, the cells were incubated for 60 min at 37 °C. Control cells were then imaged with MitoPY1 (A), Mitotracker Deep Red (B), overlay of MitoPY1 (green), Mitotracker Deep Red (red), and Hoechst (blue) (C), or overlay of bright field and Hoechst (blue) (D) with 40 μm scale bar. H_2O_2-treated cells were imaged with MitoPY1 (E), Mitotracker Deep Red (F), overlay of MitoPY1 (green), Mitotracker Deep Red (red), and Hoechst (blue) (G), or overlay of bright field and Hoechst (blue) (H) with 40 μm scale bar. The region of H_2O_2-treated cells denoted in (E) is enlarged, showing MitoPY1 (I), Mitotracker Deep Red (J), overlay of MitoPY1 (green), Mitotracker Deep Red (red), and Hoechst (blue) (K), or overlay of bright field and Hoechst (blue) (L) with 10 μm scale bar. *Reprinted with permission from Dickinson, Lin, and Chang (2013). Copyright 2013 Nature Publishing Group.*

(APF), a green probe that detects highly reactive oxygen species (hROS; Setsukinai, Urano, Kakinuma, Majima, & Nagano, 2003). The growth factor stimulation experiment was performed with adult hippocampal neural progenitor (AHP) cells using a cytosolic trappable probe, PF6-AM, to demonstrate the detection of H_2O_2 in a physiologically relevant cell line. As sample preparation is highly dependent on the specific biological questions being addressed, we focus on the methods most applicable to imaging

H_2O_2 in a variety of systems. This section concludes with a discussion of control experiments to verify that the observed fluorescent response from the probes is hydrogen peroxide-dependent.

4.1. Imaging hydrogen peroxide and hROS simultaneously in macrophages

4.1.1 Materials and instrumentation

Media. (1) DMEM (Mediatech) with 10% heat-deactivated FBS (HyClone) and GlutaMAX™ (Invitrogen); (2) washing media: DPBS (Invitrogen), DMEM containing no dye, serum, or antibiotics.

Probes. 5 m*M* PO1 and 5 m*M* APF (Invitrogen, A36003) stock solutions in anhydrous DMSO made the day of the experiment.

Exogenous H_2O_2 and HOCl. 100 m*M* aqueous stocks made by dissolving 30% H_2O_2 (Sigma-Aldrich) or HOCl in H_2O.

Cell culture supplies. Standard supplies for mammalian cell culture.

Instrumentation. We performed fluorescence imaging experiments with a LSM 510 or LSM 710 laser scanning confocal microscope (Carl Zeiss).

4.1.2 Cell culture, dye loading, stimulation, and imaging

RAW264.7 macrophages were cultured in DMEM containing high glucose with GlutaMAX™ and supplemented with 10% FBS. The cells were passaged every 3–4 days at nearly 100% confluence. We typically assay cells with passage numbers of 4–20, both to ensure a stable, exponentially growing culture and to avoid cumulative changes at high passage numbers.

Two days before imaging. The cells were passaged and plated in culture plates suitable for imaging. At the time of the experiment, the confluence level was ca. 70%.

Approximately 1 h before imaging. The culturing media of the RAW264.7 macrophages was replaced with DPBS containing 5 μ*M* PO1 and 5 μ*M* APF and the cells incubated for 20 min at 37 °C. At least one well of cells for each experimental condition was prepared to be imaged simultaneously. After the 20 min incubation, the cells were treated with either experimental or control conditions. For example, one well was treated with H_2O as a control, one well with 100 μ*M* H_2O_2, one well with 100 μ*M* HOCl, and one well with 1 μg/mL phorbal myristate acetate (PMA), a small molecule activator of protein kinase C. The cells were incubated at 37 °C for another 20 min.

Immediately before imaging. The dye-containing media and stimulants were removed from culture dishes. The cells were washed twice with

2 mL of prewarmed DPBS and bathed in 2 mL of dye- and serum-free DMEM for use during imaging.

4.1.3 Imaging and results

Excitation of PO1- and APF-loaded cells at 488 and 543 nm was carried out with Ar and HeNe lasers, respectively, and emission was collected using a META detector between 495–538 and 548–602 nm, respectively, using sequential scans. Image analysis was performed in ImageJ. Additional types of microscopes can be used, but the settings will be specific to the given microscope. In general, care must be taken to find the optimal settings that permit detection of both the PO1 and APF channels independently from one another.

In order to compare the fluorescence intensities before and after addition of exogenous H_2O_2, the images must be acquired and analyzed with identical parameters. As seen in Fig. 2.5, the addition of H_2O_2 resulted in an increase in fluorescent intensity in the PO1 channel, while the addition of HOCl, a hROS detected by APF, was detected only in the APF channel.

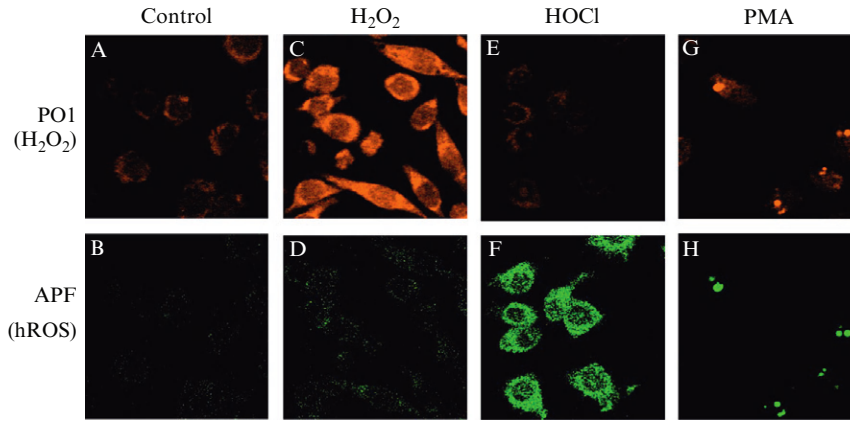

Figure 2.5 Confocal fluorescence images of PMA-induced ROS production in live RAW264.7 macrophages with PO1 and APF simultaneously. Macrophages incubated with 5 μ*M* PO1 and 5 μ*M* APF for 40 min at 37 °C and imaged for PO1 (A) and APF (B). Macrophages incubated with 5 μ*M* PO1 and 5 μ*M* APF for 40 min at 37 °C with 50 μ*M* H_2O_2 added for the final 20 min and imaged for PO1 (C) and APF (D). Macrophages incubated with 5 μ*M* PO1 and 5 μ*M* APF for 40 min at 37 °C with 100 μ*M* HOCl added for the final 20 min and imaged for PO1 (E) and APF (F). Macrophages incubated with 5 μ*M* PO1 and 5 μ*M* APF for 40 min at 37 °C with 1 μg/mL PMA added for the final 20 min and imaged for PO1 (G) and APF (H). *Reprinted with permission from Dickinson, Huynh, and Chang (2010). Copyright 2010 American Chemical Society.*

Activation of the macrophages by PMA, which leads to a robust respiratory burst response and endogenous production of a variety of ROS, including H_2O_2 and HOCl, resulted in punctate staining in both the PO1 and APF channels. Experiments such as these permit the measurement of multiple classes of endogenously produced ROS simultaneously in live specimens.

4.2. Growth factor stimulation

4.2.1 Materials and instrumentation

Media. (1) DMEM (Mediatech) with 10% heat-deactivated FBS (HyClone) and GlutaMAX™ (Invitrogen); (2) washing media: DPBS (Invitrogen), DMEM containing no dye, serum, or antibiotics.

Probes. 5 m*M* PF6-AM stock solution in anhydrous DMSO made the day of the experiment.

Exogenous H_2O_2. 100 m*M* aqueous stock made by dissolving 11 μL of 30% H_2O_2 (Sigma-Aldrich) in 989 μL H_2O.

Cell culture supplies. Standard supplies for mammalian cell culture.

Instrumentation. We performed fluorescence imaging experiments with a LSM510 or LSM 710 laser scanning confocal microscope (Zeiss).

4.2.2 Cell culture, dye loading, stimulation, and imaging

AHP cells were isolated from the hippocampi of 6-week-old female Fisher 344 rats as described (Palmer, Markakis, Willhoite, Safar, & Gage, 1999). Cells were cultured on tissue culture polystyrene coated with poly-ornithine and 5 μg/mL of laminin (Invitrogen) and grown in (DMEM)/F-12 (1:1) high-glucose medium (Invitrogen) containing N-2 supplement (Invitrogen) and 20 ng/mL recombinant human FGF-2 (Peprotech). Cells for H_2O_2 production assays were grown in home-made incubators ((2006). *Nature Protocols*, *1*, 2088) under an atmosphere of 2% O_2/5% CO_2/94% N_2.

The cells were passaged every 2–3 days at ca. 80% confluence. We typically assay cells with passage numbers of 10–30, both to ensure a stable, exponentially growing culture and to avoid cumulative changes at high passage numbers.

Two days before imaging. The cells were passaged and plated in culture plates suitable for imaging. At the time of the experiment, the confluence level was ca. 50%.

12 h before imaging. The culturing media was replaced with (DMEM)/F-12 (1:1) high-glucose medium containing N-2 supplement without FGF-2.

Approximately 1 h before imaging. The culturing media of the AHPs was replaced with (DMEM)/F-12 (1:1) high-glucose medium with N-2 supplement and 5 μ*M* PF6-AM. Cells were incubated for 20 min at 37 °C. At least one well of cells was prepared for each experimental condition to be imaged simultaneously. After the 30 min incubation, the cells were treated with either experimental or control conditions. For example, one well was treated with H_2O as a control and one well with 20 ng/mL FGF-2. The cells were incubated at 37 °C for 30 min, then imaged.

Immediately before imaging. The dye-containing media and stimulants were removed from the culture dishes. The cells were washed twice with 2 mL of prewarmed (DMEM)/F-12 (1:1) high-glucose medium and bathed in 2 mL of dye- and serum-free (DMEM)/F-12 (1:1) high-glucose medium for use during imaging.

4.2.3 Imaging and results

Confocal fluorescence imaging studies were performed with a Zeiss LSM510 NLO Axiovert 200 laser scanning microscope and a 40× Achroplan IR water-immersion objective lens. Excitation of PF6-AM-loaded cells at 488 nm was carried out with an Ar laser and emission was collected using a META detector between 501 and 554 nm. Image analysis was performed in ImageJ. Additional types of microscopes can be used, but the settings should be specific to the given microscope.

In order to compare the fluorescence intensities before and after addition of FGF-2, the images must be acquired and analyzed with identical parameters. As seen in Fig. 2.6, the addition of FGF-2 results in an increase in

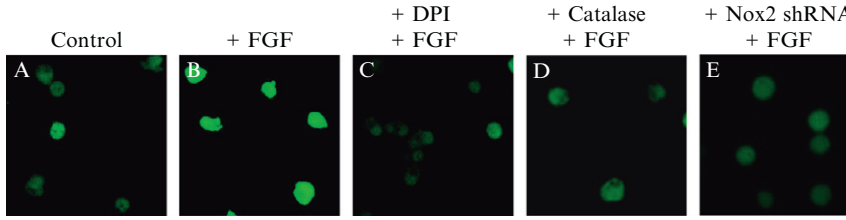

Figure 2.6 FGF-2 stimulated H_2O_2 production in AHPs. After FGF-2 starvation, AHPs were loaded with 5 μM PF6-AM for 30 min, stimulated with H_2O carrier (A) or 20 ng/mL FGF-2 (B), and then imaged. For DPI treatment, cells were preincubated in media containing 5 μ*M* DPI before FGF-2 stimulation (C). For catalase addition, AHPs were transfected with either Catalase or control vector prior to FGF-2 stimulation (D). For Nox2 shRNA addition, AHPs were transfected with either Nox2-shRNA or control vector prior to treatment with FGF-2 (E).

fluorescent intensity. This increase can be attenuated through the use of inhibitors, antioxidants, or genetic manipulation of the molecular source (Fig. 2.6) as outlined in Section 4.3.

4.3. Controls utilizing inhibitors of H_2O_2

In order to confirm that signal differences detected from a particular boronate probe are indeed due to endogenous H_2O_2 production, it is critical to perform a variety of additional control experiments. The specific controls will depend upon the cell or tissue type under examination and the purported source of the H_2O_2 signal. In this section, we list selected control experimental conditions that may be useful to validate the H_2O_2 signal and identify its source in a particular biological system.

The production of H_2O_2 may be suppressed via chemical means, enzyme scavenging, or gene silencing. Diphenylene iodonium (DPI) is a general flavin inhibitor that inhibits the most common intracellular sources of H_2O_2, including the mitochondrial respiratory chain and Noxs. *N*-acetylcysteine (NAC) is a thiol-based general antioxidant that increases the redox capacity of the cell. Catalase is a highly reactive and specific H_2O_2 scavenger enzyme. After validating the endogenous H_2O_2 production by the aforementioned pharmacological and molecular approaches, genetic manipulation of the putative source using RNAi will provide further verification of the cellular machinery responsible for the observed H_2O_2.

DPI. Incubate the cells or tissue samples with 5–10 μ*M* DPI chloride (Sigma-Aldrich, D2926) from a 5 m*M* stock in DMSO for 20–40 min prior to stimulation. The DPI can be administered simultaneously with fluorescent probes. For systems sensitive to chloride, a DPI sulfate salt is also available.

NAC. Incubate cells with 1–10 m*M* NAC from a 1 *M* stock for 40 min prior to stimulation. The NAC can be administered simultaneously with the fluorescent probes.

Catalase. Catalase can be expressed from a pCMV6 mammalian expression vector (Origene) and the empty vector, without the catalase gene, can be utilized as a control. The vectors should be delivered to the cell or tissue type under study via the DNA delivery system commonly used for that system. After transfection, the cells should be allowed to recover and produce catalase for at least 24 h prior to analysis.

RNAi. Short-hairpin RNA (shRNA) constructs or small-interfering RNA (siRNA) directed against the putative source of H_2O_2 can be designed by OligoEngine or other design tools, along with relevant control vectors. Each siRNA oligomer or shRNA expression vector should be validated using Western Blot to confirm the transfection has sufficiently knocked down the target protein.

Performing a series of control experiments can allow for the elucidation of H_2O_2 generation pathways. In the previous section, we discussed the use of PF6-AM as an imaging agent to detect endogenous H_2O_2 production via FGF-2 stimulation in AHPs. AHPs can be transfected with vectors producing shRNA directed against either Nox2, the source of FGF-2 stimulated H_2O_2 production, or Nox3, a related isoform of the Nox proteins. After transfection, the cells were allowed to recover for 24 h and then imaged for H_2O_2 production.

In order to confirm that the changes in signal from PF6-AM in the AHPs are due to intracellular H_2O_2 production and to determine the specific molecular source, a variety of control imaging experiments were performed. Stimulation of PF6-AM-loaded AHPs with 20 ng/mL FGF-2 results in an increase in PF6-AM fluorescence intensity (Fig. 2.6A and B). However, pretreatment with 5 μ*M* DPI, expression of catalase, or expression of Nox2-directed shRNA all abolish the signal increase compared to relevant control experiments (Fig. 2.6C–E). This combination of experiments confirms that the changes in PF6-AM signal are due to (1)intracellular enzymatic activity (validated by DPI inhibition), (2) H_2O_2 (validated by catalase expression), and (3) Nox2-dervied ROS (validated by Nox2 shRNA knockdown).

5. CONCLUSIONS

Installation of the boronate functionality on a variety of fluorescent scaffolds has provided access to a diverse selection of fluorescent hydrogen peroxide probes with a range of spectroscopic properties and *in cellulo* characteristics. Chemical principles have allowed for the design of molecules with traits tailored for different types of biological applications, including *in vitro* assays and fluorescence microscopy of monolayer cell culture which can elucidate the spatial and temporal distribution of hydrogen peroxide in cells. The combination of these chemoselective tools with existing and newly developed methods for the study of hydrogen peroxide in living systems enables further exploration of novel biological systems and the

discovery and elucidation of the essential roles for hydrogen peroxide in a variety of signaling and stress pathways.

ACKNOWLEDGMENTS

We thank the University of California, Berkeley, the Packard Foundation, and the National Institute of General Medical Sciences (NIH GM 79465), as well as Amgen, Astra Zeneca, and Novartis for funding our work on redox imaging probes. B. C. D. is a fellow of the Jane Coffin Childs Memorial Fund for Medical Research. C. J. C. is an investigator with the Howard Hughes Medical Institute.

REFERENCES

Albers, A. E., Okreglak, V. S., & Chang, C. J. (2006). A FRET-based approach to ratiometric fluorescence detection of hydrogen peroxide. *Journal of the American Chemical Society*, *128*, 9640–9641.

Albrecht, S. C., Barata, A. G., Grosshans, J., Teleman, A. A., & Dick, T. P. (2011). In vivo mapping of hydrogen peroxide and oxidized glutathione reveals chemical and regional specificity of redox homeostasis. *Cell Metabolism*, *14*, 819–829.

Bedard, K., & Krause, K.-H. (2007). The NOX family of ROS-generating NADPH oxidases: Physiology and pathophysiology. *Physiological Reviews*, *87*, 245–313.

Belousov, V. V., Fradkov, A. F., Lukyanov, K. A., Staroverov, D. B., Shakhbazov, K. S., Terskikh, A. V., et al. (2006). Genetically encoded fluorescent indicator for intracellular hydrogen peroxide. *Nature Methods*, *3*, 281–286.

Bilan, D. S., Pase, L., Joosen, L., Gorokhovatsky, A. Y., Ermakova, Y. G., Gadella, T. W. J., et al. (2013). HyPer-3: A genetically encoded H_2O_2 probe with improved performance for ratiometric and fluorescence lifetime imaging. *ACS Chemical Biology*, *8*, 535–542.

Chan, J., Dodani, S. C., & Chang, C. J. (2012). Reaction-based small-molecule fluorescent probes for chemoselective bioimaging. *Nature Chemistry*, *4*, 973–984.

Chang, M. C. Y., Pralle, A., Isacoff, E. Y., & Chang, C. J. (2004). A selective, cell-permeable optical probe for hydrogen peroxide in living cells. *Journal of the American Chemical Society*, *126*, 15392–15393.

Cho, D. G., & Sessler, J. L. (2009). Modern reaction-based indicator systems. *Chemical Society Reviews*, *38*, 1647–1662.

Czarnik, A. W. (1994). Chemical communication in water using fluorescent chemosensors. *Accounts of Chemical Research*, *27*, 302–308.

D'Autréaux, B., & Toledano, M. B. (2007). ROS as signaling molecules: Mechanisms that generate specificity in ROS homeostasis. *Nature Reviews Molecular Cell Biology*, *8*, 813–824.

Dickinson, B. C., & Chang, C. J. (2008). A targetable fluorescent probe for imaging hydrogen peroxide in the mitochondria of living cells. *Journal of the American Chemical Society*, *130*, 9638–9639.

Dickinson, B. C., & Chang, C. J. (2011). Chemistry and biology of reactive oxygen species in signaling or stress responses. *Nature Chemical Biology*, *7*, 504–511.

Dickinson, B. C., Huynh, C., & Chang, C. J. (2010). A palette of fluorescent probes with varying emission colors for imaging hydrogen peroxide signaling in living cells. *Journal of the American Chemical Society*, *132*, 5906–5915.

Dickinson, B. C., Lin, V. S., & Chang, C. J. (in press). Preparation and use of MitoPY1, a synthetic fluorophore for imaging hydrogen peroxide in mitochondria of live biological specimens. *Nature Protocols*.

Dickinson, B. C., Peltier, J., Stone, D., Schaffer, D. V., & Chang, C. J. (2011). Nox2 redox signaling maintains essential cell populations in the brain. *Nature Chemical Biology*, *7*, 106–112.

Dickinson, B. C., Tang, Y., Chang, Z., & Chang, C. J. (2011). A nuclear-localized fluorescent hydrogen peroxide probe for monitoring sirtuin-mediated oxidative stress responses *in vivo*. *Chemical Biology*, *18*, 943–948.

Du, J., Hu, M., Fan, J., & Peng, X. (2012). Fluorescent chemodosimeters using 'mild' chemical events for the detection of small anions and cations in biological and environmental media. *Chemical Society Reviews*, *41*, 4511–4535.

Exner, N., Lutz, A. K., Haass, C., & Winklhofer, K. F. (2012). Mitochondrial dysfunction in Parkinson's disease: Molecular mechanisms and pathophysiological consequences. *EMBO Journal*, *31*, 3038–3062.

Frisard, M., & Ravussin, E. (2006). Energy metabolism and oxidative stress: Impact on the metabolic syndrome and the ageing process. *Endocrine*, *29*, 27–32.

Giorgio, M., Trinei, M., Migliaccio, E., & Pelicci, P. G. (2007). Hydrogen peroxide: A metabolic by-product or a common mediator of ageing signals? *Nature Reviews Molecular Cell Biology*, *8*, 722–728.

Harris, J. M., Esain, V., Frechette, G. M., Harris, L. J., Cox, A. G., Cortes, M., et al. (2013). Glucose Metabolism Impacts the Spatiotemporal Onset and Magnitude of HSC Induction in Vivo. *Blood*, *121*, 2483–2493.

Huang, Y., & Mucke, L. (2012). Alzheimer mechanisms and therapeutic strategies. *Cell*, *148*, 1204–1222.

Jencks, W. P., & Carriulo, J. C. (1960). Reactivity of nucleophilic reagents towards esters. *Journal of the American Chemical Society*, *82*, 1778–1786.

Juillerat, A., Gronemeyer, T., Keppler, A., Gendreizig, S., Pick, H., Vogel, H., et al. (2003). Directed evolution of O6-alkylguanine-DNA alkyltransferase for efficient labeling of fusion proteins with small molecules in vivo. *Chemical Biology*, *10*, 313–317.

Jun, M. E., Roy, B., & Ahn, K. H. (2011). 'Turn-on' fluorescent sensing with 'reactive' probes. *Chemical Communications*, *47*, 7583–7601.

Keppler, A., Kindermann, M., Gendreizig, S., Pick, H., Vogel, H., & Johnsson, K. (2004). Labeling of fusion proteins of O6-alkylguanine-DNA alkyltransferase with small molecules in vivo and in vitro. *Methods*, *32*, 437–444.

Kuivila, H. G. (1954). Electrophilic displacement reactions: Kinetics of the reaction between hydrogen peroxide and benzeneboronic acid. *Journal of the American Chemical Society*, *76*, 870–874.

Kuivila, H. G., & Armour, A. G. (1957). Electrophilic displacement reactions: Effects of substituents on rates of reactions between hydrogen peroxide and benzeneboronic acid. *Journal of the American Chemical Society*, *79*, 5659–5662.

Kuivila, H. G., & Wiles, R. A. (1955). Electrophilic displacement reactions: Catalysis by chelating agents in the reaction between hydrogen peroxide and benzeneboronic acid. *Journal of the American Chemical Society*, *77*, 4830–4834.

Lambeth, J. D. (2004). NOX enzymes and the biology of reactive oxygen. *Nature Reviews Immunology*, *4*, 181–189.

Lin, M. T., & Beal, M. F. (2006). Mitochondrial dysfunction and oxidative stress in neurodegenerative diseases. *Nature*, *443*, 787–795.

Lippert, A. R., Van de Bittner, G. C., & Chang, C. J. (2011). Boronate oxidation as a bioorthogonal reaction approach for studying the chemistry of hydrogen peroxide in living systems. *Accounts of Chemical Research*, *44*, 793–804.

Mattson, M. P. (2004). Pathways towards and away from Alzheimer's disease. *Nature*, *430*, 631–639.

Miller, E. W., Albers, A. E., Pralle, A., Isacoff, E. Y., & Chang, C. J. (2005). Boronate-based fluorescent probes for imaging cellular hydrogen peroxide. *Journal of the American Chemical Society*, *127*, 16652–16659.

Miller, E. W., Dickinson, B. C., & Chang, C. J. (2010). Aquaporin-3 mediates hydrogen peroxide uptake to regulate downstream intracellular signaling. *Proceedings of the National Academy of Sciences of the United States of America*, *107*, 15681–15686.

Miller, E. W., Tulyathan, O., Isacoff, E. Y., & Chang, C. J. (2007). Molecular imaging of hydrogen peroxide produced for cell signaling. *Nature Chemical Biology*, *3*, 263–267.

Murphy, M. P., Holmgren, A., Larsson, N.-G., Halliwell, B., Chang, C. J., Kalyanaraman, B., et al. (2011). Unraveling the biological roles of reactive oxygen species. *Cell Metabolism*, *13*, 361–366.

Nelson, K. J., Klomsiri, C., Codreanu, S. G., Soito, L., Liebler, D. C., Rogers, L. C., et al. (2010). Use of dimedone-based chemical probes for sulfenic acid detection: Methods to visualize and identify labeled proteins. *Methods in Enzymology*, *473*, 95–115.

Palmer, T. D., Markakis, E. A., Willhoite, A. R., Safar, F., & Gage, F. H. (1999). Fibroblast growth factor-2 activates a latent neurogenic program in neural stem cells from diverse regions of the adult CNS. *Journal of Neuroscience*, *19*, 8487–8497.

Paulsen, C. E., & Carroll, K. S. (2010). Orchestrating redox signaling networks through regulatory cysteine switches. *ACS Chemical Biology*, *5*, 47–62.

Quang, D. T., & Kim, J. S. (2010). Fluoro- and chromogenic chemodosimeters for heavy metal ion detection in solution and biospecimens. *Chemical Reviews*, *110*, 6280–6301.

Ren, Y., & Yamataka, H. (2007). The α-effect in gas-phase S_N2 reactions: Existence and the origin of the effect. *Journal of Organic Chemistry*, *72*, 5660–5667.

Rhee, S. G. (2006). H_2O_2, a necessary evil for cell signaling. *Science*, *312*, 1882–1883.

Setsukinai, K., Urano, Y., Kakinuma, K., Majima, H. J., & Nagano, T. (2003). Development of novel fluorescence probes that can reliably detect reactive oxygen species and distinguish specific species. *Journal of Biological Chemistry*, *278*, 3170–3175.

Sikora, A., Zielonka, J., Lopez, M., Joseph, J., & Kalyanaraman, B. (2009). Direct oxidation of boronates by peroxynitrite: Mechanism and implications in fluorescence imaging of peroxynitrite. *Free Radical Biology & Medicine*, *47*, 1401–1407.

Srikun, D., Albers, A. E., & Chang, C. J. (2011). A dendrimer-based platform for simultaneous dual fluorescence imaging of hydrogen peroxide and pH gradients produced in living cells. *Chemical Science*, *2*, 1156–1165.

Srikun, D., Albers, A. E., Nam, C. I., Iavarone, A. T., & Chang, C. J. (2010). Organelle-targetable fluorescent probes for imaging hydrogen peroxide in living cells via SNAP-tag protein labeling. *Journal of the American Chemical Society*, *132*, 4455–4465.

Srikun, D., Miller, E. W., Domaille, D. W., & Chang, C. J. (2008). An ICT-Based approach to ratiometric fluorescence imaging of hydrogen peroxide produced in living cells. *Journal of the American Chemical Society*, *130*, 4596–4597.

Stone, J. R., & Yang, S. (2006). Hydrogen peroxide: A signaling messenger. *Antioxid Redox Signaling*, *8*, 243–270.

Tsien, R. Y. (1981). A non-disruptive technique for loading calcium buffers and indicators into cells. *Nature*, *290*, 527–528.

Urano, Y., Kamiya, M., Kanda, K., Ueno, T., Hirose, K., & Nagano, T. (2005). Evolution of fluorescein as a platform for finely tunable fluorescence probes. *Journal of the American Chemical Society*, *127*, 4888–4894.

Van de Bittner, G. C., Bertozzi, C. R., & Chang, C. J. (2013). A strategy for dual-analyte luciferin imaging: In vivo bioluminescence detection of hydrogen peroxide and caspase activity in a murine model of acute inflammation. *Journal of the American Chemical Society*, *135*, 1783–1795.

Van de Bittner, G. C., Dubikovskaya, E. A., Bertozzi, C. R., & Chang, C. J. (2010). In vivo imaging of hydrogen peroxide production in a murine tumor model with a

chemoselective bioluminescent reporter. *Proceedings of the National Academy of Sciences of the United States of America*, *107*, 21316–21321.
Veal, E. A., Day, A. M., & Morgan, B. A. (2007). Hydrogen peroxide sensing and signaling. *Molecular Cell*, *26*, 1–14.
Winterbourn, C. C. (2008). Reconciling the chemistry and biology of reactive oxygen species. *Nature Chemical Biology*, *4*, 278–286.
Xun, Z., Rivera-Sánchez, S., Ayala-Peña, S., Lim, J., Budworth, H., Skoda, E. M., et al. (2012). Targeting of XJB-5-131 to mitochondria suppresses oxidative DNA damage and motor decline in a mouse model of Huntington's Disease. *Cell Reports*, *2*, 1137–1142.
Zelko, I. N., Mariani, T. J., & Folz, R. J. (2002). Superoxide dismutase multigene family: A comparison of the CuZn-SOD (SOD1), Mn-SOD (SOD2), and EC-SOD (SOD3) gene structures, evolution, and expression. *Free Radical Biology & Medicine*, *33*, 337–349.

CHAPTER THREE

Visualization of Intracellular Hydrogen Peroxide with HyPer, a Genetically Encoded Fluorescent Probe

Nataliya M. Mishina[*,†], Kseniya N. Markvicheva[*], Dmitry S. Bilan[*,†], Mikhail E. Matlashov[*], Marina V. Shirmanova[†], David Liebl[‡], Carsten Schultz[§], Sergey Lukyanov[*,†], Vsevolod V. Belousov[*,†,1]

[*]Shemyakin-Ovchinnikov Institute of Bioorganic Chemistry, RAS, Moscow, Russia
[†]Nizhny Novgorod State Medical Academy, Nizhny Novgorod, Russia
[‡]Institute for Molecular Bioscience, The University of Queensland, St. Lucia, Queensland, Australia
[§]EMBL Heidelberg, Heidelberg, Germany
[1]Corresponding author: e-mail address: vsevolod.belousov@gmail.com

Contents

1. Introduction 46
2. Experimental Design 48
   2.1 Choosing transfection method 48
   2.2 Parameter selection for image acquisition 48
3. Materials 49
   3.1 Equipment setup 51
4. Procedure 51
   4.1 Transfection 51
   4.2 Preparation of transfected cells for the experiment 52
   4.3 Primary visualization 53
   4.4 Imaging settings 53
   4.5 Imaging 55
   4.6 Anticipated results 57
Acknowledgments 58
References 58

Abstract

The fluorescent sensor HyPer allows monitoring of intracellular H_2O_2 levels with a high degree of sensitivity and specificity. Here, we provide a detailed protocol of ratiometric imaging of H_2O_2 produced by cells during phagocytosis, including instructions for experiments on different commercial confocal systems, namely, Leica SP2, Leica SP5, and Carl Zeiss LSM, as well as wide-field Leica 6000 microscope. The general

Methods in Enzymology, Volume 526
ISSN 0076-6879
http://dx.doi.org/10.1016/B978-0-12-405883-5.00003-X

© 2013 Elsevier Inc.
All rights reserved.

experimental scheme is easily adaptable for imaging H_2O_2 production by various cell types under a variety of conditions.

1. INTRODUCTION

Cells use oxygen not only for energy demands but also to produce reactive oxygen species (ROS). Superoxide anion radical, hydroxyl radical, hydrogen peroxide, and nitric oxide are the most investigated ROS in biological systems (Dröge, 2002). ROS are capable of generating nonspecific damage to biomolecules under pathological conditions, a process summarized as oxidative stress. At the level of physiological regulation, subtoxic production of ROS, namely H_2O_2, is used by cells to modify signaling cascades via selective oxidation of a relatively small number of protein thiol groups (Winterbourn, 2008). Since the 1960s, ROS production was mainly investigated in the context of pathogen killing by phagocytes. Phagocytes, namely neutrophils and macrophages, represent the first line of host defense against pathogens such as fungi and bacteria. Phagocytes engulf opsonized microbial cells into endocytic phagosomes, ultimately leading to pathogen destruction. The main mechanism of intraphagosomal killing is associated with ROS produced by NADPH oxidase (Nox) at the phagocyte plasma membrane and other membrane compartments (Rada & Leto, 2008).

The appearance of the first data on specific roles of oxygen radicals in microbial destruction determined the view on ROS as poisoning substances during the next decades. However, a growing set of the data supports now a second messenger role of ROS (D'Autréaux & Toledano, 2007). Particularly, H_2O_2 serves as a regulator of intracellular signaling cascades in nonphagocyting cell types. Further studies of H_2O_2-dependent signaling reveal its participation in the process of phagocytosis as well (Forman & Torres, 2002). Apparently, almost all eukaryotic cell types express Nox family enzymes, which are the main source of H_2O_2 in cells upon stimulation with various growth factors and cytokines (Bae et al., 2000; Bedard & Krause, 2007; Lange et al., 2009; Leto, Morand, Hurt, & Ueyama, 2009; Mishina et al., 2011; Tabet et al., 2008). The NADPH oxidase complex consists of a membrane-bound cytochrome b558 (Nox1-5) associated with p22 and several cytosolic subunits including p40phox, p47phox, p67phox, and the small GTPases Rac1 or Rac2 (Bedard & Krause, 2007).

H_2O_2 is much more stable than the other ROS, mainly because it is less reactive. H_2O_2 has been postulated to be able to diffuse over a long distance within or between cells. Although the properties of H_2O_2 make this molecule a good candidate for the "second messenger" role, a prerequisite for this function is the precise control of H_2O_2 in time and space.

Since the discovery of ROS, many methodologies for their detection have been developed. Most of them allow very selective and sensitive detection of ROS produced *in vitro* by isolated enzymes or organelles (Gomes, Fernandes, & Lima, 2005). Some of these techniques detect ROS released by cultured cells to the extracellular media (Wardman, 2007). However, the problem of intracellular ROS detection was not solved until recently. The most widely used approach to ROS detection is based on using the cell-permeable low molecular weight compound dichlorodihydrofluorescein diacetate (H_2DCFDA) and its analogues (Invitrogen, Molecular Probes). However, this compound has several drawbacks that make its use too complicated and the results are often uninterpretable (Bonini, Rota, Tomasi, & Mason, 2006; Crow, 1997; Marchesi, Rota, Fann, Chignell, & Mason, 1999; Rota, Chignell, & Mason, 1999; Rota, Fann, & Mason, 1999; Wardman, 2007). Promising improvement in ROS imaging via synthetic small molecules was recently achieved by the introduction of Peroxy Green 1 and Peroxy Crimson 1 dyes (Miller, Tulyathan, Tulyanthan, Isacoff, & Chang, 2007) However, these dyes have several caveats: (i) they are not ratiometric and therefore require a control dye for proper quantification and (ii) they are irreversibly oxidized with ROS. Therefore, they are often less well suitable for dynamic real-time imaging of ROS-dependent events in live cells. However, due to the intrinsic memory effect, they are useful to report on ROS changes in a global fashion and in cases where low levels of ROS are produced over extended periods of time.

To overcome the drawbacks of chemical probes, we designed and developed HyPer, a genetically encoded ratiometric fluorescent sensor for H_2O_2 (Belousov et al., 2006). The properties of the H_2O_2-sensing domain of HyPer, derived from bacterial OxyR protein, dictate perfect selectivity of the probe, high sensitivity and, importantly, reversibility. HyPer may be expressed in any cell compartment by transfecting cells with DNA encoding HyPer fused with a subcellular localization tag. HyPer has two excitation peaks corresponding to protonated (420 nm) and charged (500 nm) forms of Tyr residue of the YFP chromophore. Both forms can be easily visualized by laser excitation of a confocal system or with wide-field fluorescent microscopy. Imaging the emission after excitation at both peaks

ratiometrically avoids artifacts associated with cell movement or differences in the sensor expression level between cells. However, for cells that do not move significantly and do not change the shape in course of the experiment, single wavelength monitoring is possible (Belousov et al., 2006; Markvicheva, Bogdanova, Staroverov, Lukyanov, & Belousov, 2009).

2. EXPERIMENTAL DESIGN

2.1. Choosing transfection method

For cell lines that are easy to transfect (such as HEK, HeLa, NIH-3T3), we recommend the use of liposome transfection. We obtain the best transfection efficiency with FuGene6 transfection reagent (Jacobsen, Calvin, Colvin, & Wright, 2004). For hard-to-transfect cell types (in our studies—RAW 264.7 line that gives ~5–10% transfected cells with liposome transfection), lentiviral transduction is preferred (Tiscornia, Singer, & Verma, 2006).

2.2. Parameter selection for image acquisition

2.2.1 Choosing excitation and emission wavelengths

HyPer is the probe of choice for time-lapse experiments. To record ratiometric time series, the 420-nm peak is excited with the 405-nm laser on a confocal microscope, or by using the filter set of a wide-field microscope enabling excitation in the 400–430 nm range. Emission is usually detected in the 510–550 nm range. The 500-nm peak can be excited with the 488-nm or 496-nm laser lines or with a wide-field filter set enabling excitation in the 470–500 nm range. The detection settings are the same as for the 420-nm peak. The YFP chromophore is photoconvertible (Dickson, Cubitt, Tsien, & Moerner, 1997). Excitation of the 500-nm peak converts part of the chromophores to a dark state in a light intensity-dependent manner. Excitation of the protonated form of the chromophore (420-nm peak) converts it to the fluorescent state. Therefore, to obtain maximal brightness, each frame should be first imaged with the excitation of the 420-nm peak, and then 500 nm. When using a laser scanning confocal system, we suggest changing excitation lasers between lines rather than between frames, because this produces less delay between excitation lasers in each "point" of the imaged cell.

2.2.2 Choosing light intensity, resolution, and time delay between frames

Light of the laser or lamp may cause phototoxic effects in the imaged cells. Therefore, in continuous time-lapse experiments, settings should aim not only in getting signals from the probe but also to do this with minimal light irradiation. First, maximize the time delay between frames (in our case, "frame" means microscopic field imaged at both excitation wavelengths). H_2O_2 is usually produced on a minutes scale. Thus, there is no need for fast acquisition rates. For phagocytosis experiments, the delay in producing relevant series without cell damage and HyPer bleaching should be 10–60 s. Try to minimize laser power which can be partially compensated by increasing PMT voltage. When imaging with a Leica SP2 or a Carl Zeiss 510/510 Meta, use as low resolution settings as possible, because this decreases the frame acquisition time, thus lowering the amount of illuminating light.

3. MATERIALS

Reagents

- DMEM (Invitrogen, cat. no. 41965-039)
- Minimum Essential Medium Eagle (EMEM) (Sigma–Aldrich, cat. no. M3024)
- OPTI-MEM (Invitrogen, cat. no. 31985-047)
- RPMI-1640 (Invitrogen, cat. no. 21875-034)
- Hanks Balanced Salt Solution (HBSS) (Invitrogen, cat. no. 14025-100)
- Dulbecco-PBS (Invitrogen, cat. no. 14040-091)
- Fetal calf serum, FCS (Invitrogen, cat. no. 16000-044)
- Low-endotoxin FCS (PAA, cat. no. A11-151)
- Bovine serum (Invitrogen, cat. no. 16170-078)
- Penicillin/streptomycin (Invitrogen, cat. no. 15070-063)
- L-Glutamine (Invitrogen, cat. no. 25030-024)
- Trypsin/EDTA solution (Invitrogen, cat. no. R-001-100)
- HEPES (Promega, cat. no. H5302)
- H_2O_2 (Sigma–Aldrich, cat. no. 516813)
  Caution. May cause severe skin burns and eye damage. Follow the safety guide.
- BSA (Sigma–Aldrich, cat. no. 9048-46-8)
- FuGene6 transfection reagent (Roche Diagnostics, cat. no. 11988387001)

- Mammalian cells
- Sodium bicarbonate
- Zymosan A (Sigma–Aldrich, cat. no Z4250)

Equipment

- Glass-bottom dishes (World Precision Instruments, cat. no. FD35-100)
- Standard equipment for eukaryotic cell culturing
  Critical. For hard-to-transfect cell cultures, when using lentiviral vectors for delivery of HyPer cDNA, S2 safety level cell culture facility is required.
- Confocal microscope or wide-field fluorescent microscope both equipped with a thermostating box
  Critical. For ratiometric HyPer imaging, confocal microscopes should be equipped with lasers providing violet (405 nm) and blue (488 or 496 nm) laser lines. Alternatively, mercury or xenon arc lamps can be used for the HyPer imaging.

Reagent setup

- Complete growth medium: For HeLa-Kyoto cells, we use DMEM supplemented with penicillin/streptomycin, L-glutamine, and 10% FCS; for RAW 264.7 cells, RPMI-1640 supplemented with penicillin/streptomycin, L-glutamine, and 10% heat-inactivated low-endotoxin FCS.
  Critical. For RAW 264.7 cells maintaining, it is critical to use heat-inactivated serum with low endotoxin (ideally endotoxin free) in order to obtain appropriate phagocytic activity.
- Cell starvation and imaging medium: EMEM supplemented with either 2.2 g/l sodium bicarbonate and 20 m*M* HEPES (if CO_2 supply for thermostating box available) or just 20 m*M* HEPES (use bicarbonate-free media in case no CO_2 supply for thermostating box is available in order to prevent alkalinization of the imaging media), penicillin/streptomycin, L-glutamine, and 0.5% BSA.
- Preparation of serum-opsonized zymosan A suspension: We used adult bovine serum to opsonize zymosan A. Mix the serum (1:1) with PBS. To make a 30 × stock, incubate 1.5 ml of PBS–serum mixture with 5 mg of zymosan A powder at 37 °C on a shaker for 30–60 min. Avoid stirring, shake gently. After incubation, wash zymosan with PBS for three times and finally resuspend in 500 µl of PBS. Opsonized zymosan can be stored at −70 °C. For experiment, keep an aliquot on blue ice.
  Critical. It is important to use adult nonheat-inactivated serum for opsonization. Fetal and heat-inactivated sera contain reduced amount of complement proteins, which are required for zymosan particle opsonization.

3.1. Equipment setup

3.1.1 *Inverted fluorescence microscope equipped for rapid ratio imaging*

We used a Leica DMI6000 microscope equipped with an external filter wheel CFP/YFP FRET set (11522073). CFP/YFP FRET set includes excitation filters CFP_{ex} (BP 427/10), YFP_{ex} (BP 504/12), and emission filters CFP_{em} (BP 472/30), YFP_{em} (BP 542/27). This set allows high-speed HyPer acquisition (CFP_{ex}/YFP_{em} for the 420-nm peak and YFP_{ex}/YFP_{em} for the 500-nm peak). The FRET set was used with a "FRET" filter cube. The cube was equipped only with a dichroic mirror (440/520 nm) but neither contained an excitation filter nor an emission filter. Alternatively, any confocal fluorescent microscope, either scanning or spinning disc, equipped with 405-nm and 488 (496)-nm lasers may be used. In this protocol, we describe settings for scanning confocal systems.

4. PROCEDURE

4.1. Transfection

1. Plate the cells on glass-bottom dishes.
   Pause point. After plating the cells, wait at least 12 h.
2. Transfect the cells with the HyPer encoding vector, using FuGene6 transfection reagent or by any other appropriate method. Useful tips for transient transfection are highlighted in the manufacturer's protocols and in other sources (Dalby et al., 2004; Jacobsen et al., 2004; Jordan & Wurm, 2004).
3. Culture the cells for 12–48 h at 37 °C, 5% CO_2.
   Critical step. HyPer maturates quickly at 37 °C. However, within a particular experimental system, the signal brightness depends on many parameters, including expression activity of the chosen promoter in a particular cell line, stability of mRNA, effectiveness of a protein folding, and protein turnover rate (degradation rate) of the fusion construct. Depending on these parameters, it can be necessary to incubate transfected cells for 24–48 h to get a reliable signal for easy-to-transfect cell lines (HeLa, HEK, etc.) HyPer fluorescence can be detected after 6–12 h posttransfection. After lentiviral transduction, 36–48 h may be required to detect fluorescence.
   Pause point. Incubate cells on a glass-bottom dish for 12–48 h at 37 °C, 5% CO_2.

4.2. Preparation of transfected cells for the experiment

4. A. For experiment with H_2O_2 addition: Replace complete medium with 1.5 ml preheated (37 °C) HBSS.
   B. For induction of phagocytosis: Replace complete medium with 1.5 ml preheated (37 °C) imaging medium supplemented with 0.1% (wt/vol) BSA. Incubate macrophages for 30 min at 37 °C. Keep the cells out of the CO_2 incubator if using bicarbonate-free imaging media (Table 3.1).

Table 3.1 Troubleshooting table

Step	Problem	Possible reason	Solution
4	Low number or no transfected cells	Nonoptimal transfection conditions	Optimize transfection protocol or use lentiviral transduction system
5	Low signal/background ratio	Low expression level of HyPer	Wait for 24 h to get higher protein expression level
6 (A) and (B)	Rapid "bleaching" of the probe under blue light excitation	Photoconversion of the chromophore into the dark state	Irradiate the sample with a pulse of violet light or wait for several minutes
	Fluorescence signal is saturated	(i) Too long exposure time	Decrease the exposure time/PMT voltage/light intensity. It is also helpful to decrease binning of the CCD camera
		(ii) Too high PMT voltage/excitation light intensity	
7 (A) and (B)	No phagocytosis	(i) Nonheat-inactivated FCS or serum with high concentrations of endotoxins is used for culturing the cells	(i) Change serum for heat-inactivated low-LPS FCS
			(ii) Thaw fresh aliquot of the cells, use after passage 3
		(ii) High passage number	
	Weak phagocytosis (10–50% of the cells phagocyte) or no H_2O_2 production upon phagocytosis	(i) Weak opsonization	(i) Change lot or origin of serum used for opsonization
		(ii) No or too short time of serum starvation	(ii) Increase the serum starvation time up to 60 min
		(iii) High passage number	(iii) Thaw fresh aliquot of the cells, use after passage 3

4.3. Primary visualization

5. Visualize HyPer using a mercury or xenon arc lamp. Regular GFP or FITC filter sets allow visualizing fluorescence.
   Critical. Irradiation of HyPer with light exciting the deprotonated form of the chromophore (500-nm peak) leads to photoconversion to the dark state. While illuminating the cells with blue light, you may see rapid pseudobleaching of HyPer. However, the chromophore can be reversed to the fluorescent state by pulse irradiation with light exciting the protonated form of the chromophore (420-nm excitation peak). We usually use 40 × or 63 × Plan Apochromat objectives with high numerical aperture, but other high magnitude high numerical aperture objectives may be used as well (Table 3.1).

4.4. Imaging settings

6. Setting up microscope for HyPer time-lapse imaging.

A Setting up confocal microscope for HyPer time-lapse imaging

i. Activate 405-nm and 488 (496)-nm lasers. Set the scanning resolution to 512 × 512 or 1024 × 1024. Usually, 512 × 512 points is enough to obtain all the necessary information both on fluorescence intensity and intracellular distribution. In the case of a Leica SP2 or Carl Zeiss LSM510 systems, lowering resolution allows increasing the scanning beam speed and decreases the so-called pixel time, thus reducing photodamage of the cells by laser light.

ii. Set pinhole size to ~2–4 μm. Less pinhole size is usually used to obtain structural information rather than messenger or activity dynamics. Higher pinhole size may lead to a decrease in signal-to-background ratio.

iii. Set PMT voltage to 700–800. Lower value makes images less noisy, higher value allows one to use less laser power.

iv. Set the intensity of the 405-nm laser to 5–10% and the intensity of the 488-nm 10-mW Ar laser to 1–7%.
   Critical. These numbers may vary depending on optics, lasers, laser alignment, and the equipment. Fluorescence should be clearly visible in both channels. The intensity of fluorescence should be nearly equal in both channels.

v. Set up the beam path for 420-nm peak excitation by 405-nm laser and for emission light.

vi. Set up the beam path for the 500-nm peak excitation by 488 (496 nm) laser and for emission light. Since the emission peak does not shift, upon reaction of HyPer with H_2O_2, the same detector for both channels should be used. For Leica SP2 and SP5 systems, and for the Carl Zeiss LSM710 setup, the emission range is set from 500 to 530–550 nm. For Carl Zeiss LSM510, the setup uses 505–530 or 505–550 bandpass emission filters.

vii. The "Beam expander" option available on the Leica SP2 confocal system permits increasing the irradiated volume and allows improving the fluorescence signal intensity in cells with low expression level without increasing the laser intensity. For Leica SP2, set the Beam expander to 3.

viii. Enable switching channels between lines rather than between frames. Every line in the frame should be always excited by the 405-nm laser first and then by the 488-nm (496-nm) laser.

ix. Optionally, activate the transmitted light channel. Any laser can serve as the source of the transmitted light. Set up the PMT voltage for the channel to make the cells clearly visible.

B Setting up the wide-field fluorescent microscope Leica 6000 for HyPer time-lapse imaging

i. Turn on the light source. Activate the following settings for both channels: binning (none or 2×2 or 4×4) (Note. The binning function reduces the number of pixels on the CCD chip, thus lowering resolution and increasing signal-to-noise ratio). Keep the acquisition time as low as possible.

ii. Activate filter cube "FRET" equipped with a dichroic mirror (440/520 nm).

iii. Set up excitation filter CFP (BP 427/10) to excite the 420-nm peak.

iv. Set up excitation filter YFP (BP 504/12) to excite the 500-nm peak.

v. Set up emission filter "YFP" (BP 542/27) for both channels.

vi. For Channel 1 (cyan excitation): light intensity: 2–5, exposure time: 20–500 ms.

vii. For Channel 2 (green–yellow excitation): light intensity: 2–5, exposure time: 20–500 ms.

viii. Optionally, activate transmitted light channel.

ix. Set up time delay between frames. Usually, it should be between 10 and 60 s to obtain a relevant time profile (Table 3.1).

4.5. Imaging

7. Proceed with time-lapse imaging for option A for confocal microscopes or option B for wide-field fluorescent microscopes.

A Confocal microscope

i. At least 2 h before imaging, warm up the thermal incubator box to 37 °C.
ii. Place the dish with cells onto the microscope stage. Set up focus.
iii. Switch the system to a scanning mode.
iv. Perform a single scan. Zoom selected cells with "Zoom in" function of the Leica system or the "Crop" function of Carl Zeiss system.
v. Select a region of interest (ROI) in the area of an individual transfected cell and measure the signal intensity "ROI" function of the Carl Zeiss system or the "Quantification-Histogram" function of the Leica system.
vi. Set the fluorescence intensity in each channel of ROI to be in the range between 30 and 80 by changing the light intensity and/or PMT voltage.
vii. Perform several single scans to set the final focus, adjust laser power and PMT voltage.
viii. Start time series recording. It is important to observe that the starting 405 nm/488 (496) nm excitation ratio and microscope focus are stable over this prestimulation period.
ix. Cell stimulation:
  a. H_2O_2 addition: After 5 min of imaging, add drop-by-drop H_2O_2 diluted in 500 µl of prewarmed HBSS. Changes in the F500/F420 ratio are observable immediately after H_2O_2 addition. Continue data acquisition.
  b. Induction of phagocytosis: After 5–10 min of imaging, add drop-by-drop opsonized zymosan suspension diluted in 500 µl of prewarmed EMEM. Continue data acquisition for 30–60 min.

Critical step. Do not touch the microscope stage or the culture dish.

B Wide-field fluorescent microscope

i. Carry out the same procedures as in Step 7 (A) (i)–(iv).
ii. Perform several single scans to set the final focus, adjust light power and exposure time. The initial fluorescence intensities in both channels in a ROI should be almost equal (±5–10%) and should be in the range between 30 and 70 for an 8-bit camera.
iii. Start time series recording. It is important to observe that the microscope focus is stable over the prestimulation period.

iv. Cell stimulation:

a. H_2O_2 addition: After 5 min of imaging, add drop-by-drop H_2O_2 diluted in 500 μl of prewarmed HBSS. Change in F500/F420 ratio is observable immediately after H_2O_2 addition.

b. Induction of phagocytosis: After 5–10 min of imaging, add drop-by-drop opsonized zymosan suspension diluted in 500 μl of prewarmed EMEM. Continue data acquisition for 30–60 min.

Critical step. Do not touch the microscope stage or the culture dish (Table 3.1).

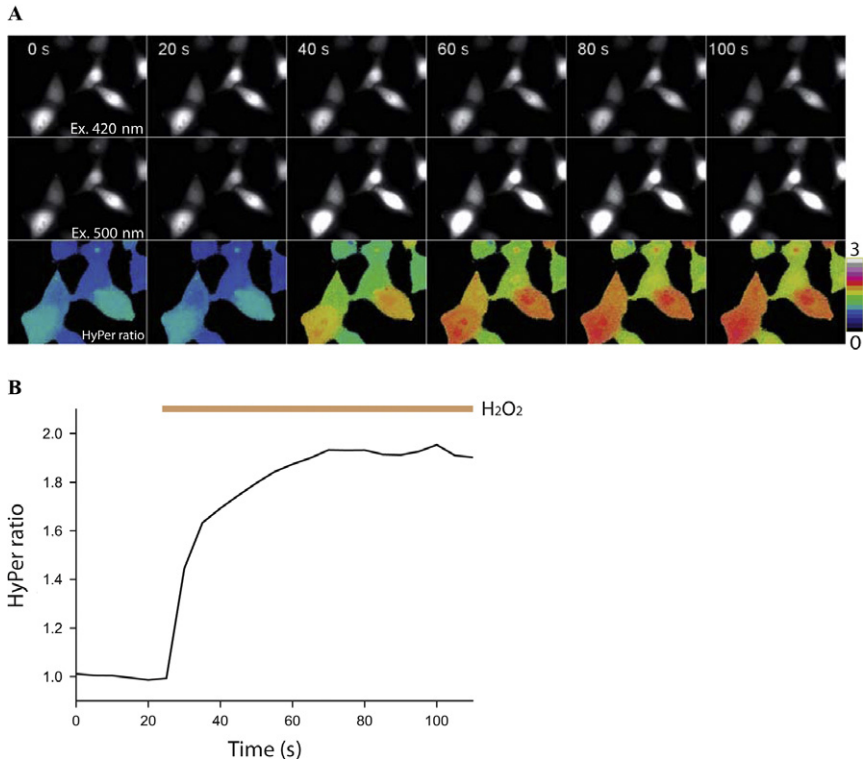

Figure 3.1 Ratio change of HyPer in HeLa-Kyoto cells upon addition of H_2O_2. (A) Images of ratio F500/F420 change in cells transfected with HyPer-cyto and exposed to 200 μ*M* H_2O_2. The lower row of the images represents subcellular distribution of HyPer ratio. Upper and middle rows of the images show fluorescence intensity in each imaging channel. Numbers indicate timing in seconds. H_2O_2 was added between the second and third frame shown. (B) Timing of the HyPer ratio change in cells is shown in panel (A). See also Supplementary Video 1 (http://www.elsevierdirect.com/companions/9780124058835). H_2O_2—hydrogen peroxide.

4.6. Anticipated results

Typical results are presented in the figures. Figure 3.1 depicts HeLa-Kyoto cells before and after addition of H_2O_2. The increase in the HyPer ratio is clearly observed upon addition of H_2O_2 (Fig. 3.1B). Figure 3.2 shows H_2O_2 production by RAW 264.7 macrophages phagocyting zymosan particles. A typical time course of phagocytosis-induced H_2O_2 generation profile in RAW 264.7 cells is shown in Fig. 3.2B. Panels represent pseudocolored images where pixel values reflect ratio F500/F420 (Fig. 3.2A). Immediately after the zymosan particle ingestion (at minute 1), cells begin to produce a wave of H_2O_2 peaking at minute 2 (Fig. 3.2A). In the course of the next 10–15 min, H_2O_2 levels progressively decrease to a basal level (Fig. 3.2B). Although in general cells exhibited single H_2O_2 burst, a small population of

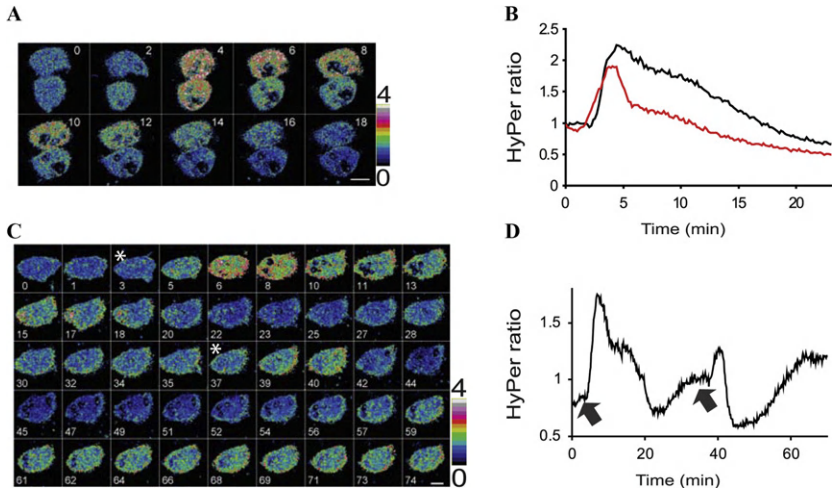

Figure 3.2 H_2O_2 production by phagocytosing macrophages expressing HyPer. (A) Ratiometric confocal images of RAW 264.7 cells at indicated time points (min) after the induction of phagocytosis of opsonized zymosan particles. Scale bar: 10 μm. See also Supplementary Video 2 (http://www.elsevierdirect.com/companions/9780124058835). (B) Time course of H_2O_2 production by individual phagocytosing RAW 264.7 cells. Black and red lines represent H_2O_2 production inside the upper cell and lower cell, respectively, shown in panel (A). (C) Ratiometric confocal images of RAW 264.7 cell demonstrating several peaks of H_2O_2 production following each phagocytosis event. The time points of phagocytosis events are marked by asterisks. Scale bar: 10 μm. See also Supplementary Video 3 (http://www.elsevierdirect.com/companions/9780124058835). (D) The time course of H_2O_2 production by phagocytosing RAW 264.7 cells is shown in panel (C). Arrows indicate phagocytosis events.

the cells displayed several H_2O_2 peaks after each ingestion event followed by constant and irreversible H_2O_2 production (Fig. 3.2C and D).

In summary, HyPer is a unique tool allowing very sensitive and specific H_2O_2 detection. Its main advantage is its simplicity of use that, we hope, is reflected in the present protocol.

ACKNOWLEDGMENTS

This work was supported by the Russian foundation for basic research (RFBR) (10-04-01561-a, V. V. B.; 11-04-12187-ofi, S. L.), a joint EMBL-RFBR grant (12-04-92427 to C. S. and V. V. B.), Measures to Attract Leading Scientists to Russian Educational Institutions program (11.G34.31.0017 to S. L.), and the ESF EuroMembrane consortium TraPPs (to C. S.).

Author contributions statements. N. M. M., K. N. M., D. S. B., M. V. S., and M. E. M. designed and performed experiments, V. V. B. conceived the project, C. S. provided expertise in cell signaling and imaging, S. L. provided project guidance and support, D. L. contributed expertise in phagocytosis model, V. V. B., N. M. M., and C. S. worked on the text.

Competing financial interests. The authors declare that they have no competing financial interests.

REFERENCES

Bae, Y. S., Sung, J. Y., Kim, O. S., Kim, Y. J., Hur, K. C., Kazlauskas, A., et al. (2000). Platelet-derived growth factor-induced H(2)O(2) production requires the activation of phosphatidylinositol 3-kinase. *The Journal of Biological Chemistry*, *275*, 10527–10531.

Bedard, K., & Krause, K.-H. (2007). The NOX family of ROS-generating NADPH oxidases: Physiology and pathophysiology. *Physiological Reviews*, *87*, 245–313.

Belousov, V. V., Fradkov, A. F., Lukyanov, K. A., Staroverov, D. B., Shakhbazov, K. S., Terskikh, A. V., et al. (2006). Genetically encoded fluorescent indicator for intracellular hydrogen peroxide. *Nature Methods*, *3*, 281–286.

Bonini, M. G., Rota, C., Tomasi, A., & Mason, R. P. (2006). The oxidation of 2',7'-dichlorofluorescin to reactive oxygen species: A self-fulfilling prophesy? *Free Radical Biology & Medicine*, *40*, 968–975.

Crow, J. P. (1997). Dichlorodihydrofluorescein and dihydrorhodamine 123 are sensitive indicators of peroxynitrite in vitro: Implications for intracellular measurement of reactive nitrogen and oxygen species. *Nitric Oxide: Biology and Chemistry/Official Journal of the Nitric Oxide Society*, *1*, 145–157.

Dalby, B., Cates, S., Harris, A., Ohki, E. C., Tilkins, M. L., Price, P. J., et al. (2004). Advanced transfection with Lipofectamine 2000 reagent: Primary neurons, siRNA, and high-throughput applications. *Methods*, *33*, 95–103.

D'Autréaux, B., & Toledano, M. B. (2007). ROS as signalling molecules: Mechanisms that generate specificity in ROS homeostasis. *Nature Reviews. Molecular Cell Biology*, *8*, 813–824.

Dickson, R. M., Cubitt, A. B., Tsien, R. Y., & Moerner, W. E. (1997). On/off blinking and switching behaviour of single molecules of green fluorescent protein. *Nature*, *388*, 355–358.

Dröge, W. (2002). Free radicals in the physiological control of cell function. *Physiological Reviews*, *82*, 47–95.

Forman, H. J., & Torres, M. (2002). Reactive oxygen species and cell signaling: Respiratory burst in macrophage signaling. *American Journal of Respiratory and Critical Care Medicine*, *166*, S4–S8.

Gomes, A., Fernandes, E., & Lima, J. L. F. C. (2005). Fluorescence probes used for detection of reactive oxygen species. *Journal of Biochemical and Biophysical Methods*, *65*, 45–80.

Jacobsen, L. B., Calvin, S. A., Colvin, K. E., & Wright, M. (2004). FuGENE 6 transfection reagent: The gentle power. *Methods*, *33*, 104–112.

Jordan, M., & Wurm, F. (2004). Transfection of adherent and suspended cells by calcium phosphate. *Methods*, *33*, 136–143.

Lange, S., Heger, J., Euler, G., Wartenberg, M., Piper, H. M., & Sauer, H. (2009). Platelet-derived growth factor BB stimulates vasculogenesis of embryonic stem cell-derived endothelial cells by calcium-mediated generation of reactive oxygen species. *Cardiovascular Research*, *81*, 159–168.

Leto, T. L., Morand, S., Hurt, D., & Ueyama, T. (2009). Targeting and regulation of reactive oxygen species generation by Nox family NADPH oxidases. *Antioxidants & Redox Signaling*, *11*, 2607–2619.

Marchesi, E., Rota, C., Fann, Y. C., Chignell, C. F., & Mason, R. P. (1999). Photoreduction of the fluorescent dye 2'-7'-dichlorofluorescein: A spin trapping and direct electron spin resonance study with implications for oxidative stress measurements. *Free Radical Biology & Medicine*, *26*, 148–161.

Markvicheva, K. N., Bogdanova, E. A., Staroverov, D. B., Lukyanov, S., & Belousov, V. V. (2009). Imaging of intracellular hydrogen peroxide production with HyPer upon stimulation of HeLa cells with epidermal growth factor. *Methods in Molecular Biology*, *476*, 76–83.

Miller, E. W., Tulyathan, O., Tulyanthan, O., Isacoff, E. Y., & Chang, C. J. (2007). Molecular imaging of hydrogen peroxide produced for cell signaling. *Nature Chemical Biology*, *3*, 263–267.

Mishina, N. M., Tyurin-Kuzmin, P. A., Markvicheva, K. N., Vorotnikov, A. V., Tkachuk, V. A., Laketa, V., et al. (2011). Does cellular hydrogen peroxide diffuse or act locally? *Antioxidants & Redox Signaling*, *14*, 1–7.

Rada, B., & Leto, T. L. (2008). Oxidative innate immune defenses by Nox/Duox family NADPH oxidases. *Contributions to Microbiology*, *15*, 164–187.

Rota, C., Chignell, C. F., & Mason, R. P. (1999). Evidence for free radical formation during the oxidation of 2'-7'-dichlorofluorescin to the fluorescent dye 2'-7'-dichlorofluorescein by horseradish peroxidase: Possible implications for oxidative stress measurements. *Free Radical Biology & Medicine*, *27*, 873–881.

Rota, C., Fann, Y. C., & Mason, R. P. (1999). Phenoxyl free radical formation during the oxidation of the fluorescent dye 2',7'-dichlorofluorescein by horseradish peroxidase. Possible consequences for oxidative stress measurements. *The Journal of Biological Chemistry*, *274*, 28161–28168.

Tabet, F., Schiffrin, E. L., Callera, G. E., He, Y., Yao, G., Ostman, A., et al. (2008). Redox-sensitive signaling by angiotensin II involves oxidative inactivation and blunted phosphorylation of protein tyrosine phosphatase SHP-2 in vascular smooth muscle cells from SHR. *Circulation Research*, *103*, 149–158.

Tiscornia, G., Singer, O., & Verma, I. M. (2006). Production and purification of lentiviral vectors. *Nature Protocols*, *1*, 241–245.

Wardman, P. (2007). Fluorescent and luminescent probes for measurement of oxidative and nitrosative species in cells and tissues: Progress, pitfalls, and prospects. *Free Radical Biology & Medicine*, *43*, 995–1022.

Winterbourn, C. C. (2008). Reconciling the chemistry and biology of reactive oxygen species. *Nature Chemical Biology*, *4*, 278–286.

CHAPTER FOUR

In Vivo Imaging of H_2O_2 Production in *Drosophila*

Ana G. Barata, Tobias P. Dick[1]
Division of Redox Regulation, German Cancer Research Center (DKFZ), DKFZ-ZMBH Alliance, Heidelberg, Germany
[1]Corresponding author: e-mail address: t.dick@dkfz.de

Contents

1. Introduction 62
   1.1 Genetically encoded probes for H_2O_2 62
   1.2 roGFP2-Orp1 transgenic flies 63
2. Materials 64
   2.1 Fly husbandry and collection of larvae 64
   2.2 Preparation of living larvae 64
   2.3 Preparation of fixed tissues 65
   2.4 Confocal microscopy 66
3. Methods 66
   3.1 Fly husbandry, larvae, and adult synchronization 66
   3.2 Sample preparation 67
   3.3 Confocal microscopy 69
4. Image and Data Analysis 71
   4.1 Generation of ratio images 71
   4.2 Analysis of raw data for verification purposes 74
5. Data Interpretation 79
Acknowledgments 81
References 81

Abstract

H_2O_2 plays many roles in cellular physiology. Therefore, we need tools for quantitative detection of H_2O_2 in tissues and whole model organisms. We recently introduced a genetically encoded H_2O_2 sensor, roGFP2-Orp1, which couples the redox-sensitive green fluorescent protein 2 (roGFP2) to the yeast H_2O_2 sensor protein Orp1. Expression of cytosolic or mitochondrial roGFP2-Orp1 in *Drosophila* allows the measurement of physiologically relevant changes in H_2O_2 levels, with compartment-specific resolution. Here, we provide a detailed protocol for the relative quantitation of H_2O_2 levels in living larvae by real-time imaging. We also describe a dissection and fixation method that conserves the redox state of the probe and thus allows reliable measurements on fixed adult tissues. Finally, we give recommendations for image processing, analysis, and interpretation, highlighting issues that require attention to detail, to ensure accuracy and validity of results.

Methods in Enzymology, Volume 526
ISSN 0076-6879
http://dx.doi.org/10.1016/B978-0-12-405883-5.00004-1

© 2013 Elsevier Inc.
All rights reserved.

1. INTRODUCTION

1.1. Genetically encoded probes for H_2O_2

There is little doubt that H_2O_2 plays important roles in metazoan physiology and pathology (see the other chapters of this volume). Consequently, it is of great interest to visualize H_2O_2 as it is generated within living cells and intact model organisms. For a long time, researchers mostly relied on chemical dyes which become fluorescent upon oxidation, making the assumption that they (also) visualize H_2O_2. Unfortunately, most conventional dyes are not very specific and can be affected by a range of variables beyond direct experimental control (e.g., differences in cellular uptake and efflux). Improved chemical probes have been developed more recently (e.g., see Chapter 2), but some limitations remain. An alternative approach, which can be considered complementary to the chemical probes, is the use of genetically encoded H_2O_2 probes (Meyer & Dick, 2010). These have become available only recently. Advanced genetically encoded probes offer significant advantages: (i) they provide a high degree of chemical specificity; (ii) they provide a ratiometric response; (iii) they respond dynamically; and (iv) they can be precisely targeted to subcellular compartments, membranes, or other defined microenvironments.

To our knowledge, there are currently two genetically encoded probes that actually qualify as *direct* H_2O_2 probes. Both have a well-defined reaction mechanism. These two probes are based on different H_2O_2-sensing modules and on different mechanisms of fluorescence modulation. HyPer (Belousov et al., 2006) makes use of the H_2O_2-sensing domain of the bacterial transcription factor OxyR, while roGFP2-Orp1 (Gutscher et al., 2009) exploits the H_2O_2-sensing signaling peroxidase Orp1 from yeast. In HyPer, a redox-dependent conformational change modulates the fluorescence of circularly permuted yellow fluorescent protein (cpYFP). In roGFP2-Orp1, Orp1 relays a disulfide bridge to redox-sensitive GFP (roGFP). Both probes are ratiometric and reversible, allowing dynamic measurements. When tested side-by-side in live cell imaging, HyPer and roGFP2-Orp1 exhibited comparable responses to exogenously applied H_2O_2 (Gutscher et al., 2009), suggesting that their sensitivity is very similar. However, neither probe can be used to determine absolute H_2O_2 concentrations, nor is absolute *in situ* calibration a practical possibility. It is nevertheless clear that both probes routinely detect intracellular H_2O_2 changes taking place somewhere within the nanomolar range.

There is one difference between the two probes that is of practical relevance, namely, pH sensitivity. In roGFP2, the β-barrel structure is fully intact, meaning that excited state proton transfer between Tyr-66 and Thr-65 is effectively shielded from the environment (Meyer & Dick, 2010). This rationalizes why the fluorescence ratio of roGFPs (reflecting the ratio of anionic and neutral chromophore) is not significantly affected by ambient pH changes within the physiological range (Schwarzländer et al., 2008). In contrast, HyPer is based on cpYFP, in which the circular permutation is known to loosen up the β-barrel structure (Akerboom et al., 2009), thus allowing ambient pH to perturb chromophore protonation. This is evidently a problem in the mitochondrial matrix, where pH is close to the pK_a of cpYFP (Schwarzländer, Logan, Fricker, & Sweetlove, 2011). Generally, it seems advisable to use a H_2O_2-insensitive mutant of HyPer (called SypHer) as a pH control (Poburko, Santo-Domingo, & Demaurex, 2011).

1.2. roGFP2-Orp1 transgenic flies

The fruit fly (*Drosophila melanogaster*) is a well-established model animal. It allows the study of fundamental physiological processes, including innate immunity, neurodegeneration, and aging. The short life-cycle and ease of genetic manipulation are key advantages. We recently generated *Drosophila* lines constitutively expressing the H_2O_2 probe roGFP2-Orp1 in either the cytosol or mitochondria. We found that the roGFP2-Orp1 redox state differs between subcellular compartments and between tissues. In addition, changes in roGFP2-Orp1 oxidation were found to take place during development and aging (Albrecht, Barata, Grosshans, Teleman, & Dick, 2011).

Larvae have a transparent cuticle and can be used directly for live imaging. In contrast, most tissues within adult flies are optically inaccessible. Thus, adult flies have to be dissected for microscopic inspection of their organs. This, in turn, raises the concern that dissection and tissue preparation, in particular tissue fixation, could change the redox state of the probe, leading to artifacts. Fortunately, this problem can be overcome by blocking the redox state of the sensor with the cell permeable alkylating agent *N*-ethyl maleimide (NEM), which is applied during dissection (Albrecht et al., 2011).

The distribution of roGFP2-Orp1 redox state in the specimen (either intact larvae or prepared adult tissues) is determined by confocal fluorescence microscopy. In general, the sample is excited sequentially by the 405- and 488-nm laser lines. For both excitation wavelengths, the emitted

fluorescence intensity is recorded between 500 and 530 nm. The ratio of the two fluorescence intensities reflects the redox state of roGFP2-Orp1. The specifics of the relationship between fluorescence ratios and redox state have been summarized previously (Meyer & Dick, 2010).

The following protocol explains the procedure from sample preparation to data interpretation, as applied to biosensor transgenic *Drosophila*. A detailed protocol for the application of roGFP2-Orp1 in mammalian cell culture has been published previously (Morgan, Sobotta, & Dick, 2011).

2. MATERIALS

2.1. Fly husbandry and collection of larvae

1. Small embryo collection cage, 6 mm diameter (Genesee Scientific No. 59-100).
2. 10 × phosphate-buffered saline (PBS): dissolve 80 g NaCl, 2 g KCl, 14.4 g Na_2HPO_4, 2.4 g KH_2PO_4 in 1 L double-distilled water (ddH_2O). Adjust pH to 7.4 with NaOH.
3. Apple agar plates: boil 10 g agar (Invitrogen) in 800 mL 1 × PBS and allow to cool down while stirring. When the solution has cooled to 60 °C, add 200 mL apple juice and 23 mL of a 10% solution (w/v) of methyl *p*-hydroxybenzoate (Sigma-Aldrich W271004) in ethanol.
4. Dry active baker's yeast.
5. Incubation system for maintaining a constant temperature of 25 °C and a 12-h light–dark cycle. Humidity is maintained by open water-filled containers inside the incubator.
6. Vials with food: use a food recipe adequate for the experimental requirements. Optimized standard food recipes can be found on the Bloomington Stock Center web site (http://flystocks.bio.indiana.edu/Fly_Work/media-recipes/media-recipes.htm). Use 27-mm diameter polypropylene vials and plug with standard cotton.

2.2. Preparation of living larvae

1. Biological material: *Drosophila* L3 larvae expressing the roGFP2-Orp1 sensor.
2. Sterile Dulbecco's phosphate-buffered saline (DPBS) without calcium chloride and magnesium chloride (Gibco 14190).
3. Forceps Dumont #5 in Inox, 11 cm length (NeoLab 2-1033).
4. Fine paintbrush.

5. Staining block (Karl Hecht 2020).
6. Tissue paper.
7. Microscope slides, 24×70 mm and 0.13–0.17 mm thickness (R. Langenbrick 01-2470/1).
8. Scotch tape.
9. Dissection slides: microscope slides with ground and polished wells (NeoLab 1-6295).
10. Dithiothreitol (DTT) stock solution (100 m*M*): dissolve 15.4 mg DTT (AppliChem A1101) in 1 mL PBS. Always prepare fresh and keep on ice. 10 m*M* DTT solution: dilute stock solution 1:10 in PBS.
11. Diamide stock solution (10 m*M*): dissolve 1.72 mg diamide (Sigma-Aldrich D3648) per 1 mL of PBS. Always prepare fresh and keep on ice. 1 m*M* Diamide solution: dilute stock solution 1:10 in PBS.
12. Microscope cover slips, 18×18 mm and 0.13–0.16 mm thickness (Thermo Scientific B10143263NR1).
13. Stereo microscope (e.g., Zeiss Stemi 2000).

2.3. Preparation of fixed tissues

1. Biological material: adult *Drosophila* flies or larvae expressing roGFP2-Orp1.
2. Sterile DPBS without calcium chloride and magnesium chloride (Gibco 14190).
3. CO_2 flow regulator with blow gun and fly pad (FlowBuddy, Genesee 59-122BC).
4. Stereo microscope (e.g., Zeiss Stemi 2000).
5. 20 m*M* NEM: dissolve 25 mg NEM (Sigma-Aldrich E3876) in 10 mL PBS. Always prepare fresh and keep on ice.
6. DTT stock solution (100 m*M*): dissolve 15.4 mg DTT (AppliChem A1101) in 1 mL PBS. Always prepare fresh and keep on ice. 20 m*M* DTT solution: dilute stock solution 1:5 in PBS.
7. Diamide stock solution (10 m*M*): dissolve 1.72 mg diamide (Sigma-Aldrich D3648) per 1 mL PBS. Always prepare fresh and keep on ice. 2 m*M* Diamide solution: dilute stock solution 1:5 in PBS.
8. Dissection slides: microscope slides with ground and polished wells (e.g., NeoLab 1-6295).
9. Forceps Dumont #5 in Inox, 11 cm length (NeoLab 2-1033).
10. Staining block (Karl Hecht 2020).
11. 1.5-mL Reaction tubes (e.g., Eppendorf).

12. Platform rocker (e.g., Heidolph).
13. 12% Paraformaldehyde (PFA) stock solution (prepare under fume hood): dissolve 12 g of PFA (Sigma-Aldrich 16005) in 60 mL ddH_2O. Add 2 mL of 2 *M* NaOH and stir at 65 °C until the PFA is completely dissolved. Add 10 mL 10 × PBS. Allow to cool and adjust pH to 7.4 with 1 *M* HCl. Adjust final volume to 100 mL with ddH_2O. Store at −20 °C. 4% PFA solution: dilute 12% PFA stock solution in PBS and keep on ice. Always prepare the 4% solution freshly before use.
14. Mounting medium: 160 mL anhydrous glycerol (MP Biomedical 800688), 20 mL 10 × PBS, 0.8 g *N*-propyl-gallate (MP Biochemicals 102747), and 10 mL ddH_2O. Mix well and store at 4 °C.
15. Microscope slides, 76 × 26 × 1 mm (Thermo Scientific 10143562CE).
16. Microscope cover slips, 18 × 18 mm and 0.13–0.16 mm thickness (Thermo Scientific B10143263NR1).
17. Standard transparent nail polish.

2.4. Confocal microscopy

1. Microscopes: In principle, any confocal microscope can be used. We use the following microscopes: (A) Leica TCS SP5. Laser lines: UV diode (405 nm) and argon multiline (488 nm). Objective: HCX PLAPO lambda blue 20 ×, 1.3 NA (oil). Detector: photomultiplier (PMT). (B) Zeiss LSM 710 ConfoCor 3. Laser lines: UV diode (405 nm) and argon multiline (488 nm). Objective: EC plan N DICI 40 ×, 1.3 NA (oil). Detector: PMT.
2. Immersion oil: Type F immersion fluid ($n_e = 1.518$; $\nu_e = 46$) (Leica Microsystems) and Immersol™ 518 F ($n_e = 1.518$; $\nu_e = 45$) (Carl Zeiss).

3. METHODS

3.1. Fly husbandry, larvae, and adult synchronization

Raise flies at 25 °C on standard medium or on a medium appropriate for the experiment. In most experiments, it will be important to collect larvae in the same developmental stage or adult flies of the same age. To control developmental stages and age, select recently hatched larvae or newly ecclosed flies according to the following procedure:

1. Place the flies of interest, either a cross or a specific strain, in the embryo collection cage with an apple agar plate sprinkled with active dry yeast to

provide protein and increase egg laying. Replace the apple agar plate every 12 h.

2. Collect newly hatched larvae from the apple agar plates and place them in the food vials. Use them for experiments during the larval stage or let them pupate and hatch.
3. Collect newly ecclosed flies. Flip flies to new food vials every other day. When flies reach the desired age, use them for dissection and imaging.

Note: Carefully plan ahead the number of larvae or adult flies to be collected according to the experimental requirements. Images should be obtained from a statistically significant number of living larvae or adult flies per condition. In addition, if different time points are to be compared, plan accordingly so that the imaging of all specimens can be performed in the same microscopy session.

3.2. Sample preparation

3.2.1 Preparation of intact larvae

1. Collect up to three larvae from the food vials using forceps or a paintbrush. *Note: Larvae are delicate and should be handled with great care. The time between collection and imaging of larvae should be minimized. Therefore, no more than three larvae should be handled in one step.*
2. Wash larvae in the staining block containing PBS and dry them by placing them briefly on a piece of tissue paper.
3. Arrange larvae on a thin microscope slide and fix with scotch tape. *Note: The tape must be tight enough to prevent the larvae from crawling.*

3.2.2 Preparation of fixed tissues

1. Pipette 40 μL of the 20 m*M* NEM solution into the well of the dissection slide. NEM is an alkylating agent that blocks the redox state of the probe and prevents PFA- and air-induced oxidation.
2. Anesthetize the flies (if imaging adult flies).
3. Place flies into the NEM solution and dissect them under the stereo microscope at room temperature (RT) using forceps. *Note: Tissues may be lost or damaged during the following blocking and fixation steps, thus plan to dissect additional flies. Moreover, it may be helpful to keep tissues attached to other parts of the body to provide support. For example, the exposed adult gut should remain attached to the cuticle.*
4. Transfer the organs/tissues of interest to a 1.5-mL reaction tube containing 1 mL of 20 m*M* NEM solution. Incubate for 10 min at RT with

gentle rocking. Aspirate the NEM solution using a pipette and rinse the tissues once with 1 mL PBS.

5. Incubate the tissues with 4% PFA for 20 min at RT with gentle rocking. Aspirate the PFA solution, rinse the tissues twice with 1 mL PBS, and wash two times for 15 min with 1 mL PBS. *Note: If you need to interrupt the protocol, leave tissues in 4% PFA on ice. Then, resume incubation with PFA at RT for 20 min with gentle rocking.*
6. Cover the tissues with mounting medium and incubate overnight at 4 °C; store the tubes upright and in the dark.
7. Place four to six drops of mounting medium in the middle of a microscope slide. Cut the tip of a 1-mL pipette tip and pipette the tissues in mounting medium to a dissection slide. Under the stereo microscope and using forceps, separate the tissues of interest from other tissues and transfer them to the mounting medium previously placed on the microscope slide. Place a cover slip on top. The space between the slide and the cover slip must be completely filled with mounting medium. If this is not the case, use a pipette to fill any empty space with mounting medium. Use nail polish to seal the gap between the cover slip and the slide.
8. Store samples at 4 °C and protect from light. Although samples can be stored for around 1 week, we advise that they are imaged as soon as possible.

3.2.3 Preparation of reference samples

3.2.3.1 Reduced and oxidized tissue samples from larvae

Unfortunately, the larval cuticle does not allow efficient penetration of DTT and diamide solutions. Therefore, larvae must be dissected and DTT and diamide solutions applied directly to the exposed tissues. Freshly prepare the fully reduced and fully oxidized samples using the following protocol:

1. Pipette 40 μL of PBS into the well of the dissection slide.
2. Place one or two larvae into the well and dissect them by pulling on both ends with forceps to expose internal organs.
3. Place 20 μL of 10 m*M* DTT onto a thin microscope slide.
4. Transfer the dissected larvae into the DTT droplet and place a cover slip on top.
5. Incubate for 5 min and image the exposed tissues.
6. Repeat the same procedure using a 1 m*M* diamide solution for the fully oxidized control.

3.2.3.2 Reduced and oxidized fixed tissue samples

To adjust laser intensity and to determine the dynamic range of the probe, fully reduced and fully oxidized samples are needed for reference. Use the following protocol to prepare fully reduced and oxidized reference fixed tissue samples:

1. Dissect flies as described in Section 3.2.2, but in the absence of NEM.
2. Transfer the tissues to a 1.5-mL reaction tube containing either 1 mL of 20 m*M* DTT or 2 m*M* diamide solutions. Incubate for 10 min at RT with gentle rocking. Aspirate the solutions with a pipette and rinse tissues twice with 1 mL PBS.
3. Incubate the tissues with 1 mL of NEM solution for 10 min at RT with gentle rocking.
4. Proceed with PFA fixation as described in Section 3.2.2.

3.3. Confocal microscopy

3.3.1 Imaging of living larvae

In principle, any confocal microscope can be used to image intact larvae expressing roGFP2-Orp1. We use the Leica SP5 or Zeiss LSM 710 microscope. The following protocol can be adapted for use with other microscopes:

1. Switch on the microscope and start the LAS AF (Leica) or Zen (Zeiss) software.
2. Switch on the 488- and 405-nm laser lines. *Note: The intensity of the argon laser can take a prolonged time to stabilize, wait for 2.5 h before starting the imaging.*
3. Select initial settings as described for the SP5 and LSM 710 microscopes in Table 4.1.
4. Laser intensity adjustment: apply immersion oil to the objective, position the normal untreated larvae on the microscope stage, and adjust the focus using the eyepiece. Switch on live mode and choose the lookup table "glow over/under." Slowly increase the intensity of the laser until you start to see the specimen and then readjust the focal plane. Adjust the 488-nm laser intensity to move the mean signal into the upper third of the intensity scale. Then, adjust the 405-nm laser intensity to position the mean signal in the lower third of the intensity scale.

Explanation: Ideally, laser intensities would be adjusted using a fully reduced intact larva for the 488-nm laser, and a fully oxidized intact larva for the 405-nm laser. However, DTT and diamide solutions do not efficiently penetrate the larval cuticle. Unfortunately, DTT or diamide-treated dissected larvae are less than ideal for reference measurements because the

Table 4.1 Initial settings commonly used for imaging of *Drosophila* larvae and fixed tissues expressing the roGFP2-Orp1 H_2O_2 sensor

	Leica SP5 (LAS AF software)	**Zeiss LSM 710 (Zen 5.5 software)**
Imaging setup		
Switch track every	"Line"	"Line"
Scan 1	405 nm	405 nm
Scan 2	488 nm	488 nm
Light path		
Scan 1 + 2	500–530 emission window	Detector range 500–530 nm
Acquisition settings		
Frame size	512 × 512 pixels	512 × 512 pixels
Scanning frequency	400 Hz	"9" 3.15 μs
Averaging	1 (living larvae); 4 (fixed tissues)	1 (living larvae); 4 (fixed tissues)
Bit depth	16 bit	16 bit
Zoom	1–1.5	1–1.5
Channel/laser settings (405- and 488-nm lines)		
Pinhole (section thickness)	65 μm	37 μm
Gain	700 V	800 V
Off-set	0	0

signal intensity obtained from intact larvae is lower than that from dissected tissues. It is, however, possible to achieve workable settings with untreated intact larvae. Normal larvae grown under standard conditions characteristically have low H_2O_2 levels in most tissues and therefore present an overall reduced roGFP2-Orp1 sensor. The 488-nm laser intensity is raised to move the mean signal into the upper third of the intensity scale. Correspondingly, the 405-nm laser intensity is adjusted to position the mean signal in the lower third of the intensity scale. With these settings, decreases in the 488 nm signal and increases in the 405 nm signal should be detectable.

5. Image samples of interest: apply immersion oil on the objective and position the larvae preparation on the microscope stage. Use the eyepiece to locate the organs of interest and then switch to live mode and adjust the focus.
6. Export images in TIFF format.

3.3.2 Imaging of fixed tissues

As for intact larvae, any confocal microscope can in principle be used to image fixed tissues. We use the Leica SP5 or Zeiss LSM 710 microscope. The following protocol can be adapted for use with other microscopes:

1. Switch on the microscope and start the LAS AF (Leica) or Zen (Zeiss) software.
2. Switch on the 488 (argon) and 405-nm laser lines. *Note: The intensity of the argon laser takes time to stabilize, wait 2.5 h before starting to image.*
3. Select initial settings as described for the SP5 and LSM 710 microscopes in Table 4.1.
4. Laser intensity adjustment: apply immersion oil to the objective and place the fully reduced sample on the microscope stage and adjust the focus with the eyepiece. Slowly increase the 488-nm laser intensity while ensuring that the sample remains properly focused. Adjust the 488-nm laser intensity to move the mean signal into the upper third of the intensity scale.
5. Repeat the same procedure for the fully oxidized sample to adjust 405-nm laser intensity.
6. Acquire images of the fully reduced and fully oxidized samples for calculation of the dynamic range.
7. Image the samples of interest: apply immersion oil to the objective and place the slide with samples on the microscope stage. Identify the tissue of interest using the eyepiece and take images.
8. Export images in TIFF format.

4. IMAGE AND DATA ANALYSIS

4.1. Generation of ratio images

We start out with one fluorescence intensity image for each of the two excitation channels (405 and 488 nm). Typically, these are uncompressed TIFF files. For the purpose of generating a 405/488 fluorescence intensity ratio image, that is, a color-coded illustration of the spatial distribution of intensity ratio values, the first step is the thresholding of the two fluorescence intensity images. Setting a minimum threshold is essential because divisions involving background pixels will dramatically distort the appearance of the final ratio image (Fig. 4.1A). It is also advisable to apply a maximum threshold to remove any saturated pixels.

In principle, it would be desirable to automate the thresholding process. Although automated thresholding can lead to satisfying results, it will frequently lead to suboptimal results. A popular method for automated

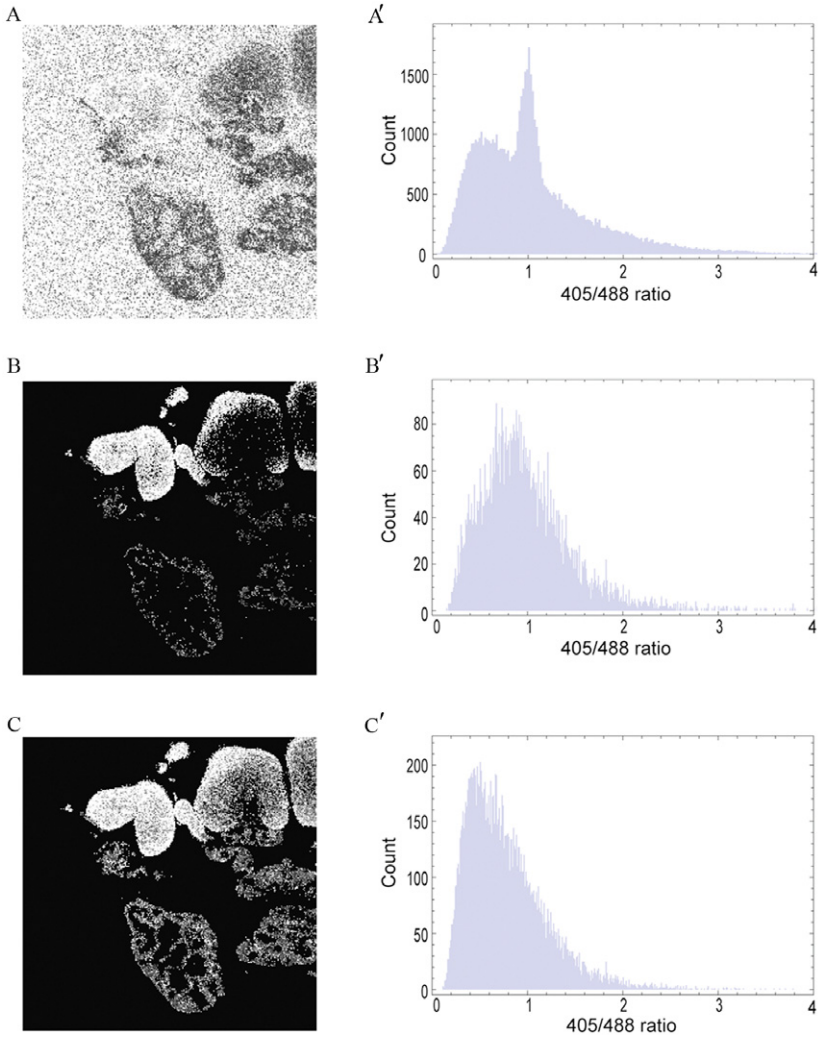

Figure 4.1 The effect of thresholding on a ratio image and its histogram. The depicted specimen is fixed fat tissue from adult *Drosophila* containing distinct regions exhibiting high and low probe oxidation. The ratio values are encoded by pixel brightness. (A, A′) Without any thresholding, the oxidized tissue parts can hardly be discriminated from the background. (B, B′) After Otsu thresholding in the 405-nm channel, only the oxidized tissue clearly stands out, but pixels belonging to the reduced tissue parts have been overly removed. (C, C′) With manual thresholding equally applied to both channels, complete background removal is combined with appropriate representation of both the oxidized and reduced tissue parts.

thresholding is based on cluster variance maximization (Otsu's algorithm). In our experience, the Otsu threshold is generally too restrictive. Although highly restrictive thresholding guarantees that only pixels with significant fluorescence intensity are considered in the generation of the ratio image, the Otsu algorithm will often remove authentic probe signals. In regions of strong probe reduction or oxidation, the 405 or 488 nm signals, respectively, may fall below the Otsu threshold and corresponding pixels disappear from the ratio image (Fig. 4.1B). We therefore recommend careful manual thresholding appropriate to the specific image content. Typically, similar or identical thresholds are applied to both channels (Fig. 4.1C).

Setting 405 and 488 nm thresholds by hand is ideally done in a computing environment (e.g., Mathematica or MATLAB) that allows changing the two intensity thresholds with sliders and to immediately judge the effect on the final ratio image and its histogram. To what extent each channel should be thresholded depends on the specific image. Of note, thresholding the 488-nm image can help to minimize autofluorescent signals (e.g., from gut content, cuticle, or tracheae, which are typically strong in the 405-nm channel, but weak in the 488-nm channel) while maintaining most of the oxidized probe signal. In any case, manual threshold settings are not arbitrary. The ratio image and ratio histogram usually give a clear sense of how much thresholding is needed to remove background pixels while maintaining a maximum of probe signal. Although too much thresholding can remove authentic signals from an image and thus create a bias, thresholding will never change pixel ratios per se.

The next step is the generation of the actual ratio image. Each pixel in the thresholded 405-nm image is divided by the intensity value of the corresponding pixel in the thresholded 488-nm image. On a technical note, to avoid divisions by zero, replace zeros with appropriate placeholders (e.g., "NaN" in ImageJ, "Indeterminate" in Mathematica) before executing the division operation.

Since corresponding 405- and 488-nm images are never absolutely congruent and due to other factors (autofluorescence), there may still exist pixels in the ratio image that do not properly reflect the probe redox state. It is therefore advisable to inspect the ratio image histogram more closely. Ratio values should be within a range that represents the maximum dynamic range of the probe (factor 10 at most). If necessary or desired, pixels exhibiting ratio values that fall outside this range can be removed by another thresholding step that is directly applied to the ratio image. Finally, a color lookup table can be applied to the ratio images (not shown).

4.2. Analysis of raw data for verification purposes

Another matter is the inspection of raw images for quality control and validation purposes. Here, the goal is not to produce a ratio image but to obtain confidence that an observed ratio difference reflects a true probe response rather than an imaging artifact. This is especially important when samples from different biological entities are compared, for example, gut tissue from young and old flies. Although the procedure of ratiometric image analysis seems straightforward, namely pixel-by-pixel division of fluorescence intensities, there is a certain risk of misinterpretation if one "blindly" generates ratio images without also taking a closer look at the primary data. The key question is: When we see a ratio difference between two samples, is it really due to opposing changes in the two excitation channels?

A simple way to examine the nature of ratio differences is to look at pixel-by-pixel scattergrams in which the 405 nm intensity is plotted on the x axis and the 488 nm intensity on the y axis. This reveals the overall relationship between intensity variations in the two channels. The disadvantage of this kind of representation is the loss of information about pixel neighborhood relationships. However, scattergrams can also be examined separately for individual regions of interest. What kind of differences do we expect to see in a scattergram if we compare reduced and oxidized samples? Just based on the fact that individual probe molecules behave as binary switches (i.e., they can be either oxidized or reduced) and on the realistic assumption that overall (macroscopic) pixel intensities are linear combinations of individual molecular intensities, we can state that

$$I_{405} = OxD \times N_{\mathrm{tot}} \times i405_{\mathrm{ox}} + (N_{\mathrm{tot}} - OxD \times N_{\mathrm{tot}}) \times i405_{\mathrm{red}} \qquad [4.1]$$

$$I_{488} = OxD \times N_{\mathrm{tot}} \times i488_{\mathrm{ox}} + (N_{\mathrm{tot}} - OxD \times N_{\mathrm{tot}}) \times i488_{\mathrm{red}}. \qquad [4.2]$$

Here, I_{405} and I_{488} are the macroscopic emission intensities at 405 and 488 nm excitation. $i405_{\mathrm{red}}$, $i405_{\mathrm{ox}}$, $i488_{\mathrm{red}}$, and $i488_{\mathrm{ox}}$ are the fluorescence intensities contributed by a single probe molecule at the indicated wavelength and redox state. N_{tot} ($=N_{\mathrm{ox}}+N_{\mathrm{red}}$) is the total number of probe molecules associated with the pixel. OxD ($=N_{\mathrm{ox}}/N_{\mathrm{tot}}$) is the degree of oxidation of the probe. N_{red} and N_{ox} are the numbers of reduced and oxidized probe molecules, respectively.

From this, it follows that the relationship between I_{488} and I_{405} is linear and given by:

$$I_{488} = I_{405} \times \frac{i488_{\mathrm{red}} \times OxD - i488_{\mathrm{ox}} \times OxD - i488_{\mathrm{red}}}{i405_{\mathrm{red}} \times OxD - i405_{\mathrm{ox}} \times OxD - i405_{\mathrm{red}}}. \qquad [4.3]$$

In the case of a fully oxidized or fully reduced probe, this relationship simplifies to:

$$I_{488} = I_{405} \times \frac{i488_{ox}}{i405_{ox}} \text{ and} \quad [4.4]$$

$$I_{488} = I_{405} \times \frac{i488_{red}}{i405_{red}}, \text{ respectively.} \quad [4.5]$$

Given the opposing response at the two excitation wavelengths, that is, $i405_{ox} > i405_{red}$ and $i488_{red} > i488_{ox}$, we expect that probe oxidation will lead to a decrease of the slope in the scattergram. In the double-logarithmic plot, this corresponds to a parallel shift (Fig. 4.2A and B).

In general, the predicted relationship between I_{405} and I_{488} describes the actual probe behavior very well. This is most obvious when observing the same population of cells shifting from one redox state to another (e.g., during live imaging). In this case, the two ratio images (before and after the redox change) show the same cells in (almost) exactly the same position, that is, 405 and 488 nm pixels can be considered homologous. The raw data from such experiments clearly display the expected scattergram structure (Fig. 4.2C and D). From a more statistical point of view, the overall shift within one intensity channel can be depicted by overlaid probability density functions (Fig. 4.2E and F). As expected for an authentic probe response, the 405 nm signal shifts to higher intensities and the 488 nm signal to lower intensities. In such a setting, there is no doubt that the observed intensity changes are in complete agreement with the known characteristics of the roGFP2 excitation spectrum.

Unfortunately, when imaging *Drosophila* tissues, we have a more complicated situation than in cell culture imaging experiments. Typically, we want to compare ratio images from tissues derived from different individuals. For example, we may want to compare the probe oxidation status in the gut tissue of flies of different age. As a prerequisite, for each condition, a statistically meaningful number of flies (typically 10) has to be analyzed. For any direct comparison it is absolutely crucial that all samples are imaged with the exact same microscope settings (and stable laser intensity) in the same session. The first step is the adjustment of microscope settings (laser power and PMT gain). 488-nm Laser power is adjusted using the fully reduced tissue sample (DTT control) and, likewise, 405-nm laser power using the fully oxidized tissue sample (diamide or H_2O_2 control), in each case ensuring good exposure levels below saturation.

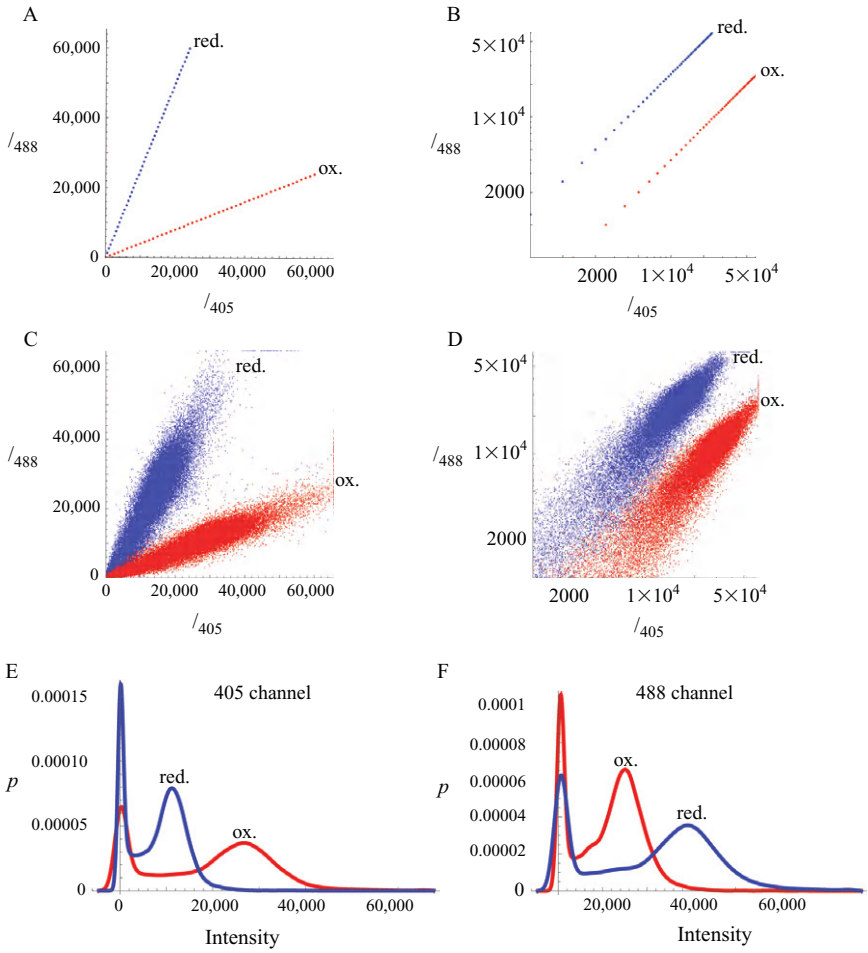

Figure 4.2 Predicted and observed relationship between I_{405} and I_{488}. (A, B) Relationship between I_{405} (x axis) and I_{488} (y axis) as predicted from first principles. Pixels are plotted on linear (A) and double-logarithmic (B) scales. Blue dots represent pixels corresponding to the reduced state; red dots represent pixels corresponding to the oxidized state. The calculation assumes microscope settings that lead to a symmetrical opposing 2.5-fold change of fluorescence intensity in each channel, corresponding to a total dynamic range of ~6. (C, D) Typical probe response as observed in cultured cells. Blue dots represent pixels from the reduced state, before exposure to H_2O_2. Red dots represent pixels after exposure to H_2O_2. (E, F) Corresponding plots of probability density functions based on smoothed kernel density estimates show the opposing shifts in the individual intensity channels. Blue curve: reduced cells; red curve: oxidized cells.

A significant complication is the unavoidable heterogeneity between the tissue samples that are obtained from different flies. Although the same type of tissue is imaged, a variance in average probe signal (due to variable probe expression and morphological tissue heterogeneity) between images is typically observed.

In Fig. 4.3, we deliberately show a somewhat difficult situation in which instrument settings are not optimal and there is substantial sample heterogeneity with some additional variable contributions of autofluorescence. Gut tissue from 1-day-old flies (condition A) is represented by 405–488 image pairs from 11 different flies and gut tissue from 14-day-old flies (condition B) by 405–488 image pairs from 10 different flies (Fig. 4.3A). For both conditions, there is a clear positive correlation between the integrated 405 and 488 signals (Fig. 4.3B and C), confirming that most of the variation is due to different numbers of probe molecules contributing to each image. In principle, relative probe level differences between samples should not pose a problem for ratiometric analysis, as relative differences within one sample also do not pose a problem (as, e.g., shown by the linearity in Fig. 4.2C). As expected (based on previous data), the overall 405/488 ratios of the raw images indicate that gut tissue under condition B is on average more oxidized (Fig. 4.3D). The significance of the ratio difference can thus be investigated by appropriate statistical tools (e.g., *t*-test).

However, it is also desirable to demonstrate directly that the difference between two conditions is actually based on opposing intensity shifts in the two channels, which is the characteristic of a true roGFP2 probe response, and can be considered the final proof that no artifact has been measured. For this, we need to make individual pairwise sample comparisons, but it is essential to compare 405–488 image pairs (condition A vs. B) with similar combined brightness (summed over both channels). Even then, it may not always be fully obvious from visual inspection of scattergrams that a significant opposing shift has occurred in the two channels (Fig. 4.3E). The comparison of histograms or corresponding probability density functions is then needed to find out if there is actually a decrease in the 488-nm channel that is coincident with an increase in the 405-nm channel or vice versa. For this particular purpose, a noise filtering algorithm, e.g., convolution of the original image with a Gaussian mask, can help to better expose relatively weak but significant intensity shifts (Fig. 4.3F and G).

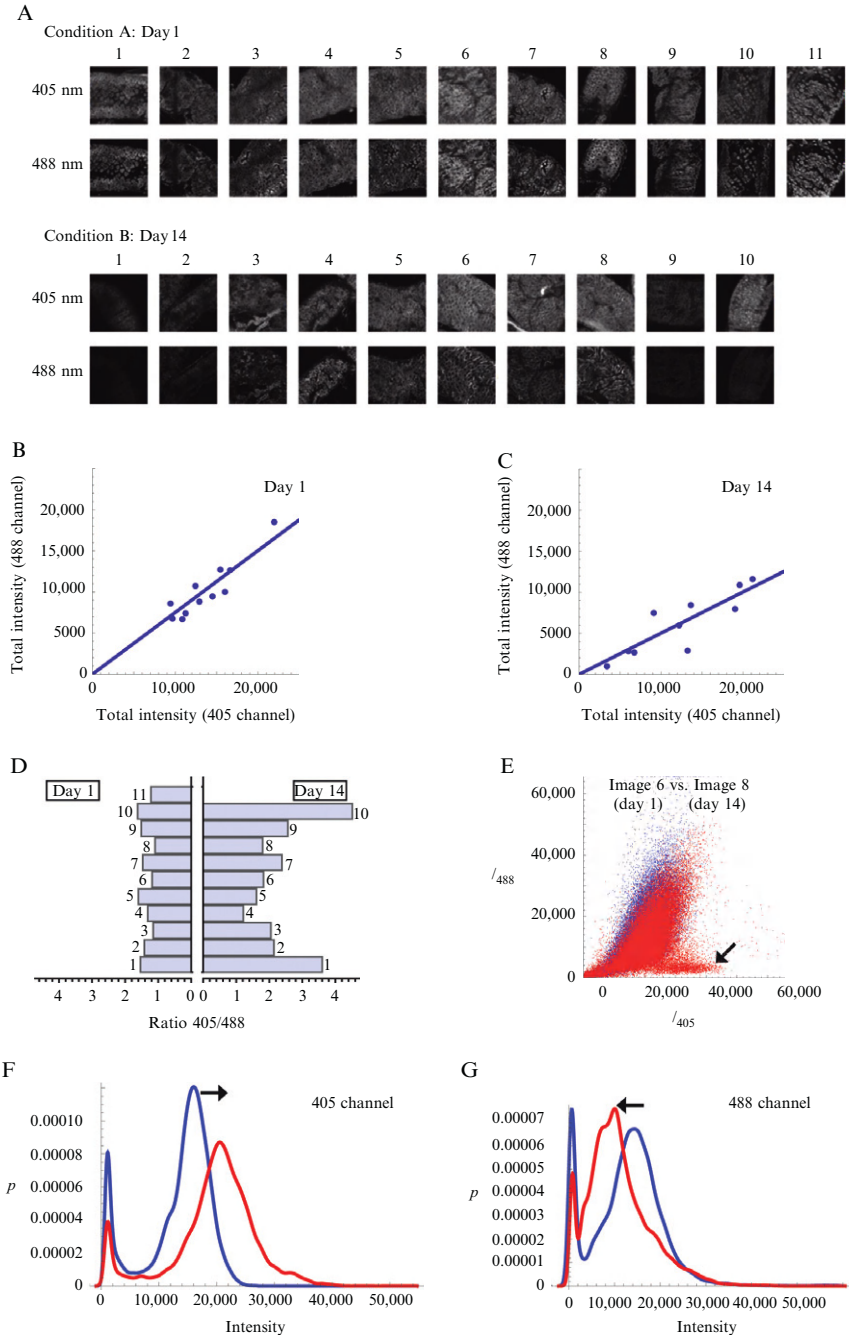
A
Condition A: Day 1
1 2 3 4 5 6 7 8 9 10 11
405 nm
488 nm
Condition B: Day 14
1 2 3 4 5 6 7 8 9 10
405 nm
488 nm
B
Day 1
Total intensity (488 channel)
20,000
15,000
10,000
5000
0
0 10,000 20,000
Total intensity (405 channel)
C
Day 14
Total intensity (488 channel)
20,000
15,000
10,000
5000
0
0 10,000 20,000
Total intensity (405 channel)
D
Day 1
Day 14
11 10 9 8 7 6 5 4 3 2 1
4 3 2 1 0 0 1 2 3 4
Ratio 405/488
E
Image 6 vs. Image 8
(day 1) (day 14)
60,000
40,000
20,000
0
/488
0 20,000 40,000 60,000
/405
F
405 channel
p
0.00010
0.00008
0.00006
0.00004
0.00002
0
0 10,000 20,000 30,000 40,000 50,000
Intensity
G
488 channel
p
0.00007
0.00006
0.00005
0.00004
0.00003
0.00002
0.00001
0
0 10,000 20,000 30,000 40,000 50,000
Intensity

5. DATA INTERPRETATION

Independent of the various technical challenges associated with imaging and image analysis, there are some general questions regarding the interpretation of H_2O_2 probe signals. Most of these apply to H_2O_2 probes in general.

First, the introduction of any indicator may perturb the observed cell in one way or the other. It is therefore worthwhile to consider how the method of observation may impact on the results and to consider strategies to minimize these effects. Obviously, all direct H_2O_2 probes (genetic or chemical) consume H_2O_2 in order to act as H_2O_2 probes. By introducing the probe, we introduce an artificial sink for H_2O_2. Thus, does the continued presence of the H_2O_2 indicator significantly lower endogenous H_2O_2 levels? Does expression of the H_2O_2 indicator influence signaling events related to H_2O_2, and therefore cellular behavior?

In the case of roGFP2-Orp1, we introduce a thiol peroxidase. Inside the cell, the probe will find itself in kinetic competition with other H_2O_2 consumers, in particular, other peroxidases and catalase (Winterbourn, 2008). How competitive is the indicator relative to other consumers? How much of the total H_2O_2 flux will be associated with the probe? On the one hand, kinetic competition depends on the second-order rate constant for the immediate reaction of the consumer with H_2O_2. This rate constant has not been determined for Orp1, but it seems to be significantly lower than that of highly reactive 2-Cys-peroxidases: in a direct comparison, the intracellular oxidation of the roGFP2-Orp1 probe was clearly slower than that of human Prx2 (Sobotta et al., 2013). On the other, competition in terms of flux rate also depends on the kinetics of probe reduction. The rate of roGFP2-Orp1 reduction also appears to be comparatively slow. Reductive

Figure 4.3 An example for the inspection of difficult (suboptimal) data sets. Comparison of gut tissue expressing mitochondrial roGFP2-Orp1 from flies of different age (day 1 vs. day 14). (A) Raw images of gut tissue from 11 different 1-day-old flies (upper two rows) and 10 different 14-day-old flies (lower two rows). (B, C) Plotting of total image fluorescence intensities. (D) Bar chart display of total image 405/488 fluorescence ratios (left: day 1; right: day 14). (E) Scattergram overlay for image 6—day 1 (blue) and image 8—day 14 (red). Note the occurrence of autofluorescent pixels (arrow). (F, G) Plotting of histogram probability density functions (here shown after application of a Gaussian mask) confirms opposing spectral shifts (highlighted by arrows). Blue curve: image 6—day 1; red curve: image 8—day 14.

recovery of roGFP2-Orp1 after a H_2O_2 pulse is at least two times slower than Prx2 reduction (Sobotta et al., 2013). Considering catalase, selenium-based glutathione peroxidases, and the catalytic efficiency, variety, and abundance of peroxiredoxins, which constitute around 0.5% of total cellular protein (Wood, Schröder, Robin Harris, & Poole, 2003), the Orp1 probe is likely to receive only a minor share of the total flux and therefore is unlikely to have a major impact on the spatiotemporal pattern of H_2O_2 in the cell. This conclusion is in agreement with observations made in yeast, where Orp1 expression did not influence acute H_2O_2 resistance (Delaunay, Pflieger, Barrault, Vinh, & Toledano, 2002). This observation prompted the conclusion that Orp1 does not have a significant scavenging function but primarily acts in signaling (Toledano, Delaunay, Monceau, & Tacnet, 2004).

The same considerations can be made for HyPer because its OxyR domain technically behaves like a thiol peroxidase (using H_2O_2 to generate a disulfide bridge). In side-by-side experiments, HyPer and roGFP2-Orp1 exhibited very similar kinetics of oxidation and reduction (Gutscher et al., 2009). Although HyPer and roGFP2-Orp1 can generally be considered sensitive H_2O_2 probes, it seems that both are clearly less efficient in turning over H_2O_2 than the most efficient peroxidases and much less than catalase. On the positive side, the limited turnover of H_2O_2 by HyPer and roGFP2-Orp1 effectively limits perturbation of H_2O_2-based redox homeostasis by these probes.

The second question is: What does it actually mean if we observe a difference or a change in the state of an H_2O_2 probe? The probe response certainly tells us something about how cells handle H_2O_2. However, thinking in terms of kinetic competition and dynamic fluxes, the interpretation may sometimes be more complex than usually considered. First, an increase in probe oxidation can be due to an increase in H_2O_2 generation (i.e., due to activation of an H_2O_2 generator) which is not (immediately) counterbalanced by increased probe reduction. It seems that in most cases, increased H_2O_2 probe oxidation is in fact caused by increased H_2O_2 generation. Second, there is also the theoretical possibility that increased probe oxidation is caused by a change in the "competitive landscape," for example, the inactivation of a competing peroxidase. In this case, the probe may receive a larger share of the H_2O_2 flux. Third, increased probe oxidation could also be the result of diminished probe reduction, for example, if NADPH levels become limiting (in this case, however, endogenous peroxidases would be likewise affected and H_2O_2 levels are expected to increase). In all three cases, the probe would properly respond to a physiological

change in H_2O_2 turnover, but the exact interpretation would differ. We do not yet understand how the various H_2O_2 sources and sinks interact and compete with each other in a spatiotemporal framework. The consideration of shifting H_2O_2 fluxes may be more productive than the concept of changing "steady state" H_2O_2 concentrations. To better understand how cells dynamically handle H_2O_2 and how probes fit into the scheme will need more comprehensive approaches, that is, simultaneous monitoring of competing H_2O_2 consumers and reductive systems.

ACKNOWLEDGMENTS

This work has been supported by the Baden-Württemberg Foundation. We thank Dr. Felix Bestvater, Dr. Damir Krunic, and Manuela Brom from the DKFZ Light Microscopy Facility for technical support. We thank Dr. Bruce Morgan and Mirko Sobotta for critical reading of the manuscript.

REFERENCES

Akerboom, J., Vélez Rivera, J. D., Guilbe, M. M. R., Malavé, E. C. A., Hernandez, H. H., Tian, L., et al. (2009). Crystal structures of the GCaMP calcium sensor reveal the mechanism of fluorescence signal change and aid rational design. *Journal of Biological Chemistry*, *284*(10), 6455–6464. http://dx.doi.org/10.1074/jbc.M807657200.

Albrecht, S. C., Barata, A. G., Grosshans, J., Teleman, A. A., & Dick, T. P. (2011). In vivo mapping of hydrogen peroxide and oxidized glutathione reveals chemical and regional specificity of redox homeostasis. *Cell Metabolism*, *14*(6), 819–829. http://dx.doi.org/10.1016/j.cmet.2011.10.010.

Belousov, V. V., Fradkov, A. F., Lukyanov, K. A., Staroverov, D. B., Shakhbazov, K. S., Terskikh, A. V., et al. (2006). Genetically encoded fluorescent indicator for intracellular hydrogen peroxide. *Nature Methods*, *3*(4), 281–286.

Delaunay, A., Pflieger, D., Barrault, M.-B. , Vinh, J., & Toledano, M. B. (2002). A thiol peroxidase is an H_2O_2 receptor and redox-transducer in gene activation. *Cell*, *111*(4), 471–481. http://dx.doi.org/10.1016/S0092-8674(02)01048-6.

Gutscher, M., Sobotta, M. C., Wabnitz, G. H., Ballikaya, S., Meyer, A. J., Samstag, Y., et al. (2009). Proximity-based protein thiol oxidation by H_2O_2-scavenging peroxidases. *Journal of Biological Chemistry*, *284*(46), 31532–31540. http://dx.doi.org/10.1074/jbc.M109.059246.

Meyer, A. J., & Dick, T. P. (2010). Fluorescent protein-based redox probes. *Antioxidants & Redox Signaling*, *13*(5), 621–650.

Morgan, B., Sobotta, M. C., & Dick, T. P. (2011). Measuring E(GSH) and H_2O_2 with roGFP2-based redox probes. *Free Radical Biology & Medicine*, *51*(11), 1943–1951. http://dx.doi.org/10.1016/j.freeradbiomed.2011.08.035.

Poburko, D., Santo-Domingo, J., & Demaurex, N. (2011). Dynamic regulation of the mitochondrial proton gradient during cytosolic calcium elevations. *Journal of Biological Chemistry*, *286*(13), 11672–11684. http://dx.doi.org/10.1074/jbc.M110.159962.

Schwarzländer, M., Fricker, M. D., Müller, C., Marty, L., Brach, T., Novak, J., et al. (2008). Confocal imaging of glutathione redox potential in living plant cells. *Journal of Microscopy*, *231*(2), 299–316. http://dx.doi.org/10.1111/j.1365-2818.2008.02030.x.

Schwarzländer, M., Logan, D. C., Fricker, M. D., & Sweetlove, L. J. (2011). The circularly permuted yellow fluorescent protein cpyfp that has been used as a superoxide probe is highly responsive to pH but not superoxide in mitochondria: Implications for the existence of superoxide 'flashes'. *Biochemical Journal*, *437*(3), 381–387. http://dx.doi.org/10.1042/bj20110883.

Sobotta, M. C., Barata, A. G., Schmidt, U., Mueller, S., Millonig, G., & Dick, T. P. (2013). Exposing cells to H_2O_2: A quantitative comparison between continuous low-dose and one-time high-dose treatments. *Free Radical Biology Medicine*, *60*, 325–335.

Toledano, M. B., Delaunay, A., Monceau, L., & Tacnet, F. (2004). Microbial H_2O_2 sensors as archetypical redox signaling modules. *Trends in Biochemical Sciences*, *29*(7), 351–357. http://dx.doi.org/10.1016/j.tibs.2004.05.005.

Winterbourn, C. C. (2008). Reconciling the chemistry and biology of reactive oxygen species. *Nature Chemical Biology*, *4*(5), 278–286.

Wood, Z. A., Schröder, E., Robin Harris, J., & Poole, L. B. (2003). Structure, mechanism and regulation of peroxiredoxins. *Trends in Biochemical Sciences*, *28*(1), 32–40. http://dx.doi.org/10.1016/S0968-0004(02)00003-8.

CHAPTER FIVE

Single Fluorescent Probe Distinguishes Hydrogen Peroxide and Nitric Oxide in Cell Imaging

Lin Yuan, Weiying Lin[1], Sasa Zhu, Kaibo Zheng, Longwei He
State Key Laboratory of Chemo/Biosensing and Chemometrics, College of Chemistry and Chemical Engineering, Hunan University, Changsha, PR China
[1]Corresponding author: e-mail address: weiyinglin@hnu.edu.cn

Contents

1. Introduction 84
2. A Guide to Single Fluorescent Probe Distinguishes H_2O_2 and NO 87
   2.1 Sensing scheme 87
   2.2 Spectroscopic properties 89
   2.3 Selectivity 94
   2.4 Cellular response 94
3. Fluorescence Imaging of Endogenously Produced H_2O_2 and NO in RAW 264.7 Macrophages Cells 98
   3.1 Materials and instrumentation 98
   3.2 Raw 264.7 murine macrophages culture and imaging 98
   3.3 Results 99
4. Summary 102
Acknowledgments 102
References 103

Abstract

In combination with synthetic fluorescent probes, fluorescence microscopy has emerged as a powerful technique to investigate the production, localization, trafficking, and function of biomolecules in living systems in a noninvasive manner. Prompted by our interest in providing a molecular tool to disentangle the complicated interrelationship between H_2O_2 and NO in the signal transduction and oxidative pathways, our laboratory has developed a single fluorescent probe, FP–H_2O_2–NO, that can report H_2O_2, NO, and H_2O_2/NO with three different sets of fluorescence signal patterns. In this chapter, we provide essential information about the probe FP–H_2O_2–NO in order to assist researchers interested to apply our probe to investigate H_2O_2 and NO biology. We describe the use of FP–H_2O_2–NO with the representative examples of imaging both exogenous and endogenous H_2O_2 and NO in live Hela and RAW 264.7 macrophage cells by fluorescence microscopy.

Methods in Enzymology, Volume 526
ISSN 0076-6879
http://dx.doi.org/10.1016/B978-0-12-405883-5.00005-3

© 2013 Elsevier Inc.
All rights reserved.

1. INTRODUCTION

All living systems functioning in aerobic conditions contain reactive oxygen species (ROS), which are a class of radical or nonradical oxygen-containing species that play critical roles not only in physiological pathways but also in pathological processes (Bashan, Kovsan, Kachko, Ovadia, & Rudich, 2009; Kuznetsov et al., 2011; Pandey, Tripathi, PremKumar, Shrivastav, & Chaube, 2010; Peyrot & Ducrocq, 2008). In general, ROS can be produced in two ways. The mitochondrial respiration pathway is the main way to generate ROS. The mitochondrial respiratory chain transfers electrons to molecular oxygen to afford ROS as a by-product of oxidative phosphorylation (Bashan et al., 2009; Kuznetsov et al., 2011). In addition, ROS can also be exogenously produced under stimulation by xenobiotics, infectious agents, and ultraviolet radiation (Caporaso, 2003; Cooke, Evans, Dizdaroglu, & Lunec, 2003; Gomes, Fernandes, & Lima, 2005). H_2O_2, an important ROS, plays signal/stress dichotomy roles in living systems. H_2O_2 can function as a signaling molecule in a wide variety of signaling transduction processes, an oxidative stress marker in aging and disease, and a defense agent in response to pathogen invasion (Reth, 2002; Rhee, 2006; Winterbourn, 2008). H_2O_2 is involved in the reversible oxidation of proteins to regulate cellular processes such as protein phosphorylation and gene expression (Rhee, 2006). However, excessive H_2O_2 production is involved in the pathogenesis of many diseases, including cancer, diabetes, and cardiovascular and neurodegenerative disorders (Galaris, Skiada, & Barbouti, 2008; Krohn, Maier, & Paschke, 2007; Lin & Beal, 2006).

On the other hand, reactive nitrogen species (RNS) are another class of chemically reactive species that are also required for signaling transduction pathways (Alderton, Cooper, & Knowles, 2001; Bashan et al., 2009; Pandey et al., 2010; Peyrot & Ducrocq, 2008; Soneja, Drews, & Malinski, 2005). Nitric oxide (NO), the prototypical RNS, is endogenously produced by NO synthases, a group of evolutionarily conserved cytosolic or membrane-bound isoenzymes that convert their substrates L-arginine to citrulline and NO (Alderton et al., 2001; Soneja et al., 2005). NO acts as a secondary messenger to activate soluble guanylyl cyclase, which can in turn induce a downstream pathway for vascular smooth muscle relaxation (Cary, Winger, Derbyshire, & Marletta, 2006; Mayer, 2000). However, unregulated production of NO is implicated with many diseases such as

stroke, heart disease, hypertension, neurodegeneration, erectile dysfunction, and gastrointestinal distress (Mayer, 2000).

The complicated relationship of H_2O_2 and NO in the signal transduction and oxidative pathways is well documented (Bashan et al., 2009; Kotamraju et al., 2003; Pandey et al., 2010; Peyrot & Ducrocq, 2008; Rauen, Li, Ioannidis, & de Groot, 2007; Sartoretto, Kalwa, Pluth, Lippard, & Michel, 2011). The production of H_2O_2 and NO can be interdependent and sometimes they are concurrently present during various physiological processes (Eguchi, Fujiwara, Sakiyama, Yoshihara, & Suzuki, 2011; Li, Liu, et al., 2009; Milligan, Owens, & Grisham, 1996; Shiota et al., 2002). For instance, H_2O_2 and NO play interrelated roles as signaling molecules during the ABA-dependent stomatal closure (Zhang et al., 2007). H_2O_2 and NO are produced within cardiac myocytes to regulate the cardiovascular signaling pathway (Sartoretto et al., 2011). A delicate balance between the levels of H_2O_2 and NO is required to control the process of defense against pathogens and decides when the cell death is induced. Intercommunication between these two signaling molecules is necessary during the programmed cell death process in some living systems. The cytotoxic activity of H_2O_2 in several cells such as human ovarian cancer cells (Yoshioka, Kitao, Kishino, Yamamuro, & Maeda, 2006), lymphoma cells (Filep, Lapierre, Lachance, & Chan, 1997), hepatoma cells (Ioannidis & de Groot, 1993), and several other types of cells (Hoffmann et al., 2006; Rauen et al., 2007) can be enhanced by NO. However, the H_2O_2-induced apoptosis/stress in macrophages, Chinese hamster fibroblasts cells (Ridnour et al., 2005), endothelial cells (Kotamraju et al., 2003), and cardiomyoblasts (Chae et al., 2001) is inhibited by NO (Farias-Eisner, Chaudhuri, Aeberhard, & Fukuto, 1996; Krohn et al., 2007). On the other hand, H_2O_2 can trigger the production of NO in some types of animal and plant cells (Eguchi et al., 2011; Li, Liu, et al., 2009; Milligan et al., 1996; Sartoretto et al., 2011; Shiota et al., 2002). However, the H_2O_2 level in neuronal cells can be boosted by exposure to extracellular NO donor (Wei, Chen, Hou, Xin, & Mori, 2000).

Given the fact that H_2O_2 and NO have complicated interrelationship in the signal transduction and oxidative pathways, it is important to develop molecular tools to dissect their complex roles. Toward this end, Cao, Guo, Xu, and Zhao (2005) reported a procedure to simultaneously monitor NO free radical and ROS in plant and animal systems using an electron spin resonance trapping technique. However, this procedure requires the biological samples to be destructed before the measurement can be performed. Thus, although this procedure is interesting, it is not able to provide the

information of NO and ROS in the native biological environment. In contrast, fluorescence microscopy with synthetic fluorescent probes offers a powerful means to investigate biomolecules of interest in a noninvasive manner with high spatial and temporal resolution. This method is valuable for providing the information regarding the production, localization, trafficking, and function of biomolecules in intact living systems. Accordingly, recently, some elegant synthetic fluorescent probes which are specific for H_2O_2 (Abo et al., 2011; Dickinson, Huynh, & Chang, 2010; Srikun, Miller, Domaille, & Chang, 2008) or NO (Gabe, Urano, Kikuchi, Kojima, & Nagano, 2004; McQuade et al., 2010; Zheng, Shang, Yang, Gao, & Xu, 2008) have been created, and they have been employed to study H_2O_2 or NO biology. However, as these probes are selective for H_2O_2 or NO, they are not capable of reporting H_2O_2, NO, or H_2O_2/NO with distinct fluorescence signal. Obviously, one potential solution to the problem is to simultaneously use different types of fluorescent probes which are specific for H_2O_2 or NO in a cell (Sartoretto et al., 2011; She, Song, & He, 2004). Unfortunately, this approach is problematic, as combination of several fluorescent probes may produce cross-talk of fluorescence signals, a larger invasive effect to living samples, and different localization and metabolisms of distinct types of fluorescent probes. Thus, it is more desirable to use a single fluorescent probe which can differentiate H_2O_2, NO, or H_2O_2/NO.

Such a fluorescent probe must satisfy certain criteria to be effective for biological studies. First, the probe should have two distinct reaction sites for H_2O_2 and NO, so that it can respond to H_2O_2 and NO independently. To minimize the potential interference (i.e., steric hindrance) between the two reaction sites, they should be strategically located on the two ends of the probe to render them as far as possible. Second, the probe should respond to H_2O_2, NO, and H_2O_2/NO with distinct fluorescence signals, for instance, a significant increase of fluorescence intensity or a shift of emission wavelengths. In particular, the emission wavelengths of the probe before and after interactions with the target molecule should be well resolved to ensure no cross-talk in the emission spectra. This is favorable for multiple-color imaging of H_2O_2 and NO by fluorescence microscopy. Third, the probe should be cell permeable and nontoxic for potential applications in complex cellular environments. Finally, the probe should be synthetically accessible. These requirements render the development of such a fluorescent probe very challenging.

During the past several years, our group has developed a toolbox of synthetic organic fluorescent probes for diverse targets including metal ions,

anions, pH, and biomolecules, and we have also employed them for biological imaging at the levels of living cells, tissues, and animals (Lin, Long, Chen, Tan, & Gao, 2010; Lin, Yuan, Cao, Feng, & Long, 2009; Lin, Yuan, Cao, Feng, & Song, 2010; Yuan, Lin, Xie, Chen, & Zhu, 2012; Yuan, Lin, Yang, & Chen, 2012; Yuan, Lin, Zhao, et al., 2012). Very recently, our group has successfully developed a single fluorescent probe which can distinguish H_2O_2 and NO with distinct fluorescence signal patterns (Yuan, Lin, Xie, et al., 2012). This chapter is intended to provide readers with the information regarding the design of such a unique fluorescent probe and its applications for studying biology of H_2O_2 and NO. We first present a guide to single fluorescent probe distinguishes H_2O_2 and NO based on its sensing mechanism and photophysical properties. In the next section, we provide an illustrative protocol for two-color fluorescence imaging of exogenous H_2O_2 and NO in living Hela cells and endogenously produced H_2O_2 and NO in RAW 264.7 macrophages cells.

2. A GUIDE TO SINGLE FLUORESCENT PROBE DISTINGUISHES H_2O_2 AND NO

In this section, we highlight the characteristics of a single fluorescent capable of reporting H_2O_2, NO, and H_2O_2/NO with distinct fluorescence signals in solution, to help researchers understand the sensing scheme and optical properties of this unique fluorescence probe and how to apply it for imaging in living cells.

2.1. Sensing scheme

We recently formulated a fluorescent platform which is capable of responding to any combination of two targets with distinct fluorescence signals (Fig. 5.1). The fluorescence platform is based on the well-known fluorophores such as coumarin and rhodamine. The maximal absorption wavelengths of 7-hydroxycoumarin (400 nm) and rhodamine (550 nm) dyes are well separated. This indicates that these two dyes can be independently excited. Furthermore, the maximal emission wavelengths of 7-hydroxycoumarin (460 nm) and rhodamine (580 nm) are also well resolved, and there is almost no cross-talk in the emission profiles. This allows them to be employed simultaneously in optical microscopy, ensuring the two-color imaging of H_2O_2 and NO in living cells to be performed. Notably, the photophysical properties of 7-hydroxycoumarin can be modulated by modifications on

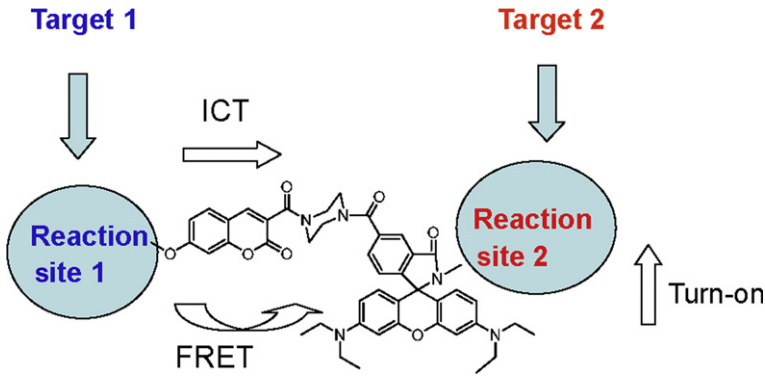

Figure 5.1 Design scheme for a fluorescent platform capable of responding to two targets with distinct fluorescence signals.

the key hydroxyl group (Huang et al., 2010; Reymond, Fluxà, & Maillard, 2009), and those of rhodamine can be tuned by the unique ring opened–closed processes (Beija, Afonso, & Martinho, 2009; Chen, Pradhan, Wang, Kim, & Yoon, 2012; Kim, Lee, Kim, Kim, & Yoon, 2008). As we would like to improve the shift in the emission, so we selected the coumarin–rhodamine pair. However, the downside of this system is that it has relatively limited overlap integral ($J_{DA} = 3.62 \times 10^{14}\ M^{-1}\ cm^{-1}\ nm^4$). Thus, to improve the Förster resonance energy transfer (FRET) efficiency, the selection of a short rigid linker is very critical (Kikuchi, Takakusa, & Nagano, 2004). In our energy transfer platform, a rigid piperazine linker was chosen to ensure an appropriate distance ($R = 11.07$ Å) between the coumarin donor and the rhodamine acceptor and high energy transfer efficiency ($R_0 = 36.00$ Å, $E > 99\%$).

A salient feature of the fluorescent platform is that it bears two distinct reaction sites specific for two different targets. These two distinct reaction sites are carefully located in the two ends of the platform to ensure their independent operation. The coumarin–rhodamine fluorescent platform is versatile and can independently or simultaneously report the targets with a fluorescence signal. Conceivably, there are three different cases in which the coumarin–rhodamine fluorescence platform can interact with the targets. First, when the coumarin–rhodamine fluorescence platform independently interacts with target 1 only, we should observe a change in the optical properties of the coumarin moiety due to intramolecular charge transfer (ICT). Second, independent interaction of the coumarin–rhodamine

fluorescence platform with target 2 only should trigger the ring opening of the rhodamine dye and a turn-on fluorescence response. Third, simultaneous interaction of the coumarin–rhodamine fluorescent platform with both targets 1 and 2 should elicit the transfer of the excited energy of the coumarin dye to the rhodamine dye by FRET. Thus, interestingly, a single coumarin–rhodamine fluorescence platform can well integrate two distinct targets with three different fluorescence signaling mechanisms (ICT, rhodamine-based turn-on, FRET) to open up opportunities for multiple fluorescence signals. The modular nature of the coumarin–rhodamine fluorescence platform allows a wide variety of reaction sites to be incorporated. Thus the platform should be applicable for various biomolecules of interest.

As the development of a single fluorescent probe which can report H_2O_2, NO, and H_2O_2/NO with distinct fluorescence signals is highly valuable, we decided to realize such a unique fluorescent probe by employing the above coumarin–rhodamine fluorescence platform. Toward this end, we engineered fluorescent probe FP–H_2O_2–NO (Fig. 5.2) by using the coumarin–rhodamine fluorescent platform. The selection of the reaction sites for H_2O_2 and NO is based on the well-developed H_2O_2-specific boronate chemistry (Dickinson et al., 2010; Srikun et al., 2008) and NO-specific phenylenediamine-based chemistry (Gabe et al., 2004; Zheng et al., 2008). These two reaction sites are chemically orthogonal, which renders that the probe FP–H_2O_2–NO can differentiate H_2O_2, NO, and H_2O_2/NO by optical signals.

2.2. Spectroscopic properties

The free probe FP–H_2O_2–NO has almost no emission at 460 and 580 nm when excited at 400 nm (Fig. 5.3A) and no emission at 580 nm when excited at 550 nm (Fig. 5.3B), as the hydroxyl group of the coumarin moiety is modified by the boronate chemistry with a "self-immolative" spacer and the rhodamine unit exists predominately as the spirocyclic form. Thus, the fluorescence signal pattern for the free probe is black–black–black as shown in Fig. 5.2. However, addition of gradually increasing concentrations of H_2O_2 elicits intense emission at around 460 nm when excited at 400 nm (Fig. 5.3A). By contrast, no significant emission at 581 nm was observed with excitation at 400 (Fig. 5.3A) or 550 nm (Fig. 5.3B). Hence, in the presence of H_2O_2, FP–H_2O_2–NO displays a fluorescence signal pattern of blue–black–black, consistent with that shown in the design scheme (Fig. 5.2). This is because the boronate group of FP–H_2O_2–NO is removed to afford

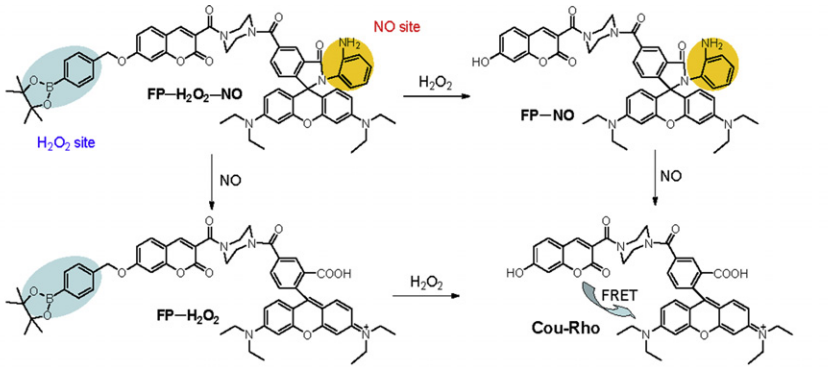

Input	Ex. 400 nm		Ex. 550 nm	Fluorescence signal pattern
	Em. 460 nm	Em. 580 nm	Em.580 nm	
Free				black–black–black
H_2O_2				blue–black–black
NO				black–black–red
H_2O_2 + NO				black–red–red

Figure 5.2 Sensing mechanism and spectroscopic properties of probe FP–H_2O_2–NO to H_2O_2, NO, and H_2O_2/NO with three different sets of fluorescence signals: blue–black–black, black–black–red, and black–red–red. *Reprinted with permission from Yuan, Lin, Xie, et al. (2012). Copyright 2012 American Chemical Society.*

compound FP–NO (Fig. 5.2), which contains the 7-hydroxycoumarin dye and the rhodamine in the spirocyclic form.

On the other hand, when the probe is incubated with NO, a large fluorescence turn-on at 581 nm is noted upon excitation at 550 nm (Fig. 5.3D). However, no marked fluorescence variations at 460 and 581 nm are detected with excitation at 400 nm (Fig. 5.3C). Thus, in the presence of NO, FP–H_2O_2–NO exhibits a fluorescence signal pattern of black–black–red, as the phenylenediamine group of FP–H_2O_2–NO is eliminated by NO to give compound FP–H_2O_2 (Fig. 5.2), which bears the

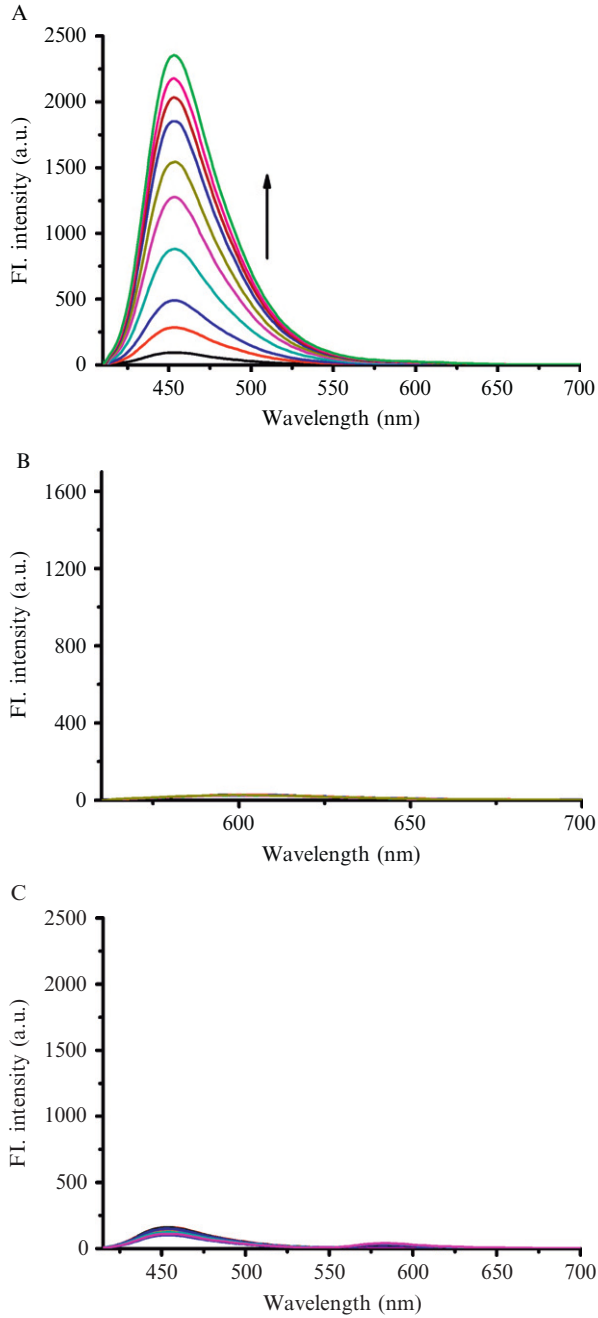

Figure 5.3—Cont'd

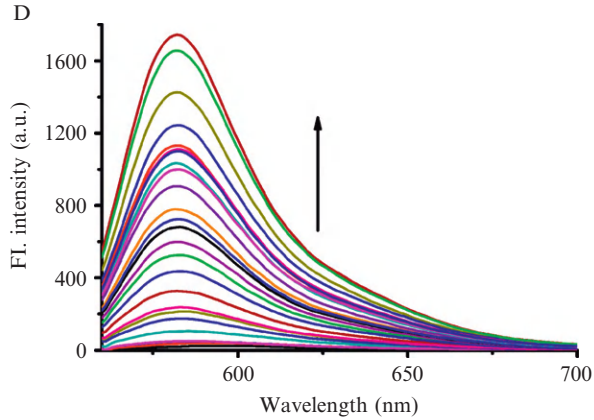

Figure 5.3 (A and B) The emission spectra of FP–H_2O_2–NO (1 μ*M*) in the presence of different equivalence of H_2O_2 (0–50 equiv.) excited at 400 nm (A) or 550 nm (B). (C and D) The emission spectra of FP–H_2O_2–NO (1 μ*M*) in the presence of different equivalence of NO (0–200 equiv.) excited at 400 nm (C) or 550 nm (D). Conditions: pH 7.4 PBS buffer with 20% CH_3CN. *Reprinted with permission from Yuan and Lin (2012). Copyright 2012 American Chemical Society.*

7-alkoxycoumarin dye and the rhodamine in the ring-opened form. These data suggest that the boronate-based and phenylenediamine-based reaction sites of the probe FP–H_2O_2–NO selectively respond to H_2O_2 and NO, respectively. It is worthy to note that H_2O_2 and NO induce the formation of the emission peaks at 460 and 581 nm, respectively. Thus, the large difference in the emission wavelength shift, up to 121 nm, renders the probe FP–H_2O_2–NO suitable for dual-color imaging of H_2O_2 and NO.

The study of the fluorescence response of the probe FP–H_2O_2–NO to the coexistence of H_2O_2 and NO is quite challenging, as the chemical reaction between H_2O_2 and NO may occur in solution, although these two signaling molecules can simultaneously be present in many physiological processes and have interplaying roles in the complex signal transduction and oxidative pathways (Bashan et al., 2009; Eguchi et al., 2011; Kotamraju et al., 2003; Li, Liu, et al., 2009; Milligan et al., 1996; Pandey et al., 2010; Peyrot & Ducrocq, 2008; Rauen et al., 2007; Sartoretto et al., 2011; Shiota et al., 2002). To make the scenario simpler in cuvettes, we decided to only investigate the fluorescence pattern of the probe when first treated with H_2O_2 and then with NO. Another motivation for incubation of the probe with H_2O_2 prior to NO is based on the previous reports

that H_2O_2 can function as an up-stream signal to elicit the production of NO in some types of animal and plant cells (Eguchi et al., 2011; Li, Liu, et al., 2009; Milligan et al., 1996; Sartoretto et al., 2011; Shiota et al., 2002; Zhang et al., 2007).

The fluorescence response of FP–H_2O_2–NO in the presence of H_2O_2 and NO is shown in Fig. 5.4. Introduction of H_2O_2 to FP–H_2O_2–NO induces a large fluorescence enhancement at 460 nm with excitation at 400 nm. By sharp contrast, the emission intensity at 581 nm with excitation at 400 or 550 nm displays essentially no change. These results are in good agreement with the transformation of FP–H_2O_2–NO to FP–NO in the presence of H_2O_2. At the time point of 20 min, NO was further added to the solution. A marked enhancement of the fluorescence intensity at 581 nm with excitation at 400 or 550 nm and a drastic decrease of fluorescence intensity at 460 nm with excitation at 400 nm is observed. This is consistent with the conversion of FP–H_2O_2–NO to Cou-Rho upon further addition of NO, as when Cou-Rho is excited at 400 nm, the emission of 7-hydroxycoumarin is quenched by the rhodamine dye due to FRET. Thus, FP–H_2O_2–NO has no emission at 460 nm when excited at 400 nm and displays strong emission at 580 nm when excited at 400 or 550 nm in the presence of H_2O_2 and NO. In other words, the fluorescence signal pattern for the probe in the presence of H_2O_2/NO is black–red–red.

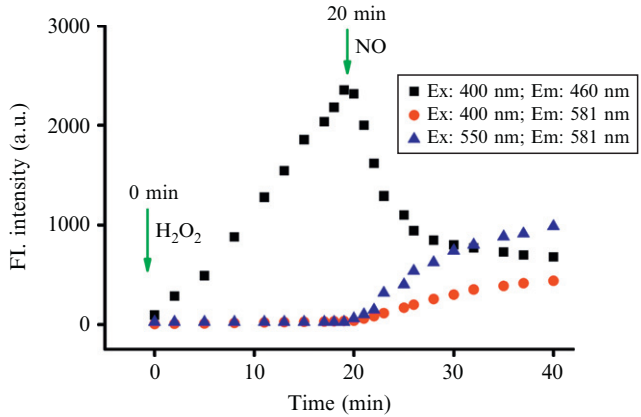

Figure 5.4 Time-dependent fluorescence intensity of FP–H_2O_2–NO at 460 nm excited at 400 nm (■), at 581 nm excited at 400 nm (●) or excited at 550 nm (▲). Notably, H_2O_2 (50 μ*M*) was introduced to FP–H_2O_2–NO (1 μ*M*) at 0 min, and then NO (100 μ*M*) was further added at 20 min. *Reprinted with permission from Yuan and Lin (2012). Copyright 2012 American Chemical Society.*

Notably, to ensure success in this experiment, an excessive amount of NO is needed, as some NO can be consumed by residual H_2O_2.

2.3. Selectivity

The selectivity is a very critical parameter for a fluorescent probe. In particular, for any fluorescent probes intended for biological imaging applications, it is highly desirable for the probes to be specific for the biological target, as the complex cellular environment is filled with a wide variety of endogenous biomolecules. Toward this end, the probe FP–H_2O_2–NO is incubated with a number of potentially interfering biomolecules such as ROS, RNS, and other biologically relevant species represented by hydrogen peroxide (H_2O_2), hypochlorous acid (HOCl), superoxide ($O_2^{\cdot-}$), hydroxyl radical (OH), *tert*-butyl hydroperoxide (TBHP), *tert*-butoxy radical (O*t*Bu), NO, NO_3^-, NO_2^-, ascorbic acid, and dehydroascorbic acid at the level of 100 μ*M* for evaluation of its selectivity. As shown in Fig. 5.5A, H_2O_2 triggers a large fluorescence enhancement at 460 nm upon excitation at 400 nm. By contrast, HOCl, $O_2^{\cdot-}$ and other species only cause a minor or minimal fluorescence change. The data suggest that the probe has a high selectivity for H_2O_2 over other biospecies tested when monitored at 460 nm with excitation at 400 nm, in good agreement with the fact that the boronate-based reaction site is chemospecific to H_2O_2. On the other hand, only NO elicits a significant fluorescence increase at 581 nm upon excitation at 550 nm (Fig. 5.5B). However, essentially no variation of fluorescence intensity at 581 nm is detected when the probe FP–H_2O_2–NO is incubated with other species tested. The data indicate that the probe is highly selective to NO when monitored at 581 nm with excitation at 550 nm, consistent with the fact that the phenylenediamine-based reaction site can be selectively removed by NO. In a fluorescence microscope, 460 and 580 nm locate in two emission channels. Thus, taken together, these results demonstrate that the probe FP–H_2O_2–NO can be employed to independently and simultaneously detect H_2O_2 and NO in living cells by dual-color fluorescence imaging.

2.4. Cellular response

2.4.1 Materials and instrumentation

Mammalian cells HeLa cells (Obtained from the third hospital of Xiangya as a gift).

Media (1) Growth medium: Dulbecco's Modified Eagle's Medium (DMEM) supplemented with 10% heat inactivated fetal calf serum

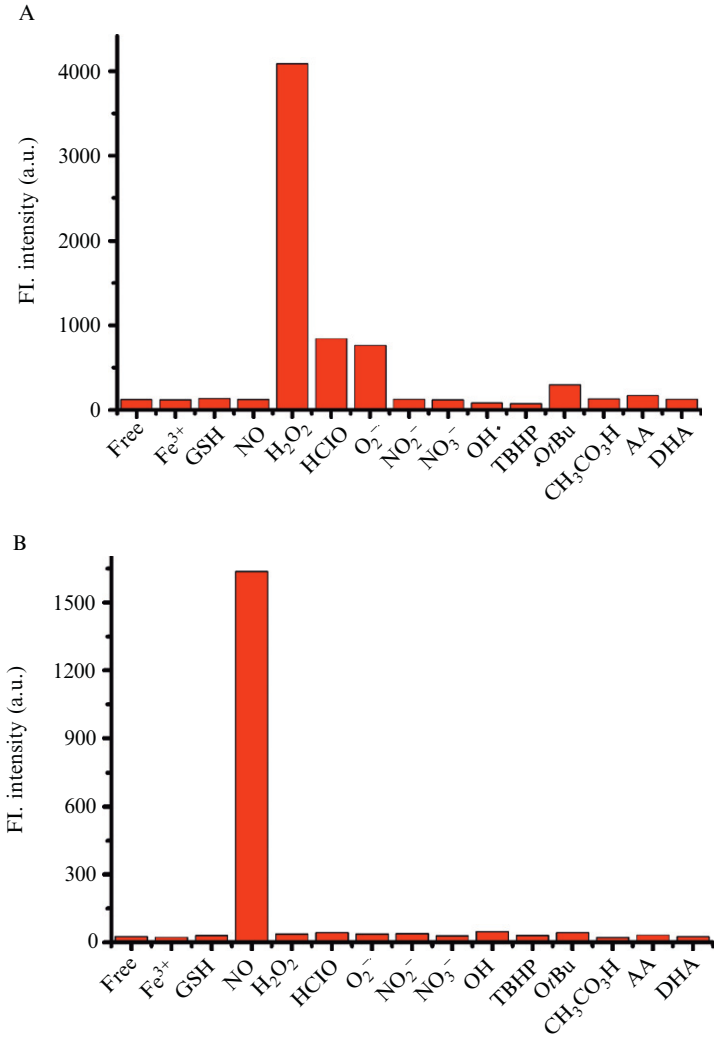

Figure 5.5 (A) The fluorescence intensity of the probe FP–H_2O_2–NO (1 μ*M*) at 460 nm excited at 400 nm in the presence of various biologically relevant species (100 μ*M*). (B) The fluorescence intensity of the probe FP–H_2O_2–NO (1 μ*M*) at 581 nm excited at 550 nm in the presence of various biologically relevant species (100 μ*M*). *Reprinted with permission from Yuan and Lin (2012). Copyright 2012 American Chemical Society.*

(FCS), 2 m*M* L-glutamine, 50 μg ml^{-1} penicillin, and 50 μg ml^{-1} streptomycin; (2) washing media: phosphate-buffered saline (PBS). Until use, DMEM-based media and PBS are kept at 4 °C and at room temperature, respectively.

Probe 1 m*M* FP–H_2O_2–NO stock solution in CH_3CN.
NO donor diethylamine NONOate 1 m*M* diethylamine NONOate stock solution in 0.01 *M* NaOH.
H_2O_2 1 m*M* H_2O_2 stock solution in water.
Cell culture HeLa cells were cultured in DMEM supplemented with 10% heat inactivated FCS, 2 m*M* L-glutamine, 50 μg ml^{-1} penicillin, and 50 μg ml^{-1} streptomycin in an atmosphere of 5% CO_2 and 95% air at 37 °C. One day before imaging, the cells were plated on six-well plates and allowed to adhere for 24 h. Subsequently, the cells were incubated with FP–H_2O_2–NO (5 μ*M*) for 0.5 h at 37 °C and then washed with PBS three times. After incubating with H_2O_2 (50 μ*M*) or NO donor diethylamine NONOate (50 μ*M*) for another 0.5 h at 37 °C, the cells were rinsed with PBS three times, and the fluorescence imaging was performed.
Instrumentation We performed fluorescence imaging experiments on Olympus inverted fluorescence microscope (IX71) equipped with a CCD digital camera, excitation wavelength at 405 and 543 nm. The images were obtained at blue (emission of coumarin) and red (emission of rhodamine) channels.

2.4.2 HeLa cells imaging

Figure 5.6 displays the typical fluorescence images of HeLa cells incubated with the probe FP–H_2O_2–NO and subsequently treated with H_2O_2, NO, or H_2O_2/NO. The images obtained need to be adjusted to the same intensity scale in order to compare the fluorescence intensities before and after addition of exogenous H_2O_2 and NO. The HeLa cells treated with FP–H_2O_2–NO (5 μ*M*) for 30 min at 37 °C give essentially no fluorescence in the blue channel (Fig. 5.6B) with excitation at around 405 nm and the red channel with excitation at either 405 nm (Fig. 5.6C) or 540 nm (Fig. 5.6D). By contrast, when HeLa cells stained with FP–H_2O_2–NO for 30 min at 37 °C and further incubated with H_2O_2, only intense fluorescence in the blue channel with excitation at around 405 nm is observed (Fig. 5.6F). These data demonstrate that the probe FP–H_2O_2–NO is cell membrane permeable and can report intracellular H_2O_2 in living cells. In addition, when the living HeLa cells were loaded with FP–H_2O_2–NO and then treated with the NO donor diethylamine NONOate, only a marked increase in the red emission (Fig. 5.6L) on excitation at around 540 nm is detected. These data suggest that FP–H_2O_2–NO is responsive to intracellular NO in living cells. Furthermore, the living cells were pretreated with FP–H_2O_2–NO for 30 min, then incubated with H_2O_2 for another 30 min,

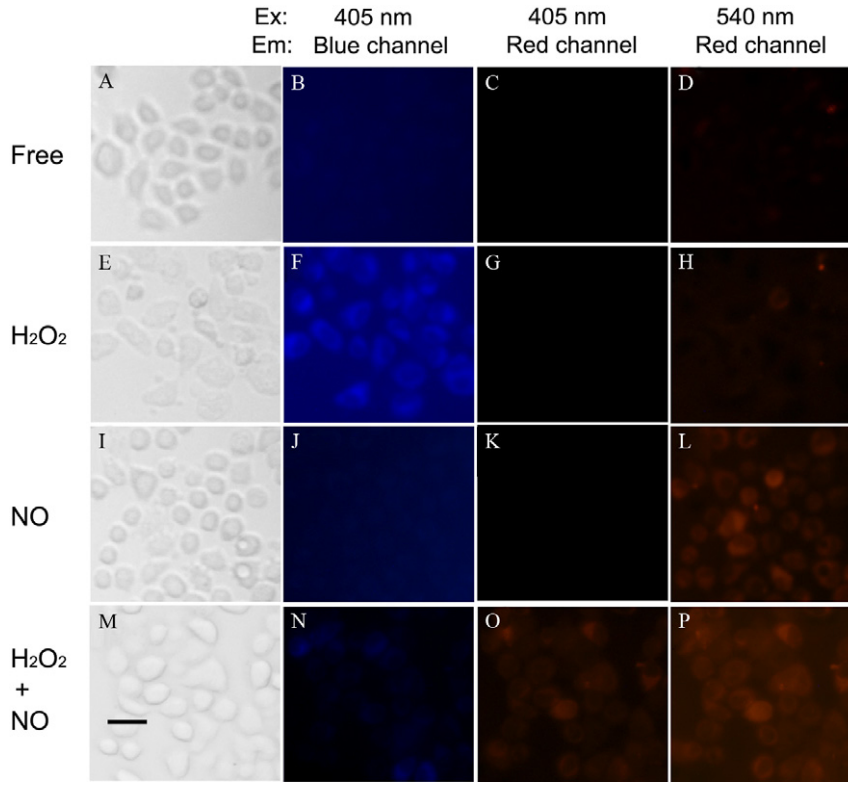

Figure 5.6 Representative images of HeLa cells treated with the probe FP–H_2O_2–NO. (A–D) Brightfield and fluorescence images of HeLa cells incubated with only the probe FP–H_2O_2–NO (5 μ*M*) for 30 min. (E–F) Brightfield and fluorescence images of HeLa cells incubated with FP–H_2O_2–NO (5 μ*M*) for 30 min and then further incubated with H_2O_2 (50 μ*M*) for another 30 min. (I–L) Brightfield and fluorescence images of HeLa cells incubated with FP–H_2O_2–NO (5 μ*M*) for 30 min and then further incubated with NO donor diethylamine NONOate (50 μ*M*) for another 30 min. (M–P) Brightfield and fluorescence images of HeLa cells preincubated with FP–H_2O_2–NO (5 μ*M*) for 30 min, then treated with H_2O_2 (50 μ*M*) for another 30 min, and further loaded with NO donor diethylamine NONOate (50 μ*M*) for 30 min. Scale bar = 20 μm. *Reprinted with permission from Yuan and Lin (2012). Copyright 2012 American Chemical Society.*

and further loaded with the NO donor diethylamine NONOate for 30 min, a significant enhancement in the red emission with excitation at around 405 nm (Fig. 5.6O) or 540 nm (Fig. 5.6P) is noted. Taken together, these results establish that FP–H_2O_2–NO can report added H_2O_2, NO, and H_2O_2/NO in living cells with different fluorescence signal patterns, promising for dual-color imaging of endogenous H_2O_2 and NO in living cells.

3. FLUORESCENCE IMAGING OF ENDOGENOUSLY PRODUCED H_2O_2 AND NO IN RAW 264.7 MACROPHAGES CELLS

Optimization of cell culture, probe loading, and microscope setup procedures is often necessary for fluorescence imaging. These parameters are related to the character of the biological samples and the probe, the type of microscope, and the specific purpose of the imaging experiment. In this section, we present a representative protocol for imaging endogenous H_2O_2 and NO in RAW 264.7 macrophages cells.

RAW 264.7 macrophages cells are the model living cells of the choice for testing the response of the fluorescent probe FP–H_2O_2–NO in an intact living system, as both H_2O_2 and NO can be generated in activated RAW 264.7 macrophages cells by acute inflammation. In addition, RAW 264.7 macrophages cells proliferate rapidly, easily adhere to glass slides during culture, and have been broadly applied as a model living system for studying the biology of ROS and RNS (Abo et al., 2011; Dickinson et al., 2010; McQuade et al., 2010; Srikun et al., 2008).

3.1. Materials and instrumentation

Raw 264.7 murine macrophages Obtained from the third hospital of Xiangya.

NO donor diethylamine NONOate 1 m*M* diethylamine NONOate stock solution in 0.01 *M* NaOH.

Lipopolysaccharide (LPS) LPS is dissolved in PBS at a concentration of 1.0 mg ml^{-1} and stored at −20 °C before use.

Phorbol 12-myristate 13-acetate (PMA) PMA is dissolved in DMSO at a concentration of 1.0 mg ml^{-1} and stored at −20 °C before use.

PEG-catalase A stock solution of the PEG-catalase (10 U ml^{-1}) is prepared in 0.10 *M* phosphate buffer and stored at −20 °C before use.

2-(4-Carboxyphenyl)-4,4,5,5,-tetramethyl-imidazoline-1-oxyl-3-oxide (carboxyl PTIO) A stock solution of the carboxyl PTIO (20 mg ml^{-1}) is prepared in 0.10 *M* phosphate buffer and stored at −20 °C before use.

3.2. Raw 264.7 murine macrophages culture and imaging

Raw 264.7 murine macrophages are cultured in DMEM supplemented with 10% FBS (fetal bovine serum) in an atmosphere of 5% CO_2 and 95% air at 37 °C. For imaging studies, the cells were plated on 6-well plates and

allowed to adhere for 24 h. Subsequently, the RAW 264.7 macrophage cells are coincubated with FP–H_2O_2–NO (5 μ*M*) and PMA (1 μg ml^{-1}) for 1 h in an atmosphere of 5% CO_2 and 95% air at 37 °C. Alternatively, the RAW 264.7 macrophage cells are treated with LPS (1 μg ml^{-1}) for 12 h, then loaded with FP–H_2O_2–NO (5 μ*M*) for 1 h in an atmosphere of 5% CO_2 and 95% air at 37 °C. Immediately before the experiments, the cells are rinsed with PBS three times, and the fluorescence images are acquired through an Olympus inverted fluorescence microscope (IX71) equipped with a cooled CCD camera (objective magnification: 20-fold, exposition-acquisition times: 400 ms). The culture and imaging experiments in the presence or absence of the stimulants (LPS, PMA) and the corresponding scavengers (PTIO, PEG-catalase) are performed in an analogous manner.

3.3. Results

It is known that PMA can effectively induce the production of H_2O_2 (Li, Li, et al., 2009) but only slight generation of NO (Chen, Kuhn, Gaydos, & Demers, 1996) in RAW264.7 macrophage cells. Thus, PMA can function as a useful stimulant for the selective generation of endogenous H_2O_2 in RAW264.7 macrophage cells to evaluate the response of the probe FP–H_2O_2–NO. As shown in Fig. 5.7B–D, the RAW264.7 macrophage cells stained only with the probe exhibit very slight fluorescence in the blue channel (Fig. 5.7B) and the red channel with excitation at around 405 (Fig. 5.7C) and 540 nm (Fig. 5.7D). By contrast, when the RAW264.7 macrophage cells coincubated with PMA and FP–H_2O_2–NO for 1 h, a marked enhancement in the blue channel is observed, but the red channel is still almost nonfluorescent (Fig. 5.7G and H). Thus, the macrophage cells loaded with PMA and FP–H_2O_2–NO show a fluorescence pattern of blue–black–black (Fig. 5.7F–H), in good agreement with that shown in Fig. 5.2 for the probe in the presence of H_2O_2. On the other hand, the previous reports indicate that LPS can efficiently trigger the generation of both endogenous H_2O_2 and NO (Hikosaka et al., 2006; Lee et al., 2007; Lee & Lim, 2008; Park et al., 1999). Thus, LPS can be employed as a practical stimulant for the generation of endogenous H_2O_2 and NO in RAW264.7 macrophage cells to examine the fluorescence signal pattern of the probe FP–H_2O_2–NO. When the RAW264.7 macrophage cells are preloaded with LPS for 12 h, then treated with the probe for 1 h, a significant enhancement in the red emission excited at 405 (Fig. 5.7K) or 540 nm (Fig. 5.7L) is noted. Thus, the macrophage cells loaded with LPS and FP–H_2O_2–NO display a fluorescence signal pattern of

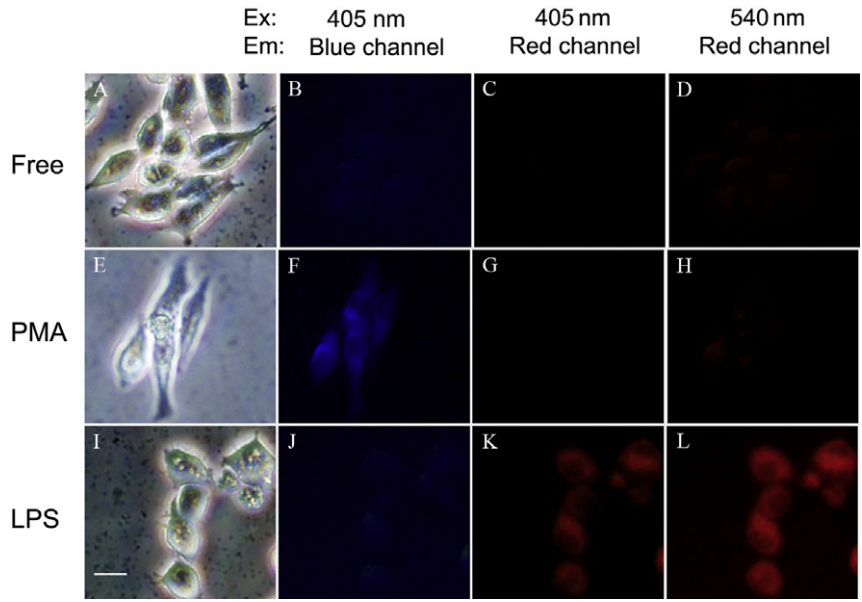

Figure 5.7 Representative images of RAW 264.7 macrophages treated with the probe FP–H_2O_2–NO in the absence or presence of stimulants. (A–D) DIC and fluorescence images of RAW 264.7 macrophages incubated with only the probe FP–H_2O_2–NO (5 μ*M*) for 1 h. (E–H) DIC and fluorescence images of RAW 264.7 macrophages coincubated with FP–H_2O_2–NO (5 μ*M*), PMA (1 μg ml^{-1}) for 1 h. (I–L) DIC and fluorescence images of RAW 264.7 macrophages incubated with LPS (1 μg ml^{-1}) for 12 h, then treated with FP–H_2O_2–NO (5 μ*M*) for 1 h. Scale bar = 20 μm. *Reprinted with permission from Yuan and Lin (2012). Copyright 2012 American Chemical Society.*

black–red–red (Fig. 5.7J–L), in accordance with that shown in Fig. 5.2 for the probe in the presence of both H_2O_2 and NO.

PTIO is a well-known scavenger for NO (Roy, Fung, Liu, & Pahan, 2006), and PEG-catalase is an efficient scavenger for H_2O_2 (Beckman et al., 1988; Cogolludo et al., 2006). Thus, PTIO and PEG-catalase can be employed in control experiments to ensure that the fluorescence changes really originate from the interactions of endogenous H_2O_2 and NO with the probe FP–H_2O_2–NO (Yuan, Lin, Xie, et al., 2012). The RAW 264.7 macrophages cells preloaded with LPS for 6 h, then treated with PTIO, and further loaded with FP–H_2O_2–NO give a noticeable fluorescence increase in the blue channel (Fig. 5.8F) but almost no fluorescence in the red channel (Fig. 5.8G and H). The data are in good agreement with those obtained from the cells treated with exogenous H_2O_2 and the probe in Hela cells

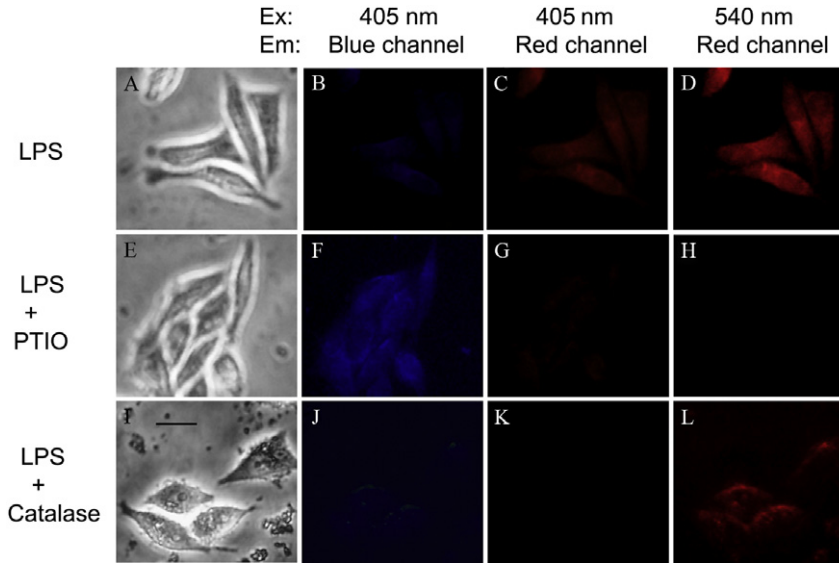

Figure 5.8 Images of RAW 264.7 macrophages treated with the probe FP–H_2O_2–NO in the absence or presence of stimulants and scavengers. (A) DIC image of RAW 264.7 macrophage cells incubated with LPS (1 μg ml^{-1}) for 12 h, then treated with FP–H_2O_2–NO (5 μ*M*) for 1 h. (B) Fluorescence image of (A) from blue channel excited at around 405 nm. (C) Fluorescence image of (A) from red channel excited at around 405 nm; (D) Fluorescence image of (A) from red channel excited at around 540 nm. (E) DIC image of RAW 264.7 macrophages pretreated with LPS (1 μg ml^{-1}) for 6 h, then treated with PTIO (a scavenger for NO) for 6 h, and further incubated with FP–H_2O_2–NO (5 μ*M*) for 1 h. (F) Fluorescence image of (E) from blue channel excited at around 405 nm. (G) Fluorescence image of (E) from red channel excited at around 405 nm. (H) Fluorescence image of (E) from red channel excited at around 540 nm. (I) DIC image of RAW 264.7 macrophages pretreated with LPS (1 μg ml^{-1}) for 6 h, then loaded with PEG-catalase (a scavenger for H_2O_2) for 6 h, and further incubated with FP–H_2O_2–NO (5 μ*M*) for 1 h. (J) Fluorescence image of (I) from blue channel excited at around 405 nm. (K) Fluorescence image of (I) from red channel excited at around 405 nm. (L) Fluorescence image of (I) from red channel excited at around 540 nm. Scale bar = 20 μm. *Reprinted with permission from Yuan and Lin (2012). Copyright 2012 American Chemical Society.*

(Fig. 5.6F–H), confirming that the fluorescence variations observed in macrophages cells are indeed induced by H_2O_2.

In addition, the RAW 264.7 macrophages cells preloaded with LPS for 6 h, then incubated with cell-permeable PEG-catalase, and further treated with the probe FP–H_2O_2–NO provide essentially no fluorescence in the blue channel (Fig. 5.8J) and the red channel with excitation at 405 nm

(Fig. 5.8K) but bright fluorescence in the red channel with excitation at 540 nm (Fig. 5.8L). The data are in good agreement with those obtained from the cells treated with exogenous NO and the probe in Hela cells (Fig. 5.6J–L), confirming that the fluorescence variations observed in macrophages cells are indeed induced by NO. Hence, taken together, these results demonstrate that the probe FP–H_2O_2–NO is suitable for simultaneously detecting endogenously produced NO and H_2O_2 in living macrophages cells in two-color imaging, indicating that the probe may be potentially useful for dissecting the complicated interrelationship of NO and H_2O_2 in the signal transduction and oxidative pathways. Notably, all of the above experiments are performed at 1 h after incubation of the probe with the RAW264.7 macrophage cells, as we observe that longer incubation (e.g., 12 h) even in the absence of PMA or LPS may result in strong background fluorescence in the red channel excited at 405 or 540 nm likely due to the production of endogenous H_2O_2 and NO in RAW264.7 macrophage cells accumulated over an extensive period of time. Thus, a short incubation time (1 h) for the RAW264.7 macrophage cells with the probe is recommended in this type of imaging experiments. As the fluorescence profile of 7-hydroxycoumarin moiety is sensitive to pH changes, it is recommended that the pH of the buffer solutions should be constant to ensure that no marked variations in the cellular environment.

4. SUMMARY

The fluorescent probe FP–H_2O_2–NO can respond to H_2O_2, NO, and H_2O_2/NO with a fluorescence signal pattern of blue–black–black, black–black–red, and black–red–red, respectively, thereby opening a avenue for studying the physiology and pathology of H_2O_2 and NO using dual-color fluorescence imaging. The selection guide in this chapter should help readers to understand the design scheme and optical properties of FP–H_2O_2–NO, and the representative protocols presented herein for imaging added and endogenous H_2O_2 and NO in live Hela cells and RAW 264.7 macrophages can serve as a guide to using the probe for fluorescence microscopy in studies of the interplaying roles of H_2O_2 and NO in the complex interaction networks of the signal transduction and oxidative pathways.

ACKNOWLEDGMENTS

Funding was partially provided by NSFC (20872032, 20972044, 21172063), NCET (08-0175), the Doctoral Fund of Chinese Ministry of Education (20100161110008), and the Fundamental Research Funds for the Central Universities, Hunan university.

REFERENCES

Abo, M., Urano, Y., Hanaoka, K., Terai, T., Komatsu, T., & Nagano, T. (2011). Development of a highly sensitive fluorescence probe for hydrogen peroxide. *Journal of the American Chemical Society*, *133*, 10629–10637.

Alderton, W. K., Cooper, C. E., & Knowles, R. G. (2001). Nitric oxide synthases: Structure, function and inhibition. *The Biochemical Journal*, *357*, 593–615.

Bashan, N., Kovsan, J., Kachko, I., Ovadia, H., & Rudich, A. (2009). Positive and negative regulation of insulin signaling by reactive oxygen and nitrogen species. *Physiological Reviews*, *89*, 27–71.

Beckman, J. S., Minor, R. L., White, C. W., Repine, J. E., Rosen, G. M., & Freeman, B. A. (1988). Superoxide dismutase and catalase conjugated to polyethylene glycol increases endothelial enzyme activity and oxidant resistance. *The Journal of Biological Chemistry*, *263*, 6884–6892.

Beija, M., Afonso, C. A. M., & Martinho, J. M. G. (2009). Synthesis and applications of Rhodamine derivatives as fluorescent probes. *Chemical Society Reviews*, *38*, 2410–2433.

Cao, Y., Guo, P., Xu, Y., & Zhao, B. (2005). Simultaneous detection of NO and ROS by ESR in biological systems. *Methods in Enzymology*, *396*, 77–83.

Caporaso, N. (2003). The molecular epidemiology of oxidative damage to DNA and cancer. *Journal of the National Cancer Institute*, *95*, 1263–1265.

Cary, S. P. L., Winger, J. A., Derbyshire, E. R., & Marletta, M. A. (2006). Nitric oxide signaling: No longer simply on or off. *Trends in Biochemical Sciences*, *31*, 231–239.

Chae, H. J., Kim, H. R., Kwak, Y. G., Ko, J. K., Joo, C. U., & Chae, S. W. (2001). Signal transduction of nitric oxide donor-induced production in hydrogen peroxide-mediated apoptosis in H9C2 cardiomyoblasts. *Immunopharmacology and Immunotoxicology*, *23*, 187–204.

Chen, F., Kuhn, D. C., Gaydos, L. J., & Demers, L. M. (1996). Induction of nitric oxide and nitric oxide synthase mRNA by silica and lipopolysaccharide in PMA-primed THP-1 cells. *Acta Pathologica, Microbiologica, et Immunologica Scandinavica*, *104*, 176–182.

Chen, X., Pradhan, T., Wang, F., Kim, J. S., & Yoon, J. (2012). Fluorescent chemosensors based on spiroring-opening of xanthenes and related derivatives. *Chemical Reviews*, *112*, 1910–1956.

Cogolludo, A., Frazziano, G., Cobeño, L., Moreno, L., Lodi, F., Villamor, E., et al. (2006). Role of reactive oxygen species in Kv channel inhibition and vasoconstriction induced by TP receptor activation in rat pulmonary arteries. *Annals of the New York Academy of Sciences*, *1091*, 41–51.

Cooke, M. S., Evans, M. D., Dizdaroglu, M., & Lunec, J. (2003). Oxidative DNA damage: Mechanisms, mutation, and disease. *The FASEB Journal*, *17*, 1195–1214.

Dickinson, B. C., Huynh, C., & Chang, C. J. (2010). A palette of fluorescent probes with varying emission colors for imaging hydrogen peroxide signaling in living cells. *Journal of the American Chemical Society*, *132*, 5906–5915.

Eguchi, H., Fujiwara, N., Sakiyama, H., Yoshihara, D., & Suzuki, K. (2011). Hydrogen peroxide enhances LPS-induced nitric oxide production via the expression of interferon beta in BV-2 microglial cells. *Neuroscience Letters*, *494*, 29–33.

Farias-Eisner, R., Chaudhuri, G., Aeberhard, E., & Fukuto, J. M. (1996). The chemistry and tumoricidal activity of nitric oxide/hydrogen peroxide and the implications to cell resistance/susceptibility. *The Journal of Biological Chemistry*, *271*, 6144–6151.

Filep, J. G., Lapierre, C., Lachance, S., & Chan, J. S. D. (1997). Nitric oxide co-operates with hydrogen peroxide in inducing DNA fragmentation and cell lysis in murine lymphoma cells. *The Biochemical Journal*, *321*, 897–901.

Gabe, Y., Urano, Y., Kikuchi, K., Kojima, H., & Nagano, T. (2004). Highly sensitive fluorescence probes for nitric oxide based on boron dipyrromethene chromophore-rational design of potentially useful bioimaging fluorescence probe. *Journal of the American Chemical Society*, *126*, 3357–3367.

Galaris, D., Skiada, V., & Barbouti, A. (2008). Redox signaling and cancer: The role of "labile" iron. *Cancer Letters*, *266*, 21–29.

Gomes, A., Fernandes, E., & Lima, J. L. F. C. (2005). Fluorescence probes used for detection of reactive oxygen species. *Journal of Biochemical and Biophysical Methods*, *65*, 45–80.

Hikosaka, K., Koyama, Y., Motobu, M., Yamada, M., Nakamura, K., Koge, K., et al. (2006). Reduced lipopolysaccharide (LPS)-induced nitric oxide production in peritoneal macrophages and inhibited LPS-induced lethal shock in mice by a sugar cane (Saccharum officinarum L.) extract. *Bioscience, Biotechnology, and Biochemistry*, *70*, 2853–2858.

Hoffmann, O., Zweigner, J., Smith, S. H., Freyer, D., Mahrhofer, C., Dagand, E., et al. (2006). Interplay of pneumococcal hydrogen peroxide and host-derived nitric oxide. *Infection and Immunity*, *74*, 5058–5066.

Huang, S.-T., Teng, C.-J., Lee, Y.-H., Wu, J.-Y., Wang, K.-L., & Lin, C.-M. (2010). Design and synthesis of a long-wavelength latent fluorogenic substrate for salicylate hydroxylase: A useful fluorimetric indicator for analyte determination by dehydrogenase-coupled biosensors. *Analytical Chemistry*, *82*, 7329–7334.

Ioannidis, I., & de Groot, H. (1993). Cytotoxicity of nitric oxide in Fu5 rat hepatoma cells: Evidence for co-operative action with hydrogen peroxide. *The Biochemical Journal*, *296*, 341–345.

Kikuchi, K., Takakusa, H., & Nagano, T. (2004). Recent advances in the design of small molecule-based FRET sensors for cell biology. *Trends in Analytical Chemistry*, *23*, 407–415.

Kim, H. N., Lee, M. H., Kim, H. J., Kim, J. S., & Yoon, J. (2008). A new trend in rhodamine-based chemosensors: Application of spirolactam ring-opening to sensing ions. *Chemical Society Reviews*, *37*, 1465–1472.

Kotamraju, S., Tampo, Y., Keszler, A., Chitambar, C. R., Joseph, J., Haas, A. L., et al. (2003). Nitric oxide inhibits H_2O_2-induced transferrin receptor-dependent apoptosis in endothelial cells: Role of ubiquitin-proteasome pathway. *Proceedings of the National Academy of Sciences of the United States of America*, *100*, 10653–10658.

Krohn, K., Maier, J., & Paschke, R. (2007). Mechanisms of disease: Hydrogen peroxide, DNA damage and mutagenesis in the development of thyroid tumors. *Nature Reviews. Endocrinology*, *3*, 713–720.

Kuznetsov, A. V., Kehrer, I., Kozlov, A. V., Haller, M., Redl, H., Hermann, M., et al. (2011). Mitochondrial ROS production under cellular stress: Comparison of different detection methods. *Analytical and Bioanalytical Chemistry*, *400*, 2383–2390.

Lee, D., Khaja, S., Velasquez-Castano, J. C., Dasari, M., Sun, C., Petros, J., et al. (2007). In vivo imaging of hydrogen peroxide with chemiluminescent nanoparticles. *Nature Materials*, *6*, 765–769.

Lee, S.-J., & Lim, K.-T. (2008). Phytoglycoprotein inhibits interleukin-1β and interleukin-6 via p38 mitogen-activated protein kinase in lipopolysaccharide-stimulated RAW 264.7 cells. *Naunyn-Schmiedebergs Archives of Pharmacology*, *377*, 45–54.

Li, H., Li, Q., Wang, X., Xu, K., Chen, Z., Gong, X., et al. (2009). Simultaneous determination of superoxide and hydrogen peroxide in macrophage RAW 264.7 cell extracts by microchip electrophoresis with laser-induced fluorescence detection. *Analytical Chemistry*, *81*, 2193–2198.

Li, J.-H., Liu, Y.-Q., Lü, P., Lin, H.-F., Bai, Y., Wang, X.-C., et al. (2009). A signaling pathway linking nitric oxide production to heterotrimeric G protein and hydrogen peroxide regulates extracellular calmodulin induction of stomatal closure in Arabidopsis. *Plant Physiology*, *150*, 114–124.

Lin, M. T., & Beal, M. F. (2006). Mitochondrial dysfunction and oxidative stress in neurodegenerative diseases. *Nature*, *443*, 787–795.

Lin, W., Long, L., Chen, B., Tan, W., & Gao, W. (2010). Fluorescence turn-on detection of Cu^{2+} in water samples and living cells based on the unprecedented copper-mediated dihydrorosamine oxidation reaction. *Chemical Communications*, *46*, 1311–1313.

Lin, W., Yuan, L., Cao, Z., Feng, Y., & Long, L. (2009). A sensitive and selective fluorescent thiol probe in water based on the conjugate 1,4-addition of thiols to α, β-unsaturated ketones. *Chemistry: A European Journal*, *15*, 5096–5103.

Lin, W., Yuan, L., Cao, Z., Feng, Y., & Song, J. (2010). Through-bond energy transfer cassettes with minimal spectral overlap between the donor emission and acceptor absorption: Coumarin-rhodamine dyads with large pseudo-stokes shifts and emission shifts. *Angewandte Chemie, International Edition*, *49*, 375–379.

Mayer, B. (Ed.), (2000). *Nitric oxide: Handbook of experimental pharmacology*, (Vol. 143). Berlin: Springer.

McQuade, L. E., Ma, J., Lowe, G., Ghatpande, A., Gelperin, A., & Lippard, S. J. (2010). Visualization of nitric oxide production in the mouse main olfactory bulb by a cell-trappable copper(II) fluorescent probe. *Proceedings of the National Academy of Sciences of the United States of America*, *107*, 8525–8530.

Milligan, S. A., Owens, M. W., & Grisham, M. B. (1996). Augmentation of cytokine-induced nitric oxide synthesis by hydrogen peroxide. *The American Journal of Physiology—Lung Cell*, *271*, L114–L120.

Pandey, A. N., Tripathi, A., PremKumar, K. V., Shrivastav, T. G., & Chaube, S. K. (2010). Reactive oxygen and nitrogen species during meiotic resumption from diplotene arrest in mammalian oocytes. *Journal of Cellular Biochemistry*, *111*, 521–528.

Park, S. Y., Ji, G. E., Ko, Y. T., Jung, H. K., Ustunol, Z., & Pestka, J. J. (1999). Potentiation of hydrogen peroxide, nitric oxide, and cytokine production in RAW 264.7 macrophage cells exposed to human and commercial isolates of Bifidobacterium. *International Journal of Food Microbiology*, *46*, 231–241.

Peyrot, F., & Ducrocq, C. (2008). Potential role of tryptophan derivatives in stress responses characterized by the generation of reactive oxygen and nitrogen species. *Journal of Pineal Research*, *45*, 235–246.

Rauen, U., Li, T., Ioannidis, I., & de Groot, H. (2007). Nitric oxide increases toxicity of hydrogen peroxide against rat liver endothelial cells and hepatocytes by inhibition of hydrogen peroxide degradation. *American Journal of Physiology. Cell Physiology*, *292*, C1440–C1449.

Reth, M. (2002). Hydrogen peroxide as second messenger in lymphocyte activation. *Natural Immunity*, *3*, 1129–1134.

Reymond, J.-L., Fluxà, V. S., & Maillard, N. (2009). Enzyme assays. *Chemical Communications*, *45*, 34–46.

Rhee, S. G. (2006). H_2O_2, a necessary evil for cell signaling. *Science*, *312*, 1882–1883.

Ridnour, L. A., Sim, J. E., Choi, J., Dickinson, D. A., Forman, H. J., Ahmad, I. M., et al. (2005). Nitric oxide-induced resistance to hydrogen peroxide stress is a glutamate cysteine ligase activity-dependent process. *Free Radical Biology & Medicine*, *38*, 1361–1371.

Roy, A., Fung, Y. K., Liu, X., & Pahan, K. (2006). Up-regulation of microglial CD11b expression by nitric oxide. *The Journal of Biological Chemistry*, *281*, 14971–14980.

Sartoretto, J. L., Kalwa, H., Pluth, M. D., Lippard, S. J., & Michel, T. (2011). Hydrogen peroxide differentially modulates cardiac myocyte nitric oxide synthesis. *Proceedings of the National Academy of Sciences of the United States of America*, *108*, 15792–15797.

She, X.-P., Song, X.-G., & He, J.-M. (2004). Role and relationship of nitric oxide and hydrogen peroxide in light/dark-regulated stomatal movement in Vicia faba. *Acta Botanica Sinica*, *46*, 1292–1300.

Shiota, K., Shimizu, S., Ishii, M., Yamamoto, S., Iwasaki, M., Yamamoto, T., et al. (2002). Hydrogen peroxide stimulates the LPS-induced tetrahydrobiopterin synthesis in mouse brain microvascular endothelial cells. *Pteridines*, *13*, 21–25.

Soneja, A., Drews, M., & Malinski, T. (2005). Role of nitric oxide, nitroxidative and oxidative stress in wound healing. *Pharmacological Reports*, *57*(Suppl.), 108–119.

Srikun, D., Miller, E. W., Domaille, D. W., & Chang, C. J. (2008). An ICT-based approach to ratiometric fluorescence imaging of hydrogen peroxide produced in living cells. *Journal of the American Chemical Society*, *130*, 4596–4597.

Wei, T., Chen, C., Hou, J., Xin, W., & Mori, A. (2000). Nitric oxide induces oxidative stress and apoptosis in neuronal cells. *Biochimica et Biophysica Acta*, *1498*, 72–79.

Winterbourn, C. C. (2008). Reconciling the chemistry and biology of reactive oxygen species. *Nature Chemical Biology*, *4*, 278–286.

Yoshioka, Y., Kitao, T., Kishino, T., Yamamuro, A., & Maeda, S. (2006). Nitric oxide protects macrophages from hydrogen peroxide-induced apoptosis by inducing the formation of catalase. *The Journal of Immunology*, *176*, 4675–4681.

Yuan, L., Lin, W., Xie, Y., Chen, B., & Zhu, S. (2012). Single fluorescent probe responds to H_2O_2, NO, and H_2O_2/NO with three different sets of fluorescence signals. *Journal of the American Chemical Society*, *134*, 1305–1315.

Yuan, L., Lin, W., Yang, Y., & Chen, H. (2012). Changsha fluorophores as a unique class of near-infrared functional fluorescent dyes with carboxylic-acid-modulated fluorescence ON/OFF switching: Rational design, synthesis, optical properties, theoretical calculations, and the applications for fluorescence imaging in living animals. *Journal of the American Chemical Society*, *134*, 1200–1211.

Yuan, L., Lin, W., Zhao, S., Gao, W., Chen, B., He, L., et al. (2012). A unique approach to development of near-infrared fluorescent sensors for in vivo imaging. *Journal of the American Chemical Society*, *134*, 13510–13523.

Zhang, A., Jiang, M., Zhang, J., Ding, H., Xu, S., Hu, X., et al. (2007). Nitric oxide induced by hydrogen peroxide mediates abscisic acid-induced activation of the mitogen-activated protein kinase cascade involved in antioxidant defense in maize leaves. *The New Phytologist*, *175*, 36–50.

Zheng, H., Shang, G.-Q., Yang, S.-Y., Gao, X., & Xu, J.-G. (2008). Fluorogenic and chromogenic rhodamine spirolactam based probe for nitric oxide by spiro ring opening reaction. *Organic Letters*, *10*, 2357–2360.

CHAPTER SIX

Electrochemical Biosensors for On-Chip Detection of Oxidative Stress from Cells

James Enomoto, Zimple Matharu, Alexander Revzin[1]
Department of Biomedical Engineering, University of California, Davis, California, USA
[1]Corresponding author: e-mail address: arevzin@ucdavis.edu

Contents

1. Introduction 108
2. Experimental Components and Procedures 109
   2.1 Preparation of substrate using photolithography 109
   2.2 Matrices for encapsulation of biomolecules 110
   2.3 Preparation of prepolymer enzyme hydrogel solution 111
   2.4 Fabrication of hydrogel microstructures on top of patterned substrates 112
   2.5 Combining HRP-sensing electrodes with microfluidic channels 113
3. Methods of Calibrating Enzyme Sensors 115
4. Monitoring ROS Production from Cells Using Electrochemistry 116
   4.1 Seeding of cells into sensing device 116
   4.2 Measurement of ROS production from injured cells 117
   4.3 Quantification of H_2O_2 concentration from cells 118
5. Summary 118
References 118

Abstract

The production of reactive oxygen species (ROS) in the body has been shown to play a significant role in the development and progression of numerous diseases. This makes it important to develop a method of detection for hydrogen peroxide (H_2O_2), the most stable ROS. Several methods such as the use of fluorescent probes and electrochemistry have been utilized in the past to detect the imbalance in ROS levels generated from injured or stimulated cells. An imbalance in the levels of ROS leads to a state of oxidative stress within the body. Different enzymes such as horseradish peroxidase (HRP) and superoxide dismutase have been used in the detection of ROS. HRP is commonly used as the biorecognition element in many H_2O_2 sensors. Researchers have looked into immobilizing these enzymes onto carbon nanotubes and nanoparticles to increase sensor sensitivity. In this chapter, we present experimental procedures to perform electrochemical quantification of H_2O_2, one of the major ROS release from injured cells (macrophages and hepatocytes).

Methods in Enzymology, Volume 526
ISSN 0076-6879
http://dx.doi.org/10.1016/B978-0-12-405883-5.00006-5

© 2013 Elsevier Inc.
All rights reserved.

1. INTRODUCTION

Hydrogen peroxide (H_2O_2) is a small, membrane-permeable molecule that plays an important role in cellular signaling (Veal, Day, & Morgan, 2007). The overproduction of H_2O_2 has been shown to play a role in the progression of diseases such as Alzheimer's (Tabner et al., 2005), Parkinson's (Fahn & Cohen, 1992), alcoholic liver disease (Zima & Kalousova, 2005), and cancer (Schmielau & Finn, 2001). H_2O_2, along with the hydroxyl radical ($OH^{\cdot}$) and superoxide anion ($O_2^{\cdot -}$), belongs to a group of molecules known as reactive oxygen species (ROS). ROS are chemically reactive and have toxic effects on many biological compounds. Enzymes such as catalases and glutathiones, present in the cell, can safely eliminate low concentrations of ROS. However, when the levels of ROS exceed the body's natural antioxidant defenses, an imbalance arises that triggers a sequence of inflammatory responses. This leads to a state of oxidative stress in which the normal redox state of the cell is altered, causing DNA damage, lipid peroxidation, and oxidative damage to cellular proteins. Although ROS have a number of toxic effects, they are naturally occurring in the body as a product of oxygen metabolism in cellular mitochondria and in immune cells, such as macrophages, as a means of killing bacteria.

Even with an increased interest in the study of ROS, there are still a limited number of methods available for the detection of ROS produced from cells. The two most common methods currently available are fluorescence and electrochemistry. Fluorescent probes, such as 2′,7′-dichlorodihydroluorescein diacetate and amplex Red (10-acetyl-3,7-dihydroxyphenoxazine), are oxidized into their fluorescent forms in the presence of ROS (as reviewed elsewhere; Rhee, Chang, Jeong, & Kang, 2010). However, due to photobleaching and autofluorescence, they are incapable of providing sensitive quantitative measurements. Electrochemical biosensors are capable of alleviating many of the issues presented with these fluorescence-based techniques. Many electrochemical biosensors utilize enzymes that react with a given analyte, which produces a current that can then be measured at the surface of an electrode (Pohanka & Skladai, 2008). Recent H_2O_2 biosensors have combined enzymes such as horseradish peroxidase (HRP) with a variety of materials ranging from carbon nanotubes to numerous types of polymeric matrices in an effort to improve sensor sensitivity and specificity. This chapter describes a detailed protocol for the design and fabrication of an

electrochemical biosensor based on an HRP-entrapped hydrogel matrix for the quantitative measurement of ROS levels produced from cells.

2. EXPERIMENTAL COMPONENTS AND PROCEDURES

2.1. Preparation of substrate using photolithography

Photolithography is a process that has long been used in the semiconductor and microelectronics industries to pattern small features onto silicon wafers. Photoresist, a light-sensitive compound, is exposed to UV light through a patterned photomask to generate patterns onto various substrates, such as silicon, glass, and gold. Photoresist comes in two types, positive and negative. Positive photoresists become soluble when exposed to light, while the portion of negative photoresists exposed to light becomes insoluble. The soluble resist can then be removed from the surface by placing the chip in a developer solution. This process has since been adapted for biomedical applications and has been used in the fabrication of lab-on-a-chip biosensors (Figeys & Pinto, 2000).

On-chip electrochemical biosensors utilize techniques such as photolithography and chemical etching to create miniature electrodes where the current generated from an electrochemical reaction can be measured. Electrodes are usually made from conductive materials, such as gold and platinum. However, carbon-based materials, such as graphite, have also been used in the fabrication of electrodes due to their relative inertness and conductivity (Sarma, Vatsyayan, Goswami, & Minteer, 2009). Carbon electrodes are commonly polished with an alumina slurry (1.0, 0.3, and 0.05 μm) until a glassy appearance is achieved (Qian & Yang, 2006). The following protocol describes the fabrication process used in our lab to prepare patterned gold electrode chips.

1. Layers of Cr (15 nm) and Au (100 nm) were sputter coated onto glass slides by Lance Goddard Associates (Santa Clara).
2. Au slides were baked at 115 °C for a few minutes to remove any residual surface moisture from the slides to improve photoresist adhesion.
3. S1813 (positive photoresist) is spin coated over the surface of the slide at 2000 rpm for 30 s, forming a thin uniform layer.
4. Photoresist-covered slides are soft baked at 115 °C for 1 min to harden the photoresist layer by removing excess solvent.
5. Slides are exposed to UV light for about 50–60 s through an aligned photomask using a mask aligner. Patterned photomasks were generated in

AutoCAD and converted to plastic transparencies by CAD Art Services (Portland, OR).

6. The exposed slides were developed in MF-319 developer for 1 min to remove all regions previously exposed to UV light. After the slides are fully developed, it is necessary to scratch off any remaining photoresist present between the electrode contact pads in order to ensure that each electrode is individually addressable.
7. Finally, the slides were placed in gold etchant and chrome etchant for about 20 and 30 s, respectively. This generated an array of circular electrodes on top of the glass slide.

2.2. Matrices for encapsulation of biomolecules

One of the major issues faced in the development of electrochemical biosensors is the fouling of the electrode surface. In order to optimize the sensor's performance, a membrane needs to be able to resist cell and protein adhesion, while also allowing small molecules, such as H_2O_2, to pass through the polymer matrix and interact with the entrapped enzyme (Zhang, Wright, & Yang, 2000). Li, Liu, and Pang (2004) used cellulose, an organic polymer found in the cell walls of plants, to immobilize myoglobin and hemoglobin for the detection of H_2O_2. Cellulose has been shown to be highly selective for H_2O_2 by blocking the diffusion of larger molecules (Gunasingham, Teo, Lai, & Tan, 1989). Chitosan is another organic polymer that is highly permeable to water, chemically inert, biocompatible, and possesses amino groups available for the covalent attachment of biomolecules (Koev et al., 2010; Zhou et al., 2010). Miao and Tan (2000) covalently linked HRP to a chitosan film by drying an HRP-chitosan solution over a platinum electrode. Synthetic sol–gel glass is a chemical inert, optically transparent, low-temperature encapsulation method that creates a matrix with highly tunable porosity and negligible swelling (Wang, 1999). However, since sol–gels have been shown to be susceptible to cracking and potentially changing the properties of the encapsulated biomolecules, they are usually combined with other polymers (Gupta & Chaudhury, 2007). In our lab, we chose poly (ethylene glycol) diacrylate (PEG-DA) as the encapsulation material for our electrodes (Matharu, Enomoto, & Revzin, 2013; Yan, Pedrosa, Enomoto, Simonian, & Revzin, 2011). We chose PEG-DA because it is a polymer commonly used in biomedical applications, such as tissue engineering and drug delivery, due to its biocompatibility, mechanical properties, and nonfouling nature (Peppas, Keys, Torres-Lugo, &

Lowman, 1999). Hydrogels, a matrix of polymer chains that contain high water content, also provide a hydrated environment to help maintain the functionality of entrapped proteins, making them suitable matrices for enzyme-based biosensors. With so many matrix materials available for the encapsulation of biomolecules, the proper matrix will vary on a case-by-case basis.

Further research has gone into combining nanomaterials, such as carbon nanotubes and gold or silver nanoparticles, with membrane-immobilized enzymes to enhance electron transport through the membrane (Sarma et al., 2009). Carbon nanotubes are usually formed from a rolled-up graphite sheet which can then be covalently linked to enzymes. By immobilizing these enzyme-linked nanotubes onto the surface of an electrode, more efficient electron transfer can be achieved (as reviewed elsewhere; Wang, 2005). Gold and silver nanoparticles are another option used in the enhancement of sensor sensitivity. As with carbon nantotubes, enzymes can be covalently linked to nanoparticles, which then act like small conduction centers for improved electron transport (Ren, Song, Li, & Zhu, 2005). Work done in our lab showed that glucose oxidase and HRP could be bound to gold nanoparticles. Pedrosa, Yan, Simonian, and Revzin (2011) incorporated enzyme-modified nanoparticles into a hydrogel matrix, which showed an increased sensitivity compared to the same hydrogel matrix without gold nanoparticles.

2.3. Preparation of prepolymer enzyme hydrogel solution

In the fabrication of hydrogel-based biosensors, enzymes are typically added into the prepolymer solution prior to UV exposure. Incorporation of a photoinitiator into the prepolymer solution allows for the individual PEG monomers to be cross-linked through free radical polymerization upon exposure to UV light (Sirkar & Pishko, 1998). Using PEG monomers with longer chain lengths will lead to a matrix with a larger pore size, while the use of shorter chain lengths will lead to a more stable, tightly packed matrix. However, the added stability provided by the smaller PEG monomers may impair the nonfouling properties of the hydrogel (Choi, Lee, Park, & Koh, 2008). This means that the properties of the polymer must be carefully determined in order to achieve the optimal performance of the sensor.

In the development of biosensors for the detection of oxidative stress, enzymes specific to H_2O_2 or $O_2^{\cdot -}$, such as HRP and superoxide dismutase (SOD), are typically used. Hiatt and coworkers measured the $O_2^{\cdot -}$ generated

from RAW 264.7 macrophages by creating SOD films on top of platinum disk electrodes (Hiatt et al., 2012). Since the electrochemical properties of HRP are well characterized (Dequaire, Limoges, Moiroux, & Saveant, 2002), it has been used in chitosan films alongside carbon nanotubes (Qian & Yang, 2006) and inside of sol–gel matrices (Wang, Xu, Chen, & Lu, 2003) to measure concentrations of H_2O_2. Besides HRP, other heme-containing proteins have been investigated for use in the development of H_2O_2 biosensors. Shi et al. (2009) combined soybean peroxidase with carbon nanohorns, while Liu, Dai, Chen, and Ju (2004) immobilized hemoglobin onto zirconium dioxide nanoparticles to measure the reduction of the H_2O_2.

In our lab, we created hydrogel microstructures using free radical polymerization by adding 2-hydroxy-2-methyl-propiophenone (photoinitiator) (2%) to our PEG solution (Yan et al., 2011). The prepolymer solution containing PEG 575 (Yan et al., 2011) or a mixture of PEG 575–PEG 258 (Matharu et al., 2013) and photoinitiator was then mixed for 15 min. HRP and glutaraldehyde (Glu) were added to the PEG mixture and the subsequent solution was stirred at 4 °C overnight to allow for the Glu to react with all of the free amine groups of the HRP. This process cross-linked together the individual HRP molecules, helping to improve its retention inside of the PEG hydrogel (Matharu et al., 2013). The composition of our prepolymer enzyme solution is found in Table 6.1.

2.4. Fabrication of hydrogel microstructures on top of patterned substrates

In order for PEG-DA to attach to the micropatterned glass slide, acryl groups need to be present on the glass surface. This can be accomplished by modifying the glass slides with (3-acryloxypropyl) trichlorosilane (Matharu et al., 2013; Yadavalli, Koh, Lazur, & Pishko, 2004; Yan et al., 2011). The slide is placed inside of an oxygen plasma chamber, where oxygen gas is exposed to high-frequency voltages and low pressure to ionize the gas into plasma. The plasma bombards the glass surface to introduce hydroxyl groups and

Table 6.1 Composition of our prepolymer enzyme solution

Component	Volume (μl)
HRP (10 mg/ml in PBS)	20
PEG 575	25
Glu	2

promote the attachment of the silane monolayer. After being treated with plasma, the slides are placed in a glove bag filled with nitrogen and incubated in a solution of 0.05% (3-acryloxypropyl) trichlorosilane dissolved in anhydrous toluene. The use of a glove bag is suggested during the incubation process as silane readily reacts with oxygen. After the self-assembled monolayer is formed, the slides are sonicated for 2 min in acetone to remove the photoresist covering the gold electrode array. In our experience, we have found that the photoresist must be present on top of the electrodes to prevent silane from attaching onto the gold. However, after the silane monolayer has formed on the glass surface, the photoresist must be removed to prevent the passivation of the electrode's surface by the photoresist. The slides are then placed in an oven at 100 °C for 2 h to help cross-link the silane layer.

The slides were then subjected to a two-step exposure process, as outlined by Yan et al. (2011), to create the HRP-sensing structures inside of PEG wells. In order to create the sensing element, the HRP prepolymer solution (Section 2.3) was spread over the gold electrode arrays with a glass coverslip. Exposure to UV light through an aligned photomask cross-linked the acryl groups of the PEG to the acryl groups of the silane, creating a PEG matrix for the entrapment of HRP. After development in deionized water, a PEG solution without enzyme was spread over the slide with a coverslip. Exposure to UV light through a second photomask created a nonfouling background layer of PEG, forming well-shaped cell attachment regions near the electrodes. Step-by-step procedure of sensor fabrication is shown in Fig. 6.1.

2.5. Combining HRP-sensing electrodes with microfluidic channels

Microfluidic devices are often used in the development of lab-on-a-chip devices because they are relatively cheap, easy to manufacture, and reduce the amount of expensive reagents needed. Molds for microfluidic channels are typically created from SU-8 patterned silicon wafers. These molds are filled with poly dimethyl siloxane (PDMS), a silicone rubber that is biocompatible and gas permeable (Mata, Fleischman, & Roy, 2005). These properties make it an ideal platform for use in on-chip detection of ROS from cells. PDMS devices can be designed to have multiple channels as to allow the user to test multiple samples at once (Heo & Crooks, 2005). Microfluidic devices have been shown to work well in electrochemical detection experiments from macrophages, as the small channel volumes help to concentrate the ROS produced from cells (Amatore, Arbault, Chen,

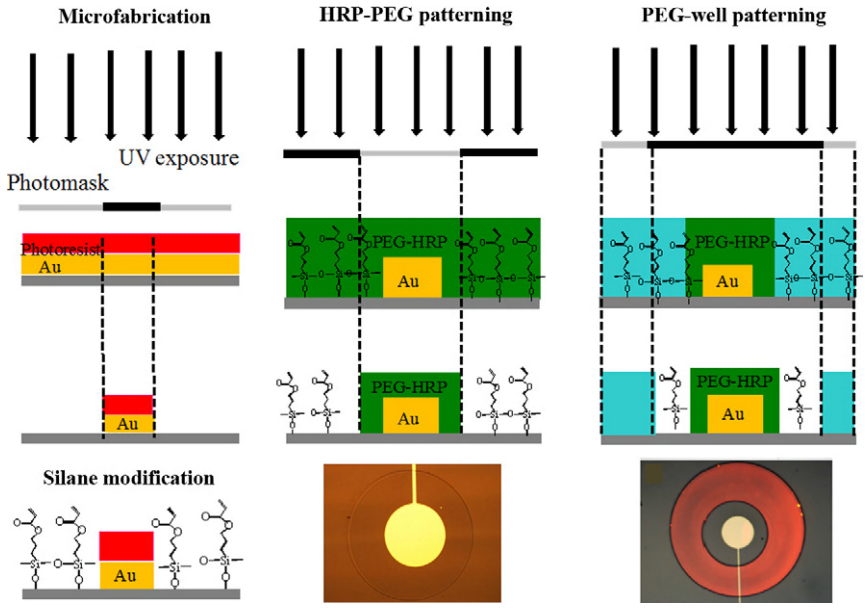

Figure 6.1 Schematic diagram showing the fabrication process of our gold electrodes, HRP-PEG microstructures, and PEG wells.

Crozatier, & Tapsoba, 2007). In our lab's design, we add a network of auxiliary channels to the PDMS device to allow for suctioning of the device onto the glass substrate using an external vacuum source (Fig. 6.2A).

In order to take electrochemical measurements in our device, a three-electrode setup that includes miniature gold working electrodes, platinum counter electrode placed in the inlet reservoir, and a flow-through Ag/AgCl (3 *M* KCl) reference electrode positioned at the outlet is used (Fig. 6.2B). In some cases, the reference and/or counter electrode can be added onto the surface of the chip (Krylov et al., 2006). Most enzyme-based electrochemical biosensors rely on the principles of amperometry and voltammetry. Amperometry allows the sensor to measure current over time at a fixed potential, while voltammetry measures current over a range of potentials. Both methods have been utilized frequently for H_2O_2 detection from cells. Li et al. (2011) used amperometry to measure the production of H_2O_2 from RAW 264.7 macrophages from HRP-hydroxyapatite nanohybrid-modified electrodes. Wang et al. (2003) used amperometric measurements to characterize the performance of their HRP/sol–gel/chitosan biosensor. Cheah et al. (2010) used cyclic voltammetry (CV) for *in situ* measurements

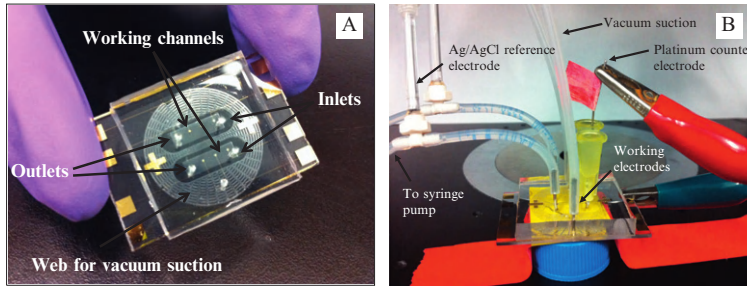

Figure 6.2 (A) PDMS microfluidic channels placed atop an array of gold electrodes. (B) Three-electrode setup used for electrochemical measurements. Setup includes gold working electrodes, platinum counter electrode, and flow-through Ag/AgCl reference electrode.

of ROS from heart tissue. Matharu et al. (2013) used CV to detect H_2O_2 from ethanol-stimulated hepatocytes using HRP-PEG microstructures.

3. METHODS OF CALIBRATING ENZYME SENSORS

As with all biosensors, calibration experiments are needed to allow the user to determine the concentration of analyte in question. Due to the inherent variability between each sensor, running a calibration curve for each sensor is ideal. In order to generate a calibration curve for a given analyte, the sensor needs to be challenged with known concentrations of the analyte. For example, to generate a calibration curve for an H_2O_2 sensor, the sensor would need to be challenged with known concentrations of H_2O_2. The sensor should be tested with concentrations of analyte beginning near the sensor's limit of detection and continuing past the linear region of the curve. The range of concentrations used needs to span the linear range of the curve, as the slope provides the sensor's sensitivity (Thevenot, Toth, Durst, & Wilson, 2001). In between the addition of each subsequent concentration of analyte, the sensor should be thoroughly washed with buffer to prevent previous concentrations from contributing to the measured signal. Figure 6.3 shows a schematic representation of amperometric and voltammetric sensor responses and their subsequent calibration curves (see inset).

It is important that there are no bubbles located inside of the channel or in the tubing connecting the working electrodes to the reference electrode. Any bubble inside of the channel would disconnect the circuit and disrupt

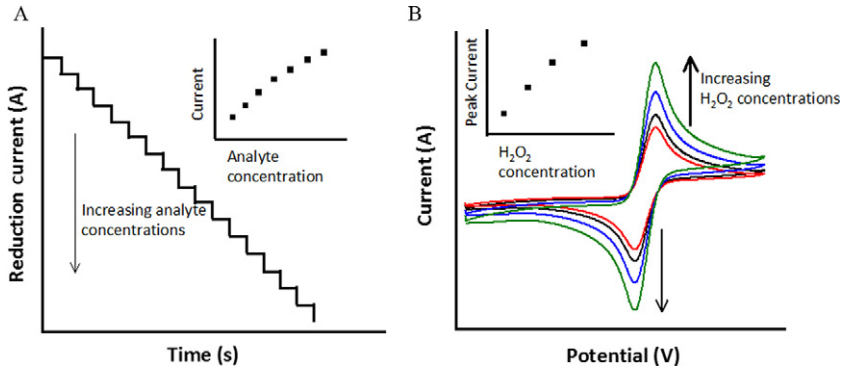

Figure 6.3 (A) Example of an amperometric response curve of an HRP-based biosensor to successive addition of H_2O_2. Inset shows the calibration plot for the biosensor. (B) Example of a voltammetric response curve of an HRP-based biosensor to successive addition of H_2O_2. Inset shows the calibration plot for the biosensor.

the signal. A sample protocol for generating a calibration curve for our electrochemical biosensor is as follows:

1. Assemble the microfluidic channels (Section 2.5) on top of the enzyme-coated electrodes.
2. Flow PBS into the channel, making sure there are no bubbles located inside of the channel.
3. Add H_2O_2 ranging from 200 n*M* to 100 μ*M* into the channel, making sure to test at least eight different concentrations.
4. Cyclic voltammograms are taken from 0.7 to −0.7 V.
5. Wash the channel twice with PBS at a flow rate of 50 μl/min to remove any residual H_2O_2 from the channel.
6. Repeat steps 3–6 for all concentrations of H_2O_2.

The data is plotted as concentration of H_2O_2 versus the change in the absolute value of the reduction current taken at −0.4 V. The reduction of the H_2O_2 occurs around −0.4 V and measuring at this potential minimizes the interference from the reduction of oxygen.

4. MONITORING ROS PRODUCTION FROM CELLS USING ELECTROCHEMISTRY

4.1. Seeding of cells into sensing device

After determining the calibration curve for a particular sensor, the chip is ready to be used in conjunction with cells. As this sensor is designed to detect

the presence of H_2O_2, any type of cell capable of producing H_2O_2, such as macrophages or hepatocytes, may be used. The cell capture region (Section 2.4) can be modified to capture the specific cell type of interest. For example, collagen may be used to capture hepatocytes, while specific antibodies can be used to capture primary blood cells. The microfluidic device is then placed atop the chip and cells are flowed into the channel and allowed to attach to the surface. The cells are then allowed to attach inside of the PEG well adjacent to the HRP-PEG-covered electrode (Fig. 6.4A and B).

4.2. Measurement of ROS production from injured cells

The PDMS microfluidic device allows for the simple introduction of stimulant to the cells. Phorbol 12-myristate 13-acetate (PMA) is commonly used to promote mitogenic production of peroxide from macrophages (Aviram, Rosenblat, Etzioni, & Levy, 1996). A heating stage or incubator should be used to keep the cells at 37 °C during the duration of the experiment. Amperometry and CV techniques have been used in our lab for detection of H_2O_2 from macrophages and hepatocytes, respectively. In a typical amperometry experiment using our device, the current is monitored at a fixed potential of −0.2 V. However, in CV experiments, cyclic voltammograms were run from 0.7 to −0.7 mV at a scan rate of 50 mV/s to measure the reduction of H_2O_2 due to its reaction with HRP. Setting the working potential between −0.2 and −0.4 V helps to minimize potential interference from biological species, including ascorbic acid, uric acid, and oxygen (Li et al., 2011; Ren et al., 2005). Time-lapse measurements were taken using a home-built multiplexer that switched between the

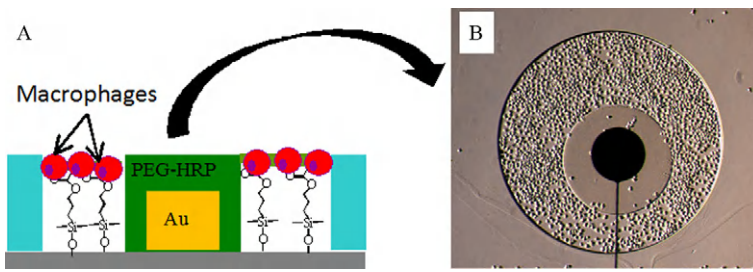

Figure 6.4 (A) Diagram showing macrophages seeded next to a PEG-HRP-covered electrode. (B) Microscopic image of macrophages attached in a PEG well next to PEG-HRP hydrogel-covered Au electrode.

different individual working electrodes at the desired time points. A sample protocol for the detection of H_2O_2 from J774 macrophages from our chip is as follows (Yan et al., 2011):

1. The HRP biosensor was fabricated as described in the previous sections.
2. J774 macrophages, cultured in DMEM, were concentrated and seeded inside of the microfluidic channel. (Since the J774 macrophages attached readily to the silane surface, further modification to promote cell attachment was not required.)
3. PBS is flowed into the channels to wash away unattached cells.
4. PMA (100 μg/ml) in serum-free DMEM is flowed into the channel to stimulate the production of H_2O_2 from the J774 macrophages.
5. Amperometric it measurements are then taken at −0.2 V for 3 h.

4.3. Quantification of H_2O_2 concentration from cells

The data obtained from the experiments are given as a current value at different time points. As with the calibration experiment, the reduction current when measuring with CV is taken at −0.4 V in order to prevent any interference from the reduction of O_2. The current measured is then compared to the initial current reading, giving a change in current at each time point. This change in current is then used in association with the calibration plot (Section 3) to produce data on the concentration of H_2O_2 at each time point.

5. SUMMARY

This chapter described the fabrication of an electrochemical biosensor utilizing HRP-PEG-covered Au electrodes for the detection of H_2O_2 from cells. The miniature Au electrodes are combined with a PDMS microfluidic device to allow for the real-time measurement of ROS produced from cells. The use of PEG allowed for cells to be seeded near, but not on top of, the electrodes, while also providing a hydrated environment to improve the stability of entrapped HRP. It is possible to adjust this protocol to detect the production of ROS from a variety of different cell types by selecting the proper cell-specific capture protein and stimulant.

REFERENCES

Amatore, C., Arbault, S., Chen, Y., Crozatier, C., & Tapsoba, I. (2007). Electrochemical detection in a microfluidic device of oxidative stress generated by macrophage cells. *Lab on a Chip*, 7(2), 233–238.

Aviram, M., Rosenblat, M., Etzioni, A., & Levy, R. (1996). Activation of NADPH oxidase is required for macrophage-mediated oxidation of low-density lipoprotein. *Metabolism, Clinical and Experimental*, *45*(9), 1069–1079.

Cheah, L. T., Dou, Y. H., Seymour, A. M., Dyer, C. E., Haswell, S. J., Wadhawan, J. D., et al. (2010). Microfluidic perfusion system for maintaining viable heart tissue with real-time electrochemical monitoring of reactive oxygen species. *Lab on a Chip*, *10*(20), 2720–2726.

Choi, D., Lee, W., Park, J., & Koh, W. (2008). Preparation of poly(ethylene glycol) hydrogels with different network structures for the application of enzyme immobilization. *Biomedical Materials and Engineering*, *18*(6), 345–356.

Dequaire, M., Limoges, B., Moiroux, J., & Saveant, J. M. (2002). Mediated electrochemistry of horseradish peroxidase. Catalysis and inhibition. *Journal of the American Chemical Society*, *124*(2), 240–253.

Fahn, S., & Cohen, G. (1992). The oxidant stress hypothesis in Parkinson's disease: Evidence supporting it. *Annals of Neurology*, *32*(6), 804–812.

Figeys, D., & Pinto, D. (2000). Lab-on-a-chip: A revolution in biological and medical sciences. *Analytical Chemistry*, *72*(9), 330a–335a.

Gunasingham, H., Teo, P. Y. T., Lai, Y. H., & Tan, S. G. (1989). Chemically modified cellulose-acetate membrane for biosensor applications. *Biosensors*, *4*(6), 349–359.

Gupta, R., & Chaudhury, N. K. (2007). Entrapment of biomolecules in sol–gel matrix for applications in biosensors: Problems and future prospects. *Biosensors & Bioelectronics*, *22*(11), 2387–2399.

Heo, J., & Crooks, R. M. (2005). Microfluidic biosensor based on an array of hydrogel-entrapped enzymes. *Analytical Chemistry*, *77*(21), 6843–6851.

Hiatt, L. A., McKenzie, J. R., Deravi, L. F., Harry, R. S., Wright, D. W., & Cliffel, D. E. (2012). A printed superoxide dismutase coated electrode for the study of macrophage oxidative burst. *Biosensors & Bioelectronics*, *33*(1), 128–133.

Koev, S. T., Dykstra, P. H., Luo, X., Rubloff, G. W., Bentley, W. E., Payne, G. F., et al. (2010). Chitosan: An integrative biomaterial for lab-on-a-chip devices. *Lab on a Chip*, *10*(22), 3026–3042.

Krylov, A. V., Adamzig, H., Walter, A. D., Lochel, B., Kurth, E., Pulz, O., et al. (2006). Parallel generation and detection of superoxide and hydrogen peroxide in a fluidic chip. *Sensors and Actuators B: Chemical*, *119*(1), 118–126.

Li, Y. M., Liu, H. H., & Pang, D. W. (2004). Direct electrochemistry and catalysis of heme-proteins entrapped in methyl cellulose films. *Journal of Electroanalytical Chemistry*, *574*(1), 23–31.

Li, C. Y., Zhang, H., Wu, P., Gong, Z. N., Xu, G. L., & Cai, C. X. (2011). Electrochemical detection of extracellular hydrogen peroxide released from RAW 264.7 murine macrophage cells based on horseradish peroxidase-hydroxyapatite nanohybrids. *Analyst*, *136*(6), 1116–1123.

Liu, S., Dai, Z., Chen, H., & Ju, H. (2004). Immobilization of hemoglobin on zirconium dioxide nanoparticles for preparation of a novel hydrogen peroxide biosensor. *Biosensors & Bioelectronics*, *19*(9), 963–969.

Mata, A., Fleischman, A. J., & Roy, S. (2005). Characterization of polydimethylsiloxane (PDMS) properties for biomedical micro/nanosystems. *Biomedical Microdevices*, *7*(4), 281–293.

Matharu, Z., Enomoto, J., & Revzin, A. (2013). Miniature enzyme-based electrodes for detection of hydrogen peroxide release from alcohol-injured hepatocytes. *Analytical Chemistry*, *85*, 932–939.

Miao, Y. Q., & Tan, S. N. (2000). Amperometric hydrogen peroxide biosensor based on immobilization of peroxidase in chitosan matrix crosslinked with glutaraldehyde. *Analyst*, *125*(9), 1591–1594.

Pedrosa, V. A., Yan, J., Simonian, A. L., & Revzin, A. (2011). Micropatterned nanocomposite hydrogels for biosensing applications. *Electroanalysis*, *23*(5), 1142–1149.

Peppas, N. A., Keys, K. B., Torres-Lugo, M., & Lowman, A. M. (1999). Poly(ethylene glycol)-containing hydrogels in drug delivery. *Journal of Controlled Release*, *62*(1–2), 81–87.

Pohanka, M., & Skladai, P. (2008). Electrochemical biosensors—Principles and applications. *Journal of Applied Biomedicine*, *6*(2), 57–64.

Qian, L., & Yang, X. (2006). Composite film of carbon nanotubes and chitosan for preparation of amperometric hydrogen peroxide biosensor. *Talanta*, *68*(3), 721–727.

Ren, C., Song, Y., Li, Z., & Zhu, G. (2005). Hydrogen peroxide sensor based on horseradish peroxidase immobilized on a silver nanoparticles/cysteamine/gold electrode. *Analytical and Bioanalytical Chemistry*, *381*(6), 1179–1185.

Rhee, S. G., Chang, T. S., Jeong, W., & Kang, D. (2010). Methods for detection and measurement of hydrogen peroxide inside and outside of cells. *Molecules and Cells*, *29*(6), 539–549.

Sarma, A. K., Vatsyayan, P., Goswami, P., & Minteer, S. D. (2009). Recent advances in material science for developing enzyme electrodes. *Biosensors & Bioelectronics*, *24*(8), 2313–2322.

Schmielau, J., & Finn, O. J. (2001). Activated granulocytes and granulocyte-derived hydrogen peroxide are the underlying mechanism of suppression of t-cell function in advanced cancer patients. *Cancer Research*, *61*(12), 4756–4760.

Shi, L., Liu, X., Niu, W., Li, H., Han, S., Chen, J., et al. (2009). Hydrogen peroxide biosensor based on direct electrochemistry of soybean peroxidase immobilized on single-walled carbon nanohorn modified electrode. *Biosensors & Bioelectronics*, *24*(5), 1159–1163.

Sirkar, K., & Pishko, M. V. (1998). Amperometric biosensors based on oxidoreductases immobilized in photopolymerized poly(ethylene glycol) redox polymer hydrogels. *Analytical Chemistry*, *70*(14), 2888–2894.

Tabner, B. J., El-Agnaf, O. M., Turnbull, S., German, M. J., Paleologou, K. E., Hayashi, Y., et al. (2005). Hydrogen peroxide is generated during the very early stages of aggregation of the amyloid peptides implicated in Alzheimer disease and familial British dementia. *Journal of Biological Chemistry*, *280*(43), 35789–35792.

Thevenot, D. R., Toth, K., Durst, R. A., & Wilson, G. S. (2001). Electrochemical biosensors: Recommended definitions and classification. *Biosensors & Bioelectronics*, *16*(1–2), 121–131.

Veal, E. A., Day, A. M., & Morgan, B. A. (2007). Hydrogen peroxide sensing and signaling. *Molecular Cell*, *26*(1), 1–14.

Wang, J. (1999). Sol–gel materials for electrochemical biosensors. *Analytica Chimica Acta*, *399*(1–2), 21–27.

Wang, J. (2005). Carbon-nanotube based electrochemical biosensors: A review. *Electroanalysis*, *17*(1), 7–14.

Wang, G., Xu, J. J., Chen, H. Y., & Lu, Z. H. (2003). Amperometric hydrogen peroxide biosensor with sol–gel/chitosan network-like film as immobilization matrix. *Biosensors & Bioelectronics*, *18*(4), 335–343.

Yadavalli, V. K., Koh, W. G., Lazur, G. J., & Pishko, M. V. (2004). Microfabricated protein-containing poly(ethylene glycol) hydrogel arrays for biosensing. *Sensors and Actuators B: Chemical*, *97*(2–3), 290–297.

Yan, J., Pedrosa, V. A., Enomoto, J., Simonian, A. L., & Revzin, A. (2011). Electrochemical biosensors for on-chip detection of oxidative stress from immune cells. *Biomicrofluidics*, *5*(3), 32008–3200811.

Zhang, S., Wright, G., & Yang, Y. (2000). Materials and techniques for electrochemical biosensor design and construction. *Biosensors & Bioelectronics*, *15*(5–6), 273–282.

Zhou, K. F., Zhu, Y. H., Yang, X. L., Luo, J., Li, C. Z., & Luan, S. R. (2010). A novel hydrogen peroxide biosensor based on Au-graphene-HRP-chitosan biocomposites. *Electrochimica Acta*, *55*(9), 3055–3060.

Zima, T., & Kalousova, M. (2005). Oxidative stress and signal transduction pathways in alcoholic liver disease. *Alcoholism, Clinical and Experimental Research*, *29*(11 Suppl.), 110S–115S.

CHAPTER SEVEN

Electrochemical Detection of H_2O_2 Formation in Isolated Mitochondria

Stefania Rapino[*], **Raluca Marcu**[*,1], **Francesco Paolucci**[†], **Marco Giorgio**[*,2]

[*]Department of Experimental Oncology, European Institute of Oncology, Milan, Italy
[†]Department of Chemistry, University of Bologna, "G. Ciamician", Bologna, Italy
[1]Present address: Mitochondria and Metabolism Center, Seattle, Washington, USA
[2]Corresponding author: e-mail address: marco.giorgio@ieo.eu

Contents

1. Introduction 124
2. The Electrochemical Chamber 124
3. The Platinized Carbon Fiber Microelectrode 126
4. Data Analysis for H_2O_2 Amperometric Measurements 126
5. H_2O_2 and O_2 Calibration Tests 128
6. Preparation of Isolated Mitochondria 129
7. Measure of H_2O_2 from Mitochondrial Suspension 130
8. Conclusions 132
Acknowledgments 133
References 134

Abstract

Mitochondrial respiration produces both complete and partially reduced oxygen species that are involved in physiological and pathological processes. Indeed, unspecific oxidative damage induced by excessive mitochondrial reactive oxygen species (ROS) plays a role in aging and several diseases, whereas low amounts of ROS act in physiological signaling processes. The exact molecular species, the rate, and the conditions of mitochondrial ROS release are not clearly evaluable by current methods based on oxidation sensitive markers. Recently, electrochemical analysis of biological samples has improved. Following latest methodology, we implemented a novel electrochemical assay for the investigation of aerobic metabolism in isolated mitochondria through simultaneous measurement of O_2 consumption and H_2O_2 production. Our experiments confirm active H_2O_2 production by respiring mouse liver mitochondria and show that ATP synthase activation increases the rate of H_2O_2, suggesting that state 3 mitochondria might induce the cell through oxidative signals.

Methods in Enzymology, Volume 526
ISSN 0076-6879
http://dx.doi.org/10.1016/B978-0-12-405883-5.00007-7

© 2013 Elsevier Inc.
All rights reserved.

ABBREVIATIONS

ETC electron transfer chain
OMEA O_2 metabolism electrochemical analyzer
PTFE polytetrafluoroethylene
ROS reactive oxygen species

1. INTRODUCTION

Incomplete reduction of O_2 during cellular metabolism generates reactive oxygen species (ROS) implicated in both physiological and pathological processes (Orrenius, Gogvadze, & Zhivotovsky, 2007; Wallace, 2005). H_2O_2, in particular, functions as signaling agent involved in growth factor/hormone/cytokine intracellular signaling, gene expression regulation, and apoptosis. Electron leakage at specific redox centers during mitochondrial electron transfer chain (ETC) reactions generates the majority of intracellular H_2O_2 (Murphy, 2009). Since the rate of mitochondrial H_2O_2 formation is modulated by O_2 availability, substrate supply, and ATP synthesis (Hoffman & Brookes, 2009; Stone & Yang, 2006), the emerging picture is that mitochondria generate H_2O_2 in a regulated manner, reflecting the metabolic activity of the cell and acting as oxygen sensor involved in the transduction of hypoxic signals (Bell et al., 2007; Hoffman, Salter, & Brookes, 2007).

Traditional assays for H_2O_2 measurement rely on fluorescent probes that lack specificity and often result in artifactual signals (Gomes, Fernandes, & Lima, 2005; Votyakova & Reynolds, 2004). Recently, reactive species produced by living cells in response to mechanical challenges have been measured directly and selectively through electrochemistry at platinized carbon microelectrodes (Amatore et al., 2008; Arbault et al., 2004). To overcome limitations of current methodologies, we implemented a novel electrochemical assay for the simultaneous evaluation of O_2 reduction metabolism and H_2O_2 production in suspensions of isolated mitochondria (Marcu et al., 2012). Here, we describe this tool and summarize the results obtained with this approach on the study of mouse liver mitochondria.

2. THE ELECTROCHEMICAL CHAMBER

Simultaneous measurements of O_2 consumption and H_2O_2 production by isolated mitochondria were performed using the "O_2 metabolism electrochemical analyzer" (OMEA) obtained by integrating an oxygraph apparatus with a system for the simultaneous detection of H_2O_2

(Hansatech Instruments, Norfolk, England) as shown schematically in Fig. 7.1A. The OMEA consists of an assay chamber bearing the Clark-type electrode for O_2 detection and the platinized carbon fiber electrode (Fig. 7.1B) used for H_2O_2 measurement. The potentials for the detection of both species (-0.7 V for O_2 and 0.6 V for H_2O_2) were supplied by two independent potentiostats. In this system, the reduction and oxidation of O_2 and H_2O_2, respectively, present in the assay chamber generate electrical currents at the detection electrodes (named shortly O_2 signal and H_2O_2 signal) that are amplified and analyzed.

The electrochemical measurement of O_2 was realized at the Clark electrode by reducing O_2 at a reduction potential of -0.7 V with respect to an Ag/AgCl reference electrode. For H_2O_2 detection, the chamber of the oxygraph was adapted in order to allocate a 10 μm platinized carbon fiber microelectrode, an Ag/AgCl reference electrode, and a Pt counter electrode. Electrochemical detection of H_2O_2 was performed by oxidizing this molecule at an oxidation potential of 0.6 V with respect to the Ag/AgCl reference electrode provided by a bipotentiostat (CH Instruments, Austin, TX). The specificity of the H_2O_2 signal was established by performing test measurement at 0.4 V.

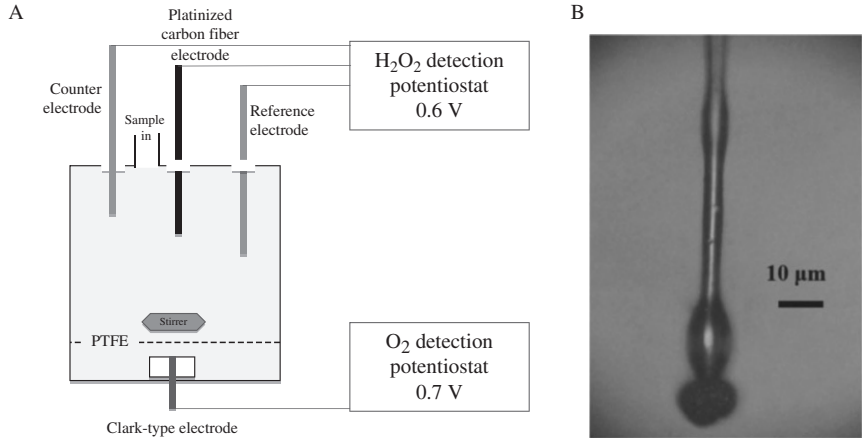

Figure 7.1 Electrochemical instrumentation for simultaneous measurement of H_2O_2 and O_2. (A) Simultaneous detection of H_2O_2 and O_2 was achieved with a two-electrode setup located in the same assay chamber. Electrochemical detection of H_2O_2 was performed with a platinized carbon fiber electrode at an oxidation potential of 0.6 V against an Ag/AgCl reference electrode (or 0.4 V for selectivity control experiments). O_2 was detected electrochemically using a Clark-type electrode at a reduction potential of -0.7 V against an Ag/AgCl reference electrode. (B) Platinized carbon fiber electrode employed for the electrochemical detection of H_2O_2: detail of the polymer and platinum depositions on the carbon fiber.

The two electrochemical cells for O_2 and H_2O_2 detection, respectively, were separated through a polytetrafluoroethylene (PTFE) membrane covering the Clark's-type electrode; the PTFE membrane is selectively permeable to O_2 so that the variation of O_2 concentration in the oxygraph chamber causes a variation of the oxygen concentration in the thin layer solution above the Clark electrode and a relative change in O_2 reduction current. The PTFE membrane assures the electrical insulation between the electrolytic solution above the Clark electrode and the oxygraph chamber solution, separating the two electrochemical cells. The modifications of H_2O_2 levels are directly measured in the oxygraph chamber as oxidation current variation at the platinized carbon fiber microelectrodes. The mixture was stirred by a magnetic bar that abolished local gradients of O_2 and H_2O_2. The chamber was isolated from the external environment through an oxygen-impermeable plastic cap, without gas phase left between the assay solution and the cap.

3. THE PLATINIZED CARBON FIBER MICROELECTRODE

For the preparation of the platinized carbon fiber microelectrodes used for the detection of H_2O_2, carbon fibers (Cytec Carbon Fibres, Greenville) were aspired inside borosilicate glass capillaries (Clark Electromedica Instruments, 1.2 mm O.D. × 0.7 mm I.D.) and then pulled with a micropipette puller (P-97, Sutter Instruments, USA) into two electrodes. The carbon fiber protruding from the glass was insulated by electrochemical deposition of a poly (oxyphenylene) polymer (Fig. 7.1B). The surface of the tip was polished by grinding on 0.3 μm alumina paper and then platinized by reducing hydrogen hexachloroplatinate in the presence of lead acetate. Notably, each measurement was performed using a single platinized carbon microelectrode that was calibrated at the end with known concentrations of H_2O_2. Before the beginning of measurements, the electrodes were left to equilibrate for 30 min in mitochondrial assay buffer.

4. DATA ANALYSIS FOR H_2O_2 AMPEROMETRIC MEASUREMENTS

Once a potential has been applied, platinized carbon fiber microelectrodes undergo an equilibration phase due to diffusion effects, slow partial oxidation, and modification of the active sites of the platinized surface.

The outcome of this equilibration process is a progressive and continuous reduction of the oxidation current registered at the electrode (Marcu et al., 2012; Fig. 7.2A).

This equilibration curve can be described by an exponential function that we used to extrapolate the baseline: $y = y_0 + A_1 \times (1 - \exp(-x/t_1)) + A_2 \times (1 - \exp(-x/t_2))$, where A_1, A_2, t_1, and t_2 are dimensionless parameters, specific for every curve, which are determined through the fitting procedure. Thus, any specific electrical event can be revealed by subtracting from the total measured signal the baseline. In particular, the addition of mitochondria induces further surface modification of the electrode that undergoes another equilibration phase which is accounted by the above fitting procedure. To isolate specific contributions to the electric signal (due to mitochondrial H_2O_2), we then subtracted the component from the overall signal due to the equilibration of the electrode. We used appropriate correction factors in order to account for the loss of sensitivity of the platinized electrode during the measurements. All fitting and mathematical procedures were performed using the origin program.

We observed that some of the substrates and drugs used to modulate mitochondrial respiration interacted with the electrode, generating an instantaneous increase or drop in the electric current at the moment they

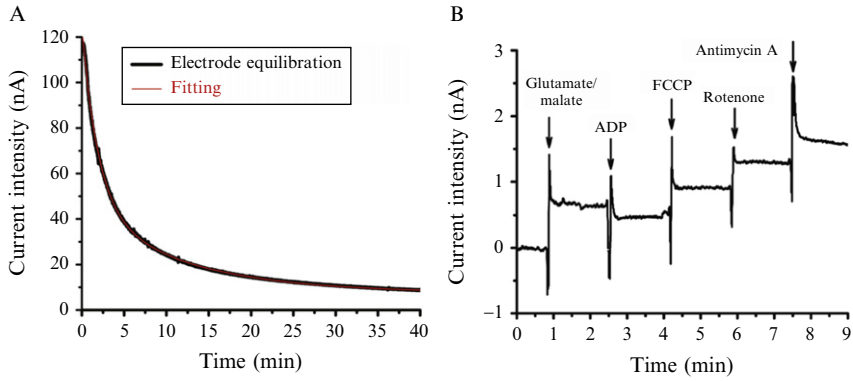

Figure 7.2 Electrode response tests. (A) Electrode equilibration. The electric signal due to the equilibration of the electrode (black line) can be normalized by fitting with an exponential function (red line). (B) Interactions with the platinized carbon electrode of various substrates and drugs used to stimulate or inhibit mitochondrial respiration. Some of the substrates and drugs used to stimulate or inhibit mitochondrial respiration interact with the electrode at the moment they are added, producing an instantaneous increase or drop in the electric current.

were added, but without other effect on the signal measured next (Fig. 7.2B). In particular, drugs dissolved in ethanol (FCCP, rotenone, antimycin, oligomycin) produce a similar increase in the oxidation current, most probably due to the oxidation and adsorption of ethanol to the platinum surface of the electrode. Other drugs, like KCN, aminotriazole, and TMPD/ascorbate, had a strong effect on the electrode that prevented us from using them during measurements.

5. H_2O_2 AND O_2 CALIBRATION TESTS

To test the sensitivity and specificity of the system, we measured H_2O_2 and O_2 signals obtained following the addition of known amounts of H_2O_2 into the assay chamber, in the absence or presence of catalase. Results, shown upon normalization in Fig. 7.3A, revealed that platinized carbon electrodes were able to detect submicromolar concentration of H_2O_2 and to provide a linear response for the entire range of concentrations tested (0.5–5 μ*M*) (Marcu et al., 2012).

The H_2O_2 signal increased after each single addition of H_2O_2, and, in the absence of catalase, remained stable and summed upon sequential

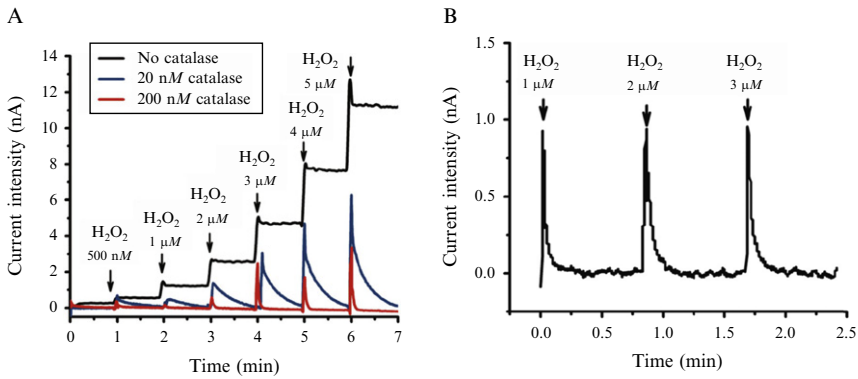

Figure 7.3 Exogenous added H_2O_2 detection. (A) Platinized carbon fiber electrodes detect submicromolar concentrations of H_2O_2 and the signal measured at the electrode is directly proportional to the concentration of H_2O_2 in the assay chamber. In the presence of different concentrations of catalase (20 n*M* catalase blue line and 200 n*M* catalase red line), single additions of H_2O_2 are rapidly scavenged as recorded by the electrode. (B) Calibration of platinized carbon electrodes with known concentrations of H_2O_2 (1, 2, and 3 μ*M*) in the presence of nonenergized mitochondria.

additions, indicating the accumulation of H_2O_2 in the assay chamber (Fig. 7.3A, black line). On the contrary, when catalase was present, while still increasing after each addition, the H_2O_2 signal was not stable in time and rapidly disappeared, reflecting the specific scavenging of H_2O_2 by catalase (Fig. 7.3A, blue line). Simultaneously, the Clark-type electrode revealed an O_2 formation rate according to a stoichiometry of 1 mol O_2 generated per 2 mol H_2O_2 degraded, in agreement with the reaction mechanism of catalases. As expected, H_2O_2 scavenging rate by catalase increased when higher concentrations of this enzyme were used (Fig. 7.3A, red line).

6. PREPARATION OF ISOLATED MITOCHONDRIA

Mitochondria were purified from mouse liver through differential centrifugations. 129Sv adult (3–6 months old) male mice were killed by cervical dislocation, and the liver was rapidly explanted and homogenized in ice-cold MTC isolation buffer (250 m*M* sucrose, 10 m*M* Tris–HCl, 1 m*M* EGTA, pH 7.4). The liver homogenate was centrifuged for 10 min at $600 \times g$ for the removal of nuclei and cell debris and the supernatant centrifuged at $7000 \times g$ for 10 min. The pellet containing the mitochondria was washed twice and finally resuspended in a minimal volume of MTC isolation buffer. All steps were performed at 4 °C. Protein concentration was measured using the Biuret method. Following experiments were performed in MTC assay buffer (125 m*M* KCl, 10 m*M* MOPS-Tris, 1 m*M* inorganic phosphate, 100 μ*M* EGTA, pH 7.4).

It is known that both inside and outside mitochondria H_2O_2 is efficiently buffered by scavenging enzymes, mainly catalases and glutathione peroxidases. Since at equilibrium OMEA electrodes showed net H_2O_2 concentration after scavenging, we verified the presence of these enzymes in our mitochondrial preparations and, as expected, we confirmed their presence by Western blotting (data not shown). Moreover, standard enzymatic activity assay measurements of total H_2O_2 scavenging together with catalase and GPx activities validated an elevated H_2O_2 scavenging activity in isolated mouse liver mitochondrial preparations. In particular, we found a catalase activity of 80 ± 0.3 U/mg proteins and a GPx activity of 0.58 ± 0.05 mU/mg proteins, respectively, suggesting a significant contribution of catalases in the scavenging process. Although these enzymes are present in mitochondrial matrix, it is likely that peroxisomal contaminations represent an important source of active catalases in preparations of isolated

mouse liver mitochondria. Indeed, testing for OMEA response to pulses of H_2O_2 in a mitochondrial suspension revealed transient H_2O_2 signals (Fig. 7.3B), indicating that catalases were actively involved in the removal of H_2O_2.

7. MEASURE OF H_2O_2 FROM MITOCHONDRIAL SUSPENSION

Addition of mitochondria into the assay chamber resulted in an H_2O_2 signal that was set to zero with respect to the electrode equilibration baseline. The following addition of energetic substrates, such as glutamate/malate or succinate, that provide electrons to complex I and complex II, respectively, of ETC stimulated stable respiration but without inducing any sensible change in the H_2O_2 signal measured by OMEA. Nevertheless, induction of state 3 respiration by addition of 200 μM ADP to mitochondria energized with either glutamate/malate or succinate, revealed by the massive and transient increase of O_2 consumption (1–1.5 min long), resulted in a synchronized increase of H_2O_2 signals (Marcu et al., 2012; Fig. 7.4A).

Despite the presence of scavenging enzymes, mainly catalase, as previously indicated, H_2O_2 accumulated in the assay chamber as long as state 3 lasted. Yet, once all ADP was phosphorylated by ATP synthase and O_2 consumption resumed to state 4 levels, the H_2O_2 signals diminished simultaneously and eventually reached levels attained prior to state 3 induction.

Notably, inhibition of ATP synthase activity with oligomycin suppressed the H_2O_2 rise induced by ADP (Fig. 7.4A, gray lines), indicating that ATP synthase activation was required for triggering H_2O_2 production observed previously. Moreover, H_2O_2 production increased as long as state 3 lasted since higher amounts of ADP prolonged both state 3 and H_2O_2 boost duration (Fig. 7.4B). Then, addition of exogenous catalase reduced the H_2O_2 peak level but not its duration (data not shown). These findings indicate that ATP synthase activity triggers an autocatalytic/self-propagating mechanism that accelerates H_2O_2 formation which progressively prevails over scavenging.

Interestingly, quantification of H_2O_2 production rate upon state 3 induction revealed a higher production of H_2O_2 when mitochondria were supplied with glutamate/malate than with succinate, despite the fact that succinate resulted in increased O_2 consumption with respect to glutamate/malate. In these conditions, the ratio of H_2O_2 production/O_2 consumption (i.e., the percentage of O_2 that is reduced partially to

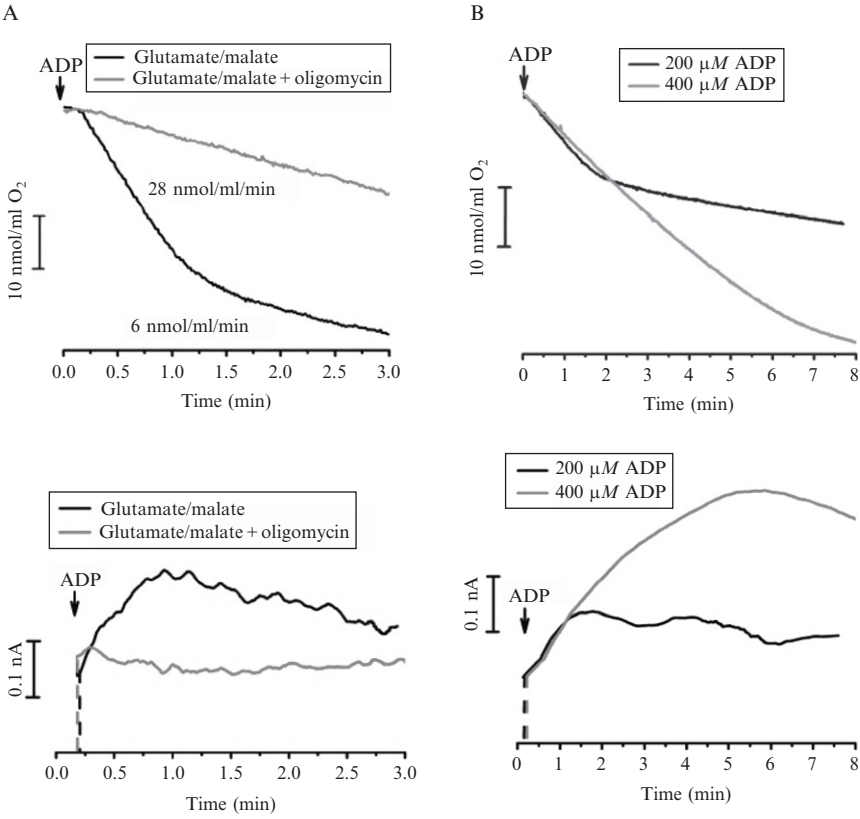

Figure 7.4 Simultaneous measurement of H_2O_2 production and O_2 consumption by isolated mouse liver mitochondria. Mitochondrial H_2O_2 production and O_2 consumption were measured simultaneously at the platinized carbon fiber electrode and Clark-type electrode, respectively. Isolated mouse liver mitochondria, 1 mg/ml, were assayed in mitochondrial assay buffer. (A) H_2O_2 production (lower panel) and respiration (upper panel) of state 3 mitochondria ± oligomycin 200 μg/ml. Where indicated by arrow 200 μ*M* ADP was added. (B) Electrochemical measurements of state 3 H_2O_2 production (lower panel) and O_2 consumption (upper panel) by mitochondria energized with 5/2.5 m*M* glutamate/malate after the addition of either 200 or 400 μ*M* ADP. The traces shown are representative of the results from six experiments each performed on different mitochondrial preparation.

H_2O_2) was higher in state 3 mitochondria that were utilizing glutamate and malate (2.46% ± 0.62) than succinate (0.38% ± 0.14). These data suggest that state 3 H_2O_2 formation does not strictly correlate with the overall amount of O_2 consumed.

8. CONCLUSIONS

OMEA allowed for the specific, sensitive, fast, and reversible measurements of aerobic metabolism. The possibility to control the electrode potential ensures the selectivity and specificity of our system for the measured species. Then, since the efficiency of O_2 reduction during aerobic metabolism is usually described as the ratio between the ROS generated by mitochondria and the total amount of O_2 reduced, it is important to obtain synchronized measurements of both H_2O_2 production and O_2 consumption at the same time.

When the mitochondrial ETC operates within the assay chamber, OMEA reveals reduction in O_2 concentration, due to active mitochondrial respiration, and formation of H_2O_2, due to partial reduction of O_2, which diffuses outside the mitochondria (see reaction scheme in Fig. 7.5).

Up to date, H_2O_2 production in living samples has been investigated only indirectly, mostly by virtue of its oxidative effects on endogenous molecules or exogenously added synthetic markers. Experiments using such approaches described reduced ROS formation from state 3 and uncoupled mitochondria (Korshunov, Skulachev, & Starkov, 1997; Starkov & Fiskum, 2003), while supporting the idea that hyperpolarization favors electron leakage from ETC. Nevertheless, other evidence indicates that ROS production is associated with transient mitochondrial depolarization.

How ATP synthase activation affects the rate of partial reduction of O_2 by ETC redox centers is unclear. It has already been shown that several processes can modulate the rate of electron leakage from ETC, including mitochondrial membrane potential (Starkov & Fiskum, 2003), membrane fluidity (Schonfeld & Wojtczak, 2008), and conformational changes in proteins of the ETC (Batandier, Leverve, & Fontaine, 2004). Recent data indicate that supramolecular organization of respiratory complexes into supercomplexes (respirasomes) favors the optimal functioning of mitochondria with possible effects also on mitochondrial ROS production (Frenzel, Rommelspacher, Sugawa, & Dencher, 2010; Wittig & Schagger, 2009). An interesting hypothesis could be that membrane depolarization associated with ATP synthesis or conformational changes occurring to FoF1-ATPase during ADP phosphorylation modify the architecture of complex I/III supercomplex, altering its reactivity toward O_2 and favoring ROS production through a mechanism that competes efficiently with scavenging. Regardless of its molecular basis, ATP synthase-synchronized ROS production above the scavenging fence may be relevant

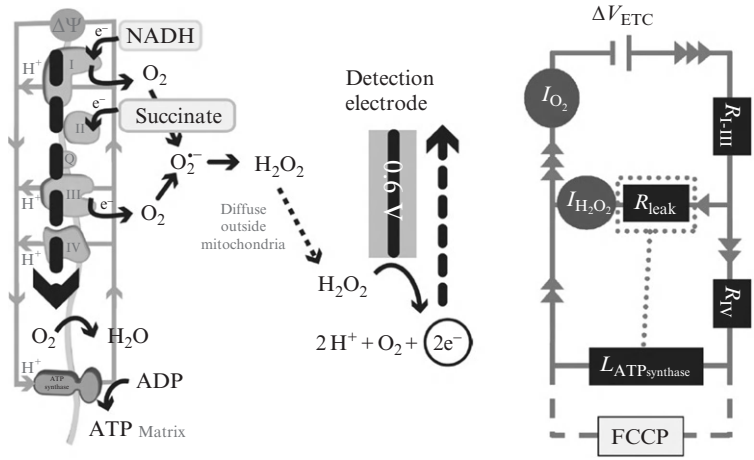

Figure 7.5 Electrochemical detection of mitochondrial H_2O_2. (A) Incomplete reduction of O_2 during electron transfer reactions at complex I and III of mitochondrial ETC leads to the formation of $O_2^{\cdot-}$ on both sides of inner mitochondrial membrane. $O_2^{\cdot-}$ is quickly dismutated by SODs into H_2O_2 that is either degraded inside mitochondria by glutathione peroxidases, peroxiredoxins, and catalases or diffused outside mitochondria being removed by extramitochondrial scavenging enzymes. The efflux of mitochondrial H_2O_2 that escapes buffering is measured through amperometric assays. (B) Electrical equivalent circuit, "orthogonal" to the proton circuit shown on the left, schematically representing the circulation of electrons in the ETC. The model includes (i) the source of electron motive force (emf $= \Delta V_{ETC}$) associated to the respiratory chain, (ii) sinks of emf (R_{I-III} and R_{IV}) associated to the internal electron transfer resistances of respiratory chain complexes and mediators, (iii) a load (L_{ATPase}) that corresponds to ATP synthase-controlled intermembrane H^+ pumping, and (iv) an electron leak pathway represented by a (variable) resistance R_{leak}. This resistance, and hence the amount of H_2O_2-generating current, receives a feedback control by the ATP synthase activity (dotted line). Two measurement gages (amperometers) are fitted in the circuit and correspond to the two amperometric devices used to measure simultaneously the total current I_{O_2} (coupled to O_2 consumption) and the leak current $I_{H_2O_2}$ (coupled to electron leaking from the respiratory chain). Also shown in the circuit is the alternative current pathway which, upon the addition of protonophore FCCP, bypasses the ATP synthase-associated load.

if occurring *in vivo* since this event can be linked to both physiological oscillating (Zorov, Juhaszova, & Sollott, 2006) and pathological acute ROS generating processes.

ACKNOWLEDGMENTS

This research was supported by the Fondazione Umberto Veronesi (FUV), the European School of Molecular Medicine (SEMM), MIUR University of Bologna, and Fondazione CARISBO.

REFERENCES

Amatore, C., Arbault, S., Bouton, C., Drapier, J. C., Ghandour, H., & Koh, A. C. (2008). Real-time amperometric analysis of reactive oxygen and nitrogen species released by single immunostimulated macrophages. *ChemBioChem*, *9*, 1472–1480.

Arbault, S., Sojic, N., Bruce, D., Amatore, C., Sarasin, A., & Vuillaume, M. (2004). Oxidative stress in cancer prone xeroderma pigmentosum fibroblasts. Real-time and single cell monitoring of superoxide and nitric oxide production with microelectrodes. *Carcinogenesis*, *25*, 509–515.

Batandier, C., Leverve, X., & Fontaine, E. (2004). Opening of the mitochondrial permeability transition pore induces reactive oxygen species production at the level of the respiratory chain complex I. *Journal of Biological Chemistry*, *279*, 17197–17204.

Bell, E. L., Klimova, T. A., Eisenbart, J., Moraes, C. T., Murphy, M. P., Budinger, G. R., et al. (2007). The Qo site of the mitochondrial complex III is required for the transduction of hypoxic signaling via reactive oxygen species production. *The Journal of Cell Biology*, *177*, 1029–1036.

Frenzel, M., Rommelspacher, H., Sugawa, M. D., & Dencher, N. A. (2010). Ageing alters the supramolecular architecture of OxPhos complexes in rat brain cortex. *Experimental Gerontology*, *45*, 563–572.

Gomes, A., Fernandes, E., & Lima, J. L. (2005). Fluorescence probes used for detection of reactive oxygen species. *Journal of Biochemical and Biophysical Methods*, *65*, 45–80.

Hoffman, D. L., & Brookes, P. S. (2009). Oxygen sensitivity of mitochondrial reactive oxygen species generation depends on metabolic conditions. *Journal of Biological Chemistry*, *284*, 16236–16245.

Hoffman, D. L., Salter, J. D., & Brookes, P. S. (2007). Response of mitochondrial reactive oxygen species generation to steady-state oxygen tension: Implications for hypoxic cell signaling. *American Journal of Physiology. Heart and Circulatory Physiology*, *292*, H101–H108.

Korshunov, S. S., Skulachev, V. P., & Starkov, A. A. (1997). High protonic potential actuates a mechanism of production of reactive oxygen species in mitochondria. *FEBS Letters*, *416*, 15–18.

Marcu, R., Rapino, S., Trinei, M., Valenti, G., Marcaccio, M., Pelicci, P. G., et al. (2012). Electrochemical study of hydrogen peroxide formation in isolated mitochondria. *Bioelectrochemistry*, *85*, 21–28.

Murphy, M. P. (2009). How mitochondria produce reactive oxygen species. *Biochemical Journal*, *417*, 1–13.

Orrenius, S., Gogvadze, V., & Zhivotovsky, B. (2007). Mitochondrial oxidative stress: Implications for cell death. *Annual Review of Pharmacology and Toxicology*, *47*, 143–183.

Schonfeld, P., & Wojtczak, L. (2008). Fatty acids as modulators of the cellular production of reactive oxygen species. *Free Radical Biology & Medicine*, *45*, 231–241.

Starkov, A. A., & Fiskum, G. (2003). Regulation of brain mitochondrial H_2O_2 production by membrane potential and NAD(P)H redox state. *Journal of Neurochemistry*, *86*, 1101–1107.

Stone, J. R., & Yang, S. (2006). Hydrogen peroxide: A signaling messenger. *Antioxidants & Redox Signaling*, *8*, 243–270.

Votyakova, T. V., & Reynolds, I. J. (2004). Detection of hydrogen peroxide with Amplex Red: Interference by NADH and reduced glutathione auto-oxidation. *Archives of Biochemistry and Biophysics*, *431*, 138–144.

Wallace, D. C. (2005). A mitochondrial paradigm of metabolic and degenerative diseases, aging, and cancer: A dawn for evolutionary medicine. *Annual Review of Genetics*, *39*, 359–407.

Wittig, I., & Schagger, H. (2009). Supramolecular organization of ATP synthase and respiratory chain in mitochondrial membranes. *Biochimica et Biophysica Acta*, *1787*, 672–680.

Zorov, D. B., Juhaszova, M., & Sollott, S. J. (2006). Mitochondrial ROS-induced ROS release: An update and review. *Biochimica et Biophysica Acta*, *1757*, 509–517.

CHAPTER EIGHT

Detection of H_2O_2 by Fluorescence Correlation Spectroscopy

Etsuro Ito[*,1], Satoshi Watabe[†], Mika Morikawa[*], Hiromi Kodama[*], Ryuichi Okada[*], Toshiaki Miura[‡]

[*]Kagawa School of Pharmaceutical Sciences, Tokushima Bunri University, Sanuki, Japan
[†]BL Co., Ltd., Numazu, Japan
[‡]Graduate School of Pharmaceutical Sciences, Hokkaido University, Sapporo, Japan
[1]Corresponding author: e-mail address: eito@kph.bunri-u.ac.jp

Contents

1. Introduction 136
2. Experimental Methods 137
   2.1 FCS measurement 137
   2.2 Analysis of the limit value of detection and the minimum value of determination 139
   2.3 Detection of H_2O_2 concentrations 139
   2.4 Detection of glucose concentrations 139
   2.5 Detection of glucose in human blood plasma 140
3. Comparison of Sensitivity Between the FCS-Based Method and an Amplex Red-Based Method 140
   3.1 Comparison of H_2O_2 concentrations between the FCS-based method and an Amplex Red-based method 140
   3.2 Comparison of glucose concentrations in buffer and glucose concentrations in human blood plasma between the FCS-based method and an Amplex Red-based method 141
4. Conclusion 141
Acknowledgments 142
References 142

Abstract

Fluorescence correlation spectroscopy (FCS) is a technique in which measurement of fluorescence intensity fluctuations is used to clarify dynamic molecular interactions within a very small space in a solution containing a small number of fluorescent molecules. The FCS-based analysis gives the average number and average diffusion time of the fluorescent molecules during their passage through a very small space. One advantage of FCS is that physical separation between free and bound fluorescent probes is not required because the properties of fluorescence fluctuations are accounted for. Therefore, when fluorescent probes are bound with proteins by peroxidase and hydrogen peroxide (H_2O_2), FCS enables us to detect H_2O_2 with high sensitivity. In

Methods in Enzymology, Volume 526
ISSN 0076-6879
http://dx.doi.org/10.1016/B978-0-12-405883-5.00008-9

© 2013 Elsevier Inc.
All rights reserved.

addition, because H_2O_2 is generated by oxidase-catalyzed reactions, a highly sensitive method for detecting H_2O_2 is applicable to the measurement of low levels of various oxidases and their substrates, such as glucose. We here describe the protocol of a *de novo*, highly sensitive method for the measurement of H_2O_2 and glucose using FCS.

1. INTRODUCTION

Fluorescence correlation spectroscopy (FCS) is a technique in which spontaneous fluorescence intensity fluctuations are measured in a microscopic detection volume of about 10^{-15} L (1 fL) defined by a tightly focused laser beam (Kim, Heinze, & Schwille, 2007). In recent years, there has been renewed interest in FCS and its derivative methodologies due to the fact that it is inherently miniaturized and therefore applicable for biological applications (Nomura, Nakamura, Feng, & Kinjo, 2007; Sadamoto, Saito, Muto, Kinjo, & Ito, 2011). Fluorescence intensity fluctuations measured by FCS represent changes in either the number or the fluorescence quantum yield of molecules resident in the detection volume (Fig. 8.1). When a fluorescent probe of low molecular weight binds to protein in sample solution, the slow-diffusing component (the protein labeled with fluorescent probes) increases with the decrease in the fast-diffusing component (the fluorescent probe), which affects the fluorescence autocorrelation curve in FCS.

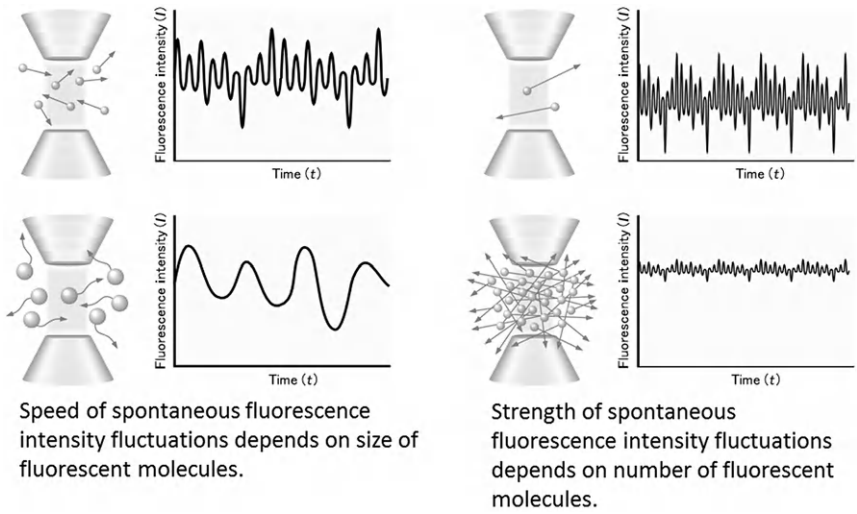
Fluorescence intensity (I)
Time (t)
Fluorescence intensity (I)
Time (t)
Fluorescence intensity (I)
Time (t)
Fluorescence intensity (I)
Time (t)
Speed of spontaneous fluorescence intensity fluctuations depends on size of fluorescent molecules.
Strength of spontaneous fluorescence intensity fluctuations depends on number of fluorescent molecules.

Figure 8.1 Spontaneous fluorescence intensity fluctuations.

The fluorescence autocorrelation curve is obtained after the fluctuations are recorded as a function of time and statistically analyzed by autocorrelation analysis.

This situation is in marked contrast to conventional fluorescence photometry, which is carried out in sample volumes of around 0.1–1.0 mL (about 10^{12} times larger than FCS measurement volumes) and provides only the macroscopic average of diffusion-dependent intensity fluctuations. In a typical FCS measurement, the fluorescence intensity is recorded for a small number of molecules in the detection volume (e.g., a few molecules/fL, equivalent to an approximately nanomolar concentration) over a time range from about 1 μs to 1 s. That is, even though FCS does not require physical separation between free and bound fluorescent probes, it enables us to detect the molecules at a nanomolar level.

The importance, from numerous viewpoints, of detecting very low levels of hydrogen peroxide (H_2O_2) will be reported in other chapters. In addition, because H_2O_2 is generated by an oxidase-mediated reaction, its detection becomes a basis for the assay of various oxidases and their substrates, such as glucose, lactate, glutamate, urate, xanthine, choline, cholesterol, and NADPH (Hu & Zhang, 2008; Luo et al., 2010; Nagaraja, Shivakumar, & Shrestha, 2009; Zhou, Diwu, Panchuk-Voloshina, & Haugland, 1997). The determination of β-D-glucose is important in the area of industrial quality control and processing applications as well as in clinical diagnosis and treatment of diabetes (Boren & Clarke, 2010; Pravda et al., 1995; Tonyushkina & Nichols, 2009). Thus, we recently developed a highly sensitive method for the determination of glucose by coupling the FCS method with glucose oxidase (GOD)-catalyzed oxidation of glucose (Watabe et al., 2011). In this chapter, we briefly introduce the methods of detection of H_2O_2 and glucose by FCS.

2. EXPERIMENTAL METHODS

2.1. FCS measurement

To develop a highly sensitive method for the assay of H_2O_2 by FCS, we used tyramide labeled with tetramethyl rhodamine (tyramide-TMR) as a fluorescent probe and bovine serum albumin (BSA) as a protein. Tyramide labeled with fluorescent probes has been utilized as a reporter fluorescent substrate for horseradish peroxidase (HRP)-catalyzed deposition (CARD), which is a signal amplification technique in immunoassay and *in situ* hybridization of nucleic acids (Bobrow, Harris, Shaughnessy, & Litt, 1989; Speel,

Hopman, & Komminoth, 1999). Similar to tyramine and tyrosine (Gross & Sizer, 1959; Tang et al., 2006; Zaitsu & Ohkura, 1980), the tyramide gives 2,2′-dihydroxydiphenyl derivatives via tyramide radicals in the HRP-catalyzed oxidation with H_2O_2 when it is present at high concentrations. However, when applied at lower concentrations in the presence of BSA, the tyramide radical binds to electron-rich moiety of BSA, such as a tyrosine residue, to give TMR-labeled BSA (Speel et al., 1999), as shown in Fig. 8.2. In the FCS experiments, when the H_2O_2 concentrations were increased, the amount of tyramide-TMR decreased while the amount of tyramide-TMR–BSA increased.

The FCS that we used consisted of an LD-excitation solid-state laser (maximum power = 1 mW) and a water immersion objective (40×, NA = 1.15). The excitation wavelength was 532 nm, and emissions were detected at 565 nm. The confocal pinhole diameter was adjusted to 25 μm. The sample volume was 500 μL. The diffusion time (τ_{free}) of tyramide-TMR was obtained from experiments with 0 μ*M* H_2O_2 solution or 0 μ*M* glucose solution, and this diffusion time was fixed throughout the FCS measurements. The diffusion time (τ_{bound}) of tyramide-TMR–BSA was obtained from experiments with 12.5 μ*M* H_2O_2 solution or 50.0 μ*M*

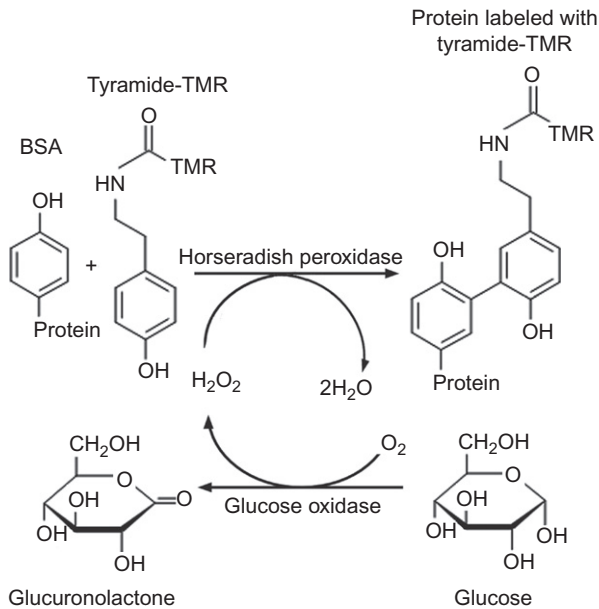

Figure 8.2 Scheme of the enzymatic reaction for detection of H_2O_2 and glucose by FCS.

glucose solution, and this time was also fixed throughout the FCS measurements. For experiments with human plasma, both the diffusion time (τ_{free}) of tyramide-TMR and the diffusion time (τ_{bound}) of tyramide-TMR–BSA were set to be the same as the values for glucose solution.

2.2. Analysis of the limit value of detection and the minimum value of determination

All the experimental data were obtained by subtracting the mean value of blank signals from each of the corresponding measured values. The limit value of detection was obtained as $3 \times$ (standard deviation of blank signals)/(slope of a regression line for experimental data), and the minimum value of determination was obtained as $10 \times$ (standard deviation of blank signals)/(slope of a regression line for experimental data).

2.3. Detection of H_2O_2 concentrations

The reaction solution consisted of 0.001% P-10, 10 n*M* tyramide-TMR, 2 mg/mL BSA, and 3 U/mL HRP in 100 m*M* Tris buffer (pH 7.5). P-10 was a detergent for the suppression of binding between tyramide-TMR and reaction tubes. The protocol was as follows:

1. Add 20 μL of various concentrations of H_2O_2 solution (0, 0.2, 0.25, 0.5, 2.0, 2.5, 5.0, 7.5, and 12.5 μ*M*) to the reaction solution of 480 μL.
2. Incubate the solution in a chambered coverslip of FCS at room temperature for 20 min.
3. Perform the measurements by FCS three times for each concentration of the H_2O_2 solution.

2.4. Detection of glucose concentrations

The reaction solution consisted of 0.001% P-10, 10 n*M* tyramide-TMR, 2 mg/mL BSA, 5 U/mL HRP, and 5 U/mL GOD in 100 m*M* Tris buffer (pH 7.5). The protocol was as follows:

1. Add 20 μL of various concentrations of glucose solution (0, 0.50, 0.75, 1.25, 2.50, 10.0, 20.0, 25.0, 30.0, 37.5, and 50.0 μ*M*) to the reaction solution of 480 μL.
2. Incubate the solution in a chambered coverslip of FCS at room temperature for 30 min.
3. Perform the measurements by FCS three times for each concentration of the H_2O_2 solution.

2.5. Detection of glucose in human blood plasma

The reaction solution was the same as that for glucose described in Section 2.4. Human blood plasma was purchased commercially. The plasma solutions were prepared by dilution with distilled water by a factor of 200, 400, 500, 1000, 1600, and 2000. The protocol was as follows:

1. Add 20 μL of various concentrations of plasma solution to the reaction solution of 480 μL.
2. Incubate the solution in a chambered coverslip of FCS at room temperature for 30 min.
3. Perform the measurements by FCS three times for each concentration of the H_2O_2 solution.

3. COMPARISON OF SENSITIVITY BETWEEN THE FCS-BASED METHOD AND AN AMPLEX RED-BASED METHOD

3.1. Comparison of H_2O_2 concentrations between the FCS-based method and an Amplex Red-based method

Many methods are now available for the assay of H_2O_2 in biological samples. They include spectrophotometry, fluorometry, chemiluminescence, and electrochemistry (Harpe & Nathan, 1985; Hu & Zhang, 2008; Hwang & Dasgupta, 1985; Luo et al., 2010; Nagaraja et al., 2009; Zaitsu & Ohkura, 1980; Zhou et al., 1997). Due to its low background fluorescence, HRP-catalyzed oxidation of 10-acetyl-3,7-dihidroxyphenoxazine (Amplex Red) with H_2O_2, which forms a highly fluorescent resorfin ($\lambda_{ex} = 563$ nm; $\lambda_{em} = 587$ nm), has been extensively utilized for the assay of low concentrations of H_2O_2 in biological samples. However, its limit value of detection for H_2O_2 is 50 n*M* (Serrano et al., 2009; Zhou et al., 1997). For a comparison with the present method, we used Amplex Red for the measurements of H_2O_2 and glucose. We measured the absorbance at 571 nm using a multimode microplate reader.

In the FCS method, a linear relation between the H_2O_2 concentration and the amount of tyramide-TMR–BSA (i.e., the existence ratio of tyramide-TMR–BSA) was obtained in the range of 28–300 n*M* H_2O_2 with a limit value of detection of 8 n*M*. When using the Amplex Red method, we found that the limit value of detection was 19 n*M* and that the range of determination was 65 n*M* to 1 μ*M*. That is, the sensitivity of the present method using FCS was slightly better than that of the method using Amplex

Red, based on the limit value of detection and the minimum value of determination for H_2O_2.

3.2. Comparison of glucose concentrations in buffer and glucose concentrations in human blood plasma between the FCS-based method and an Amplex Red-based method

In the FCS method, a linear relation between glucose concentrations and the amount of tyramide-TMR–BSA (i.e., the existence ratio of tyramide-TMR–BSA) was obtained in the range of 80 n*M* to 1.5 μ*M* glucose with a detection limit of 24 n*M*. In contrast, the Amplex Red method showed a limit value of detection of 2 μ*M* and a range of determination of 6–50 μ*M*. That is, the limit value of detection and the minimum value of determination for glucose in the FCS system were at least two orders of magnitude more sensitive than in the Amplex Red method.

In the case of human blood plasma, the limit value of detection was obtained by using plasma diluted at 0.2×10^{-4} in the FCS method. The range of determination was between that for plasma diluted at 0.4×10^{-4} and that for plasma diluted at 2.0×10^{-4}. As a result, the glucose concentrations in human blood plasma were estimated to be 4.0, 5.4, and 5.4 m*M* for plasma diluted at 0.4, 1.0, and 2.0×10^{-4}, respectively. The average value of 4.9 m*M* is in good agreement with the range of values (3.9–6.1 m*M*) presented in the textbook of physiology (Tortora & Derrickson, 2006). In addition, it is noteworthy that the FCS method needs only 20 nL plasma for this determination. That is, only about 40 nL is needed as a blood sample. Although the reasons are not entirely clear, the Amplex Red method could not detect the glucose concentrations in human blood plasma correctly.

4. CONCLUSION

A current priority is the development of simple and rapid methods that facilitate reproducible determination of various species at low concentrations (Kotzian, Brázdilová, Kalcher, & Vytřas, 2005). In the present study, we applied FCS to detect and determine H_2O_2 and glucose at low concentrations. The FCS method is versatile because it uses a commercially available fluorescent probe, but not radioisotopes or other special chemicals. We thus succeeded in determining glucose concentrations by the detection of H_2O_2 generated from the GOD-catalyzed oxidation of glucose. The limit value of detection and the minimum value of determination for glucose

were found to be at least two orders of magnitude more sensitive than with the Amplex Red method.

We should also note that we need only a small amount of blood (i.e., tens of nL) to determine the glucose concentration in blood. This means that the FCS method has the advantage of reducing the biopsy burden for patients. For example, when using alcohol oxidase, it would be possible to detect the blood alcohol concentration using only a small sample of blood.

ACKNOWLEDGMENTS

This work was partly funded by a research grant of the "New Regional Consortium Research and Development Project" from the Ministry of Economy, Trade, and Industry of Japan and the Hokkaido Bureau of Economy, Trade, and Industry and a research grant of the "Knowledge Cluster Initiative (2009)" from the Ministry of Education, Culture, Sports, Science, and Technology of Japan.

REFERENCES

Bobrow, M. N., Harris, T. D., Shaughnessy, K. J., & Litt, G. J. (1989). Catalyzed reporter deposition, a novel method of signal amplification. Application to immunoassays. *Journal of Immunological Methods*, *125*, 279–285.

Boren, S. A., & Clarke, W. L. (2010). Analytical and clinical performance of blood glucose monitors. *Journal of Diabetes Science and Technology*, *4*, 84–97.

Gross, A. J., & Sizer, I. W. (1959). The oxidation of tyramine, tyrosine, and related compounds by peroxidase. *Journal of Biological Chemistry*, *234*, 1611–1614.

Harpe, J. D., & Nathan, C. F. (1985). A semi-automated micro-assay for H_2O_2 release by human blood monocytes and mouse peritoneal macrophages. *Journal of Immunological Methods*, *78*, 323–336.

Hu, Y., & Zhang, Z. (2008). Determination of free cholesterol based on a novel flow-injection chemiluminescence method by immobilizing enzyme. *Luminescence*, *23*, 338–343.

Hwang, H., & Dasgupta, P. K. (1985). Fluorimetric determination of trace hydrogen peroxide in water with a flow injection system. *Analytica Chimica Acta*, *170*, 347–352.

Kim, S. A., Heinze, K. G., & Schwille, P. (2007). Fluorescence correlation spectroscopy in living cells. *Nature Methods*, *4*, 963–973.

Kotzian, P., Brázdilová, P., Kalcher, K., & Vytřas, K. (2005). Determination of hydrogen peroxide, glucose and hypoxanthine using (bio) sensors based on ruthenium dioxide-modified screen-printed electrodes. *Analytical Letters*, *38*, 1099–1113.

Luo, W., Li, Y. S., Yuan, J., Zhu, L., Liu, Z., Tang, H., et al. (2010). Ultrasensitive fluorometric determination of hydrogen peroxide and glucose by using multiferroic $BiFeO_3$ nanoparticles as a catalyst. *Talanta*, *81*, 901–907.

Nagaraja, P., Shivakumar, A., & Shrestha, A. K. (2009). Quantification of hydrogen peroxide and glucose using 3-methyl-2-benzothiazolinonehydrazone hydrochloride with 10,11-dihydro-5H-benz(b,f)azepine as chromogenic probe. *Analytical Biochemistry*, *395*, 231–236.

Nomura, Y., Nakamura, T., Feng, Z., & Kinjo, M. (2007). Direct quantification of gene expression using fluorescence correlation spectroscopy. *Current Pharmaceutical Biotechnology*, *8*, 286–290.

Pravda, M., Adeyoju, O., Iwuoha, E. I., Vos, J. G., Smyth, M. R., & Vytras, K. (1995). Amperometric glucose biosensors based on an osmium ($2^+/3^+$) redox polymer-mediated electron transfer at carbon paste electrodes. *Electroanalysis*, *7*, 619–625.

Sadamoto, H., Saito, K., Muto, H., Kinjo, M., & Ito, E. (2011). Direct observation of dimerization between different CREB1 isoforms in a living cell. *PLoS One*, *6*, e20285.

Serrano, J., Jové, M., Boada, J., Bellmunt, M. J., Pamplona, R., & Portero-Otín, M. (2009). Dietary antioxidants interfere with Amplex Red-coupled-fluorescence assays. *Biochemical and Biophysical Research Communications*, *388*, 443–449.

Speel, E. J. M., Hopman, A. H. N., & Komminoth, P. (1999). Amplification methods to increase the sensitivity of in situ hybridization: Play CARD(S). *Journal of Histochemistry and Cytochemistry*, *47*, 281–288.

Tang, B., Wang, Y., Liang, H., Chen, Z., He, X., & Shen, H. (2006). Studies on the oxidation reaction of tyrosine (Tyr) with H_2O_2-catalyzed by horseradish peroxidase (HRP) in alcohol-water medium by spectrofluorimetry and differential spectrophotometry. *Spectrochimica Acta Part A*, *63*, 609–613.

Tonyushkina, K., & Nichols, J. H. (2009). Glucose meters: A review of technical challenges to obtaining accurate results. *Journal of Diabetes Science and Technology*, *3*, 971–980.

Tortora, G. J., & Derrickson, B. (2006). Appendix C5. *Principles of anatomy and physiology*. (11th ed.). Hoboken, NJ: John Wiley & Sons.

Watabe, S., Sakamoto, Y., Morikawa, M., Okada, R., Miura, T., & Ito, E. (2011). Highly sensitive determination of hydrogen peroxide and glucose by fluorescence correlation spectroscopy. *PLoS One*, *6*, e22955.

Zaitsu, K., & Ohkura, Y. (1980). New fluorogenic substrates for horseradish peroxidase: Rapid and sensitive assays for hydrogen peroxide and peroxidase. *Analytical Biochemistry*, *109*, 109–113.

Zhou, M., Diwu, Z., Panchuk-Voloshina, N., & Haugland, R. P. (1997). A stable nonfluorescent derivative of resorfin for the fluorometric determination of trace hydrogen peroxide: Applications in detecting the activity of phagocyte NADPH oxidase and other oxidases. *Analytical Biochemistry*, *253*, 162–168.

CHAPTER NINE

Real-Time Monitoring of Reactive Oxygen and Nitrogen Species in a Multiwell Plate Using the Diagnostic Marker Products of Specific Probes

Jacek Zielonka[*], **Joy Joseph**[*], **Adam Sikora**[*,†], **Balaraman Kalyanaraman**[*,1]

[*]Department of Biophysics and Free Radical Research Center, Medical College of Wisconsin, Milwaukee, Wisconsin, USA
[†]Institute of Applied Radiation Chemistry, Lodz University of Technology, Lodz, Poland
[1]Corresponding author: e-mail address: balarama@mcw.edu

Contents

1. Introduction 146
2. Experimental Methods 148
   2.1 Assay plate layout 148
3. Results and Discussion 148
   3.1 HPLC analyses of HE-derived products 148
   3.2 HPLC analyses of CBA-derived products 151
   3.3 HPLC analyses of DAF-2-derived products 153
   3.4 HPLC analyses of *ortho*-Mito-PhB$(OH)_2$-derived products 154
4. Summary 156
Acknowledgments 156
References 156

Abstract

Developing rigorous assays for cellular detection of reactive oxygen and nitrogen species ($O_2^{\cdot-}$, H_2O_2, $^{\cdot}NO$, and $ONOO^-$) is an active area of research in our laboratory. Published reports suggest that diagnostic marker products are formed as a result of interaction of these species with small molecular weight fluorescent and non-fluorescent probes. In this chapter, we describe an HPLC-based methodology to detect formation of these species in biological and cellular systems. By monitoring the diagnostic marker products formed from reaction between specific chemical probes and the oxidant species, it is possible to simultaneously assay these species using a multiwell plate (e.g., 384-well plate).

Methods in Enzymology, Volume 526
ISSN 0076-6879
http://dx.doi.org/10.1016/B978-0-12-405883-5.00009-0

© 2013 Elsevier Inc.
All rights reserved.

1. INTRODUCTION

The purpose of this article is to demonstrate the feasibility of using a diagnostic marker-based high-throughput methodology for detecting reactive oxygen and nitrogen species (ROS/RNS) [e.g., superoxide ($O_2^{\cdot-}$), hydrogen peroxide (H_2O_2), nitric oxide ($^{\cdot}NO$), peroxynitrite ($ONOO^-$)] in a multiwell (96-well, 384-well) plate format. The main methodology to be used is HPLC or UHPLC with absorption and fluorescence detection or in combination with mass spectrometry. The chemical probes to be used are hydroethidine (HE) for $O_2^{\cdot-}$, coumarin boronate (CBA) for H_2O_2 and $ONOO^-$, diaminofluorescein (DAF-2) for $^{\cdot}NO$, and *ortho*-triphenylphosphonium-substituted phenylboronate [*o*-Mito-PhB$(OH)_2$] for specific detection of $ONOO^-$. The structures of the probes and diagnostic marker products derived from them as a result of interaction with specific ROS/RNS are shown in Fig. 9.1. Previously, we described a similar experimental design in which the initial screening of these species was performed using fluorescent probes (HE, CBA, DAF-2, and Amplex Red) in a 96-well plate by real-time monitoring increase in fluorescence intensity using a plate reader (Zielonka, Sikora, Hardy, Joseph, Dranka, & Kalyanaraman, 2012; Zielonka, Zielonka et al., 2012). We recommended the use of HPLC-based analyses to further confirm and rigorously identify the specific products formed from the fluorogenic probes.

Recently, significant advances have been made with regard to reaction mechanisms (rate constants, stoichiometry, and product characterization) of $O_2^{\cdot-}$, H_2O_2, $ONOO^-$, and $^{\cdot}NO$ with fluorogenic dyes that have infused increased confidence, rigor, and reliability in ROS/RNS assays (Michalski, Zielonka, Hardy, Joseph, & Kalyanaraman, 2013; Robinson et al., 2006; Sikora et al., 2011; Sikora, Zielonka, Lopez, Joseph, & Kalyanaraman, 2009; Zhao et al., 2005, 2003; Zielonka, Sikora, et al., 2012; Zielonka, Vasquez-Vivar, & Kalyanaraman, 2008; Zielonka, Zielonka, et al., 2012). For example, the long-held notion that $O_2^{\cdot-}$ reacts with HE to form ethidium (E^+) has been debunked; instead, the only major product of the reaction between HE and $O_2^{\cdot-}$ was identified as 2-hydroxyethidium (2-OH-E^+) (Zhao et al., 2003, 2005). Other oxidants ($ONOO^-$-derived oxidants including $^{\cdot}OH$, and higher oxidants derived from peroxidases) react with HE to form other oxidation products (E^+, and dimeric products), all of which can be readily separated and identified by HPLC and mass spectrometry (Zhao et al., 2005; Zielonka,

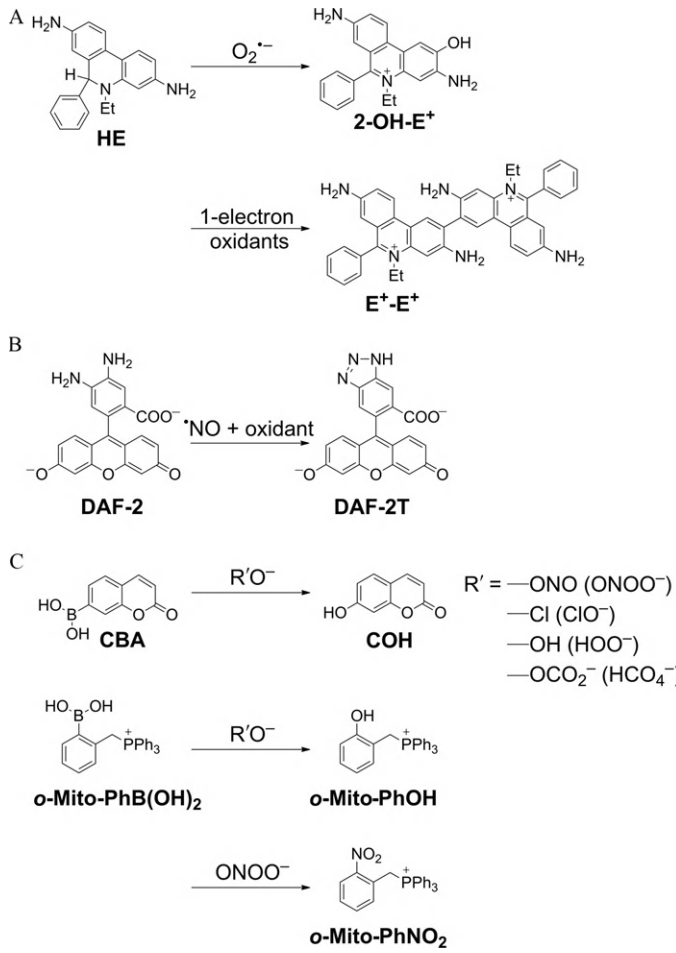

Figure 9.1 Structures of chemical probes and their diagnostic marker products formed from reaction between (A) HE and superoxide or one-electron oxidants, (B) DAF-2 and nitric oxide and oxidant, and (C) CBA/*o*-Mito-PhB(OH)$_2$ and peroxy anion or peroxynitrite.

Srinivasan, et al., 2008; Zielonka, Vasquez-Vivar, et al., 2008). These studies have exposed and highlighted the pitfalls and limitations of fluorescence microscopy in assessing intracellular and mitochondrial $O_2^{\cdot-}$ (Kalyanaraman, Dranka, Hardy, Michalski, & Zielonka, in press; Zielonka & Kalyanaraman, 2010). The discovery of a rapid, direct, and nearly stoichiometric reaction between $ONOO^-$ and boronates forming specific products has enabled the differentiation between $ONOO^-$ and myeloperoxidase/H_2O_2/NO_2^--based nitration mechanisms (Sikora et al.,

2011, 2009; Zielonka, Sikora, et al., 2012; Zielonka, Zielonka, et al., 2012). Kinetic analyses of boronate reactions with H_2O_2 and $ONOO^-$ have made it possible to clearly and distinctly interpret the data in enzymatic and cellular systems cogenerating these species (Sikora et al., 2011, 2009; Zielonka, Sikora, et al., 2012; Zielonka, Sikora, Joseph, & Kalyanaraman, 2010; Zielonka, Zielonka, et al., 2012).

Whereas the initial screening in a fluorescence plate reader followed by a rigorous HPLC characterization may be a useful approach in a high-throughput screening of several thousands of compounds from chemical libraries, the HPLC/MS detection and identification of diagnostic marker products of ROS/RNS-specific probes are most critical for elucidating the chemical, biological, and signaling pathways in cells. In this chapter, we describe the use of four different chemical probes specific for monitoring $O_2^{\cdot-}$, H_2O_2, $^{\cdot}NO$, and $ONOO^-$ formation in cell-free and cell systems.

2. EXPERIMENTAL METHODS

2.1. Assay plate layout

Prior to using the global profiling approach in cellular systems, the uninitiated investigators should become familiar with the assay using xanthine (X) or hypoxanthine (HX)/xanthine oxidase (XO) as a source of superoxide flux and the $^{\cdot}NO$ donor, DPTA-NONOate, that decomposes to slowly release $^{\cdot}NO$ (Fig. 9.2A). Defined fluxes of $O_2^{\cdot-}$ and $^{\cdot}NO$ are simultaneously generated from X (or HX)/XO and DPTA-NONOate in a 96-well plate (Fig. 9.2B). The proposed experimental approach for HPLC (or UHPLC)-based monitoring of ROS/RNS using the four different probes is shown in Fig. 9.3. HPLC conditions for fast analyses of the probes and their products have been described in earlier publications (Sikora et al., in press; Zielonka, Sikora, et al., 2012; Zielonka, Zielonka, et al., 2012).

3. RESULTS AND DISCUSSION

3.1. HPLC analyses of HE-derived products

Figure 9.2B shows the "cell-free" assay setup in a 96-well plate containing HE in the presence of varying fluxes of $^{\cdot}NO$ and $O_2^{\cdot-}$ generated from HX/XO and DPTA-NONOate. Representative HPLC chromatograms (absorption and fluorescence) of HE metabolites are shown in Fig. 9.4A. Under conditions in which only $O_2^{\cdot-}$ and H_2O_2 were generated

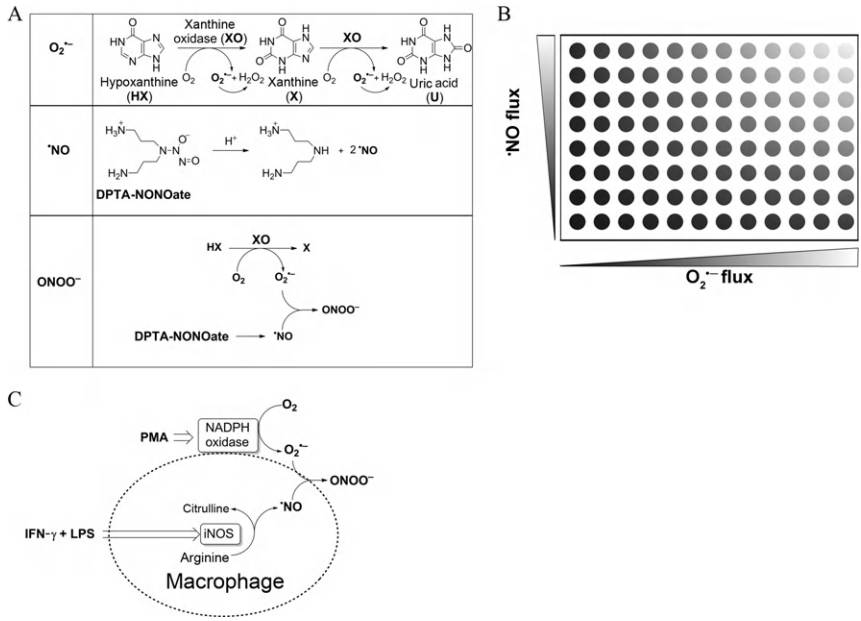

Figure 9.2 (A) Peroxynitrite generation from cogenerated $O_2^{\cdot-}$ and $^{\cdot}NO$. Schemes showing formation of $O_2^{\cdot-}$ from incubations containing hypoxanthine (100 μ*M*) and xanthine oxidase (0–0.4 mU/ml) in a phosphate buffer (pH 7.4; 50 m*M*) containing dtpa (100 μ*M*), $^{\cdot}NO$ generation from a thermal decomposition of DPTA-NONOate (0–50 μ*M*), and $ONOO^-$ formed from cogenerated $O_2^{\cdot-}$ from HX/XO and $^{\cdot}NO$ from DPTA-NONOate. (B) Diagrammatic representation of global profiling experiments. Varying fluxes of cogenerated $^{\cdot}NO$ and $O_2^{\cdot-}$ in a 96-well plate. The top right corner well represents conditions generating maximal (1:1) amount of $^{\cdot}NO$ and $O_2^{\cdot-}$ and bottom right corner well represents conditions generating maximal $O_2^{\cdot-}$ and H_2O_2 alone. (C) Reactive oxygen and nitrogen species formation from RAW 264.7 macrophages activated with LPS, IFN-γ, and PMA.

(right bottom corner well in Fig. 9.2B), the HPLC profile corresponds mainly to 2-OH-E^+, the diagnostic marker product of HE/$O_2^{\cdot-}$ reaction and very little E^+ or dimers. Under conditions in which both $O_2^{\cdot-}$ and $^{\cdot}NO$ are maximally produced at a 1:1 ratio (top right corner well in Fig. 9.2B), 2-OH-E^+ was dramatically inhibited; instead, there was increased formation of E^+ and dimers (HE-E^+, E^+-E^+). Under other conditions, different levels of these products were formed. Indeed, a complete profile of 2-OH-E^+ formation under different fluxes of $^{\cdot}NO$ and $O_2^{\cdot-}$ has been reported (Zielonka, Zielonka, et al., 2012).

From these results, we conclude the following: (1) 2-OH-E^+, the specific marker product of HE reaction with $O_2^{\cdot-}$, increased with increasing $O_2^{\cdot-}$ flux

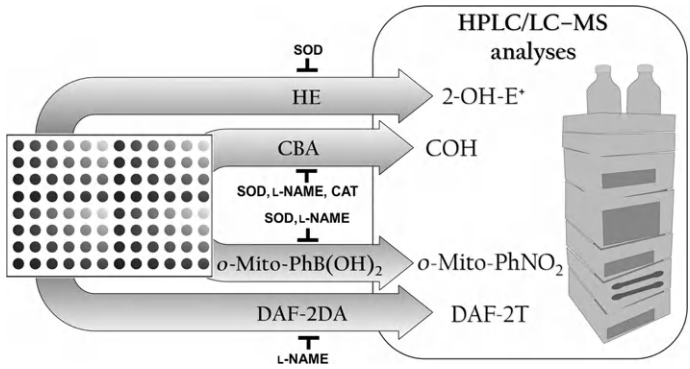

Figure 9.3 Schematic representation of the proposed experimental approach for HPLC (or UHPLC)-based specific monitoring of superoxide (HE oxidation to 2-OH-E^+), nitric oxide (nitrosation of DAF-2 to DAF-2T), and peroxynitrite (oxidation of CBA to COH and transformation of *o*-Mito-PhB$(OH)_2$ to *o*-Mito-PhOH and *o*-Mito-PhNO_2). The identity of the species detected is confirmed by using specific inhibitors and/or scavengers. Rapid separation and detection with UHPLC systems enable analysis of samples in 96- or 384-well plate format.

and $^{\cdot}NO$ inhibited 2-OH-E^+ formation in a concentration-dependent fashion. (2) With increasing $^{\cdot}NO$ and $O_2^{\cdot-}$, the levels of E^+ and dimeric (e.g., E^+-E^+) products increased, suggesting the formation of one-electron oxidants ($^{\cdot}NO$ and O_2 and $ONOO^-$-derived oxidants). (3) Although the HPLC data show a marked decrease in 2-OH-E^+, the fluorescence intensity remained high due to increased levels of E^+. Clearly, the measurements of HE oxidation-derived fluorescence cannot be equated to $O_2^{\cdot-}$ formation. The mechanism of formation of 2-OH-E^+ and E^+ is very different.

Once the investigators become conversant with the HPLC analyses in the well-defined "cell-free" model system, they will be able to perform studies in cellular systems. To investigate oxidation products of HE by endogenously generated $O_2^{\cdot-}$, $^{\cdot}NO$, and $ONOO^-$, we used a system consisting of RAW 264.7 macrophages stimulated with a mixture of LPS, IFN-γ, and PMA (Fig. 9.2C). Oxidation of HE was monitored in a 96-well plate and products formed in cells and in media were analyzed by HPLC. Macrophages were seeded in 96-well plates, and PMA, LPS, or IFN-γ were added as indicated in the presence of HE. The corresponding HPLC profiles are shown in Fig. 9.4B. As shown, 2-OH-E^+ formation increased in the presence of macrophages activated by PMA. Similar to the cell-free system, costimulation of $^{\cdot}NO$ and $O_2^{\cdot-}$ production during the combined treatment with IFN-γ, LPS, and PMA decreased the yield of 2-OH-E^+ with a concomitant increase in HE-derived dimeric products.

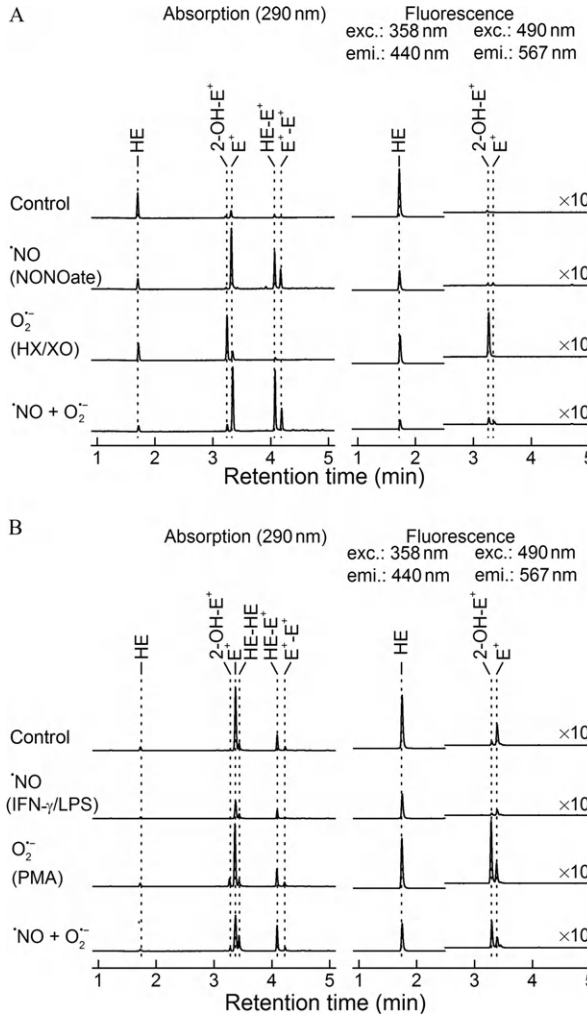

Figure 9.4 Oxidation products formed from HE. (A) HPLC profiles of HE oxidation in cell-free incubations containing DPTA-NONOate alone, hypoxanthine and xanthine oxidase, and both DPTA-NONOate and hypoxanthine and xanthine oxidase, and (B) HPLC profiles obtained from cell lysates of RAW 264.7 macrophages stimulated to produce $^{\cdot}NO$, $O_2^{\cdot-}$, and both $^{\cdot}NO$ and $O_2^{\cdot-}$.

3.2. HPLC analyses of CBA-derived products

The "cell-free" assay setup is similar to conditions described in Fig. 9.2B but using coumarin boronic acid (CBA) probe (Fig. 9.1). Oxidation products of CBA were monitored under varying fluxes of $^{\cdot}NO$ and $O_2^{\cdot-}$.

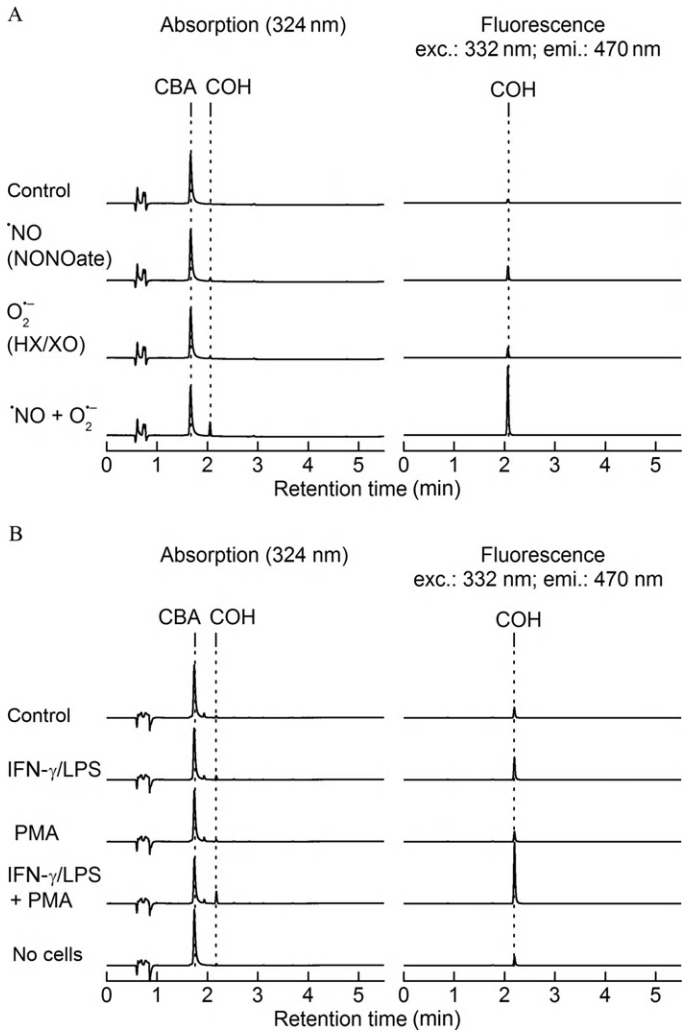

Figure 9.5 Oxidation products formed from CBA. (A) HPLC profiles of CBA oxidation in cell-free incubations containing DPTA-NONOate alone, hypoxanthine and xanthine oxidase, and both DPTA-NONOate and hypoxanthine and xanthine oxidase, and (B) HPLC profiles obtained from cell media of RAW 264.7 macrophages stimulated to produce $^{\cdot}NO$, $O_2^{\cdot-}$, and both $^{\cdot}NO$ and $O_2^{\cdot-}$.

Representative HPLC chromatograms are shown in Fig. 9.5A. As can be seen, there is very little oxidation of CBA to 7-hydroxycoumarin (COH) in the presence $^{\cdot}NO$ or $O_2^{\cdot-}$ alone. However, there is a dramatic increase in the formation of COH in the presence of both $^{\cdot}NO$ and $O_2^{\cdot-}$. This is consistent with the very rapid reaction between $ONOO^-$

and CBA. CBA reacts with H_2O_2 stoichiometrically. However, because this reaction is rather slow, much higher concentrations (millimolar range) of CBA are needed to detect and quantitate H_2O_2. Thus, in the presence of $ONOO^-$, it is essential to measure catalase-inhibitable amount of COH in order to assess H_2O_2 formation. The reaction between CBA and H_2O_2 to form COH is catalase sensitive, whereas the $ONOO^-$/CBA reaction is catalase insensitive (Zielonka, Sikora, et al., 2012; Zielonka et al., 2010; Zielonka, Zielonka, et al., 2012). The oxidation of CBA by activated macrophages was monitored in a 96-well plate. Macrophages were stimulated with LPS, IFN-γ, and PMA, as described previously. Representative HPLC profiles are shown in Fig. 9.5B. Substantial oxidation of CBA to COH was observed in the presence of IFN-γ, LPS, and PMA. L-NAME significantly inhibited COH formation, as did SOD. These results suggest that CBA can be used to selectively detect $ONOO^-$ formed from macrophages activated to cogenerate $^{\cdot}NO$ and $O_2^{\cdot -}$.

3.3. HPLC analyses of DAF-2-derived products

The formation of a triazole, DAF-2T, formed from nitrosation of DAF-2 has been used to monitor intracellular $^{\cdot}NO$ formation (Thomas, Kotamraju, Zielonka, Harder, & Kalyanaraman, 2007). The "cell-free" assay setup is similar to experimental conditions described in Fig. 9.2B. Nitrosation of DAF-2 was monitored in a 96-well plate in the presence of cogenerated $^{\cdot}NO$ and $O_2^{\cdot -}$. $^{\cdot}NO$ alone induces formation of DAF-2T in the presence of oxygen or superoxide. Oxidation of DAF-2 may "activate" the probe to react with $^{\cdot}NO$ and thus increase the yield of DAF-2T. The representative HPLC traces are shown in Fig. 9.6. It is clear that $^{\cdot}NO$ is required to produce DAF-2T, both in cell-free and cellular systems. However, other factors may also affect the yield of the product, as exemplified by the amplifying effect of superoxide on the yield of DAF-2T in cell-free system (Fig. 9.6A). As shown previously, bell-shaped response of DAF-2 nitrosation to different superoxide fluxes indicates the possibility of both enhancement and inhibition of DAF-2T formation, depending on the actual ratio of superoxide and nitric oxide fluxes. Under the conditions of excess of superoxide, virtually all $^{\cdot}NO$ is scavenged and the yield of DAF-2T decreased. In this case, the decrease of DAF-2T formation may be therefore interpreted as a diminished bioavailability of "free" $^{\cdot}NO$, as exemplified in Fig. 9.6B.

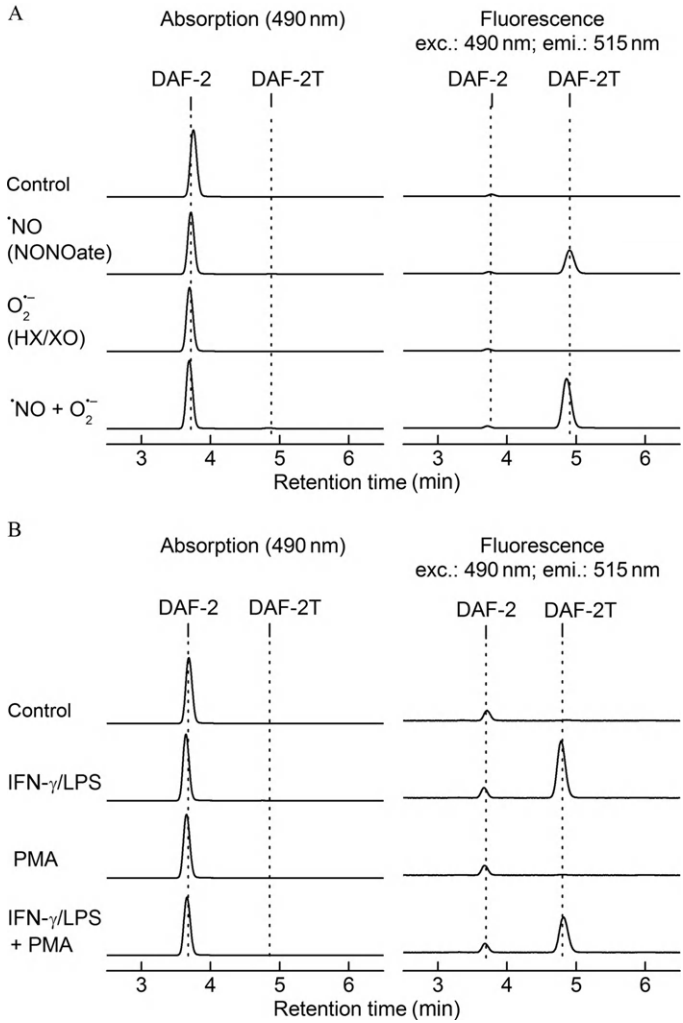

Figure 9.6 HPLC profiles of DAF-2-derived products. (A) Nitrosation of DAF-2 (5 μ*M*) was monitored in a "cell-free" system. As shown, •NO is required to form the specific nitrosated product, DAF-2T. (B) Nitrosation of DAF-2 (5 μ*M*) in media of activated RAW 264.7 macrophages.

3.4. HPLC analyses of *ortho*-Mito-PhB(OH)$_2$-derived products

The oxidative transformation of *o*-Mito-PhB(OH)$_2$ probe in the presence of peroxynitrite is shown in Fig. 9.7A. In contrast to other arylboronates, with *o*-Mito-PhB(OH)$_2$, the relative yield of the minor nitration product

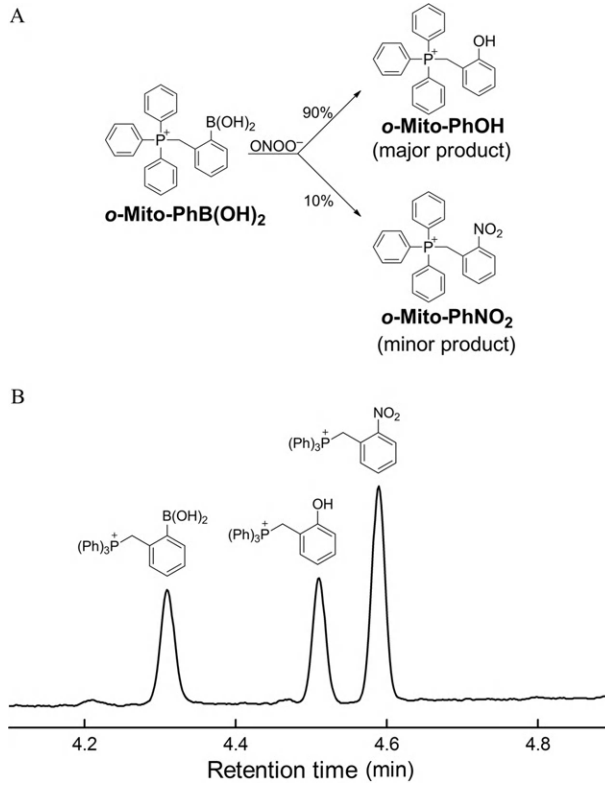

Figure 9.7 HPLC profiles of *o*-Mito-PhB$(OH)_2$-derived products. (A) Scheme showing the major (*o*-Mito-PhOH) and minor (*o*-Mito-PhNO_2) products of the reaction of *o*-Mito-PhB$(OH)_2$ with $ONOO^-$. (B) HPLC chromatogram of the standards of *o*-Mito-PhB$(OH)_2$, *o*-Mito-PhOH and *o*-Mito-PhNO_2.

(*o*-Mito-PhNO_2) is independent of the presence of biologically relevant reductants (Sikora et al., in press). The ratio between *o*-Mito-PhNO_2 and *o*-Mito-PhOH during $ONOO^-$-dependent oxidation of *o*-Mito-PhB$(OH)_2$ remained constant. The actual yields of both products can be used to determine the contribution of different oxidants ($ONOO^-$ or H_2O_2) to oxidation of the probe. As *o*-Mito-PhNO_2 is not formed by H_2O_2 or HOCl or MPO/H_2O_2/NO_2^- system, it can be used as a specific diagnostic marker of $ONOO^-$ (Sikora et al., in press). As shown in Fig. 9.7B, HPLC separation of different products can be achieved within 5 min, and the analysis time is expected to be significantly shortened with the use of UHPLC systems.

4. SUMMARY

The HPLC assays using ROS/RNS-specific chemical probes reported here with well-defined redox chemistry are simple yet rigorous and can readily be implemented in cell-based high-throughput studies (e.g., in 384- and 1536-well plates) using automated liquid-handling systems. Increased understanding of the free radical and non-free radical chemistry of fluorescent probes has exposed and highlighted the limitations of fluorescence microscopy-based ROS/RNS assays.

ACKNOWLEDGMENTS

This work was supported by funds received from NHLBI (R01 HL063119). A. S. was supported by a grant from the Foundation for Polish Science (FNP) within the "Homing Plus" program and a grant coordinated by JCET, No. POIG.01.01.02-00-069/09 (both grants are supported by the European Union from the resources of the European Regional Development Fund under the Innovative Economy Programme).

REFERENCES

Kalyanaraman, B., Dranka, B. P., Hardy, M., Michalski, R., & Zielonka, J. (in press). HPLC-based monitoring of products formed from fluorogenic probes—The ultimate approach for intra-and extracellular superoxide detection. *Biochimica et Biophysica Acta General Subjects*. http://dx.doi.org/10.1016/j.bbagen.2013.05.008.

Michalski, R., Zielonka, J., Hardy, M., Joseph, J., & Kalyanaraman, B. (2013). Hydropropidine: A novel, cell-impermeant fluorogenic probe for detecting extracellular superoxide. *Free Radical Biology & Medicine*, *43*, 135–147.

Robinson, K. M., Janes, M. S., Pehar, M., Monette, J. S., Ross, M. F., Hagen, T. M., et al. (2006). Selective fluorescent imaging of superoxide in vivo using ethidium-based probes. *Proceedings of the National Academy of Sciences of the United States of America*, *103*, 15038–15043.

Sikora, A., Zielonka, J., Adamus, J., Debski, D., Dybala-Defratyka, A., Michalowski, B., et al. (in press). Reaction between peroxynitrite and triphenylphosphonium-substituted arylboronic acid isomers—Identification of diagnostic marker products and biological implications. *Chemical Research in Toxicology*. http://dx.doi.org/10.1021/tx300499c.

Sikora, A., Zielonka, J., Lopez, M., Dybala-Defratyka, A., Joseph, J., Marcinek, A., et al. (2011). Reaction between peroxynitrite and boronates: EPR spin-trapping, HPLC analyses, and quantum mechanical study of the free radical pathway. *Chemical Research in Toxicology*, *24*, 687–697.

Sikora, A., Zielonka, J., Lopez, M., Joseph, J., & Kalyanaraman, B. (2009). Direct oxidation of boronates by peroxynitrite: Mechanism and implications in fluorescence imaging of peroxynitrite. *Free Radical Biology & Medicine*, *47*, 1401–1407.

Thomas, S., Kotamraju, S., Zielonka, J., Harder, D. R., & Kalyanaraman, B. (2007). Hydrogen peroxide induces nitric oxide and proteosome activity in endothelial cells: A bell-shaped signaling response. *Free Radical Biology & Medicine*, *42*, 1049–1061.

Zhao, H., Joseph, J., Fales, H. M., Sokoloski, E. A., Levine, R. L., Vasquez-Vivar, J., et al. (2005). Detection and characterization of the product of hydroethidine and intracellular superoxide by HPLC and limitations of fluorescence. *Proceedings of the National Academy of*

Sciences of the United States of America, *102*, 5727–5732 [Erratum: *Proceedings of the National Academy of Sciences of the United States of America*, 102, 9086, 2005.].

Zhao, H., Kalivendi, S., Zhang, H., Joseph, J., Nithipatikom, K., Vasquez-Vivar, J., et al. (2003). Superoxide reacts with hydroethidine but forms a fluorescent product that is distinctly different from ethidium: Potential implications in intracellular fluorescence detection of superoxide. *Free Radical Biology & Medicine*, *34*, 1359–1368.

Zielonka, J., & Kalyanaraman, B. (2010). Hydroethidine- and MitoSOX-derived red fluorescence is not a reliable indicator of intracellular superoxide formation: Another inconvenient truth. *Free Radical Biology & Medicine*, *48*, 983–1001.

Zielonka, J., Sikora, A., Hardy, M., Joseph, J., Dranka, B. P., & Kalyanaraman, B. (2012). Boronate probes as diagnostic tools for real time monitoring of peroxynitrite and hydroperoxides. *Chemical Research in Toxicology*, *25*, 1793–1799.

Zielonka, J., Sikora, A., Joseph, J., & Kalyanaraman, B. (2010). Peroxynitrite is the major species formed from different flux ratios of co-generated nitric oxide and superoxide: Direct reaction with boronate-based fluorescent probe. *Journal of Biological Chemistry*, *285*, 14210–14216.

Zielonka, J., Srinivasan, S., Hardy, M., Ouari, O., Lopez, M., Vasquez-Vivar, J., et al. (2008). Cytochrome c-mediated oxidation of hydroethidine and mito-hydroethidine in mitochondria: Identification of homo- and heterodimers. *Free Radical Biology & Medicine*, *44*, 835–846.

Zielonka, J., Vasquez-Vivar, J., & Kalyanaraman, B. (2008). Detection of 2-hydroxyethidium in cellular systems: A unique marker product of superoxide and hydroethidine. *Nature Protocols*, *3*, 8–21.

Zielonka, J., Zielonka, M., Sikora, A., Adamus, J., Hardy, M., Ouari, O., et al. (2012). Global profiling of reactive oxygen and nitrogen species in biological systems: High-throughput real-time analyses. *Journal of Biological Chemistry*, *287*, 2984–2995.

CHAPTER TEN

H_2O_2 Delivery to Cells: Steady-State Versus Bolus Addition

H. Susana Marinho*, Luísa Cyrne*, Enrique Cadenas†, Fernando Antunes*,1

*Departamento de Química e Bioquímica and Centro de Química e Bioquímica, Faculdade de Ciências, Universidade de Lisboa, Lisboa, Portugal
†Pharmacology & Pharmaceutical Sciences, School of Pharmacy, University of Southern California, Los Angeles, California, USA
1Corresponding author: e-mail address: fantunes@fc.ul.pt

Contents

1. Introduction 160
   1.1 Bolus addition 161
   1.2 Glucose oxidase 161
   1.3 Steady state 163
2. Experimental Components and Considerations 163
   2.1 Theoretical consideration on how to set up a steady state 163
   2.2 Reagents 164
3. Pilot Experiments 164
   3.1 H_2O_2 calibration curve 165
   3.2 Determination of kinetics of H_2O_2 consumption by cells 166
   3.3 Determination of H_2O_2 production by GO 166
   3.4 Data handling 166
4. Steady-State Experimental Implementation 169
   4.1 H_2O_2 calibration curve 169
   4.2 Steady-state implementation 169
   4.3 Additional points 170
5. Summary 171
Acknowledgments 172
References 172

Abstract

Hydrogen peroxide (H_2O_2) is a ubiquitous biological molecule whose wide range of biological functions depends on its concentration. In this chapter, we compare the delivery of H_2O_2 to cells as (1) a single initial dose (bolus addition); (2) a continuous source using, for example, glucose oxidase; and (3) a steady state, in which H_2O_2 concentration is kept constant during the assay. Both the bolus addition and the use of a continuous source of H_2O_2 have as outcome concentration profiles of H_2O_2 that are dependent on experimental conditions and that are difficult to reproduce from the information that is usually

Methods in Enzymology, Volume 526
ISSN 0076-6879
http://dx.doi.org/10.1016/B978-0-12-405883-5.00010-7

© 2013 Elsevier Inc.
All rights reserved.

revealed in the experimental section of most research articles. On the other hand, the outcome of delivering H_2O_2 as a steady state is a concentration profile that is independent of experimental conditions. The implementation of the steady state starts with the determination of the kinetics of H_2O_2 consumption in the system under study. Then, the amount of glucose oxidase needed to produce H_2O_2 at a rate that matches the rate of its consumption by cells at the desired H_2O_2 steady-state concentration is calculated. The setup of the steady state is initiated by adding this amount of glucose oxidase simultaneously with the desired concentration of H_2O_2. Because H_2O_2 consumption and delivery rates are matched, the initial H_2O_2 concentration added is kept constant during the assay. Detailed explanations on how to implement the steady state, including H_2O_2 measurements and adjustments in the amount of H_2O_2 or glucose oxidase during the assay, are described.

1. INTRODUCTION

Hydrogen peroxide (H_2O_2) is a small diffusible species produced in aerobic cells that acts as a mild oxidant *in vivo*. Depending on its concentration, H_2O_2 may oxidize sulfhydryl groups in proteins to different degrees and, as an outcome, changes in protein activity occur leading to important regulatory effects (Winterbourn & Hampton, 2008). In the presence of transition metals, H_2O_2 can be decomposed to the highly reactive hydroxyl radical that reacts virtually with the first species it collides in the vicinity of its production site (Koppenol, 1993). Thus, the biological effects of H_2O_2 are strongly dependent on its concentration (Antunes & Cadenas, 2001; De Oliveira-Marques, Cyrne, Marinho, & Antunes, 2007; Quinn et al., 2002) and opposite effects may be observed for a relative narrow range of concentrations (Matias, Marinho, Cyrne, Herrero, & Antunes, 2011). Another key characteristic of H_2O_2 metabolism is its rapid consumption by cellular antioxidant enzymes which include glutathione peroxidases, catalase, peroxiredoxins, cytochrome *c* peroxidase, and rubredoxins (Chance, Sies, & Boveris, 1979; Pedone, Bartolucci, & Fiorentino, 2004). When studying its cellular effects, researchers manipulate H_2O_2 concentrations either by influencing its cellular metabolism or by adding external H_2O_2 to the cells under study. In this chapter, we compare three alternative H_2O_2-delivering systems: H_2O_2 bolus addition, glucose oxidase (GO) addition, and steady-state incubation. We also describe in detail how to set up a steady-state incubation in cell cultures.

1.1. Bolus addition

The direct addition of H_2O_2 to the system under study at the desired concentration is the simplest approach to study the effect of H_2O_2. Because of the rapid consumption of H_2O_2 by cellular antioxidants, its concentration starts to decrease as soon as the dose is given. The concentration profile of H_2O_2 during the incubation is strongly dependent on the cellular density used and, for attached culture cells, the volume of the incubation media also affects the H_2O_2 profile (Fig. 10.1A). Therefore, this commonly used methodology is very dependent on the experimental setting and, consequently, experiments are difficult to reproduce. In addition, because H_2O_2 is consumed rapidly, in order to observe biological effects, often large initial concentrations of H_2O_2 are given, and so, the relevance of the results obtained is doubtful. This methodology helped to acquire useful data when the aim was studying damaging oxidative effects by large concentrations of H_2O_2, but to study fine regulatory roles exerted by H_2O_2, this methodology is clearly unsuitable.

1.2. Glucose oxidase

An alternative that avoids the need to add large initial doses of H_2O_2 is to add a system that continuously produces H_2O_2, thus compensating for its continuous consumption. GO, which uses glucose in the media to produce H_2O_2 (Eq. 10.1), is an example of such a system.

$$\beta\text{-D-Glucose} + O_2 \xrightarrow{\text{glucose oxidase}} H_2O_2 + \text{D-glucono-1,5-lactone} \quad [10.1]$$

Alternatively, if for some reason GO cannot be used, for example, if incubating a microorganism cell culture in the stationary phase of growth where glucose is absent, other H_2O_2-forming enzymes can be used. An example is amino acid oxidase that catalyzes H_2O_2 formation from amino acids present in the growth medium (Cyrne, Antunes, Sousa-Lopes, Diaz-Bérrio, & Marinho, 2010; Sousa-Lopes, Antunes, Cyrne, & Marinho, 2004).

After adding GO to the cell culture, the H_2O_2 concentration will increase initially until a steady state is reached where the production of H_2O_2 by the enzymatic system is compensated by its consumption by the cellular antioxidants. Both the value of this steady state and the time that it takes to reach it are dependent on the rate of H_2O_2 consumption in the experimental system. Often, both these values are unknown as the H_2O_2 concentration is not monitored during the assay, and the H_2O_2 incubation is reported as units of the enzyme added. This approach is also difficult

to reproduce as it is strongly dependent on the experimental conditions. If the amount of GO is adjusted based on the volume of the incubation media, the final steady state will depend on the number of cells present in the assay (Fig. 10.1B); if the amount of GO is adjusted based on the number of cells in the assay, the final H_2O_2 concentration will be independent of experimental conditions, but the time needed to reach the steady state will be dependent on these conditions (Fig. 10.1C). In this regard, notice that the H_2O_2 concentration profile obtained in an experiment with adherent cells seeded in a 100-mm dish with 10 mL of growth media differs from that obtained in a well of a 96-well plate with 0.1 mL of growth media (assuming the same cell density in both cases) (Fig. 10.1C).

Thus, for both bolus and GO additions, the H_2O_2 concentration profiles and, consequently, the results obtained have a low reproducibility.

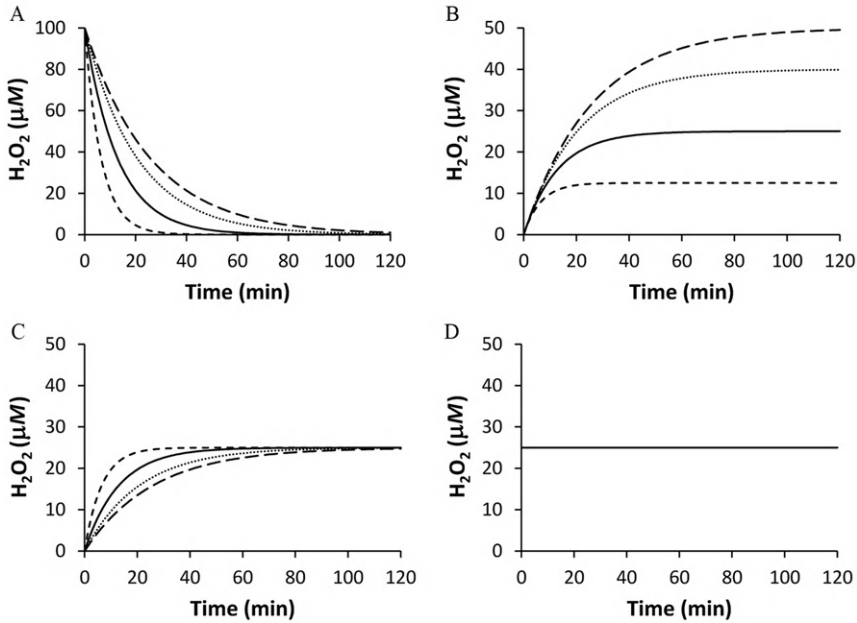

Figure 10.1 Different methods of H_2O_2 delivery to cells. MCF-7 cells were seeded at a density of 3.2×10^4 cells/cm^2 in a 100-mm dish in 10 mL of growth media (——), 1.6×10^4 cells/cm^2 in a 100-mm dish in 10 mL of growth media (– – –), 3.2×10^4 cells/cm^2 in a 100-mm dish in 5 mL of growth media (- - -), and 3.2×10^4 cells/cm^2 in 96-well plate in 0.1 mL of growth media (· · · · · ·). Cells were exposed to H_2O_2 by adding a 100 μ*M* bolus addition (A), by adding GO that produces H_2O_2 at 1.9 μ*M*/min (B), by adding GO that produces H_2O_2 at 0.011 μmol/10^6 cells (C), and by adding a steady state of 25 μ*M* H_2O_2 (D). Curves are simulations based on a first-order rate constant 0.43 min$^{-1}\times$ mL/10^6 cells for the consumption of H_2O_2 by MCF-7 cells.

Moreover, often, it is impossible to reproduce the experimental H_2O_2 concentration profile applied in a given work, because details such as the volume of the growth media and the number of cells used are usually absent in publications.

1.3. Steady state

In the steady-state approach, the addition of an initial concentration of H_2O_2 is combined with the addition of either GO or another H_2O_2-producing system. The dose given corresponds to the H_2O_2 concentration of interest, and the amount of GO is adjusted in order to balance the consumption of H_2O_2 at the concentration of interest, thus keeping the H_2O_2 concentration steady during the experiment. A key aspect of this methodology is that the H_2O_2 concentration is monitored during the assay and its level is adjusted in order to keep the concentration constant. Thus, this approach implies a higher effort when compared with either the bolus or the GO addition, but on the other hand, the H_2O_2 concentration profile obtained does not depend on the experimental conditions (Fig. 10.1D) facilitating experimental reproducibility, either in the same laboratory or between laboratories.

2. EXPERIMENTAL COMPONENTS AND CONSIDERATIONS

2.1. Theoretical consideration on how to set up a steady state

A steady state for H_2O_2 is obtained when the rates of H_2O_2 production and consumption match each other. At this stage, the concentration of H_2O_2 does not change and a steady state is reached. Mathematically, this is obtained by setting the differential equation that describes H_2O_2 dynamics to zero (Eq. 10.2).

$$\frac{d[H_2O_2]}{dt} = V_{production} - V_{consumption} = 0 \Rightarrow V_{production} = V_{consumption} \quad [10.2]$$

When setting up a steady state experimentally, the first step is to determine $V_{consumption}$. Once this is determined, $V_{production}$ can be obtained from Eq. (10.2), and the amount of GO, or of another H_2O_2-generating system, that is necessary to add to the system can be calculated. $V_{consumption}$ varies with the H_2O_2 concentration. Fortunately, for sublethal H_2O_2 concentrations, the kinetics of H_2O_2 consumption can be often approximated to first-order kinetics (Antunes & Cadenas, 2000; Branco, Marinho, Cyrne, &

Antunes, 2004; Gülden, Jess, Kammann, Maser, & Seibert, 2010; Makino, Mochizuki, Bannai, & Sugita, 1994). This is consistent with the known catalase and glutathione peroxidase kinetics (Chance et al., 1952, 1979; Flohe, Loschen, Gunzler, & Eichele, 1972). Under these conditions, $V_{production}$ can be calculated from Eq. (10.3), where k is the first-order rate constant for the consumption of H_2O_2.

$$V_{production} = k \times [H_2O_2] \quad [10.3]$$

The rate of H_2O_2 production is calculated by replacing in Eq. (10.3) the first-order rate constant k obtained experimentally and the desired steady-state H_2O_2 concentration to be established in the experiment ($[H_2O_2]$). If the kinetics of H_2O_2 consumption is more complex, an equivalent of Eq. (10.3) is obtained, and by replacing the desired H_2O_2 concentration and the determined kinetics constants, the rate of production can be calculated.

2.2. Reagents

1. *H_2O_2*. Make fresh every day the solution using concentrated *Perhydrol* [30% (m/m) H_2O_2, density 1.11 g/mL, MW = 34.02, 9.79 *M*] from Merck. The original *Perhydrol*, 30% concentrated solution, should be aliquoted in order to avoid its frequent manipulation. To obtain the stock solution of H_2O_2 (approximately 9–10 m*M*), dilute 1/1000 the concentrated H_2O_2 solution. For that make an initial dilution of 1/100 in water (10 μL + 990 μL water or, alternatively, two sequential 1/10 dilutions) in an *Eppendorf* tube. Then perform a 1/10 dilution using 500 μL of H_2O_2 diluted 1/100 and adding 4.5 mL of water. Confirm the concentration by reading the absorbance of this 1/1000 diluted stock solution at 240 nm ($\varepsilon = 43.4\ M^{-1}cm^{-1}$). Keep on ice.
2. *Catalase* (bovine liver, Sigma C-1345, 2000–5000 U/mg protein) 1 mg/mL (in water). It can be stored for weeks.
3. *GO* from *Aspergillus niger*, Sigma G-0543, ≥200 U/mg protein, ≤0.1 U/mg catalase, buffered aqueous solution (in 100 m*M* sodium acetate, 40 m*M* KCl, with 0.004% thimerosal), pH 4.5, low catalase activity. Storage temperature, 2–8 °C. A working diluted solution (1/100, 1/1000, or 1/10,000 dilution in water) should be made daily.
4. *0.1 M Potassium phosphate buffer, pH 6.5.*

3. PILOT EXPERIMENTS

Pilot experiments consist of the determination of the kinetics of H_2O_2 consumption and the rate of formation of H_2O_2 catalyzed by GO under the

experimental conditions to be used for the steady-state incubation. For each cell type or for each new GO batch, the following procedures should be carried out.

3.1. H_2O_2 calibration curve

H_2O_2 is assayed by the formation of O_2 after the addition of catalase (Eq. 10.4) using an oxygen electrode.

$$2H_2O_2 \xrightarrow{\text{catalase}} O_2 + 2H_2O \quad [10.4]$$

We use a chamber oxygen electrode (Oxygraph system, Hansatech Instruments Ltd., Norfolk, UK) with a magnetic stirrer and temperature control. All measurements are either performed at room temperature (for cell lines) or at 30 °C (for yeast) and with a final volume of 800 μL. The electrode should be given a stable baseline. For that, it is recommended to add 800 μL of distilled water and to connect the stirring a few hours before the measurements.

A H_2O_2 calibration curve within the range of 10–90 μ*M*, in which the O_2 electrode we use has a linear response, should be made. For that, do the following (see also Marinho, Cyrne, Cadenas, & Antunes, 2013):

1. Pipet from 10 μL up to 100 μL of the 9 m*M* H_2O_2 stock solution to different test tubes and add distilled water to a final volume of 5 mL. Keep the test tubes at the same temperature of the electrode chamber.
2. Add 400 μL of H_2O_2 from one of the test tubes, starting with the lowest concentration, to 400 μL of 0.1 *M* potassium phosphate buffer, pH 6.5, already in the electrode chamber. Readings can also be done without using the buffer, but the oxygen electrode has a more stable output when the buffer is used.
3. Start recording and, when a baseline is established, rapidly add 15 μL of catalase using a Hamilton syringe (being careful not to add air bubbles as they interfere in the measurement). This addition should cause a rapid increase in the reading as O_2 is formed from the H_2O_2 present by the action of catalase. After a new baseline is established, stop the recording. The value of the difference between the two baselines should be used to make a plot versus H_2O_2 concentration.
4. Remove the content of the oxygen electrode chamber and clean thoroughly with distilled water (fill the chamber up until the middle at least four times and then up until the top four times) in order to be sure to remove all the catalase before the next H_2O_2 assay.

3.2. Determination of kinetics of H_2O_2 consumption by cells

The consumption of H_2O_2 in cells should be done under the same conditions (cell density, media used, and incubation conditions) of the H_2O_2 steady-state assay.

1. The experiment is initiated with the addition of 100 μ*M* H_2O_2 (bolus addition) to the medium.
2. Take 800 μL aliquots at different times, add to the electrode chamber, and measure O_2 formation after adding 15 μL of catalase.
3. Remove the content of the oxygen electrode chamber and clean thoroughly with distilled water as described in the previous section in order to be sure to remove all the catalase before the next H_2O_2 assay.

At least six time points should be recorded. Use the calibration curve to calculate the concentrations. Time between aliquots depends on how fast H_2O_2 is being consumed in the assay, but data points spanning the range between 10 and 90 μ*M* should be obtained.

3.3. Determination of H_2O_2 production by GO

The determination of the rate of H_2O_2 production by GO should be done under the same conditions (media used and incubation conditions) of the H_2O_2 steady-state assay. For example, for cell lines, we use the following procedure:

1. Add 10 μL of GO to 990 μL of water (1/100 dilution of the original stock solution).
2. Add 10 μL of the previous solution to a 100-mm cell-culture dish with 8 mL of prewarmed and CO_2-preequilibrated media.
3. Put dish in the cell incubator.
4. Take 800 μL aliquots at different times, add to the electrode chamber, and measure O_2 formation after adding 15 μL of catalase.

At least five time points should be recorded. Use the calibration curve to calculate the H_2O_2 concentrations. Time between aliquots depends on glucose activity, but typically under these conditions, we take aliquots every 4–5 min. The maximum concentration recorded should be lower than 90 μ*M* and points should follow a linear increase (Fig. 10.2).

3.4. Data handling

3.4.1 Determination of k

The data obtained in Section 3.2 is plotted as ln [H_2O_2] versus time. If H_2O_2 is consumed as a first-order process, this plot should be linear with a negative

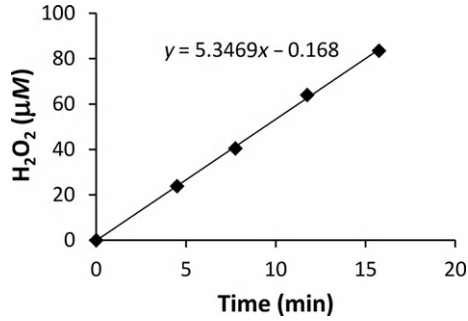

Figure 10.2 Determination of glucose oxidase activity. Production of H_2O_2 was followed in an oxygen electrode by measuring the oxygen formed after the addition of catalase. 10 μL of a 1/100 dilution of the original GO solution is added to 8 mL of prewarmed RPMI-1640 media.

slope. The first-order rate constant is determined from the slope ($k = -$slope), and it will have units of time^{-1}. If the determination is done in suspension cells, this value has to be divided by the cell density (usually million of cells/mL or, in the case of microorganisms, OD_{600}).

If the determination is done in attached cells, a plot of the ln [H_2O_2] versus time cannot be done directly from the experimental data, because after taking each 800 μL aliquot, the reaction volume covering the cells decreases, and H_2O_2 will be consumed faster as the number of the cells in the assay remains constant. So, before plotting the data, data points should be corrected according to the procedure shown in Fig. 10.3. The rate constant can be obtained from the slope of the semilogarithmic plot of the corrected H_2O_2 concentrations versus time. The rate constant is equal to slope × (reaction volume)/(number of cells), where reaction volume unit is mL and the number of cells comes in million. Formally, this is identical to the rate constant described above for the suspension cells (slope/cell density). Taking as an example the data in Fig. 10.3 for HT-4 cells, slope is −0.0239 min^{-1}, so the rate constant is

$$0.0239\,\mathrm{min}^{-1} \times 10\mathrm{mL}/\left(1.8 \times 10^6 \mathrm{cells}\right) = 0.13\,\mathrm{min}^{-1}\mathrm{mL}/10^6\mathrm{cells}$$

3.4.2 Calculation of GO activity

The slope determined from the plot in Fig. 10.2 was 5.35 μM min^{-1}. Multiplying by the volume of the assay in which the activity was determined (8 mL) and dividing by the volume of GO 1/100 dilution added (10 μL),

A

	B	C	D
1	H_2O_2 experimental	Correction	Corrected H_2O_2
2	(μM)	factor	(μM)
3	100.0		100.0
4	93.0	1	93.0
5	65.0	0.9	67.4
6	47.1	0.8	52.0
7	29.1	0.7	37.2
8	17.9	0.6	27.8
9			
10	D4: =EXP(LN(B4/B3)*C4)*D3		
11	D4 from Row 4 through Row 8		

B

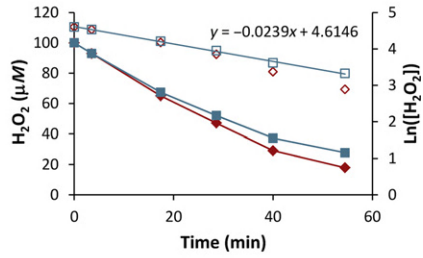

Figure 10.3 Calculation of the first-order rate constant for H_2O_2 consumption by attached HT-4 cells (1.8 million cells in a 100-mm dish). (A) The experimental H_2O_2 values (Column B) are corrected to account for the removal of 1 mL aliquots at each time point (Column D); the initial volume of incubation media was 10 mL. The correction factor (Column C) is calculated as the ratio between the volume in which H_2O_2 consumption was measured and the initial reaction volume. At 3.5 min, the first 1 mL aliquot is taken and, in this case, the correction factor is one, that is, no correction is needed because consumption during the first 3.5 min was done in the original volume of 10 mL. At 17.4 min, a second 1 mL aliquot was taken and a correction of factor of 9/10 was introduced because H_2O_2 consumption between 3.5 and 17.4 min was done in 9 mL (and not in the original 10 mL). (B) Plot of uncorrected (◆) and corrected (■) H_2O_2 concentrations in normal (closed symbols) and semilogarithmic scale (open symbols). Note the deviation from linearity for the uncorrected H_2O_2 concentration in the semilogarithmic plot.

we obtain the number of moles produced per unit time per μL of the 1/100 dilution of GO:

$$\left(5.35\,\mu M\,\mathrm{min}^{-1}\right) \times 8\,\mathrm{mL}/10\,\mu\mathrm{L} = 4.28\,\mathrm{nmol\ of\ H_2O_2\ min^{-1}\mu L^{-1}\ of\ 1/100\ GO\ solution}$$

3.4.3 Calculation of the amount of GO to be added

The amount of GO to be added to the steady-state assay is calculated in three steps. The rate of H_2O_2 production needed is calculated by applying Eq. (10.3), where the k obtained in Section 3.4.1 and the desired steady state ($[H_2O_2]$ss) are replaced; the conditions of the assay (cell density for suspension cells or number of cells and reaction volume for attached cells) are also included:

$$V_{\mathrm{production}} = k \times [\mathrm{H_2O_2}]\mathrm{ss} \times \mathrm{cell\ density} \quad \text{or}$$
$$V_{\mathrm{production}} = k \times [\mathrm{H_2O_2}]\mathrm{ss} \times \mathrm{number\ of\ cells/reaction\ volume}$$

1. $V_{production}$ obtained has units of concentration × time^{-1}. For example, if a 25 μ*M* steady state is to be established in an assay with 1.8 million HT-4 cells attached in a 100-mm dish with 10 mL of reaction volume, $V_{production}$ would be as follows:

$$\left(0.13\,\text{min}^{-1}\text{mL}/10^6\,\text{cells}\right) \times 25\,\mu M \times 1.8 \times 10^6\,\text{cells}/10\,\text{mL} = 0.585\,\mu M\,\text{min}^{-1}.$$

2. The number of molecules of H_2O_2 produced is obtained by multiplying the value obtained in step 1 by the reaction volume. Continuing with the previous example,

$$\left(0.585\,\mu M\,\text{min}^{-1}\right) \times 10\,\text{mL} = 5.85\,\text{nmol}\,\text{min}^{-1}.$$

3. By dividing the number obtained in the previous step by the activity calculated in Section 3.4.2, we obtain the volume in μL of the 1/100 glucose dilution needed to obtain the desired steady state. In our example,

$$\left(5.85\,\text{nmol}\,\text{min}^{-1}\right)/\left(4.28\,\text{nmol}\,\text{min}^{-1}\mu\text{L}^{-1}\right) = 1.37\,\mu\text{L}$$

We would need 1.37 μL of a 1/100 dilution of the original glucose oxidation. To minimize pipetting error, a 13.7 μL of a 1/1000 diluted solution would be advisable.

4. STEADY-STATE EXPERIMENTAL IMPLEMENTATION

4.1. H_2O_2 calibration curve

A H_2O_2 calibration curve as described in Section 3.1 should be made daily in a range around the steady state of interest. For example, for 25 μ*M*, we usually use concentrations of 15, 20, 25, 30, and 35 μ*M*.

4.2. Steady-state implementation

The incubating media should be replaced with prewarmed media 1 h before experiment. Used media may have an inherent H_2O_2 consumption rate, because many cells export glutathione (Bannai & Tsukeda, 1979; Griffith et al., 1979). To start the steady state, add simultaneously the desired amount of H_2O_2 and an amount of GO calculated as in Section 3.4.3. The steady state should be checked every hour, or for short incubations, an aliquot should be taken just before the end of the experiment to measure the real

H_2O_2 concentration. To this end, take an 800 μL aliquot and measure the H_2O_2 concentration as described before. Adjust the H_2O_2 concentration in the following way:

1. If the H_2O_2 concentration measured is lower than the desired steady state, correct by adding the missing H_2O_2 and GO. GO addition should be calculated as a direct proportion to the deviation from the desired steady state observed. For example, if a steady state of 25 μ*M* was the aim, and a 22.5 μ*M* concentration is observed, that is, 10% lower than the aim, then add 10% of both the GO and H_2O_2 amounts added initially.
2. If the H_2O_2 concentration measured is higher than the desired steady state, in case of a cell suspension, nothing can be done. If working with attached cells, remove a volume of incubation medium calculated as a direct proportion to the deviation from the desired steady state observed. If the observed concentration is 10% superior to the desired one, remove 10% of the incubation media and replace with fresh prewarmed and CO_2-preequilibrated media. By doing this, the excess of both GO and H_2O_2 is removed.
3. In the case of attached cells, GO additions and media removal have to take into account the volume of the aliquot taken to check the steady state. For example, if the incubation media is 8 mL and a 800 μL aliquot is taken and the steady state matches exactly the desired steady state, add, in 800 μL of fresh media, 10% of GO and 10% of H_2O_2 amounts that were added initially to compensate for the removal of the aliquot. If the steady state measured is 10% higher than the desired steady state, just add 800 μL of fresh media. If the steady state is 10% lower than the desired, it is necessary to add 20% of the initially added GO and H_2O_2 amounts.
4. For cells growing in suspension, the considerations in the previous point do not apply, because when taking aliquots, only the overall volume is decreasing, while relative GO activity, H_2O_2 concentration, and number of cells remain constant.

4.3. Additional points

Steady-state incubations are usually carried out in RPMI, a growth medium that consumes H_2O_2 at a very low rate. Other media consume H_2O_2 at significant amounts, which can be compensated by giving an additional amount of GO (Clément, Ramalingam, Long, & Halliwell, 2001; Hoffman, Pine, & Bell, 1983; Martín-Romero, Miguel-Lasobras, Domínguez-Arroyo, González-Carrera, & Alvarez, 2008). However, if

H_2O_2 is consumed extracellularly at significant rates, one can question whether the cellular H_2O_2 effects are due to the interaction of H_2O_2 with cellular components, or due to the products being formed extracellularly from the reactions of H_2O_2 with medium components.

The generation of H_2O_2 catalyzed by GO is based on the oxidation of glucose to D-glucono-1,5-lactone (Eq. 10.1). It is important to test that D-glucono-1,5-lactone does not interfere in the system. One simple control that can be done is to add catalase. If the biological effects triggered by the steady-state incubation are absent in the presence of catalase, then D-glucono-1,5-lactone is not interfering with the measurements. The consumption of O_2 by GO can also affect the results, and in this case, the addition of catalase does not provide a definitive answer because half of the O_2 consumed in the reaction catalyzed by GO is released in the catalase-catalyzed reaction. If the cellular consumption of H_2O_2 by the cells is much lower than the cellular O_2 consumption, the depletion of O_2 caused by GO is not a problem. However, if cellular H_2O_2 and O_2 consumptions are of the same order of magnitude, the O_2 concentration in solution should be checked.

After the steady state is set up, a good reproducibility is usually achieved. When the H_2O_2 concentration measured deviates more than 20% of the desired concentration, a correction as described in Section 4.2 is not attempted and the experiment is discarded.

Further information on the application of the steady-state delivery in specific situations is described in detail in Covas, Marinho, Cyrne, and Antunes (2013) and Cyrne, Oliveira-Marques, Marinho, and Antunes (2013).

5. SUMMARY

In this chapter, the exposure of cells to H_2O_2 steady states was described in detail. Compared with the common bolus addition, in which H_2O_2 is delivered as a single initial dose, the steady-state incubation is much more complex to implement. However, the addition of H_2O_2 as a steady state provides more reproducible results and, by providing a rigorous control of H_2O_2 delivery, it allows to observe cellular effects that occur in narrow H_2O_2 concentration ranges that would be difficult to observe with the bolus addition. In our experience, after an initial learning curve, the higher complexity of the experimental procedure involved in the implementation of a H_2O_2 steady state is largely compensated by the higher experimental reproducibility that allows achieving statistically significant results with a lower number of experimental replicates. Moreover, the initial setup, in which

the kinetics of H_2O_2 consumption for the system under study is determined, may also provide useful information and unexpected findings. For example, the discovery of the regulation of plasma membrane permeability by H_2O_2 was triggered by the observation that H_2O_2-adapted yeast cells, which have higher levels of antioxidant enzymes, have kinetics of H_2O_2 consumption similar to control cells (Branco et al., 2004). In the field of nitric oxide research, it was soon recognized that the use of donors that provide continuous release of nitric oxide is more appropriate than the use of bolus additions of nitric oxide. Unfortunately, after several decades of research, in the field of H_2O_2, the use of a bolus addition is still the method of choice by a vast majority of researchers. The use of a H_2O_2 bolus addition, and the inherent lack of standardization, is responsible for apparently contradictory findings and a lack of rigorous quantitative data, which has delayed the development of the field (Brigelius-Flohé & Flohé, 2011). We suggest that the delivery of H_2O_2 to cells as a steady state should be the method of choice when studying regulatory effects of H_2O_2.

ACKNOWLEDGMENTS

Supported by Fundação para a Ciência e a Tecnologia (FCT), Portugal (Grants PTDC/QUI/69466/2006, PTDC/QUI-BIQ/104311/2008, and PEst-OE/QUI/UI0612/2011) and by NIH Grants RO1AG016718 (to E. C.) and PO1AG026572 (to Roberta D. Brinton).

REFERENCES

Antunes, F., & Cadenas, E. (2000). Estimation of H_2O_2 gradients across biomembranes. *FEBS Letters*, *475*, 121–126.

Antunes, F., & Cadenas, E. (2001). Cellular titration of apoptosis with steady-state concentrations of H_2O_2. Sub-micromolar levels of H_2O_2 induce apoptosis through Fenton chemistry independent of cellular thiol state. *Free Radical Biology & Medicine*, *30*, 1008–1018.

Bannai, S., & Tsukeda, H. (1979). The export of glutathione from human diploid cells in culture. *The Journal of Biological Chemistry*, *254*(9), 3444–3450.

Branco, M. R., Marinho, H. S., Cyrne, L., & Antunes, F. (2004). Decrease of H_2O_2 plasma membrane permeability during adaptation to H_2O_2 in *Saccharomyces cerevisiae*. *The Journal of Biological Chemistry*, *279*, 6501–6506.

Brigelius-Flohé, R., & Flohé, L. (2011). Basic principles and emerging concepts in the redox control of transcription factors. *Antioxidants & Redox Signaling*, *15*(8), 2335–2381.

Chance, B., Greenstein, D. S., & Roughton, F. J. W. (1952). The mechanism of catalase action. I. Steady-state analysis. *Archives of Biochemistry and Biophysics*, *37*, 301–339.

Chance, B., Sies, H., & Boveris, A. (1979). Hydroperoxide metabolism in mammalian organs. *Physiological Reviews*, *59*, 527–605.

Clément, M.-V., Ramalingam, J., Long, L. H., & Halliwell, B. (2001). The in vitro cytotoxicity of ascorbate depends on the culture medium used to perform the assay and involves hydrogen peroxide. *Antioxidants & Redox Signaling*, *3*(1), 157–163.

Covas, G., Marinho, H., Cyrne, L., & Antunes, F. (2013). Activation of Nrf2 by H_2O_2: De novo synthesis versus nuclear translocation. *Methods in Enzymology*, *526*.

Cyrne, L., Antunes, F., Sousa-Lopes, A., Diaz-Bérrio, J., & Marinho, H. S. (2010). Glyceraldehyde-3-phosphate dehydrogenase is largely unresponsive to low regulatory levels of hydrogen peroxide in *Saccharomyces cerevisiae*. *BMC Biochemistry*, *11*, 49.

Cyrne, L., Oliveira-Marques, V., Marinho, H., & Antunes, F. (2013). Activation of Nrf2 by H_2O_2: De novo synthesis versus nuclear translocation. *Methods in Enzymology*, *526*.

De Oliveira-Marques, V., Cyrne, L., Marinho, H., & Antunes, F. (2007). A quantitative study of NF-kappa B activation by H_2O_2: Relevance in inflammation and synergy with TNF-alpha. *The Journal of Immunology*, *178*, 3893–3902.

Flohe, L., Loschen, G., Gunzler, A., & Eichele, E. (1972). Glutathione peroxidase, V. The kinetic mechanism. *Hoppe-Seyler's Zeitschrift für Physiologische Chemie*, *353*, 987–999.

Griffith, O. W., Novogrodsky, A., & Meister, A. (1979). Translocation of glutathione from lymphoid cells that have markedly different γ-glutamyl transpeptidase activities. *Proceedings of the National Academy of Sciences*, *76*(5), 2249–2252.

Gülden, M., Jess, A., Kammann, J., Maser, E., & Seibert, H. (2010). Cytotoxic potency of H_2O_2 in cell cultures: Impact of cell concentration and exposure time. *Free Radical Biology & Medicine*, *49*(8), 1298–1305.

Hoffman, P. S., Pine, L., & Bell, S. (1983). Production of superoxide and hydrogen peroxide in medium used to culture *Legionella pneumophila*: Catalytic decomposition by charcoal. *Applied and Environmental Microbiology*, *45*(3), 784–791.

Koppenol, W. H. (1993). The centennial of the Fenton reaction. *Free Radical Biology & Medicine*, *15*, 645–651.

Makino, N., Mochizuki, Y., Bannai, S., & Sugita, Y. (1994). Kinetic studies on the removal of extracellular hydrogen peroxide by cultured fibroblasts. *The Journal of Biological Chemistry*, *269*(2), 1020–1025.

Marinho, H., Cyrne, L., Cadenas, E., & Antunes, F. (2013). The cellular steady-state of H_2O_2: Latency concepts and gradients. *Methods in Enzymology*, *526*.

Martín-Romero, F. J., Miguel-Lasobras, E. M., Domínguez-Arroyo, J. A., González-Carrera, E., & Alvarez, I. S. (2008). Contribution of culture media to oxidative stress and its effect on human oocytes. *Reproductive Biomedicine Online*, *17*(5), 652–661.

Matias, A. C., Marinho, H. S., Cyrne, L., Herrero, E., & Antunes, F. (2011). Biphasic modulation of fatty acid synthase by hydrogen peroxide in *Saccharomyces cerevisiae*. *Archives of Biochemistry and Biophysics*, *515*, 107–111.

Pedone, E., Bartolucci, S., & Fiorentino, G. (2004). Sensing and adapting to environmental stress: The archaeal tactic. *Frontiers in Bioscience*, *9*, 2909–2926.

Quinn, J., Findlay, V. J., Dawson, K., Millar, J. B. A., Jones, N., Morgan, B. A., et al. (2002). Distinct regulatory proteins control the graded transcriptional response to increasing H(2)O(2) levels in fission yeast *Schizosaccharomyces pombe*. *Molecular Biology of the Cell*, *13*(3), 805–816.

Sousa-Lopes, A., Antunes, F., Cyrne, L., & Marinho, H. S. (2004). Decreased cellular permeability to H_2O_2 protects *Saccharomyces cerevisiae* cells in stationary phase against oxidative stress. *FEBS Letters*, *578*(1–2), 152–156.

Winterbourn, C. C., & Hampton, M. B. (2008). Thiol chemistry and specificity in redox signaling. *Free Radical Biology & Medicine*, *45*(5), 549–561.

CHAPTER ELEVEN

Imaging H_2O_2 Microdomains in Receptor Tyrosine Kinases Signaling

Nataliya M. Mishina[*,†], Kseniya N. Markvicheva[*], Arkady F. Fradkov[*], Elena V. Zagaynova[†], Carsten Schultz[‡], Sergey Lukyanov[*,†], Vsevolod V. Belousov[*,†,1]

[*]Shemyakin-Ovchinnikov Institute of Bioorganic Chemistry, RAS, Moscow, Russia
[†]Nizhny Novgorod State Medical Academy, Nizhny Novgorod, Russia
[‡]EMBL Heidelberg, Heidelberg, Germany
[1]Corresponding author: e-mail address: vsevolod.belousov@gmail.com

Contents

1. Introduction 176
2. Experimental Design 176
   2.1 Choosing cell lines and stimuli 176
   2.2 Immobilizing HyPer within the cell 176
   2.3 Choosing transfection method and parameter selection for image acquisition 177
   2.4 Image processing and quantification 177
3. Materials 178
4. Procedure 179
   4.1 Creating HyPer fusion proteins 179
5. Transfection 180
   5.1 Preparation of transfected cells for the experiment 180
   5.2 Primary visualization 181
   5.3 Imaging settings 181
   5.4 Imaging 181
   5.5 Images processing and quantification 182
6. Anticipated Results 184
Acknowledgments 186
References 186

Abstract

HyPer, a ratiometric genetically encoded fluorescent sensor, is a popular tool for intracellular hydrogen peroxide detection. When expressed in cultured cells, the freely diffusing version of the sensor (HyPer-cyto) detects temporal patterns of H_2O_2 generation. However, rapid diffusion of the probe within the nucleocytoplasmic compartment averages the H_2O_2 signal even in cases of local oxidant production. Consequently, we

Methods in Enzymology, Volume 526
ISSN 0076-6879
http://dx.doi.org/10.1016/B978-0-12-405883-5.00011-9

© 2013 Elsevier Inc.
All rights reserved.

immobilized the sensor within specific subcellular compartments allowing it to monitor local increases in H_2O_2. Here, we provide a protocol of ratiometric imaging and ImageJ-based quantification of H_2O_2 microdomains produced by cells upon physiological stimulation.

1. INTRODUCTION

HyPer is a genetically encoded fluorescent indicator for H_2O_2 with ratiometric readout. Being expressed in its nontargeted version, HyPer diffuses freely within the nucleocytoplasmic compartment. This limits spatial resolution of H_2O_2 visualization. In case of a local H_2O_2 release by a particular organelle into the cytoplasm, diffusion of the sensor delocalizes the signal. The spatial resolution of the method can be easily improved by immobilizing HyPer near the potential source of H_2O_2 within the cell (Mishina et al., 2011). Here, we provide our view on immobilization strategies and detailed imaging protocols.

2. EXPERIMENTAL DESIGN

2.1. Choosing cell lines and stimuli

Generally, HyPer allows visualizing H_2O_2 production in different types of adherent cell cultures stimulated by various substances. Many growth factors and cytokines induce H_2O_2 production within cells upon activation of cell surface receptors. So far, HyPer has been successfully used in visualization of H_2O_2 production in PC12 cells stimulated with NGF (Belousov et al., 2006), HeLa and HT29 cells stimulated with epidermal growth factor (EGF) (Markvicheva, Bogdanova, Staroverov, Lukyanov, & Belousov, 2009; Miller, Tulyathan, Tulyanthan, Isacoff, & Chang, 2007; Mishina et al., 2011), fibroblasts stimulated with platelet-derived growth factor (PDGF) (Miller, Dickinson, & Chang, 2010; Mishina et al., 2011), angiotensin II stimulated cardiac myocytes (Malinouski, Zhou, Belousov, Hatfield, & Gladyshev, 2011), and RAW 264.7 macrophages phagocyting zymosan particles. The imaging conditions are generally the same for all cell types and stimuli.

2.2. Immobilizing HyPer within the cell

HyPer can be used in nontargeted and organelle-targeted versions. However, the best spatial resolution can be achieved by fusing the sensor with

proteins located just near the source of the oxidant. H_2O_2 has been shown to diffuse to a very short distance within the cell; therefore, the closer the sensor is to the H_2O_2 generator, the better the signal achieved. In recent work (Mishina et al., 2011), we suggested that the H_2O_2 sources in receptor tyrosine kinase (RTK) signaling colocalize with either activated receptor or PTP-1B phosphatase at the ER membrane as H_2O_2 oxidizes PTP-1B to prevent RTK dephosphorylation (Lee, Kwon, Kim, & Rhee, 1998; Lou et al., 2008; Meng, Buckley, Galic, Tiganis, & Tonks, 2004; Salmeen et al., 2003; Sartoretto, Kalwa, Pluth, Lippard, & Michel, 2011). Indeed, we found H_2O_2 generation in close proximity to both RTK and PTP-1B. Analysis of the curves suggests that the sources of the oxidant differ between these two locations. Generally, HyPer can be fused to a protein of interest just like regular fluorescent protein. Both N- and C-terminal fusions are possible (Belousov et al., 2006; Mishina et al., 2011). In the current protocol, we describe imaging of H_2O_2 with HyPer fused to RTKs as well as monitoring of near-ER H_2O_2 using HyPer attached to a "tail-anchor" C-terminal sequence of PTP-1B (Meng, Fukada, & Tonks, 2002). All fusions were prepared earlier (Mishina et al., 2011) using corresponding fusions with GFP variants by replacing the GFP-coding region with HyPer-coding DNA.

2.3. Choosing transfection method and parameter selection for image acquisition

These aspects are described in detail by Mishina et al. in Chapter 3.

2.4. Image processing and quantification

We process image time series using ImageJ software which is available as freeware from the Web. The aim of processing ratiometric time series is to obtain a series of images where each pixel except the background has value, indicating not only the intensity of the fluorescence, but also the ratio between intensities of the fluorescence excited with the 488-nm (or 496 nm) and the 405-nm lasers of the confocal system or the corresponding filters of a wide-field microscope. The time-course of the ratio change can be represented by line graphs. For this, a region of interest (ROI) is determined from which the average signal intensity is recorded. The data are then exported to an electronic table format (Excel or Origin).

3. MATERIALS

Reagents

- Vector pHyPer-cyto (Evrogen, cat. no. FP941) for the expression of HyPer-cyto in mammalian cells
- Vector pHyPer-nuc (Evrogen, cat. no. FP944) for the expression of HyPer with nuclear localization in mammalian cells and generation of fusion to C-terminus of HyPer (by replacing NLS sequence with the sequence encoding protein of interest)
- Vector pHyPer-dMito (Evrogen, cat. no. FP942) for the expression of HyPer with mitochondrial localization in mammalian cells and generation of fusions to N-terminus of HyPer (by replacing the double MTS with the sequence encoding protein of interest)
- DMEM (Invitrogen, cat. no. 41965-039)
- Minimum Essential Medium Eagle (EMEM) (Sigma–Aldrich, cat. no. M3024)
- OPTI-MEM (Invitrogen, cat. no. 31985-047)
- Hanks Balanced Salt Solution (HBSS) (Invitrogen, cat. no. 14025-100)
- Dulbecco-PBS (Invitrogen, cat. no. 14040-091)
- Fetal calf serum, FCS (Invitrogen, cat. no. 16000-044)
- Penicillin/streptomycin (Invitrogen, cat. no. 15070-063)
- L-Glutamine (Invitrogen, cat. no. 25030-024)
- Trypsin/EDTA solution (Invitrogen, cat. no. R-001-100)
- HEPES (Promega, cat. no. H5302)
- BSA (Sigma–Aldrich, cat. no. 9048-46-8)
- FuGene6 transfection reagent (Roche Diagnostics, cat. no. 11988387001)
- Mammalian cells

Critical. This protocol describes the use of HeLa-Kyoto and NIH-3T3 cell lines. However, the overall technique is applicable to any transfectable or transducible cell culture.

- Sodium bicarbonate
- PDGF (Sigma–Aldrich, cat. no. P8147)
- EGF (Sigma–Aldrich, cat. no. E4127)

Equipment

- Glass-bottom dishes (World Precision Instruments, cat. no. FD35-100)
- Standard equipment for eukaryotic cell culturing

Critical. For hard to transfect cell cultures, when using lentiviral vectors for delivery of HyPer cDNA, S2 safety level cell culture facility is required.

- Confocal microscope or wide-field fluorescent microscope, both equipped with a thermostating box

Critical. We found that efficient H_2O_2 production during growth factor stimulation requires 37 °C.

Critical. For ratiometric HyPer imaging, confocal microscopes should be equipped with lasers providing violet (405 nm) and blue (488 or 496 nm) laser lines. Alternatively, mercury or xenon arc lamps can be used for the HyPer imaging.

- ImageJ software (National Institutes of Health)
- Excel (Microsoft) or Origin (OriginLab Corporation)

Reagent setup

- Complete growth medium: For *NIH-3T3* cells, we use DMEM supplemented with penicillin/streptomycin, L-glutamine, and 10% FCS; for *HeLa-Kyoto* cells we use EMEM supplemented with 2.2 g/l sodium bicarbonate penicillin/streptomycin, L-glutamine, and 10% FCS.
  Critical. We found that the use of high-glucose DMEM abolishes H_2O_2 production by HeLa-Kyoto cells.
- Cell starvation and imaging medium: EMEM supplemented with either 2.2 g/l sodium bicarbonate and 20 m*M* HEPES (if CO_2 supply for thermostating box available) or just 20 m*M* HEPES (use bicarbonate-free media in case no CO_2 supply for thermostating box is available in order to prevent alkalinization of the imaging media), penicillin/streptomycin, L-glutamine, and 0.5% BSA.
- Preparation of growth factors for experiment: Usually, growth factor suppliers recommend the optimal protocol for storage. Just before the experiment, dilute a small aliquot of the growth factor in EMEM to prepare a 1000× stock solution (100 μg/ml EGF or 10 μg/ml PDGF). Keep on blue ice.

Equipment setup

Described in detail by Mishina et al. in Chapter 3.

4. PROCEDURE

4.1. Creating HyPer fusion proteins

1. Clone the protein of interest in-frame with HyPer using the appropriate cloning vector. When determining the composition of the construct (selecting the N- or C-terminal fusion variants and linkers lengths), take into account the locations of the functional domains and their ability to perform in fusion with FPs in order to maintain the protein function.

Preferably, consult the literature concerning the behavior of the protein of interest in N- or C-terminal fusion with one of the common monomeric fluorescent proteins, such as EGFP. Either N- or C-terminal fusion via appropriate amino acid linker may be more suitable to label the particular protein. HyPer is pH-sensitive. In case pH changes are anticipated in a particular experimental model, pH changes should be monitored with HyPer-C199S, which is not sensitive to H_2O_2 but retains pH sensitivity.

5. TRANSFECTION

2. Plate the cells on glass-bottom dishes.

   Pause point. After plating the cells, wait at least 12 h.

3. Transfect the cells with the HyPer or HyPer fusion encoding vector, using FuGene6 transfection reagent or by any other appropriate method. Useful tips for liposome-based transfection are highlighted in the manufacturer's protocols and in other sources (Dalby et al., 2004; Dickson, Cubitt, Tsien, & Moerner, 1997; Tiscornia, Singer, & Verma, 2006).

   Critical step. After 4-h incubation with liposome: DNA complex, we recommend rinsing the cells with HBSS and changing the medium to fresh prewarmed liposome-free complete culture medium. Transfection reagent protocols, including the one for FuGene6, usually allow leaving the liposome-containing medium unchanged before imaging. Indeed, the presence of the FuGene6 does not affect cell viability and target protein expression. However, it affects the efficiency of growth factor stimulation, probably inducing nonspecific endocytosis and oxidative stress.

4. Culture the cells for 12–48 h at 37 °C, 5% CO_2.

   Critical step. We found that for large fusions, such as RTK-HyPer, strong fluorescence appears in 24–36 h. Smaller fusions such as tail-anchored HyPer become visible in 12 h. After lentiviral transduction, 36–48 h may be required to detect fluorescence.

   Pause point. Incubate cells on a glass-bottom dish for 12–48 h at 37 °C, 5% CO_2.

5.1. Preparation of transfected cells for the experiment

5. For stimulation with growth factor, replace complete medium with 1.5 ml preheated (37 °C) imaging medium supplemented with 0.1% (wt/vol) BSA. Incubate for 2 h (for HeLa-Kyoto) or 4–6 h

(for NIH-3T3) at 37 °C. Keep the cells out of the CO_2 incubator if using bicarbonate-free imaging media.

Critical step. HeLa-Kyoto cells are sensitive to serum starvation. Keeping them without serum for more than 2 h may result in cytotoxicity. In contrast, NIH-3T3 fibroblasts survive during longer periods of serum starvation. Moreover, in some cases, even in cells starved for 6 h, background signaling could be observed resulting in filopodia formation and some NADPH oxidase activity.

5.2. Primary visualization

6. Visualize HyPer using a mercury or xenon arc lamp. Regular GFP or FITC filter sets allow visualizing fluorescence.

5.3. Imaging settings

Use the same microscope settings for HyPer time-lapse imaging as described by Mishina et al. in Chapter 3.

5.4. Imaging

7. Proceed with time-lapse imaging for option A for confocal microscopes or option B for wide-field fluorescent microscopes.

A. Confocal microscopy

i. At least 2 h before imaging, warm up the thermal incubator box to 37 °C.

ii. Place the dish with cells onto the microscope stage. Set up focus.

iii. Switch the system to a scanning mode.

iv. Perform a single scan. Zoom selected cells with "Zoom in" function of the Leica system or the "Crop" function of Carl Zeiss system.

v. Select an ROI in the selected cell and measure the signal intensity "ROI" function of the Carl Zeiss system or the "Quantification-Histogram" function of the Leica system.

vi. Set the fluorescence intensity in each channel of ROI to be in the range between 30 and 80 by changing the light intensity and/or PMT voltage.

vii. Perform several single scans to set the final focus, adjust laser power, and PMT voltage.

viii. Start time series recording. It is important to observe that the starting 405-/488 (496)-nm excitation ratio and microscope focus are stable over this prestimulation period.

ix. Growth factor stimulation: After 5–10 min of imaging, add drop by drop the growth factor diluted in 500 μl of prewarmed EMEM. Continue data acquisition for 30–60 min.

Critical step. Do not touch the microscope stage or the culture dish.

B. Wide-field fluorescent microscopy

i. Carry out the same procedures as in Step 7 (A) (i)–(iv).

ii. Perform several single scans to set the final focus, adjust light power, and exposure time. The initial fluorescence intensities in both channels in an ROI should be almost equal (±5–10%) and should be in the range between 30 and 70 for an 8-bit camera.

iii. Start time series recording. It is important to observe that the microscope focus is stable over the prestimulation period.

iv. Growth factor stimulation: After 5–10 min of imaging, add drop by drop the growth factor diluted in 500 μl of prewarmed EMEM. Continue data acquisition for 30–60 min.

Critical step. Do not touch the microscope stage or the culture dish.

Pause point. After data acquisition, the images can be analyzed offline at any time (Table 11.1).

5.5. Images processing and quantification

Analyze acquired data (from Step 7) offline in ImageJ software.

8. Opening data series. There are numerous ImageJ functions and plugins allowing time series opening. Both Leica ***.lei** and ***.lif** files as well as Carl Zeiss ***.lsm** files can be opened via the **LOCI/Bio-Formats Importer** plugin. Activate an option **Open each channel in its**

Table 11.1 Troubleshooting table

Step	Problem	Possible reason	Solution
7AB	No H_2O_2 production upon growth factor stimulation	**(i)** No or too short time of serum starvation **(ii)** Inappropriate cell culture medium **(iii)** Too high or too low cell passage number	**(i)** Increase the serum starvation time **(ii)** Check the recommended medium at the ATCC Web site. Change the FCS lot or manufacturer **(iii)** Thaw fresh cells or wait for several passages, respectively

own window. For Leica SP2, files can also be opened using the **File/Import/Image sequence** menu. The series will be opened containing all channels in sequential order for each frame. To split the channels use the plugin **Stacks/Shuffling/Deinterleave**. Each channel will appear in separate windows as single series of ***.tif** files. Single images inside SP2 metafile can be opened using the **File/Open** menu option. Carl Zeiss 510 files can be opened by the LSM reader plugin or the LSM toolbox plugin.

9. Measure background values in each channel using the instrument **Elliptical** or freehand selection and **Analysis/Measure** in the menu (or **Ctrl**+**M**). Then, after removing the selection, subtract the background values in each fluorescence channel using the **Process/Math/Subtract** command in the menu. If the background changes during the recording, use plugin **ROI/BG subtraction from ROI**.
10. Optionally, filter image series to improve the signal-to-noise ratio using **Process/Filters/Gaussian blur**. Use pixel radius 1 or 2 (the same for both channels).

Critical. This step should be excluded in case of nonconfocal wide-field series processing.

11. Convert image series to 32 bit using the **Image/Type/32-bit** command.
12. Remove pixel values from the background of the 420-nm stack via thresholding. Activate the **Image/Adjust/Threshold** command. A dialog window appears. By moving the roller bars, choose threshold values. Upper threshold levels should be maximal. All pixels above threshold appear highlighted in red. Background pixels should be black. Press the **Apply** button and choose to set background pixels to **Not-a-Number** (**NaN**). Pressing the **Reset** button will remove the red highlighting. Close the dialog window.

Critical step. This procedure should be applied only to the 420-nm stack.

13. Divide the 500-nm stack by the 420-nm stack using the **Process/Image calculator** dialog window. Choose the 500-nm image stack as **Image 1**, the 420-nm image stack as **Image 2** and the Operation **Divide**. The pixel values in the resulting stack will represent the ratio between the fluorescence intensities in both channels. Division of pixel values of the 500-nm stack background to the corresponding Not-a-Number pixels in the 420-nm stack will give Not-a-Number background in the resulting ratio stack. The resulting stack can be depicted in pseudocolors using a **Ratio** lookup table.

14. Choose single or multiple ROIs using the **Plugins/ROI/Multi Measure** tool or with the **Analyse/Tools/ROI manager** dialog box. These tools allow quantifying the time profiles. The resultant table can be saved and used in **.xls** format for Excel or Origin.

6. ANTICIPATED RESULTS

Imaging of EGF-induced H_2O_2 production in HeLa cells using nontargeted HyPer in a nonratiometric mode has been described before (Markvicheva et al., 2009). However, nontargeted HyPer (HyPer-cyto) does not reveal local sites of H_2O_2 formation. The protocol can be used to compare the kinetics of the responses of various HyPer localizations to growth factor stimulation. Figure 11.1 demonstrates typical EGFR-HyPer

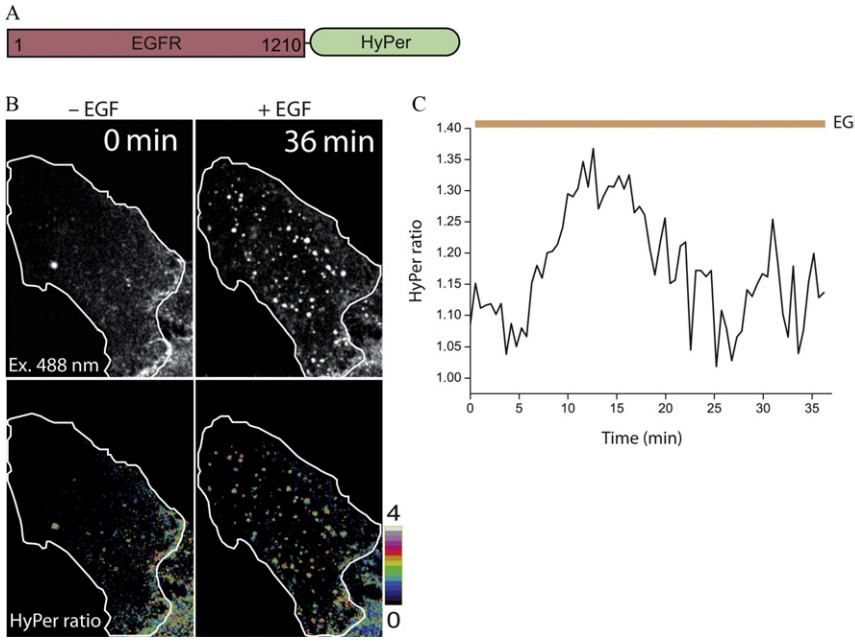

Figure 11.1 Targeting of HyPer to plasma and endosomal membranes. (A) Scheme of EGFR-HyPer construct. (B) Confocal images of EGFR-HyPer-expressing HeLa-Kyoto cells at the indicated time points before and 36 min after stimulation of the cell with 50 ng/ml EGF. Lower row of images represents the subcellular distribution of HyPer ratio. Upper row of images shows the subcellular distribution of EGFR-HyPer. Cell boundaries are highlighted. (C) Profile of HyPer ratio change near the cytoplasmic surface of the endosomes of cell shown on the panel (B). See also Supplementary Video 1 (http://www.elsevierdirect.com/companions/9780124058835). EGFR—epidermal growth factor receptor.

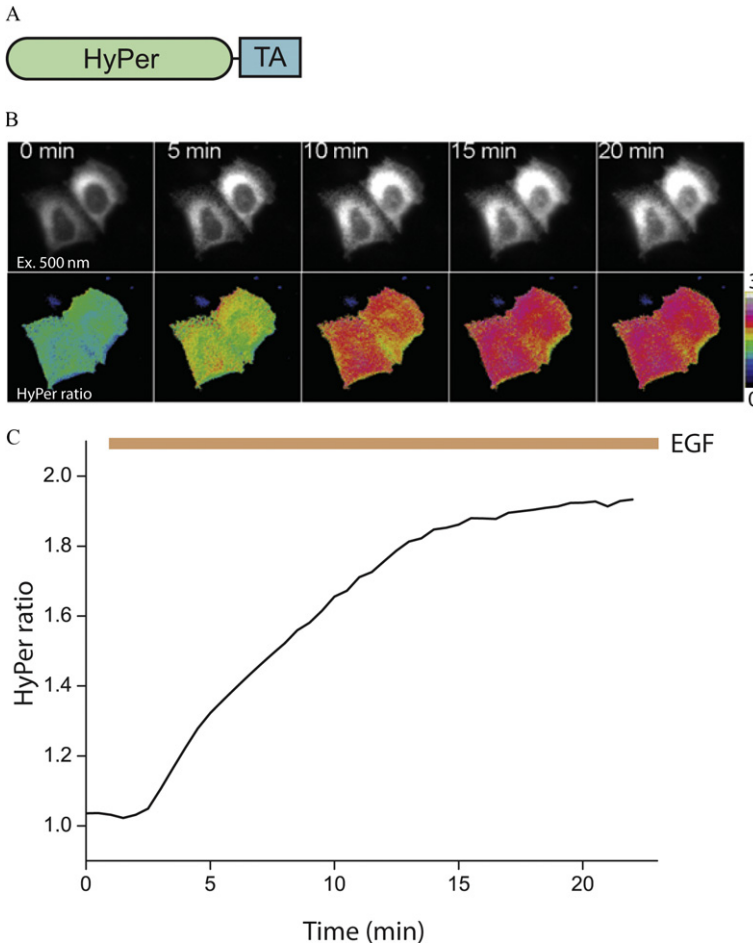

Figure 11.2 Targeting of HyPer to the cytoplasmic surface of the endoplasmic reticulum membrane. (A) Scheme of HyPer-TA construct. (B) Wide-field fluorescence images of HyPer-TA-expressing HeLa-Kyoto cells at indicated time points. Lower row of images represents subcellular distribution of HyPer ratio. Upper row of images shows the subcellular distribution of HyPer-TA. EGF (50 ng/ml) was added between the second and third frames shown. (C) Profile of HyPer ratio change near the cytoplasmic surface of the endoplasmic reticulum of cells shown on the panel (B). See also Supplementary Video 2 (http://www.elsevierdirect.com/companions/9780124058835). TA, tail anchor.

localization in serum-starved HeLa-Kyoto cells. Upon serum starvation, most of the fluorescence was localized at the plasma membrane of the cells (Fig. 11.1B, left). Stimulation of HeLa cells with EGF resulted in internalization of EGFR-HyPer into endocytic vesicles (Fig. 11.1B, right). HyPer ratio dynamics near endosomal membranes is shown in Fig. 11.1C.

Figure 11.2 illustrates HyPer-TA localized to the ER in HeLa cells. Upon stimulation of EGFR in HeLa cells, HyPer-TA monitored increases of H_2O_2 near the ER membrane (Fig. 11.2C). It is to be noted that the dynamics of [H_2O_2] near endosomes and ER upon growth factor stimulation are different.

In summary, HyPer is a unique tool allowing very sensitive and specific H_2O_2 detection. Its main advantage is its simplicity of use that, we hope, is reflected in the present protocol.

ACKNOWLEDGMENTS

This work was supported by the Russian foundation for basic research (RFBR) (10-04-01561-a, V. V. B.; 11-04-12187-ofi, S. L.), a joint EMBL-RFBR grant (12-04-92427 to C. S. and V. V. B.), Measures to Attract Leading Scientists to Russian Educational Institutions program (11.G34.31.0017 to S. L.), and the ESF EuroMembrane consortium TraPPs (to C. S.).

Author Contributions Statements. N. M. M. and K. N. M. designed and performed experiments, A. F. F. participated in cloning, V. V. B. conceived the project, C. S. provided expertise in cell signaling and imaging, E. V. Z. and S. L. provided project guidance and support, V. V. B., N. M. M., and C. S. worked on the text.

Competing financial interests. The authors declare that they have no competing financial interests.

REFERENCES

Belousov, V. V., Fradkov, A. F., Lukyanov, K. A., Staroverov, D. B., Shakhbazov, K. S., Terskikh, A. V., et al. (2006). Genetically encoded fluorescent indicator for intracellular hydrogen peroxide. *Nature Methods*, *3*, 281–286.

Dalby, B., Cates, S., Harris, A., Ohki, E. C., Tilkins, M. L., Price, P. J., et al. (2004). Advanced transfection with Lipofectamine 2000 reagent: Primary neurons, siRNA, and high-throughput applications. *Methods*, *33*, 95–103.

Dickson, R. M., Cubitt, A. B., Tsien, R. Y., & Moerner, W. E. (1997). On/off blinking and switching behaviour of single molecules of green fluorescent protein. *Nature*, *388*, 355–358.

Lee, S. R., Kwon, K. S., Kim, S. R., & Rhee, S. G. (1998). Reversible inactivation of protein-tyrosine phosphatase 1B in A431 cells stimulated with epidermal growth factor. *The Journal of Biological Chemistry*, *273*, 15366–15372.

Lou, Y.-W., Chen, Y.-Y., Hsu, S.-F., Chen, R.-K., Lee, C.-L., Khoo, K.-H., et al. (2008). Redox regulation of the protein tyrosine phosphatase PTP1B in cancer cells. *The FEBS Journal*, *275*, 69–88.

Malinouski, M., Zhou, Y., Belousov, V. V., Hatfield, D. L., & Gladyshev, V. N. (2011). Hydrogen peroxide probes directed to different cellular compartments. *PLoS One*, *6*, e14564.

Markvicheva, K. N., Bogdanova, E. A., Staroverov, D. B., Lukyanov, S., & Belousov, V. V. (2009). Imaging of intracellular hydrogen peroxide production with HyPer upon stimulation of HeLa cells with epidermal growth factor. *Methods in Molecular Biology*, *476*, 76–83.

Meng, T.-C., Buckley, D. A., Galic, S., Tiganis, T., & Tonks, N. K. (2004). Regulation of insulin signaling through reversible oxidation of the protein-tyrosine phosphatases TC45 and PTP1B. *The Journal of Biological Chemistry*, *279*, 37716–37725.

Meng, T.-C. , Fukada, T., & Tonks, N. K. (2002). Reversible oxidation and inactivation of protein tyrosine phosphatases in vivo. *Molecular Cell*, *9*, 387–399.

Miller, E. W., Dickinson, B. C., & Chang, C. J. (2010). Aquaporin-3 mediates hydrogen peroxide uptake to regulate downstream intracellular signaling. *Proceedings of the National Academy of Sciences of the United States of America*, *107*, 15681–15686.

Miller, E. W., Tulyathan, O., Tulyanthan, O., Isacoff, E. Y., & Chang, C. J. (2007). Molecular imaging of hydrogen peroxide produced for cell signaling. *Nature Chemical Biology*, *3*, 263–267.

Mishina, N. M., Tyurin-Kuzmin, P. A., Markvicheva, K. N., Vorotnikov, A. V., Tkachuk, V. A., Laketa, V., et al. (2011). Does cellular hydrogen peroxide diffuse or act locally? *Antioxidants & Redox Signaling*, *14*, 1–7.

Salmeen, A., Andersen, J. N., Myers, M. P., Meng, T.-C., Hinks, J. A., Tonks, N. K., et al. (2003). Redox regulation of protein tyrosine phosphatase 1B involves a sulphenyl-amide intermediate. *Nature*, *423*, 769–773.

Sartoretto, J. L., Kalwa, H., Pluth, M. D., Lippard, S. J., & Michel, T. (2011). Hydrogen peroxide differentially modulates cardiac myocyte nitric oxide synthesis. *Proceedings of the National Academy of Sciences of the United States of America*, *108*, 15792–15797.

Tiscornia, G., Singer, O., & Verma, I. M. (2006). Production and purification of lentiviral vectors. *Nature Protocols*, *1*, 241–245.

CHAPTER TWELVE

The Determination and Analysis of Site-Specific Rates of Mitochondrial Reactive Oxygen Species Production

Casey L. Quinlan*, Irina V. Perevoschikova*, Renata L.S. Goncalves*, Martin Hey-Mogensen*,†, Martin D. Brand*,1

*The Buck Institute for Research on Aging, Novato, California, USA
†Center for Healthy Aging, Department of Biomedical Sciences, Copenhagen University, Copenhagen, Denmark
1Corresponding author: e-mail address: mbrand@buckinstitute.org

Contents

1. Introduction 190
2. H_2O_2 Production Measurements in Isolated Mitochondria 191
   2.1 Techniques for the measurement of mitochondrial H_2O_2 release 193
   2.2 Background correction and calibration curve 194
   2.3 H_2O_2 detection: Platereader- versus cuvette-based assays 195
   2.4 Accounting for the antioxidant system 197
3. Maximum Production Rates from Specific Sites: The Nature and Capacity of the Machinery 198
   3.1 Complex I, NADH-ubiquinone oxidoreductase 200
   3.2 Complex II, succinate:ubiquinone oxidoreductase 203
   3.3 Complex III, cytochrome bc_1 complex 205
   3.4 Glycerol 3-phosphate dehydrogenase 207
   3.5 Electron-transferring flavoprotein–ETF ubiquinone oxidoreductase 209
   3.6 Dihydrolipoamide-containing enzyme complexes 211
4. Concluding Remarks 211
Acknowledgments 212
References 213

Abstract

Mitochondrial reactive oxygen species (ROS) are widely implicated in physiological and pathological pathways. We propose that it is critical to understand the specific sites of mitochondrial ROS production and their mechanisms of action. Mitochondria possess at least eight distinct sites of ROS production in the electron transport chain and matrix compartment. In this chapter, we describe the nature of the mitochondrial

Methods in Enzymology, Volume 526
ISSN 0076-6879
http://dx.doi.org/10.1016/B978-0-12-405883-5.00012-0

© 2013 Elsevier Inc.
All rights reserved.

ROS-producing machinery and the relative capacities of each site. We provide detailed methods for the measurement of H_2O_2 release and the conditions under which maximal rates from each site can be achieved in intact skeletal muscle mitochondria.

1. INTRODUCTION

The best-described role for mitochondria is as the primary supplier of cellular ATP. However, during this energy-transducing process, electrons can escape the electron transport chain and partially reduce oxygen to give rise to reactive oxygen species (ROS). There are at least eight sites capable of producing considerable amounts of ROS in the mitochondria (Brand, 2010). Most mitochondrial sites catalyze a monovalent reduction of oxygen to generate superoxide, but some sites are capable of direct formation of hydrogen peroxide (H_2O_2) from divalent reduction of oxygen. However, since we directly measure H_2O_2 with our detection system (after dismutation of superoxide to H_2O_2), and in many cases we cannot distinguish whether the originally formed species was superoxide or H_2O_2, we will use the general term ROS to mean superoxide/H_2O_2.

The mitochondrial electron transport chain ROS producers with the greatest capacity, in order of magnitude, are complex III (at the site of quinol oxidation: site III_{Q_o}), and complex I (at the ubiquinone-binding site: site I_Q) and complex II (at the flavin: site II_F) (Quinlan, Gerencser, Treberg, & Brand, 2011; Quinlan, Orr, et al., 2012; Treberg, Quinlan, & Brand, 2011), with each site generating greater than 1 nmol H_2O_2 min^{-1} mg $protein^{-1}$ under V_{max} conditions in skeletal muscle mitochondria. Of course, the rates of mitochondrial ROS production from a given site are tissue specific. For example, the rates of H_2O_2 measured from mitochondrial glycerol 3-phosphate dehydrogenase (mGPDH) are significantly lower from heart mitochondria than brown fat mitochondria due to the higher expression level of mGPDH in brown fat, whereas both brown fat and heart mitochondria are capable of very high rates of ROS production from site I_Q (Orr, Quinlan, Perevoshchikova, & Brand, 2012). Other mitochondrial ROS-producing sites include the flavin of complex I (site I_F) (Kussmaul & Hirst, 2006), electron-transferring flavoprotein ubiquinone oxidoreductase (ETFQOR) (Perevoshchikova, Quinlan, Orr, & Brand, 2013), the pyruvate dehydrogenase complex (PDH), and oxoglutarate dehydrogenase (OGDH) complex

(Bunik & Sievers, 2002), as well as less well-defined sites such as proline dehydrogenase and dihydroorotate dehydrogenase (Brand, 2010).

Due to their central role in cell metabolism and their ability to produce ROS, mitochondria are thought to be involved in many different physiological and pathological events, including cell differentiation, insulin secretion, cancer, and neurological disorders (Boden et al., 2012; Ralph & Neuzil, 2009; Sundaresan, Yu, Ferrans, Irani, & Finkel, 1995; Witte, Geurts, de Vries, van der Valk, & van Horssen, 2010). The free radical theory of aging (Harman, 1956) states that mitochondrial ROS are detrimental and ultimately causative of the aging process. In favor of this hypothesis, oxidative damage to mitochondrial DNA is observed in aged individuals (Golden & Melov, 2001). However, it is now appreciated that the role of ROS in aging is probably more nuanced than is allowed by the free radical theory. Increasing evidence indicates that a transient increase in ROS formation is a positive adaptive event that is associated with increased stress resistance and life span extension (Ristow & Schmeisser, 2011; Schulz et al., 2007; Zarse et al., 2012). In this sense, low levels of ROS seem to be positive, while high levels of ROS are detrimental (hormesis).

The apparently critical role of mitochondrial ROS in cellular processes makes characterization and quantification of the specific sites of ROS production of particular interest. In this chapter, we describe the experimental protocols that we use to measure site-specific ROS production from isolated mitochondria. We present mechanistic information about the sites and how we manipulate the conditions of our assays to maximize the rate from each site. This information provides a framework from which to interpret less contrived experiments, that is, experiments under "native" or non-V_{max} conditions. Figure 12.1 illustrates the eight known mitochondrial sites that will be discussed in this context.

2. H_2O_2 PRODUCTION MEASUREMENTS IN ISOLATED MITOCHONDRIA

Since the discovery of superoxide dismutase in mammalian cells and the resultant evidence for *in situ* ROS production (Boveris, Oshino, & Chance, 1972; McCord & Fridovich, 1969), there has been great interest in assessing cellular ROS levels and rates of production. As will be detailed in this chapter, there are multiple sites within the mitochondrion that are capable of reducing oxygen to superoxide. After its formation, superoxide is dismutated to hydrogen peroxide (H_2O_2) either spontaneously or by

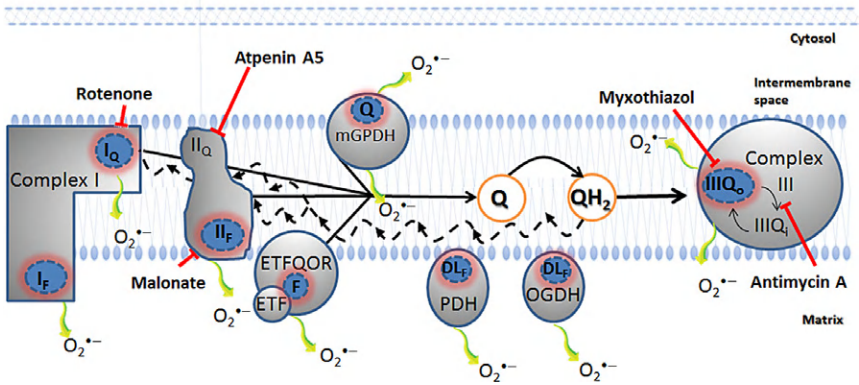

Figure 12.1 Eight sites of mitochondrial superoxide/H_2O_2 production are identified. Complex I oxidizes NADH from the tricarboxylic acid cycle and produces superoxide at the flavin site (I_F) and ubiquinone-binding site (I_Q), both sites release superoxide to the matrix side. Complex II, a tricarboxylic acid cycle enzyme bound to the mitochondrial inner membrane, oxidizes succinate to fumarate and generates superoxide/H_2O_2 both in the reverse and forward reactions through the flavin site (II_F). Glycerol 3-phosphate dehydrogenase (mGPDH) is part of an important shuttle for oxidation of cytosolic NADH and releases superoxide to both matrix and cytosol. The electron-transferring flavoprotein (ETF) and electron-transferring flavoprotein ubiquinone oxidoreductase (ETFQOR) represent the final steps for β-oxidation; it is not known which of the two sites is responsible for superoxide/H_2O_2 production during β-oxidation. The III_{Q_o} site of complex III is also a source of superoxide to both cytosol and matrix. In addition to the electron transport chain sites, pyruvate dehydrogenase (PDH) and oxoglutarate dehydrogenase (OGDH) both contain the dihydrolipoamide (DL) dehydrogenase subunit that can generate superoxide/H_2O_2, possibly through the DL or flavin moieties. The black solid line shows complex I, complex II, mGPDH, and ETFQOR feeding electrons into the ubiquinone (Q)-pool. With a very reduced Q-pool (QH_2), the electrons can run in reverse through complex I and complex II, promoting ROS generation at sites I_Q, I_F, and II_F (black dashed lines). The blunted arrows indicate the sites where the inhibitors rotenone, malonate, atpenin A5, myxothiazol, and antimycin A bind. The use of such inhibitors is necessary to pharmacologically isolate the sites of ROS production from each other.

the matrix located manganese-superoxide dismutase (Mn-SOD) or the cytosolic copper/zinc-superoxide dismutase. H_2O_2 possesses a longer half-life than superoxide and is considered to be less reactive. Furthermore, in contrast to superoxide, H_2O_2 is membrane permeant which enables its release from the mitochondrial matrix to the intermembrane space (Nohl & Jordan, 1980). Its stability and the membrane permeability make H_2O_2 the chosen species for detection of mitochondrial ROS production.

2.1. Techniques for the measurement of mitochondrial H_2O_2 release

The most commonly used and sensitive techniques for hydrogen peroxide detection are the enzyme-linked fluorescent techniques where horseradish peroxidase (HRP) reacts with hydrogen peroxide generating a compound which readily reacts with a probe (AH_2 in Eq. 12.1) that either becomes nonfluorescent or generates a fluorescent compound (A in Eq. 12.1) (Meng, High, Antonello, Washabaugh, & Zhao, 2005).

$$\mathrm{HRP} + \mathrm{H_2O_2} \rightarrow \mathrm{HRP} - \mathrm{H_2O_2} + \mathrm{AH_2} \rightarrow \mathrm{HRP} + 2\mathrm{H_2O} + \mathrm{A} \qquad [12.1]$$

Over the years, several H_2O_2 probes have been used, including scopoletin (Boveris, Martino, & Stoppani, 1977), *p*-hydroxyphenylacetate (Hyslop & Sklar, 1984), and homovanillic acid (Ruch, Cooper, & Baggiolini, 1983). Presently, however, Amplex Red (*N*-acetyl-3,7-dihydroxyphenoxazine) is the preferred probe by most groups when investigating ROS production from mitochondria. Amplex Red is not fluorescent itself but produces the fluorescent compound resurofin (7-hydroxy-3*H*-phenoxazin-3-one) when it reacts with HRP–H_2O_2 (Mohanty, Jaffe, Schulman, & Raible, 1997; Zhou, Diwu, Panchuk-Voloshina, & Haugland, 1997). Since resurofin is stable and accumulates in the extramitochondrial environment, the fluorescent signal will increase when H_2O_2 is released from the mitochondria. It is possible to detect resurofin by monitoring its absorbance at 557–620 nm, but the most sensitive detection is with spectrofluorimetric techniques (Staniek & Nohl, 1999).

Studies have shown that HRP/Amplex Red is selective for H_2O_2 (Mohanty et al., 1997) and highly sensitive, with the capacity to detect H_2O_2 amounts as low as 5 pmol (Zhou et al., 1997). In contrast to other well-known probes like scopoletin or homovallinic acid, the wavelengths used in the Amplex Red assay are relatively high (ex/em 560/590), making the assay less prone to interference from autofluorescent changes in biological samples (Zhou et al., 1997). Membranes are not permeable to HRP/Amplex Red, and therefore the assay detects only extramitochondrial H_2O_2 (Mohanty et al., 1997). Since the mitochondrial ROS-producing sites generate predominantly superoxide, the Amplex Red technique relies heavily on the endogenous Mn-SOD to convert the superoxide to H_2O_2. We also routinely add exogenous SOD to ensure detection of the superoxide that is released to extramitochondrial space (e.g., superoxide from mGPDH is released to both sides of the mitochondrial membrane). This also provides a useful tool when characterizing a specific ROS-producing site: withdrawal

or addition of exogenous SOD makes it possible to distinguish superoxide produced to the matrix from that produced to the intermembrane space (St-Pierre, Buckingham, Roebuck, & Brand, 2002).

Amplex Red reacts with HRP-H_2O_2 in a 1:1 stoichiometry. However, a linear relationship exists between H_2O_2 and resurofin fluorescence only when Amplex Red is fivefold in excess above the H_2O_2 concentration. This is because resurofin is prone to oxidation and generation of a nonfluorescent compound when it reacts directly with H_2O_2 at high concentrations (Mohanty et al., 1997). However, high concentrations of resurofin (above 5 μ*M*) can also cause an "inner filter" effect resulting in an underestimation of the signal and thus a nonlinear relationship with H_2O_2 (Brotea & Thibert, 1988). In our experiments, we use 50 μ*M* Amplex Red and our range of experimental detection is up to ~2 nmol H_2O_2, after which we start to see nonlinearity in the H_2O_2:resorufin fluorescence relationship.

2.2. Background correction and calibration curve

As with many fluorescent probes, Amplex Red is light sensitive and prone to oxidation and should therefore be protected from light during both experiments and storage (Zhou et al., 1997). During a standard assay, there is some spontaneous oxidation of Amplex Red/UltraRed causing a small background signal, which in our hands corresponds to 8–10 pmol H_2O_2 min^{-1} mg $protein^{-1}$ (typical assay conditions described below). Assuming that this rate is constant during the experiment, this background can be subtracted from all rates determined in the same sample/cuvette (this should, of course, be checked by running a background sample for the time duration of the experiment).

A benefit of the 1:1 stoichiometry provided by Amplex Red is that resorufin fluorescence is easily calibrated to molar units of H_2O_2. An essential feature of this calculation is established by a calibration curve between the fluorescent signal and a known concentration of H_2O_2. Several points are important when establishing this calibration curve:

1. The calibration curve should be generated in the exact experimental medium and in the presence of the isolated mitochondria. Previous studies have shown that mitochondria will scavenge some of the H_2O_2 during calibration (St-Pierre et al., 2002).
2. Many of the compounds used in different protocols have the potential to affect the fluorescent signal. For example, bovine serum albumin (BSA) has a moderate quenching effect (Muller et al., 2008), and therefore

calibrations should be done in its presence. The same is true for many of the pharmacological compounds and even some substrates commonly used, which may quench or have fluorescent properties. Thus, it is essential to generate the calibration curves under conditions that mimic the experimental conditions.

3. Since H_2O_2 will decay when in dilute solution, calibration curves should always be generated using freshly diluted H_2O_2. Typically, we make a working stock solution of 0.25 m*M* H_2O_2 and titrate from 0.25 to 1.5 nmol H_2O_2.

2.2.1 A brief note on Amplex UltraRed

We have recently switched from Amplex Red to Amplex UltraRed because it improves upon the performance of Amplex Red by providing brighter fluorescence and enhanced sensitivity in peroxidase-coupled assays. One of the disadvantages of many HRP-H_2O_2-related probes is their fluorescence instability with changes in pH. Amplex UltraRed exhibits much less sensitivity to pH changes and is more stable in the presence of H_2O_2 and thiols than its predecessor. Amplex UltraRed is stable for hours in the presence of mitochondria (unpublished observation) suggesting lower reactivity than its predecessor and is therefore preferred in our experiments. The structural differences between the compounds are not reported by the vendor (Invitrogen).

2.3. H_2O_2 detection: Platereader- versus cuvette-based assays

The rates of H_2O_2 generation by isolated mitochondria can be evaluated using a standard spectrofluorimeter equipped with one or more cuvette holders, or in a platereader capable of the appropriate excitation/emission. In our laboratory, the cuvette-based assays are performed in a Varian Cary Eclipse spectrofluorimeter or a Shimadzu RF5301-PC spectrofluorimeter. We typically use the excitation/emission wavelength pair 560/590 nm, respectively, in a total volume of 2 mL. For assays using 96-well microplates, we use a BMG Labtech microplate reader with filters suitable for excitation at 540 nm and emission at 590 nm, in a total volume of 0.2 mL.

The choice to use a platereader- or cuvette-based assay is the experimenter's prerogative, but there are constraints that might indicate the use of one technique as more sensible than the other. The principal advantage of cuvette-based assays is accuracy. In general, the experimenter has more control over the conditions in the cuvette and is able to monitor the conditions in real time. The mixing and temperature control are usually more

accurate in the cuvette than in the platereader, and the maintenance of a well-mixed suspension at the appropriate temperature is critical for precisely measuring rates of H_2O_2 generation. Another benefit to the cuvette-based assay is that different additions can be performed in series while the run is monitored, giving more flexibility to the assay. However, due to the limited number of cuvettes, the total assay time can be longer. The volume of the assay also necessitates the use of large amounts of protein (0.2–0.3 mg protein mL^{-1}).

Our assays in the cuvette are performed in a total volume of 2 mL. Each run is started with mitochondria (0.3 mg protein mL^{-1}), 50 μ*M* Amplex UltraRed (10 m*M* stock solution in DMSO), 5 units mL^{-1} HRP (1000 units mL^{-1} stock solution in H_2O), and 25 units mL^{-1} SOD (5000 units mL^{-1} stock solution in H_2O). A typical buffer is 120 m*M* KCl, 5 m*M* HEPES, 5 m*M* KH_2PO_4, 2.5 m*M* $MgCl_2$, 1 m*M* EGTA, and 0.3% (w/v) BSA, pH 7.0, 37 °C. Typically, we allow the mitochondria to oxidize endogenous substrates for 3–5 min before we add any inhibitors. After this initial phase, two protocols are possible: one with the inhibitors present before the substrate and the other with the substrate present before the inhibitors. In the first scenario, we collect a background rate in the presence of the inhibitors for several more minutes before we add the substrate of interest. In the second scenario, we add a substrate in the absence of inhibitors, collect a rate for several minutes and then add inhibitors in series. Typically, we perform experiments in both ways to dissect out the specific behavior of a given site or sites.

When working with a limited amount of protein (e.g., mitochondria isolated from cell culture or *Drosophila*), it is recommended to measure the rates of H_2O_2 production using the platereader since only 0.015 mg of mitochondrial protein are required per well. It is also preferred to create each test condition in parallel rather than to make additions in series, to minimize the number of times the platereader is opened, and to avoid fluctuations in the assay temperature. Typically, in our protocols, we establish a number of different experimental conditions in parallel in different wells and perform one addition to the wells mid run. For example, at time zero, the assay starts with the Amplex UltraRed/HRP detection system, mitochondria, and the desired inhibitors. After the establishment of a baseline, the run is paused to add the substrate and the signal is monitored for another 5 min.

Our assay in the platereader is set to a final volume of 0.2 mL in a buffer similar to the one exemplified above. The run starts with a volume of 180 μL, where 60 μL is from the mitochondrial stock (0.25 mg mL^{-1}), 60 μL from HRP stock (16.66 units mL^{-1}), 40 μL of the Amplex UltraRed

stock (0.25 m*M*), and 20 μL of the inhibitor stocks (the concentration varies according to the drug). All the components are diluted in the same assay buffer (e.g., the original 10 m*M* Amplex UltraRed stock in DMSO is diluted 40 × into assay buffer before use in the platereader assay). After several minutes to establish the background rate, 20 μL of substrate is added. We have observed that in the platereader the background rate, in the presence of Amplex UltraRed, HRP, and mitochondria, is in general higher than when using a standard spectrofluorimeter. This is likely due to the high intensity of incident light and broader spectrum of emitted light from the platereader. It is important to subtract the appropriate background for each condition. For this reason, a control parallel well with the H_2O_2-consuming enzyme catalase should be run to get a measure of the non-H_2O_2-specific probe oxidation. The H_2O_2 calibration curve is typically performed in multiple wells, with each well-containing mitochondria, Amplex UltraRed/HRP, the relevant inhibitors, and one concentration of H_2O_2 (typically, we titrate from 0.25 to 1.25 nmol H_2O_2).

2.4. Accounting for the antioxidant system

There are significant antioxidant systems within mitochondria, especially for the decomposition of H_2O_2 by glutathione (GSH) peroxidase (Schafer & Buettner, 2001). The fact that much of the mitochondrial ROS is generated within the matrix compartment means that any matrix antioxidant system has preferential access to H_2O_2 prior to its diffusion out into the medium where the detection system is present. Thus, the use of H_2O_2 production by mitochondria as a quantitative measure of the superoxide formed must assume zero or minimal interference from the antioxidant system. As the antioxidant system always functions to some extent, this assumption is unlikely to be correct and the measured rates of mitochondrial H_2O_2 production will always underestimate the true rates of production.

Matrix GSH peroxidases can decompose H_2O_2 into H_2O, forming GSSG (oxidized glutathione disulfide), which is reduced back to GSH as a result of NADPH oxidation by glutathione reductase. Since GSH is central to this peroxidase system, GSH-depleting agents are able to compromise the mitochondrial capacity to decompose H_2O_2. The observed mitochondrial H_2O_2 production can be increased by pretreatment with 1-chloro-2,4-dinitrobenzene (CDNB), which acts as a GSH-depleting agent through the irreversible conjugation of CDNB and GSH by glutathione-*S* transferase (Han, Canali, Rettori, & Kaplowitz, 2003; Treberg, Quinlan, & Brand,

2010). We have found that careful pretreatment of mitochondria with CDNB will give an increased ROS signal without significant damage to mitochondrial components. However, care should be taken when treating with CDNB because excess or acute CDNB treatment will result in increased ROS from complex I through a non-GSH pool-dependent mechanism (Liu, Fiskum, & Schubert, 2002; Treberg et al., 2010).

Our CDNB pretreatment protocol (Treberg et al., 2010) is based on Han et al. (2003). The final skeletal muscle mitochondria pellet is resuspended to a concentration of 5 mg protein mL^{-1} in our standard mitochondrial isolation buffer (100 m*M* KCl, 50 m*M* Tris, 2 m*M* EGTA, pH 7.1 at 25 °C). A 50 m*M* stock solution of CDNB is prepared in ethanol. The mitochondria are treated with either 35 μ*M* CDNB or ethanol control for 5 min at room temperature. Following the 5 min incubation, the suspensions are diluted with an equal volume of ice-cold isolation buffer and centrifuged for 5 min at 15,000 × *g* (at 2–4 °C). The pellets are then washed twice more by resuspending in ice-cold buffer and centrifuging as above to remove any residual CDNB/ethanol. The final pellets are resuspended to approximately 20 mg protein mL^{-1}.

Following CDNB treatment, a calibration curve can be built for a given set of conditions. For example, a titration with malate in the presence rotenone will generate matrix-directed superoxide. When this condition is compared between the CDNB- and control-treated mitochondria, we observe an increase in the rate of H_2O_2 production from the CDNB-treated mitochondria. We can then plot the CDNB rate against the control rate (as in Quinlan, Treberg, Perevoshchikova, Orr, & Brand, 2012; Treberg et al., 2010). Figure 12.2 is an example of a CDNB calibration curve (see legend for details). This CDNB calibration curve can be used to get a closer approximation of the production rates before interference by the antioxidant system. As mentioned above, this treatment is an approximation and is very particular to the conditions, so it should be determined robustly for every experimental system.

3. MAXIMUM PRODUCTION RATES FROM SPECIFIC SITES: THE NATURE AND CAPACITY OF THE MACHINERY

We are particularly interested in the nature of the mitochondrial ROS-producing machinery, and we have invested considerable effort in recent years to determine the specific behavior and capacity of several

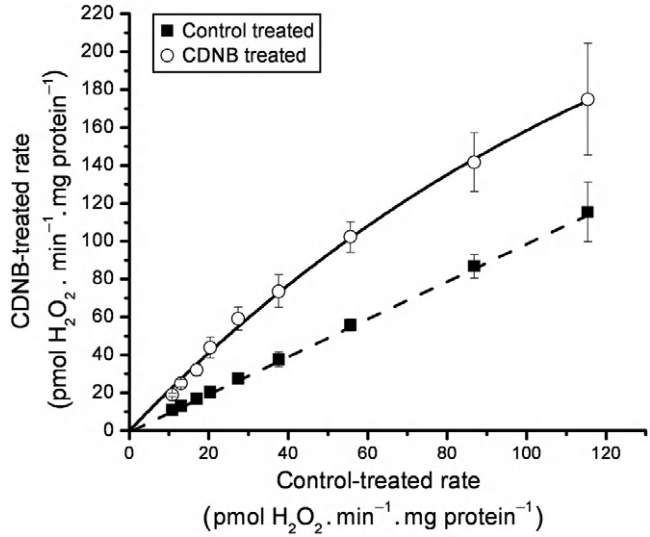

Figure 12.2 CDNB calibration curve. We generated this relationship by titrating malate (0.01–5 m*M*) into CDNB- and ethanol control-treated mitochondria. The rates of H_2O_2 production were measured after the addition of 4 μ*M* rotenone and assumed to be purely matrix directed. Points were fitted to give hyperbolic parameter values. The dashed line indicates a 1:1. *Adapted from Quinlan, Treberg, et al. (2012).*

mitochondrial ROS-producing sites (Lambert & Brand, 2004b; Orr et al., 2012; Perevoshchikova et al., 2013; Quinlan et al., 2011; Quinlan, Orr, et al., 2012; Quinlan, Treberg, et al., 2012; Treberg et al., 2011). In this section, we give an overview of the mechanisms and conditions needed to achieve maximum rates of ROS production from complex I, complex II, complex III, mGPDH, electron-transferring flavoprotein–ETF ubiquinone oxidoreductase (ETF-ETFQOR), and OGDH. The experiments described here were performed in simple KCl buffers using isolated mitochondria. Rat skeletal muscle mitochondria were isolated at 4 °C in Chappell-Perry buffer (CP1; 100 m*M* KCl, 50 m*M* Tris, 2 m*M* EGTA, pH 7.1 at 25 °C) by standard procedures (for a detailed protocol, see Affourtit, Quinlan, & Brand, 2012). Mitochondria were diluted to a final concentration of 0.3 mg protein mL^{-1} in KHE buffer (120 m*M* KCl, 5 m*M* HEPES, 1 m*M* EGTA, in the presence or absence of 5 m*M* phosphate and 2.5 m*M* magnesium, and supplemented with 0.3% (w/v) BSA, pH 7.0 at 37 °C). The measurements were performed in a Varian Cary spectrofluorimeter at the wavelength couple ex = 560 nm and em = 590 nm in the presence of 50 μ*M* Amplex UltraRed, 5 units mL^{-1} HRP, and 25 units mL^{-1} SOD.

The samples were added to a four-sided clear cuvette, under constant stirring and temperature control. The inhibitors were added to the concentrations described in each section below.

3.1. Complex I, NADH-ubiquinone oxidoreductase

Complex I (NADH-ubiquinone oxidoreductase) oxidizes NADH to NAD^+ and reduces ubiquinone (Q) to quinol (QH_2). During this process two electrons are transferred and four protons are pumped from the matrix to intermembrane space (Brown & Brand, 1988; Treberg & Brand, 2011). The overall reaction can be presented as:

$$NADH + H^+ + 4H^+_{inside} + Q \leftrightarrow NAD^+ + 4H^+_{outside} + QH_2$$

The electron transfer through the complex occurs at several steps using intermediate redox centers with increasing value of their redox potentials (Fig. 12.3).

As well as transducing energy, NADH-ubiquinone oxidoreductase is known to produce superoxide at two different sites within the complex (Treberg & Brand, 2011). The existence of a second site of superoxide production by complex I has been disputed (Kussmaul & Hirst, 2006; Pryde &

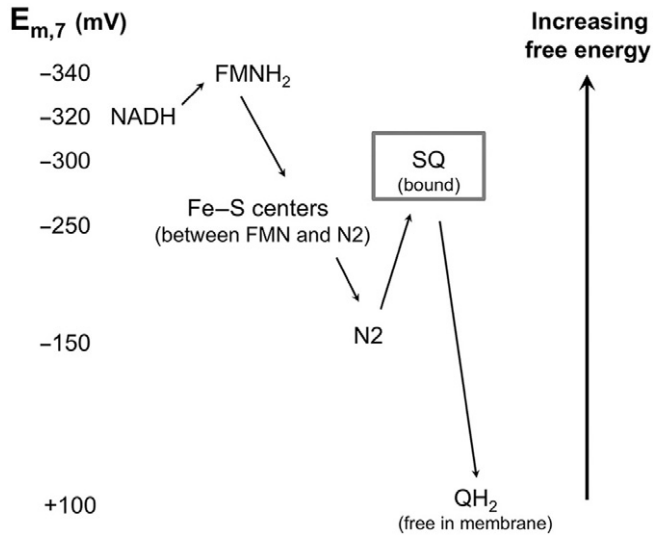

Figure 12.3 Reduction potentials of complex I redox centers. Electrons are moved from NADH to QH_2 through redox centers of increasing potentials. Center N2 is the terminal and highest mid-point potential [4Fe–4S] cluster. SQ is the proposed semiquinone ROS producer. *Adapted from Treberg and Brand (2011).*

Hirst, 2011), but we and others think that the experimental evidence supports two different sites of superoxide production rather than a single site (Ohnishi, Shinzawa-Itoh, Ohta, Yoshikawa, & Ohnishi, 2010; Treberg et al., 2011; Vinogradov & Grivennikova, 2005).

The first superoxide-producing candidate is the NADH-oxidizing site or flavin site (site I_F). Superoxide production by this site is thought to occur by the leak of electrons from the reduced flavin (FMNH and/or $FMNH_2$) to molecular oxygen (Kussmaul & Hirst, 2006; Pryde & Hirst, 2011). For purposes of simplicity and consistency, we will refer to the fully reduced flavin, $FMNH_2$, as the electron donor to oxygen (Kussmaul & Hirst, 2006). The oxidation of NADH at complex I reduces FMN. Because electrons can be transferred to oxygen from the flavin only when it is reduced, the steady-state concentration of reduced $FMNH_2$ will determine the rate of superoxide production. In turn, the higher the NADH/NAD ratio, the higher the rates of superoxide production from site I_F (Hansford, Hogue, & Mildaziene, 1997; Kushnareva, Murphy, & Andreyev, 2002; Starkov & Fiskum, 2003).

Any protocol that fully reduces the NADH pool would be predicted to maximize ROS production from site I_F, but depending on the source of electrons that are used to accomplish full NADH reduction, recruitment of other matrix ROS producers (e.g., OGDH) may or may not be predicted. It is necessary to distinguish site I_F from other matrix located enzymes that also respond to the reduced NADH pool. As an example, a protocol with 5 m*M* glutamate plus 5 m*M* malate and 4 μ*M* rotenone will fully reduce the NADH pool and provide a measurable ROS signal. However, this signal does not necessarily all arise from site I_F but could be partially assigned to OGDH. With respect to this, matrix sites have not routinely been distinguished from each other in intact mitochondria, and quoted rates of site I_F ROS production usually include ROS production from OGDH.

The second site of superoxide production within complex I is the ubiquinone-reducing site, site I_Q. The leak of electrons to molecular oxygen is proposed to occur from the semiquinone ($QH^{\cdot -}$) moiety formed as an intermediate during electron transfer from center N2 to oxidized ubiquinone (Treberg & Brand, 2011). Superoxide production at site I_Q can be instigated by two different conditions. The first condition, commonly referred to as "reverse electron transfer," is achieved in the presence of a high proton motive force and oxidized NAD pool. This involves a full reversal of complex I in which QH_2 is oxidized and NAD^+ is reduced. It is proposed that a semiquinone superoxide producer is stabilized in the complex in the presence of high protonmotive force. In this case, reduction of the

ubiquinone pool (Q-pool) and generation of a high protonmotive force can be achieved through several pathways. For example, maximum rates of superoxide production from site I_Q can be approached during oxidation of succinate or glycerol 3-phosphate (electrons enter the Q-pool through complex II or glycerol 3-phosphate dehydrogenase, respectively), which both reduce the Q-pool and generate a sufficiently high protonmotive force. High protonmotive force was found to be an important component to trigger reverse electron flow into site I_Q (Adam-Vizi & Chinopoulos, 2006; Korshunov, Skulachev, & Starkov, 1997; Lambert & Brand, 2004b; Miwa, St-Pierre, Partridge, & Brand, 2003; Votyakova & Reynolds, 2001). However, between the two components of protonmotive force (protonmotive force $= \Delta\psi_m - 60\Delta pH$, where $\Delta\psi_m$ is the membrane potential across the mitochondrial inner membrane), ΔpH has the strongest influence (Lambert & Brand, 2004b). The rate of I_Q superoxide production can be suppressed by collapsing the ΔpH with the K^+/H^+ ionophore nigericin or inorganic P_i, without abolishing $\Delta\psi_m$ (Lambert & Brand, 2004b). The rate of superoxide production in this case is sensitive to the I_Q site inhibitor rotenone, which blocks the oxidation of QH_2 and limits the formation of the superoxide-generating semiquinone. In the presence of rotenone, the Q site likely stays fully reduced as QH_2 and does not contribute to superoxide production.

The second condition known to stimulate I_Q superoxide production can be reached during forward electron flow (oxidation of reduced NADH) in the presence of Q site inhibitors (rotenone) and protonmotive force generated by ATP hydrolysis (Lambert & Brand, 2004a; Treberg et al., 2011). Under this condition, both sites (I_F and I_Q) contribute to the total observed rate, but I_Q shows the higher rate of superoxide production and a strong ΔpH sensitivity (Lambert & Brand, 2004a). As in the first condition, the I_Q site produces superoxide by the leak of electrons from the semiquinone moiety. However, when electrons are fluxing in the forward direction, the formation of ΔpH (generated by ATP hydrolysis) reverses the proton pumps and drives electrons from QH_2 to center N2 (Treberg et al., 2011). Therefore, semiquinone can be formed even in the presence of rotenone. Here, center N2 is reduced by forward electron flow as a result of the highly reduced NADH pool. This condition stabilizes the semiquinone in site I_Q and results in superoxide production.

Experimentally, maximum rates from site I_Q are best achieved from reverse electron transport. Conditions favoring V_{max} are found in a buffer lacking phosphate so that a large pH gradient is maintained. Although site

I_Q still generates ROS with phosphate present and a minimized ΔpH, the rates are lower. The chosen substrate should be one that will reduce the Q-pool and generate a high protonmotive force. In most tissues, succinate oxidation will accomplish this. However, any substrate that donates electrons to the Q-pool and generates a protonmotive force will suffice (e.g., glycerol 3-phosphate). Rotenone (4 μ*M*) should be added to dissect the rate that is specific to site I_Q versus the rate arising from other sites (e.g., sites I_F and III_{Q_o} both likely contribute to the total observed rates under conditions of a high protonmotive force and reduced NAD and Q-pools).

3.2. Complex II, succinate:ubiquinone oxidoreductase

Succinate dehydrogenase (SDH), succinate:ubiquinone oxidoreductase, or complex II are the common names for the only tricarboxylic acid cycle enzyme that is also part of the mitochondrial electron transport chain; it couples the two-electron oxidation of succinate to the reduction of the Q-pool. When succinate is oxidized to fumarate, electrons are moved from the flavin moiety through three iron–sulfur clusters to the membrane-embedded subunits that contain the cytochrome *b* heme moiety and the hydrophobic subunits that provide the binding site for ubiquinone (Sun et al., 2005; Yankovskaya et al., 2003).

There are several lines of evidence that indicate that complex II is capable of ROS production. The enzyme isolated from *Escherichia coli* or purified from bovine heart has been reported to generate superoxide under some conditions (Messner & Imlay, 2002; Zhang, Yu, & Yu, 1998). Recently, we found in isolated skeletal muscle mitochondria that a large SDH-specific ROS signal can be observed when the succinate concentration is low and electron efflux out of the complex is limited (details below) (Quinlan, Orr, et al., 2012). From this study, we drew the conclusion that SDH is capable of generating ROS at high rates both in the forward (from succinate to the Q-pool) and reverse (from the reduced Q-pool backward to the flavin site) reactions (Quinlan, Orr, et al., 2012). It has been suggested that both the flavin site (site II_F) and the ubiquinone-binding site (site II_Q) are capable of donating electrons directly to O_2 and producing ROS (Paranagama et al., 2010). However, our experimental data support the hypothesis that ROS formation occurs only at site II_F (Quinlan, Orr, et al., 2012).

In isolated mitochondria, succinate is commonly used to stimulate high rates of oxygen consumption and ROS generation. Most of the ROS signal observed during the oxidation of 5 m*M* succinate is rotenone sensitive and

therefore attributable to the ubiquinone-binding site of complex I (site I_Q) due to the backflow of electrons from the reduced Q-pool (as described in Section 3.1). After addition of rotenone, the remaining rate can be further suppressed by addition of the complex III Q_o site inhibitor, myxothiazol. Under this condition, when sites I_Q and III_{Q_o} are inhibited (and site I_F generates little ROS because the NAD pool remains mostly oxidized), it is still possible to measure significant rates of H_2O_2 production. We found that in the presence of rotenone and myxothiazol, peak H_2O_2 production was triggered at low succinate concentrations (e.g., 400 μ*M*). In fact, we observed a bell-shaped dependence of the ROS production rates on succinate concentration, with the left end of the curve presumably limited by substrate availability and the right end limited by succinate itself. We observed that the ROS production from complex II was exquisitely sensitive to its substrate and substrate analogues (i.e., fumarate, oxaloacetate, malonate) and also partially sensitive to inhibitors of the Q-binding site (carboxins and atpenin A5).

To assess peak ROS production by complex II in the forward direction, the mitochondria should be incubated with electron transport chain inhibitors before the substrate. The inhibitors are: 4 μ*M* rotenone (to block reverse electron transfer from the reduced QH_2 pool at site I_Q) and 2 μ*M* myxothiazol (to inhibit any contribution of site III_{Q_o} to ROS formation). The rationale of adding the inhibitors before succinate is to limit the accumulation of the products of succinate oxidation that will reduce NADH (this condition favors malate exchange on the dicarboxylate carrier rather than malate oxidation and NADH formation by malate dehydrogenase). Therefore, the ROS signal is cleaner without concerns of contributions from those ROS producers that are in communication with the NADH pool (e.g., site I_F and OGDH). From here, a titration of succinate should be performed to look for the peak rate under this condition. There is a "sweet spot" that is likely to be different in different mitochondrial preparations. In skeletal muscle mitochondria, we found that peak ROS production by complex II was stimulated by 400 μ*M* succinate (generating ~1.1 nmol H_2O_2 min^{-1} mg $protein^{-1}$) (Quinlan, Orr, et al., 2012). In this condition, the ROS rates are predictably sensitive to the addition of the competitive inhibitor malonate (0.5 m*M*). However, a 50% reduction in the rate is also observed after the addition of the Q-binding site inhibitor atpenin A5 (1 μ*M*). It is important to note in this condition that inhibitors of the Q-binding site have direct effects on substrate oxidation (i.e., they behave noncompetitively and lower the V_{max} of the enzyme). Indeed, upon analysis of the enzyme activation state in the presence

of atpenin A5, we drew the conclusion that the inhibition in ROS rates observed after addition of atpenin A5 could be ascribed to inhibitory effects at site II_F, not inhibition of ROS production at II_Q (Quinlan, Orr, et al., 2012).

To assess maximal ROS production by complex II in the reverse direction, mitochondria are again incubated in the presence of the inhibitors (4 μ*M* rotenone and 2 μ*M* myxothiazol) before the addition of substrate. For an easily interpretable ROS signal, we have worked with glycerol 3-phosphate as the reductant of the Q-pool (20 m*M* in skeletal muscle mitochondria, plus 200 n*M* free Ca^{2+} to increase the affinity of mGPDH for its substrate—see Section 3.4). Glycerol 3-phosphate reduces Q directly through mGPDH without affecting tricarboxylic acid cycle intermediates. Under this condition, the SDH contribution to the total signal can be assessed by its sensitivity to either 0.5 m*M* malonate or 1 μ*M* atpenin A5. It is also of note that the equivalent response to two inhibitors that bind at different sites is strong evidence that the ROS arise from a single site (II_F). ROS production driven by reverse electron transport from QH_2 into complex II during oxidation of glycerol 3-phosphate can also be observed during state 4 respiration, in the absence of complex III inhibitors, but it is a smaller proportion of the total in this condition (Quinlan, Orr, et al., 2012).

3.3. Complex III, cytochrome bc_1 complex

Complex III is an important site of energy transduction in the electron transport chain; it transfers reducing equivalents from ubiquinol in the lipid phase to the higher potential acceptor in the aqueous phase (cytochrome *c*) while performing a critical role in energy conservation. Complex III operates by a Q-cycle mechanism (Crofts, 2004; Mitchell, 1975; Trumpower, 1990). The enzyme's kinetic mechanism proceeds through a bifurcated electron transfer at the quinol oxidation site (Q_o site) that results in the first electron moving down the high potential chain (Rieske Fe–S to cytochrome c_1 to cytochrome *c*) as the second electron is sent down the low potential chain (cytochrome b_{566} to cytochrome b_{562}) where it ultimately reduces a ubiquinone (in the Q_i site) to regenerate quinol as part of the Q-cycle. In this way, two turns of the Q-cycle result in the oxidation of two quinols in the Q_o site and the reduction of one ubiquinone in the Q_i site. Energy conservation is achieved by the net movement of two electrons from quinol to cytochrome *c*, which drives the loss of two protons from the matrix and the

appearance of four protons in the intermembrane space (ΔpH), and the transfer of two negative charges inward to the matrix ($\Delta\psi_m$).

Complex III is suspected to be a physiologically relevant source of mitochondrial ROS (Bell et al., 2007; Klimova & Chandel, 2008). It is well established that the complex generates significant amounts of superoxide in the presence of antimycin A, an inhibitor of the quinol reduction site (Q_i site) (Boveris & Cadenas, 1975; Muller, Roberts, Bowman, & Kramer, 2003). These high rates arise because antimycin blocks electron flux out of the *b* cytochromes in the low potential chain and increases formation of the superoxide-precursor semiquinone in the Q_o site (Van den Berg et al., 1979). As the precursor to superoxide is the semiquinone (Muller, Crofts, & Kramer, 2002), one would predict that the highest rates of superoxide production would be observed when site III_{Q_o} is saturated with substrate (fully reduced Q-pool). However, somewhat surprisingly, it has been observed that conditions that slightly oxidize the Q-pool result in maximal rates of superoxide production from complex III (Drose & Brandt, 2008; Erecinska, Wilson, & Miyata, 1976; Quinlan et al., 2011). For example, mitochondria oxidizing 5 m*M* succinate in the presence of antimycin will generate superoxide at high rates (~1.2 nmol H_2O_2 min^{-1} mg $protein^{-1}$), but these rates are only ~50% of the maximal rates that are achieved when the condition is 5 m*M* succinate plus 5 m*M* malonate (Quinlan et al., 2011). In a recent study, we correlated the maximal rates of production from site III_{Q_o} with an intermediate reduction state of cytochrome b_{566} (70–80% reduced). We modeled this behavior and found that the phenomenon could be explained by a decrease in the rate constant for quinol oxidation (semiquinone formation) when antimycin is present and an even greater decrease when cytochrome b_{566} is maximally reduced. We also found that the reduction state of cytochrome b_{562} was correlated to the stability of the semiquinone in the Q_o site (Quinlan et al., 2011).

The relationship between the reduction states of cytochrome b_{566} and b_{562} is critical to the mechanism of superoxide production at complex III. We observed that in the presence of antimycin and an applied membrane potential (generated through ATP hydrolysis), the peak superoxide production at intermediate b_{566} reduction was lost. This phenomenon can be explained by the electron distribution between the two cytochromes. Due to its more positive mid-point potential, b_{562} is the preferred electron acceptor when there is no membrane potential (West, Mitchell, & Rich, 1988). However, in the presence of an electrical potential across the

membrane, the distribution of electrons between cytochrome b_{566} and cytochrome b_{562} is expected to be equalized. This is an important observation for the physiological mechanism of superoxide production from site III_{Q_o}: under normal physiological conditions, as cytochrome b_{566} becomes more reduced, superoxide production from this site will increase exponentially. Indeed, this is what we and others have found (Quinlan et al., 2011; Quinlan, Treberg, et al., 2012; Rottenberg, Covian, & Trumpower, 2009).

To design an experiment to observe maximum rates from site III_{Q_o}, mitochondria should be incubated with 2 μ*M* antimycin A and subsaturating substrate. This condition can be met as described above by titrating succinate with malonate until an intermediate Q-pool reduction state is achieved, or another substrate combination (e.g., glutamate plus malate) can be titrated down to subsaturating concentrations. These titrations will exhibit a bell-shaped curve for superoxide production from site III_{Q_o}, with the highest rates associated with 70–80% reduction of cytochrome b_{566}. However, in the presence of a membrane potential (i.e., in the absence of antimycin A), one would predict the superoxide rates from site III_{Q_o} to increase as the reduction of cytochrome b_{566} increases, without a peak observed at an intermediate reduction state (Quinlan et al., 2011; Quinlan, Treberg, et al., 2012). The rate that is assigned as specific to III_{Q_o} should be determined by its sensitivity to Q_o site inhibitors myxothiazol or stigmatellin.

3.4. Glycerol 3-phosphate dehydrogenase

mGPDH is located at the outer leaflet of the mitochondrial inner membrane (Klingenberg, 1970) and comprises part of the glycerolphosphate shuttle. mGPDH oxidizes glycerol 3-phosphate to dihydroxyacetone phosphate, and in turn, dihydroxyacetone phosphate is reduced back to glycerol 3-phosphate by the cytosolic form of GPDH. In this way, reducing equivalents in the cytosol (from NADH oxidation) are transported to the mitochondria (through QH_2 formation) where they can contribute to mitochondrial generation of ATP (Klingenberg, 1970).

The cytosol-facing orientation of mGPDH means that its substrate, glycerol 3-phosphate, does not require transport into the mitochondria. mGPDH is an FAD-linked ubiquinone oxidoreductase that donates its electrons directly to the Q-pool. Oxidation of glycerol 3-phosphate is known to

stimulate mitochondrial ROS production (Drahota et al., 2002; Miwa et al., 2003; Tretter, Takacs, Hegedus, & Adam-Vizi, 2007). By virtue of its point of electron entry (a direct reductant of the Q-pool), mGPDH is capable of generating ROS from many sites in the mitochondria (i.e., sites III_{Q_o}, I_F, I_Q, and II_F may all be reduced when electrons enter through mGPDH). However, mGPDH is also known to generate ROS (likely superoxide) itself, which are released to both the matrix and the intermembrane space (Orr et al., 2012).

ROS production from mGPDH is affected by several factors. The enzyme has a calcium-binding domain, which results in an increased affinity for its substrate (decreased K_M) when calcium concentrations are increased (Wernette, Ochs, & Lardy, 1981). Furthermore, since electrons from the enzyme are donated to the Q-pool, the redox poise of the Q-pool also affects ROS production from mGPDH (Orr et al., 2012). In a recent study, we showed that in mitochondria the important variables controlling ROS production from mGPDH were expression of the enzyme (dependent on tissue type), substrate concentration, calcium concentration, and reduction state of the Q-pool (Orr et al., 2012).

When designing an experiment to assess mGPDH ROS production, there are several important factors to take into consideration. First, the secondary effects of glycerol 3-phosphate itself need to be assessed and mitigated. Progressive inhibition of H_2O_2 production, respiration, and membrane potential has been observed at higher glycerol 3-phosphate concentrations (Orr et al., 2012). We found that this response was usually observed at concentrations above 20 m*M* and could be attributed to the type and amount of counter ion in the glycerol 3-phosphate preparation. To minimize artifacts caused by excess glycerol 3-phosphate, we perform experiments in the presence of 250 n*M* free Ca^{2+} to decrease the enzyme's K_M for glycerol 3-phosphate (Orr et al., 2012). We also use only the disodium salt of glycerol 3-phosphate and keep the final concentration in the experiment below 20 m*M*. The total concentration of glycerol phosphate can also be decreased by employing only the active isomer (*sn*-glycerol 3-phosphate) as substrate. However, even with these precautions, glycerol 3-phosphate has effects on the Amplex UltraRed detection system and those should be taken into account by performing the H_2O_2 calibration in its presence. Once these factors have been taken into account, to assess superoxide production from mGPDH without contribution from other sites, the experiment should be performed in the presence of 4 μ*M* rotenone, 0.5 m*M*

malonate, and 2 μ*M* myxothiazol. This will block electron flux through complexes I, II, and III, respectively and should provide a relatively pure mGPDH signal as long as NAD remains oxidized.

3.5. Electron-transferring flavoprotein–ETF ubiquinone oxidoreductase

ETF–ETFQOR transfers electrons from β-oxidation and the branched-chain amino acid metabolic pathways to the Q-pool. By this pathway, energy from fat and amino acid oxidation can be used to generate protonmotive force and contribute to ATP synthesis. ETF is a soluble FAD-containing protein in the matrix that accepts electrons from nine primary flavoprotein dehydrogenases, including the four straight-chain-specific fatty acyl-CoA dehydrogenases (medium-, short-, long-, and very-long-chain dehydrogenases), as well as several dehydrogenases involved in the catabolism of amino acids (isovaleryl-CoA dehydrogenase, Ikeda & Tanaka, 1983b; glutaryl-CoA dehydrogenase, Lenich & Goodman, 1986; and short-branched-chain-CoA dehydrogenase, Ikeda & Tanaka, 1983a) and choline (sarcosine and dimethylglycine dehydrogenases, Frisell & Mackenzie, 1962). ETFQOR is an inner membrane-bound protein that contains two main redox centers, FAD and Fe–S, and has a ubiquinone-binding site (Watmough & Frerman, 2010; Zhang, Frerman, & Kim, 2006). Its main function is to oxidize reduced ETF and transfer electrons to the Q-pool. Flavoprotein dehydrogenases transfer a total of two electrons to ETF with the formation of semireduced ETF as an intermediate (Ramsay, Steenkamp, & Husain, 1987; Ruzicka & Beinert, 1977). The rate constant of the first electron transfer reaction is several fold faster than that of the second electron transfer reaction and therefore the FAD moiety in ETF is thought to be stabilized as a semiflavin (Hall & Lambeth, 1980; Ramsay et al., 1987). This makes ETF a good candidate for superoxide or H_2O_2 production and this has been shown at the level of the isolated enzyme (Rodrigues & Gomes, 2012). Electron transfer events in ETFQOR are also thought to form the semireduced state of the FAD moiety and likely semiquinone as an intermediate. However, ETFQOR is proposed to possess a low reactivity toward oxygen based on the crystal structure of the protein and, to the best of our knowledge, there are no data supporting or opposing this suggestion (Zhang et al., 2006). Therefore, H_2O_2 production detected upon reduction of the ETF-ETFQOR system is attributed to two proteins (ETF and ETFQOR) without clear distinction between them at this point.

When designing an experiment to assess ROS production during fatty acid oxidation, there are several important factors to take into account. The choice of substrate is important; we prefer palmitoylcarnitine to palmitoyl-CoA because palmitoyl-CoA requires modification to palmitoylcarnitine to cross the mitochondrial inner membrane. This reaction is catalyzed by carnitinepalmitoyl transferase-1, which can have strong rate limitation in this system (Eaton, 2002). Palmitate cannot be used as a substrate for β-oxidation in isolated mitochondria without addition of ATP, CoA, and the cytoplasmic enzyme acyl-CoA synthetase. Therefore, when investigating ROS production from long-chain fatty acid oxidation, we use 15 μ*M* palmitoylcarnitine. We prefer the L-isomer, rather than the DL mix because the mixture of isomers seems to have a stronger uncoupling effect at increasing concentrations, possibly due to higher contamination with free palmitate, which acts as a detergent. For our stock solutions, we prepare L-palmitoylcarnitine to 10 m*M* in our assay buffer in the absence of BSA and phosphate. The L-palmitoylcarnitine is incubated at 37 °C to ensure it is fully dissolved, and then it is aliquoted and frozen. Before use, it is warmed again to 37 °C to ensure full dissolution in the buffer. In the assay, we supplement the L-palmitoylcarnitine with 2 m*M* free carnitine. Carnitine severs two purposes here: one, it is required to maximize accumulation of palmitoylcarnitine inside the mitochondria; and two, it supports high flux through β-oxidation by forming acetylcarnitine from the excess acetyl-CoA that accumulates as an end product (Perevoshchikova et al., 2013). Instead of carnitine, supplementation of L-palmitoylcarnitine with 5 m*M* malate can stimulate the oxidation of acetyl-CoA in the TCA cycle, but it is less desirable as a substrate because it will recruit other enzymes into the pathway and make dissection of the ROS sites more complicated.

We have found (Perevoshchikova et al., 2013) that the maximum rate of H_2O_2 production by the ETF–ETFQOR system is achieved during oxidation of 15 μ*M* palmitoylcarnitine plus 2 m*M* free carnitine and 0.5 m*M* malonate (to inhibit ROS production arising from complex II). Additionally, the Q-pool needs to be highly reduced (accomplished in the presence of 2 μ*M* myxothiazol), and the antioxidant defense system compromised (in the presence of 4 μ*M* of the uncoupler FCCP). In this case, uncoupling of mitochondria may compromise the antioxidant defense system by decreasing NAD(P)H formation through the energy-dependent transhydrogenase and thereby limiting reduction of the GSH pool (Rydstrom, 2006). With the addition of substrate, the upstream redox centers (NAD^+, ETFQOR, ETF) are reduced; and we propose it is this

condition that results in a stabilized semireduced ETF and the maximum (but still low) rates from this system (Perevoshchikova et al., 2013).

3.6. Dihydrolipoamide-containing enzyme complexes

PDH and OGDH complexes are both mitochondrial matrix enzyme complexes that contain an FAD-linked dihydrolipoamide (DL) dehydrogenase component. Flavins can make radicals, including both superoxide and H_2O_2, and the isolated PDH and OGDH complexes have been shown to generate ROS (Bunik & Sievers, 2002; Starkov et al., 2004). However, it has not been definitively shown that the flavin is the ROS-producing site in these enzymes. The second product of the reaction catalyzed by these enzymes, the thiyl radical of the complex-bound DL, may be a significant source of ROS production as well (Bunik, 2003).

We have limited experience with ROS production by PDH. However, we have some experience with OGDH. In skeletal muscle mitochondria, we have observed significant rates of production from OGDH in the presence of phosphate and ADP, which lower the K_d of the enzyme. An assay designed to observe a pure ROS signal from OGDH *in situ* is not possible without correction for site I_F, which will always contribute to the observed signal in intact mitochondria. However, with 5 m*M* oxoglutarate as substrate, 2 m*M* ADP and 5 m*M* phosphate present as activators, and 0.5 m*M* malonate present to inhibit complex II, the addition of rotenone (4 μ*M*) will generate a substantial rate from OGDH + I_F. We surmise that most of the rate observed under this condition can be assigned to OGDH (unpublished observation).

4. CONCLUDING REMARKS

The information given here is intended to provide the reader with a mechanistic understanding of the major mitochondrial ROS producers. We have presented it in the context of the maximum attainable rates, but this information is readily transferable to less contrived systems. In summary, Fig. 12.4 is a compilation of the maximum rates of H_2O_2 production from each site in skeletal muscle mitochondria. In concert with a mechanistic understanding of the ROS producers in mitochondria, we are developing a system that allows us to predict the contributions from different sites under complex and near-physiological conditions. We recently outlined the principles of using "endogenous reporters" to predict the ROS contributions from specific sites (Quinlan, Treberg, et al., 2012). In particular, we have calibrated the rate of ROS production from site I_F to the reduction state of the endogenous NAD(P)H pool,

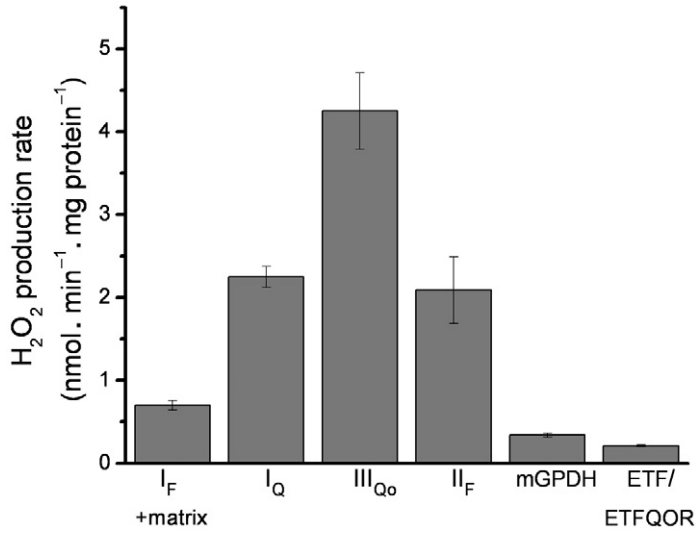

Figure 12.4 Maximum rates of superoxide/H_2O_2 production from different mitochondrial sites. Data were corrected for H_2O_2 consumption by matrix peroxidases using the CDNB protocol described in Section 2.4. In all cases, measurements were made under the conditions that we have found to maximize superoxide production rates from these sites, as described in Section 3. The rate from the complex I flavin site includes any other matrix sites that may respond to NADH reduction and is therefore referred to as I_F + matrix. Data for this graph are means ± SEM ($n \geq 3$) and were compiled from Orr et al. (2012), Perevoshchikova et al. (2013), Quinlan et al. (2011), Quinlan, Orr, et al. (2012), and Treberg et al. (2010).

and the rate of ROS production from site III_{Q_o} to the reduction state of cytochrome b_{566}. The endogenous reporter technique, combined with the above information, allows us to assess ROS production from mitochondria-oxidizing complex substrate mixes and predict which sites are the dominant ROS producers under near-physiological conditions. It is important to recognize, when interpreting an undifferentiated ROS signal, that any given scenario may foster a single or multiple sites of mitochondrial ROS production. Understanding the conditions that foster one site over another allows rational interpretation of a global ROS signal and enhanced understanding of physiological and pathological ROS pathways.

ACKNOWLEDGMENTS

This work was supported by National Institutes of Health, grants P01 AG025901, PL1 AG032118, and R01 AG03354 (to M. D. B.); TL1 AG032116 (to C. L. Q.); and The Ellison Medical Foundation, grant AG-SS-2288-09 (to M. D. B.). Fellowship support was

from The Glenn Foundation (to I. V. P.), the Brazilian Government through the Coordenação de Aperfeiçoamento de Pessoal de Nível Superior (to R. L. S. G.), and The Carlsberg Foundation (to M. H.-M.).

REFERENCES

Adam-Vizi, V., & Chinopoulos, C. (2006). Bioenergetics and the formation of mitochondrial reactive oxygen species. *Trends in Pharmacological Sciences*, *27*, 639–645.

Affourtit, C. L., Quinlan, C. L., & Brand, M. D. (2012). Measurement of proton leak and electron leak in isolated mitochondria. *Methods in Molecular Biology*, *810*, 165–182.

Bell, E. L., Klimova, T. A., Eisenbart, J., Moraes, C. T., Murphy, M. P., Budinger, G. R. S., et al. (2007). The Q_o site of the mitochondrial complex III is required for the transduction of hypoxic signaling via reactive oxygen species production. *The Journal of Cell Biology*, *177*, 1029–1036.

Boden, M. J., Brandon, A. E., Tid-Ang, J. D., Preston, E., Wilks, D., Stuart, E., et al. (2012). Overexpression of manganese superoxide dismutase ameliorates high-fat diet-induced insulin resistance in rat skeletal muscle. *American Journal of Physiology. Endocrinology and Metabolism*, *303*, E798–E805.

Boveris, A., & Cadenas, E. (1975). Mitochondrial production of superoxide anions and its relationship to the antimycin insensitive respiration. *FEBS Letters*, *54*, 311–314.

Boveris, A., Martino, E., & Stoppani, A. O. M. (1977). Evaluation of the horseradish peroxidase-scopoletin method for the measurement of hydrogen peroxide formation in biological systems. *Analytical Biochemistry*, *80*, 145–158.

Boveris, A., Oshino, N., & Chance, B. (1972). The cellular production of hydrogen peroxide. *The Biochemical Journal*, *128*, 617–630.

Brand, M. D. (2010). The sites and topology of mitochondrial superoxide production. *Experimental Gerontology*, *45*, 466–472.

Brotea, G. P., & Thibert, R. J. (1988). Fluorometric determination of hydrogen peroxide using resorufin and peroxidase. *Microchemical Journal*, *37*, 368–376.

Brown, G. C., & Brand, M. D. (1988). Proton/electron stoichiometry of mitochondrial complex I estimated from the equilibrium thermodynamic force ratio. *The Biochemical Journal*, *252*, 473–479.

Bunik, V. I. (2003). 2-Oxo acid dehydrogenase complexes in redox regulation. *European Journal of Biochemistry*, *270*, 1036–1042.

Bunik, V. I., & Sievers, C. (2002). Inactivation of the 2-oxo acid dehydrogenase complexes upon generation of intrinsic radical species. *European Journal of Biochemistry*, *269*, 5004–5015.

Crofts, A. R. (2004). The cytochrome bc1 complex: Function in the context of structure. *Annual Reviews of Physiology*, *66*, 689–733.

Drahota, Z., Chowdhury, S. K., Floryk, D., Mracek, T., Wilhelm, J., Rauchova, H., et al. (2002). Glycerophosphate-dependent hydrogen peroxide production by brown adipose tissue mitochondria and its activation by ferricyanide. *Journal of Bioenergetics and Biomembranes*, *34*, 105–113.

Drose, S., & Brandt, U. (2008). The mechanism of mitochondrial superoxide production by the cytochrome bc_1 complex. *The Journal of Biological Chemistry*, *283*, 21649–21654.

Eaton, S. (2002). Control of mitochondrial beta-oxidation flux. *Progress in Lipid Research*, *41*, 197–239.

Erecinska, M., Wilson, D. F., & Miyata, Y. (1976). Mitochondrial cytochrome b-c complex: Its oxidation-reduction components and their stoichiometry. *Archives of Biochemistry and Biophysics*, *177*, 133–143.

Frisell, W. R., & Mackenzie, C. G. (1962). Separation and purification of sarcosine dehydrogenase and dimethylglycine dehydrogenase. *The Journal of Biological Chemistry*, *237*, 94–98.
Golden, T., & Melov, S. (2001). Mitochondrial DNA mutations, oxidative stress, and aging. *Mechanisms of Ageing and Development*, *122*, 1577–1589.
Hall, C. L., & Lambeth, J. D. (1980). Studies on electron transfer from general acyl-CoA dehydrogenase to electron transfer flavoprotein. *The Journal of Biological Chemistry*, *255*, 3591–3595.
Han, D., Canali, R., Rettori, D., & Kaplowitz, N. (2003). Effect of glutathione depletion on sites and topology of superoxide and hydrogen peroxide production in mitochondria. *Molecular Pharmacology*, *64*, 1136–1144.
Hansford, R. G., Hogue, B. A., & Mildaziene, V. (1997). Dependence of H_2O_2 formation by rat heart mitochondria on substrate availability and donor age. *Journal of Bioenergetics and Biomembranes*, *29*, 89–95.
Harman, D. (1956). Aging: A theory based on free radical and radiation chemistry. *Journal of Gerontology*, *11*, 298–300.
Hyslop, P. A., & Sklar, L. A. (1984). A quantitative fluorimetric assay for the determination of oxidant production by polymorphonuclear leukocytes: Its use in the simultaneous fluorimetric assay of cellular activation processes. *Analytical Biochemistry*, *141*, 280–286.
Ikeda, Y., & Tanaka, K. (1983a). Purification and characterization of 2-methyl-branched chain acyl coenzyme A dehydrogenase, an enzyme involved in the isoleucine and valine metabolism, from rat liver mitochondria. *The Journal of Biological Chemistry*, *258*, 9477–9487.
Ikeda, Y., & Tanaka, K. (1983b). Purification and characterization of isovaleryl coenzyme A dehydrogenase from rat liver mitochondria. *The Journal of Biological Chemistry*, *258*, 1077–1085.
Klimova, T., & Chandel, N. S. (2008). Mitochondrial complex III regulates hypoxic activation of HIF. *Cell Death and Differentiation*, *15*, 660–666.
Klingenberg, M. (1970). Localization of the glycerol-phosphate dehydrogenase in the outer phase of the mitochondrial inner membrane. *European Journal of Biochemistry*, *13*, 247–252.
Korshunov, S. S., Skulachev, V. P., & Starkov, A. A. (1997). High protonic potential actuates a mechanism of production of reactive oxygen species in mitochondria. *FEBS Letters*, *416*, 15–18.
Kushnareva, Y., Murphy, A. N., & Andreyev, A. (2002). Complex I-mediated reactive oxygen species generation: Modulation by cytochrome c and NAD(P)+ oxidation-reduction state. *The Biochemical Journal*, *368*, 545–553.
Kussmaul, L., & Hirst, J. (2006). The mechanism of superoxide production by NADH: Ubiquinone oxidoreductase (complex I) from bovine heart mitochondria. *Proceedings of the National Academy of Sciences of the United States of America*, *103*, 7607–7612.
Lambert, A. J., & Brand, M. D. (2004a). Inhibitors of the quinone-binding site allow rapid superoxide production from mitochondrial NADH:ubiquinone oxidoreductase (complex I). *The Journal of Biological Chemistry*, *279*, 39414–39420.
Lambert, A. J., & Brand, M. D. (2004b). Superoxide production by NADH:ubiquinone oxidoreductase (complex I) depends on the pH gradient across the mitochondrial inner membrane. *The Biochemical Journal*, *382*, 511–517.
Lenich, A. C., & Goodman, S. I. (1986). The purification and characterization of glutaryl-coenzyme A dehydrogenase from porcine and human liver. *The Journal of Biological Chemistry*, *261*, 4090–4096.
Liu, Y., Fiskum, G., & Schubert, D. (2002). Generation of reactive oxygen species by the mitochondrial electron transport chain. *Journal of Neurochemistry*, *80*, 780–787.

McCord, J. M., & Fridovich, I. (1969). Superoxide dismutase. An enzymic function for erythrocuprein (hemocuprein). *The Journal of Biological Chemistry*, *244*, 6049–6055.

Meng, Y., High, K., Antonello, J., Washabaugh, M. W., & Zhao, Q. (2005). Enhanced sensitivity and precision in an enzyme-linked immunosorbent assay with fluorogenic substrates compared with commonly used chromogenic substrates. *Analytical Biochemistry*, *345*, 227–236.

Messner, K. R., & Imlay, J. A. (2002). Mechanism of superoxide and hydrogen peroxide formation by fumarate reductase, succinate dehydrogenase, and aspartate oxidase. *The Journal of Biological Chemistry*, *277*, 42563–42571.

Mitchell, P. (1975). The protonmotive Q cycle: A general formulation. *FEBS Letters*, *59*, 137–139.

Miwa, S., St-Pierre, J., Partridge, L., & Brand, M. D. (2003). Superoxide and hydrogen peroxide production by Drosophila mitochondria. *Free Radical Biology & Medicine*, *35*, 938–948.

Mohanty, J. G., Jaffe, J. S., Schulman, E. S., & Raible, D. G. (1997). A highly sensitive fluorescent micro-assay of H_2O_2 release from activated human leukocytes using a dihydroxyphenoxazine derivative. *Journal of Immunological Methods*, *202*, 133–141.

Muller, F., Crofts, A. R., & Kramer, D. M. (2002). Multiple Q-cycle bypass reactions at the Q_o site of the cytochrome bc_1 complex. *Biochemistry*, *41*, 7866–7874.

Muller, F. L., Liu, Y., Abdul-Ghani, M. A., Lustgarten, M. S., Bhattacharya, A., Jang, Y. C., et al. (2008). High rates of superoxide production in skeletal-muscle mitochondria respiring on both complex I- and complex II-linked substrates. *The Biochemical Journal*, *409*, 491–499.

Muller, F. L., Roberts, A. G., Bowman, M. K., & Kramer, D. M. (2003). Architecture of the Q_o site of the cytochrome bc1 complex probed by superoxide production. *Biochemistry*, *42*, 6493–6499.

Nohl, H., & Jordan, W. (1980). The metabolic fate of mitochondrial hydrogen peroxide. *European Journal of Biochemistry*, *111*, 203–210.

Ohnishi, S. T., Shinzawa-Itoh, K., Ohta, K., Yoshikawa, S., & Ohnishi, T. (2010). New insights into the superoxide generation sites in bovine heart NADH-ubiquinone oxidoreductase (Complex I): The significance of protein-associated ubiquinone and the dynamic shifting of generation sites between semiflavin and semiquinone radicals. *Biochimica et Biophysica Acta*, *1797*, 1901–1909.

Orr, A. L., Quinlan, C. L., Perevoshchikova, I. V., & Brand, M. D. (2012). A refined analysis of superoxide production by mitochondrial sn-glycerol 3-phosphate dehydrogenase. *The Journal of Biological Chemistry*, *287*, 42921–42935.

Paranagama, M. P., Sakamoto, K., Amino, H., Awano, M., Miyoshi, H., & Kita, K. (2010). Contribution of the FAD and quinone binding sites to the production of reactive oxygen species from Ascaris suum mitochondrial complex II. *Mitochondrion*, *10*, 158–165.

Perevoshchikova, I. V., Quinlan, C. L., Orr, A. L., & Brand, M. D. (2013). Sites of superoxide and hydrogen peroxide production during fatty acid oxidation in rat skeletal muscle. *Free Radical Biology & Medicine*, In press. http://dx.doi.org/10.1016/j.freeradbiomed.2013.04.006.

Pryde, K. R., & Hirst, J. (2011). Superoxide is produced by the reduced flavin in mitochondrial complex I: A single, unified mechanism that applies during both forward and reverse electron transfer. *The Journal of Biological Chemistry*, *286*, 18056–18065.

Quinlan, C. L., Gerencser, A. A., Treberg, J. R., & Brand, M. D. (2011). The mechanism of superoxide production by the antimycin-inhibited mitochondrial Q-cycle. *The Journal of Biological Chemistry*, *286*, 31361–31372.

Quinlan, C. L., Orr, A. L., Perevoshchikova, I. V., Treberg, J. R., Ackrell, B. A., & Brand, M. D. (2012). Mitochondrial complex II can generate reactive oxygen species

at high rates in both the forward and reverse reactions. *The Journal of Biological Chemistry*, *287*, 27255–27264.
Quinlan, C. L., Treberg, J. R., Perevoshchikova, I. V., Orr, A. L., & Brand, M. D. (2012). Native rates of superoxide production from multiple sites in isolated mitochondria measured using endogenous reporters. *Free Radical Biology & Medicine*, *53*, 1807–1817.
Ralph, S. J., & Neuzil, J. (2009). Mitochondria as targets for cancer therapy. *Molecular Nutrition & Food Research*, *53*, 9–28.
Ramsay, R. R., Steenkamp, D. J., & Husain, M. (1987). Reactions of electron-transfer flavoprotein and electron-transfer flavoprotein: Ubiquinone oxidoreductase. *The Biochemical Journal*, *241*, 883–892.
Ristow, M., & Schmeisser, S. (2011). Extending life span by increasing oxidative stress. *Free Radical Biology & Medicine*, *51*, 327–336.
Rodrigues, J. V., & Gomes, C. M. (2012). Mechanism of superoxide and hydrogen peroxide generation by human electron-transfer flavoprotein and pathological variants. *Free Radical Biology & Medicine*, *53*, 12–19.
Rottenberg, H., Covian, R., & Trumpower, B. L. (2009). Membrane potential greatly enhances superoxide generation by the cytochrome bc1 complex reconstituted into phospholipid vesicles. *The Journal of Biological Chemistry*, *284*, 19203–19210.
Ruch, W., Cooper, P. H., & Baggiolini, M. (1983). Assay of H_2O_2 production by macrophages and neutrophils with homovanillic acid and horse-radish peroxidase. *Journal of Immunological Methods*, *63*, 347–357.
Ruzicka, F. J., & Beinert, H. (1977). A new iron-sulfur flavoprotein of the respiratory chain. A component of the fatty acid beta oxidation pathway. *The Journal of Biological Chemistry*, *252*, 8440–8445.
Rydstrom, J. (2006). Mitochondrial NADPH, transhydrogenase and disease. *Biochimica et Biophysica Acta*, *1757*, 721–726.
Schafer, F. Q., & Buettner, G. R. (2001). Redox environment of the cell as viewed through the redox state of the glutathione disulfide/glutathione couple. *Free Radical Biology & Medicine*, *30*, 1191–1212.
Schulz, T. J., Zarse, K., Voigt, A., Urban, N., Birringer, M., & Ristow, M. (2007). Glucose restriction extends Caenorhabditis elegans life span by inducing mitochondrial respiration and increasing oxidative stress. *Cell Metabolism*, *6*, 280–293.
Staniek, K., & Nohl, H. (1999). H2O2 detection from intact mitochondria as a measure for one-electron reduction of dioxygen requires a non-invasive assay system. *Biochimica et Biophysica Acta: Bioenergetics*, *1413*, 70–80.
Starkov, A. A., & Fiskum, G. (2003). Regulation of brain mitochondrial H_2O_2 production by membrane potential and NAD(P)H redox state. *Journal of Neurochemistry*, *86*, 1101–1107.
Starkov, A. A., Fiskum, G., Chinopoulos, C., Lorenzo, B. J., Browne, S. E., Patel, M. S., et al. (2004). Mitochondrial alpha-ketoglutarate dehydrogenase complex generates reactive oxygen species. *The Journal of Neuroscience*, *24*, 7779–7788.
St-Pierre, J., Buckingham, J. A., Roebuck, S. J., & Brand, M. D. (2002). Topology of superoxide production from different sites in the mitochondrial electron transport chain. *The Journal of Biological Chemistry*, *277*, 44784–44790.
Sun, F., Huo, X., Zhai, Y., Wang, A., Xu, J., Su, D., et al. (2005). Crystal structure of mitochondrial respiratory membrane protein complex II. *Cell*, *121*, 1043–1057.
Sundaresan, M., Yu, Z. X., Ferrans, V. J., Irani, K., & Finkel, T. (1995). Requirement for generation of H_2O_2 for platelet-derived growth factor signal transduction. *Science*, *270*, 296–299.
Treberg, J. R., & Brand, M. D. (2011). A model of the proton translocation mechanism of complex I. *The Journal of Biological Chemistry*, *286*, 17579–17584.

Treberg, J. R., Quinlan, C. L., & Brand, M. D. (2010). Hydrogen peroxide efflux from muscle mitochondria underestimates matrix superoxide production—A correction using glutathione depletion. *The FEBS Journal*, *277*, 2766–2778.

Treberg, J. R., Quinlan, C. L., & Brand, M. D. (2011). Evidence for two sites of superoxide production by mitochondrial NADH-ubiquinone oxidoreductase (complex I). *The Journal of Biological Chemistry*, *286*, 27103–27110.

Tretter, L., Takacs, K., Hegedus, V., & Adam-Vizi, V. (2007). Characteristics of alpha-glycerophosphate-evoked H_2O_2 generation in brain mitochondria. *Journal of Neurochemistry*, *100*, 650–663.

Trumpower, B. L. (1990). The protonmotive Q cycle. Energy transduction by coupling of proton translocation to electron transfer by the cytochrome bc_1 complex. *The Journal of Biological Chemistry*, *265*, 11409–11412.

Van den Berg, W. H., Prince, R. C., Bashford, C. L., Takamiya, K. I., Bonner, W. D., Jr., & Dutton, P. L. (1979). Electron and proton transport in the ubiquinone cytochrome b-c2 oxidoreductase of Rhodopseudomonas sphaeroides. Patterns of binding and inhibition by antimycin. *The Journal of Biological Chemistry*, *254*, 8594–8604.

Vinogradov, A. D., & Grivennikova, V. G. (2005). Generation of superoxide-radical by the NADH:ubiquinone oxidoreductase of heart mitochondria. *Biochemistry (Moscow)*, *70*, 120–127.

Votyakova, T. V., & Reynolds, I. J. (2001). DeltaPsi(m)-Dependent and -independent production of reactive oxygen species by rat brain mitochondria. *Journal of Neurochemistry*, *79*, 266–277.

Watmough, N. J., & Frerman, F. E. (2010). The electron transfer flavoprotein: Ubiquinone oxidoreductases. *Biochimica et Biophysica Acta*, *1797*, 1910–1916.

Wernette, M. E., Ochs, R. S., & Lardy, H. A. (1981). Ca^{2+} stimulation of rat liver mitochondrial glycerophosphate dehydrogenase. *The Journal of Biological Chemistry*, *256*, 12767–12771.

West, I. C., Mitchell, P., & Rich, P. R. (1988). Electron conduction between *b* cytochromes of the mitochondrial respiratory chain in the presence of antimycin plus myxothiazol. *Biochimica et Biophysica Acta*, *933*, 35–41.

Witte, M. E., Geurts, J. J., de Vries, H. E., van der Valk, P., & van Horssen, J. (2010). Mitochondrial dysfunction: A potential link between neuroinflammation and neurodegeneration? *Mitochondrion*, *10*, 411–418.

Yankovskaya, V., Horsefield, R., Tornroth, S., Luna-Chavez, C., Miyoshi, H., Leger, C., et al. (2003). Architecture of succinate dehydrogenase and reactive oxygen species generation. *Science*, *299*, 700–704.

Zarse, K., Schmeisser, S., Groth, M., Priebe, S., Beuster, G., Kuhlow, D., et al. (2012). Impaired insulin/IGF1 signaling extends life span by promoting mitochondrial L-proline catabolism to induce a transient ROS signal. *Cell Metabolism*, *15*, 451–465.

Zhang, J., Frerman, F. E., & Kim, J. J. (2006). Structure of electron transfer flavoprotein-ubiquinone oxidoreductase and electron transfer to the mitochondrial ubiquinone pool. *Proceedings of the National Academy of Sciences of the United States America*, *103*, 16212–16217.

Zhang, L., Yu, L., & Yu, C. A. (1998). Generation of superoxide anion by succinate-cytochrome *c* reductase from bovine heart mitochondria. *The Journal of Biological Chemistry*, *273*, 33972–33976.

Zhou, M., Diwu, Z., Panchuk-Voloshina, N., & Haugland, R. P. (1997). A stable nonfluorescent derivative of resorufin for the fluorometric determination of trace hydrogen peroxide: Applications in detecting the activity of phagocyte NADPH oxidase and other oxidases. *Analytical Biochemistry*, *253*, 162–168.

CHAPTER THIRTEEN

A Microfluidic Systems Biology Approach for Live Single-Cell Mitochondrial ROS Imaging

Ariel Kniss[*], Hang Lu[†], Dean P. Jones[‡], Melissa L. Kemp[*,1]

[*]The Wallace H. Coulter Department of Biomedical Engineering, Georgia Institute of Technology and Emory University, Atlanta, Georgia, USA
[†]School of Chemical & Biomolecular Engineering, Georgia Institute of Technology, Atlanta, Georgia, USA
[‡]Division of Pulmonary, Allergy and Critical Care Medicine, Clinical Biomarkers Laboratory, Department of Medicine, Emory University School of Medicine, Atlanta, Georgia, USA
[1]Corresponding author: e-mail address: melissa.kemp@bme.gatech.edu

Contents

1. Introduction 220
2. Microfluidic Platform 222
   2.1 Densely arrayed single-cell trapping device 222
   2.2 Device preparation 223
3. Microscope System and Image Analysis 223
   3.1 Microscope setup 223
   3.2 Image analysis 223
4. Imaging Mitochondrial Superoxide Production 224
   4.1 Treating cells with MitoSOX 224
   4.2 Live cell imaging of MitoSOX Red 225
5. Imaging Mitochondrial Hydrogen Peroxide Production 226
   5.1 Stable transfection of HyPer-Mito into Jurkat cell line 226
   5.2 Live cell imaging of HyPer-Mito 226
6. Conclusion 227
7. Potential Pitfalls 228
   7.1 Device operation and image analysis 228
   7.2 Imaging with MitoSOX 228
   7.3 Imaging with HyPer-Mito 229
References 229

Abstract

Most current studies of reactive oxygen species (ROS) production report globally averaged measurements within the cell; however, ROS can be produced in distinct subcellular locations and have local effects in their immediate vicinity. A microfluidic platform for high-throughput single-cell imaging allows mitochondrial ROS production to be monitored as varying in both space and time. Using this systems biology approach, single-cell

Methods in Enzymology, Volume 526
ISSN 0076-6879
http://dx.doi.org/10.1016/B978-0-12-405883-5.00013-2

© 2013 Elsevier Inc.
All rights reserved.

variability can be viewed within a population. We discuss single-cell monitoring of contributors to mitochondrial redox state—mitochondrial hydrogen peroxide or superoxide—through the use of a small molecule probe or targeted fluorescent reporter protein. Jurkat T lymphoma cells were stimulated with antimycin A and imaged in an arrayed microfluidic device over time. Differences in single-cell responses were observed as a function of both inhibitor concentration and type of ROS measurement used.

1. INTRODUCTION

Reactive oxygen species (ROS), such as hydrogen peroxide and superoxide, have critical roles in numerous cellular processes including signal transduction and have been found to be abnormally high in many diseases such as cancer (Trachootham, Alexandre, & Huang, 2009) and autoimmune disorders (D'Autréaux & Toledano, 2007). A major source of ROS is the electron transport chain in the mitochondria, which produces superoxide and hydrogen peroxide. It has been estimated that mitochondrial respiration accounts for 50–500 μmol kg^{-1} min^{-1} cellular ROS, depending upon the metabolic rate of the cell (Jones, 2008).

Two ROS produced in the mitochondria are superoxide and hydrogen peroxide. Superoxide is generated in the mitochondria as a by-product of complex III in the electron transport chain (Fig. 13.1) and can be disproportionated to hydrogen peroxide via manganese superoxide dismutase (MnSOD or SOD2). Hydrogen peroxide can both diffuse through the mitochondrial membrane and be transported via aquaporins (Fisher, 2009). Although superoxide cannot passively diffuse through the membrane, transport has not been definitively excluded from anion transporters. Both ROS are implicated in different signaling processes, such as proliferation, apoptosis, and the cell cycle (Cadenas, 2004). Fluorescent indicators exist for both species. MitoSOX is an irreversible dye capable of localizing to the mitochondria and fluorescing upon oxidation by superoxide. This dye is commonly used as it is well studied and shows exclusive sensitivity to superoxide with $4 \times 10^6 M^{-1}\,s^{-1}$ as the rate-limiting step of oxidation by superoxide (Mezencev, Updegrove, Kutschy, Repovská, & McDonald, 2011; Robinson et al., 2006). Hydrogen peroxide has historically been more difficult to image with controversy surrounding H_2DCF-DA measurements (Kalyanaraman et al., 2012). The recombinant protein, HyPer, has been developed from cpYFP and Oxy-R and is capable of changing conformation upon oxidation by hydrogen peroxide (Belousov et al., 2006). Once transfected into cells, the reporter protein is capable of providing ratiometric

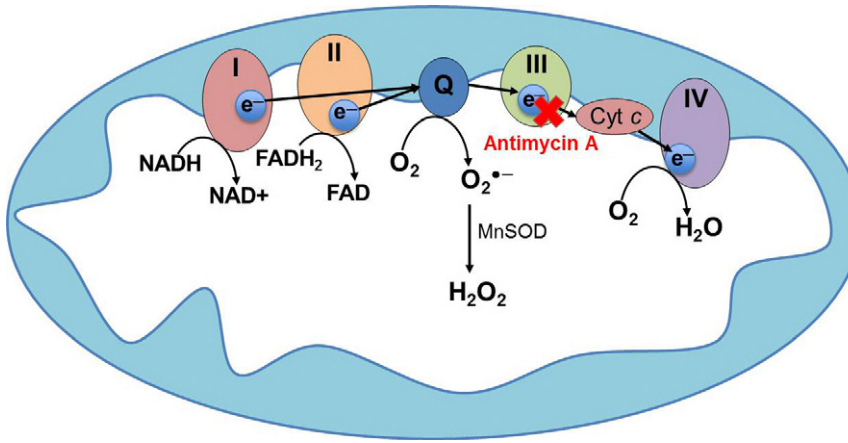

Figure 13.1 Schematic of mitochondrial ROS production. The electron transport chain is composed of four main complexes that allow electrons to be transferred, driving ATP production. Superoxide is a by-product of respiration and can be disproportionated to hydrogen peroxide via SOD2. Antimycin A is a complex III inhibitor shown to increase the rate of production of mitochondrial ROS by inhibiting the flow of electrons to cytochrome *c*.

measurements with the correct microscope setup with two excitation filters and one emission filter.

Stochastic fluctuations in transcriptional and translational regulators within a cell are now considered influential to differences in cell behavior (Elowitz, Levine, Siggia, & Swain, 2002). Such differences can be masked by techniques that analyze populations of cells instead of single cells. For instance, flow cytometry analyzes individual cells at single time points but cannot measure a single cell through multiple time points. With single time point measurements, kinetic differences between individual cells in the response to a stimulus are not observed. High magnification imaging through time can address this problem for adherent cells, but for T cells and other suspension cells, this can be difficult as the cells may drift out of the focal plane. Advances in microfluidic design offer an alternative approach to studying these differences by (i) passively trapping and analyzing the fluorescence of cells through time (Chung, Rivet, Kemp, & Lu, 2011) and (ii) allowing quantification of components of signaling networks within a single cell and then applying these findings to an overall system (Lubeck & Cai, 2012).

The ability to track individual cells through time will lead to a more complete understanding of redox signaling and ultimately more insight into diseased states. In this chapter, we discuss methods for utilizing microfluidics to analyze mitochondrial superoxide and hydrogen peroxide responses to an

oxidative stimulant, antimycin A, among single cells in a high-throughput manner. While our analysis is limited to one reporter molecule at a time, ultimately other fluorescent measurements can simultaneously be performed in multicolor live imaging microscopy (e.g., calcium, pH, mitochondrial membrane potential) to provide insight in how variations in mitochondrial function influences behavior across an array of cells.

2. MICROFLUIDIC PLATFORM

2.1. Densely arrayed single-cell trapping device

A previously developed microfluidic device was utilized for imaging mitochondrial ROS production in the Jurkat T cell line through time (Chung et al., 2011). This high-throughput single-cell trapping device has the capability to hold approximately 4000 total cells in eight different trap arrays (Chung et al., 2011). Each array contains 25 traps per row and 20 rows. The device is compatible with any mode of optical microscopy, so imaging can be done at different magnifications and, with a motorized stage, multiple chambers can be imaged within seconds (Fig. 13.2). The traps can also be placed downstream of different microfluidic platforms, allowing for different stimulus conditions. In this study, a linear serial dilution generator (Jeon et al., 2000) was used upstream to create a range of stimulus concentrations while simultaneously maintaining consistency in flow rate, dye loading, etc., between chambers containing cells from the same cultured population.

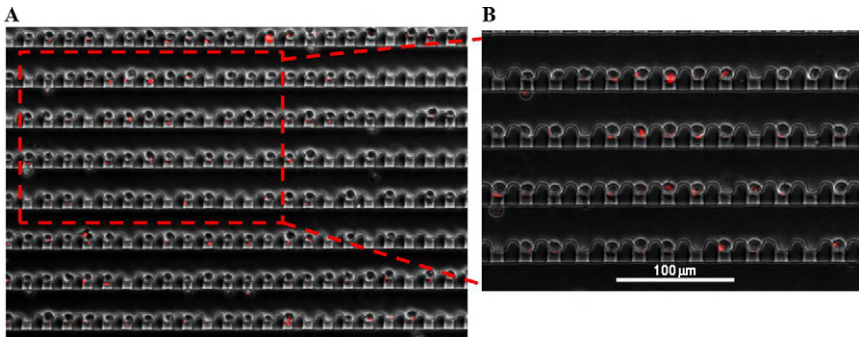

Figure 13.2 Single-cell analysis of mitochondrial superoxide production using MitoSOX Red Mitochondrial Superoxide Indicator (Invitrogen) dye in microfluidic cell traps. (A) 10× view of approximately 160 single-cell traps with MitoSOX-labeled Jurkat cells. (B) 20× view of traps.

2.2. Device preparation

Devices were molded in a polydimethylsiloxane A and B mixture of 10:1 using a SU-8 master mold developed in previously described methods (Chung et al., 2011). Devices were cut and holes were punched using a 19-gauge needle. The prepared devices were bonded via oxygen plasma to a 1-mm glass slide for imaging and polyethylene (PE3) tubing (Scientific Commodities) was used for all connections with solutions. Initially, the device was primed with a 2% bovine serum albumin in phosphate-buffered saline (PBS) solution. This removes any air bubbles from the channels and prevents unintentional cell adhesion to the walls or glass slide. Once primed, the cells were loaded at a concentration of 4×10^6 cells mL^{-1} using gravity flow and the optimized flow rate of ~ 2 μL h^{-1} found previously was used for all treatments (Chung et al., 2011).

3. MICROSCOPE SYSTEM AND IMAGE ANALYSIS

3.1. Microscope setup

Once bonded to a glass slide, the cell trap device was placed on a 37 °C heated stage and imaged using a Nikon Eclipse Ti inverted epifluorescent microscope (Fig. 13.3). Inlet tubing for flow of buffer and/or stimulus was set approximately 40 cm above the outlet tubing to allow for a gravity-based pressure-driven flow of liquid through the chip. Time-lapse microscopy was performed on an automated stage with a 0.7 s delay between imaging the separate chambers with an exposure time of 900 ms. Images were collected every 30 s for 70 min. All images within a given video were set to the same look-up tables to avoid digital differences between images during image analysis.

3.2. Image analysis

Matlab (MathWorks) scripts were written and utilized for image analysis of the time-lapse videos. The fluorescent image was converted to a binary image to identify the fluorescent cells in the trap array. To ensure cells present during the entire experiment were selected, both the first and last images were converted to a binary image using a Matlab built-in global threshold function, "graythresh." Next, manual selection was performed to select the cell areas to analyze, based on presence in both the first and last binary images. The mean fluorescence was then calculated for each region of interest. To remove differences in background fluorescence between frames, the

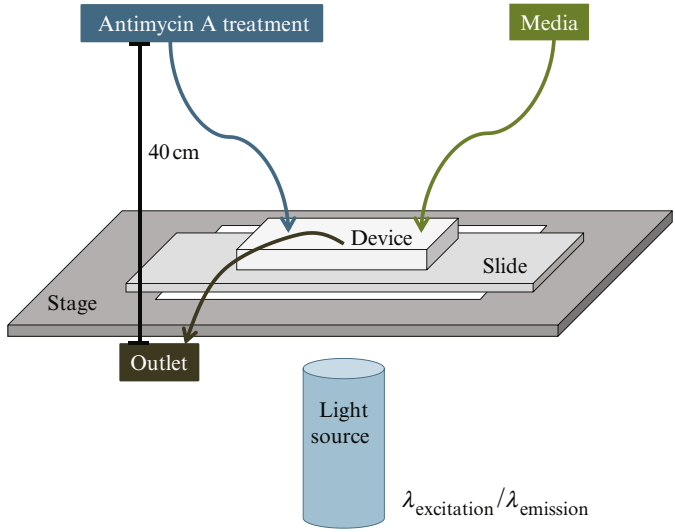

Figure 13.3 Device position with respect to microscope. Device is plasma bonded to a glass slide with tubing connections to treatment solutions and outlet. Slide is placed on a motorized stage set to 37 °C. Filter cubes are utilized for appropriate excitation and emission wavelengths.

average fluorescence of a nonoccupied portion of the trap was calculated and subtracted from each region of interest at each time point. This ensures differences in intensities were less reliant on background noise. To normalize each cell individually, measurements are divided by the first mean intensity for that region of interest.

4. IMAGING MITOCHONDRIAL SUPEROXIDE PRODUCTION

4.1. Treating cells with MitoSOX

The Jurkat E6-1 human acute T cell lymphoma cell line (American Type Culture Collection) was cultured at 37 °C in a humidified 5% CO_2 incubator in RPMI 1640 Medium without Phenol Red and with L-glutamine (Sigma–Aldrich), with 10 m*M* HEPES buffer, 1 m*M* sodium pyruvate, 100 units mL^{-1} penicillin–streptomycin (Cellgro), 1 × MEM Nonessential Amino Acids, and 10% fetal bovine serum (Sigma–Aldrich). To visualize the presence of mitochondrial superoxide, Jurkat cells were incubated with 5 μ*M* MitoSOX Red Mitochondrial Superoxide Indicator (Invitrogen)

for 10 min at 37 °C, according to previous protocols (Mezencev et al., 2011). Following incubation, cells were washed three times with 4 °C sterile PBS and resuspended in 250 μL RPMI Phenol Red-free media to be loaded in the device at a final concentration of 4×10^6 cells mL^{-1}.

4.2. Live cell imaging of MitoSOX Red

Once loaded in the device, cells were imaged using the TRITC (540/605 nm) filter cube (Nikon) and stimulated with antimycin A (Sigma–Aldrich) at various concentrations. Individual cells were tracked through time and a heat map was created to visualize the change in intensity, related to change in mitochondrial superoxide production, through time (Fig. 13.5). Within a chamber with uniform antimycin A concentration, we observed individual cellular differences in mitochondrial superoxide production (Fig. 13.4). With an irreversible dye, a monotonic increase was expected over the 70 min experiment. In several instances, lower fluorescence was observed with time; this may be due to rotation of the trapped cell with respect to the focal plane of imaging, photo bleaching of the dye, or inaccuracies in creation of the binary images. On average, we observed an increase in MitoSOX Red oxidation with increasing antimycin

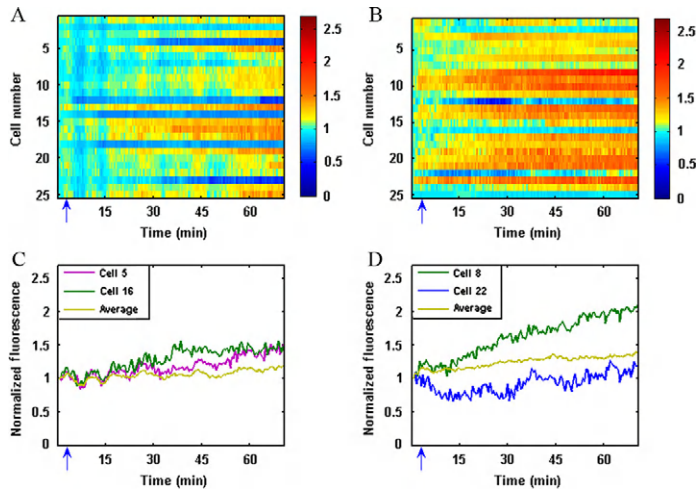

Figure 13.4 Mitochondrial superoxide production with antimycin A stimulation (blue arrow). (A, C) 1.6 μ*M* treated cells. (C, D) 50 μ*M* treated cells. (A, B) Heat map of normalized mean fluorescence of 25 analyzed cells through time. (C, D) Average and single-cell traces of mean fluorescence.

A concentration (Fig. 13.4A and C) as well as the number of cells that respond to the stimulatory condition as defined by an increase greater than 40% the original fluorescence. In the example shown, there were 7 responsive cells in the 1.6 μM inhibitor treatment compared to 16 responsive cells in the 50 μM inhibitor concentration.

5. IMAGING MITOCHONDRIAL HYDROGEN PEROXIDE PRODUCTION

5.1. Stable transfection of HyPer-Mito into Jurkat cell line

To visualize the dynamics of mitochondrial hydrogen peroxide through time, the pHyPer-dMito plasmid (Evrogen) was transfected into Jurkat cells using the Neon Transfection System (Life Technologies). Jurkat cells were cultured until logarithmic growth was observed and then washed in PBS without Ca^{2+} and Mg^{2+}. Cells were resuspended in Resuspension Buffer R (Invitrogen Neon Kit) at a final concentration of 1×10^7 cells mL^{-1} with 10 μg DNA per 100 μL transfection. Four 100 μL transfections were completed using the Neon protocol of 3 pulses of 1325 V with a 10 ms pulse width.

Once transfected, cells were cultured for 3 days without antibiotics. Selection was completed using the neomycin resistant gene on the pHyPer-dMito plasmid. On day 4, 1.4 mg mL^{-1} neomycin (G418) (KSE Scientific) was added to the media with a cell concentration of approximately 0.2×10^6 cells mL^{-1}. The selection was continued for 14 days with washing and addition of fresh media and antibiotics every 3 days, maintaining the cell concentration between 0.2 and 0.6×10^6 cells mL^{-1}. The concentration of G418 was calibrated via a cytotoxicity curve with the same lot of G418 (KSE Scientific). Following selection, a maintenance concentration of 0.6 mg mL^{-1} G418 was continued in cell culture.

5.2. Live cell imaging of HyPer-Mito

Cells were loaded into the device at a concentration of 4×10^6 cells mL^{-1}. Once sufficiently loaded, antimycin A (Sigma–Aldrich) was introduced at various concentrations. Cells were imaged using the QMAX GR TE-10 filter set (Omega Optical), as recommended by Evrogen for nonratiometric imaging of the Hyper reporter protein. The filter set for excitation between 450 and 490 nm and emission filter at 535 nm primarily represents the oxidized form of the mitochondrial hydrogen peroxide sensor, HyPer-Mito. Images were collected over the course of 70 min and revealed differences

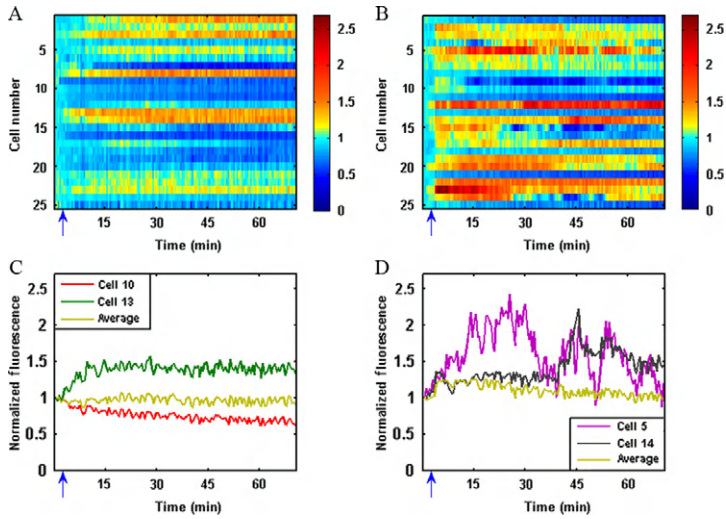

Figure 13.5 Mitochondrial hydrogen peroxide production with antimycin A stimulation (blue arrow). (A, C) 1.6 μ*M* treated cells. (C, D) 50 μ*M* treated cells. (A, B) Heat map of normalized mean fluorescence of 25 analyzed cells through time. (C, D) Average and single-cell traces of mean fluorescence.

in hydrogen peroxide signaling between different cells under the same antimycin A concentration (Fig. 13.5). As with the MitoSOX Red, we observed an increase in fluorescence intensity associated with oxidized HyPer-Mito as the concentration of antimycin A increased (Fig. 13.5A and C). With a reversible ROS reporter, however, the observed kinetics were more diverse at the single-cell level. At the 1.6 μ*M* inhibitor concentration, the cells that respond tend to do so similarly in a steadily increasing manner (Fig. 13.5A and C), whereas cells at the 50 μ*M* concentration vary in both the time to respond, and whether the H_2O_2 is sustained or changes with time. Differences can also be seen in the number of cells to respond, as defined by a 40% change from baseline. In the example shown, there were 5 responsive cells in the 1.6 μ*M* inhibitor treatment compared to 12 responsive cells in the 50 μ*M* inhibitor concentration. The quantity of cells responding was lower than that observed with MitoSOX.

6. CONCLUSION

We have demonstrated the potential to use microfluidics to study time-dependent changes of two different mitochondrial ROS in single cells,

thus supporting redox systems biology at the level of single cells. Further, we provide the ability to study heterogeneity of these processes in different cells within a population. We report that cells exposed to the same concentration of stimulus exhibited variation in mitochondrial ROS production, which could ultimately result in different cellular responses. This variation could be the result of stochastic processes within the cell, such as transcriptional or translational regulation of key components of the mitochondrial ROS pathway. Additionally, the nature of the responses differed between O_2^- and H_2O_2 kinetics. Because two different types of fluorescent reporters (irreversible small molecule vs. YFP-fusion protein) were used, it is difficult to ascertain without further analysis whether variation at the single-cell level is attributed to properties of the reporter or due to subcellular concentrations of the respective ROS. To our knowledge, this is the first description of the use of microfluidics to image and quantify single-cell redox states in mammalian T cells, a method that may help elucidate underlying dysfunctions in different cell types and diseases. Accounting for distributions of mitochondrial redox state within populations of cells will ultimately allow for a better understanding of signaling processes associated with diseases that implicate mitochondrial dysfunction, such as Alzheimer's disease (Rottkamp, 2000), autoimmune disorders (Tak, Zvaifler, Green, & Firestein, 2000), and cancer (Trachootham et al., 2009).

7. POTENTIAL PITFALLS

7.1. Device operation and image analysis

As the device is operated, cells can shift slightly in position and location. A small number of cells have been observed to squeeze through the trap and either get stuck or leave the trap completely. With these discrepancies in cell position, the image analysis methods must address changing location. Currently, the first and last images are used to ensure all cell locations are recorded through time. However, a more optimized program may track the cell at every time point for mean fluorescence calculations.

7.2. Imaging with MitoSOX

MitoSOX provides an irreversible signal of oxidation, and hence, it is difficult to analyze the dynamic changes in superoxide production through time. One workaround with sufficiently resolved temporal imaging is to analyze the derivative of the signal intensities in order to visualize changes

production rates. This approach is limited by the potential saturation (i.e., full oxidation) of the probe.

7.3. Imaging with HyPer-Mito

Transfection efficiency becomes an issue in difficult to transfect cell lines as the utility of the microfluidic device decreases when only few cells can be analyzed. Stable transfection with antibiotic selection was performed to avoid low transfection efficiency. Basal differences in the oxidized HyPer-Mito fluorescence intensity may be due to either transfection levels or degree of oxidation. Although HyPer-Mito is designed for ratiometric measurements with a dual excitation system (which would discriminate between these possibilities), we used a single excitation filter in the findings reported here. Future directions include expanding the microscope setting to contain an excitation wheel capable of dual excitation.

REFERENCES

Belousov, V. V., Fradkov, A. F., Lukyanov, K. A., Staroverov, D. B., Shakhbazov, K. S., Terskikh, A. V., et al. (2006). Genetically encoded fluorescent indicator for intracellular hydrogen peroxide. *Nature Methods*, *3*, 281–286.

Cadenas, E. (2004). Mitochondrial free radical production and cell signaling. *Molecular Aspects of Medicine*, *25*, 17–26.

Chung, K., Rivet, C. A., Kemp, M. L., & Lu, H. (2011). Imaging single-cell signaling dynamics with a deterministic high-density single-cell trap array. *Analytical Chemistry*, *83*, 7044–7052.

D'Autréaux, B., & Toledano, M. B. (2007). ROS as signalling molecules: Mechanisms that generate specificity in ROS homeostasis. *Nature Reviews. Molecular Cell Biology*, *8*, 813–824.

Elowitz, M. B., Levine, A. J., Siggia, E. D., & Swain, P. S. (2002). Stochastic gene expression in a single cell. *Science*, *297*, 1183–1186.

Fisher, A. B. (2009). Redox signaling across cell membranes. *Antioxidant & Redox Signaling*, *11*(6), 1349–1356.

Jeon, N. L., Dertinger, S. K. W., Chiu, D. T., Choi, I. S., Stroock, A. D., & Whitesides, G. M. (2000). Generation of solution and surface gradients using microfluidic systems. *Langmuir*, *16*, 8311–8316.

Jones, D. P. (2008). Radical-free biology of oxidative stress. *American Journal of Physiology. Cell Physiology*, *295*, C849–C868.

Kalyanaraman, B., Darley-Usmar, V., Davies, K. J., Dennery, P. A., Forman, H. J., Grisham, M. B., et al. (2012). Measuring reactive oxygen and nitrogen species with fluorescent probes: Challenges and limitations. *Free Radical Biology & Medicine*, *52*, 1–6.

Lubeck, E., & Cai, L. (2012). Single-cell systems biology by super-resolution imaging and combinatorial labeling. *Nature Methods*, *9*, 743–748.

Mezencev, R., Updegrove, T., Kutschy, P., Repovská, M., & McDonald, J. F. (2011). Camalexin induces apoptosis in T-leukemia Jurkat cells by increased concentration of reactive oxygen species and activation of caspase-8 and caspase-9. *Journal of Natural Medicines*, *65*, 488–499.

Robinson, K. M., Janes, M. S., Pehar, M., Monette, J. S., Ross, M. F., Hagen, T. M., et al. (2006). Selective fluorescent imaging of superoxide in vivo using ethidium-based probes. *Proceedings of the National Academy of Sciences of the United States of America*, *103*, 15038–15043.

Smith, M. A., Rottkamp, C. A., Nunomura, A., Raina, A. K., & Perry, G. (2000). Oxidative stress in Alzheimer's disease. *Biochimica et Biophysica Acta (BBA) - Molecular Basis of Disease*, *1502*(1), 139–144.

Tak, P. P., Zvaifler, N. J., Green, D. R., & Firestein, G. S. (2000). Rheumatoid arthritis and p53: How oxidative stress might alter the course of inflammatory diseases. *Immunology Today*, *21*, 78–82.

Trachootham, D., Alexandre, J., & Huang, P. (2009). Targeting cancer cells by ROS-mediated mechanisms: A radical therapeutic approach? *Nature Reviews Drug Discovery*, *8*, 579–591.

CHAPTER FOURTEEN

Detection of Oxidative Damage in Response to Protein Misfolding in the Endoplasmic Reticulum

Guy Landau*, Vamsi K. Kodali*, Jyoti D. Malhotra†, Randal J. Kaufman*,1

*Center for Neuroscience, Aging, and Stem Cell Research, Sanford-Burnham Medical Research Institute, La Jolla, California, USA
†Proteostasis Therapeutics, Cambridge, Massachusetts, USA
1Corresponding author: e-mail address: rkaufman@sanfordburnham.org

Contents

1. Introduction 232
   1.1 Oxidative protein folding 233
   1.2 Unfolded protein response 233
   1.3 ER–mitochondria cross talk 234
2. UPR-Induced Oxidative Damage 235
   2.1 Protein carbonyls 237
   2.2 Glutathione levels 239
   2.3 Lipid peroxidation 241
   2.4 Mitochondrial markers 245
3. Summary 247
References 248

Abstract

Disulfide bond formation in the endoplasmic reticulum (ER) requires the sequential transfer of electrons from thiol residues to protein disulfide isomerase and ER oxidase 1, with the final reduction of molecular oxygen to form hydrogen peroxide. Conditions that perturb correct protein folding lead to accumulation of misfolded proteins in the ER lumen, which induce ER stress and oxidative stress. Oxidative damage of cellular macromolecules is a common marker of aging and various pathological conditions including diabetes, cancer, and neurodegenerative disease. As accumulating evidence suggests a tight connection between the ER stress and oxidative stress, analysis of appropriate markers becomes particularly important. Here, we describe methods to analyze markers of oxidative damage associated with ER stress.

Methods in Enzymology, Volume 526
ISSN 0076-6879
http://dx.doi.org/10.1016/B978-0-12-405883-5.00014-4

© 2013 Elsevier Inc.
All rights reserved.

1. INTRODUCTION

Hydrogen peroxide (H_2O_2) is known as a signaling molecule involved in the regulation of diverse biological processes (Veal, Day, & Morgan, 2007). However, its uncontrolled production and/or accumulation cause severe cellular damage by modification of nucleic acids, proteins, and lipids. Inside the cell, H_2O_2 is predominantly produced not only by the mitochondria (by complexes I and III of the electron transport chain) and the endoplasmic reticulum (ER, by the ERO1 flavoenzyme, cytochromes P450 and *b*5) but also in peroxisomes (fatty acid oxidation) and at the plasma membrane (NADPH oxidases) (Brown & Borutaite, 2012; Go & Jones, 2008). The central process responsible for H_2O_2 production in the ER is oxidative protein folding, which utilizes the redox poise of the ER lumen to promote disulfide bond formation (Tu & Weissman, 2004). Suboptimal folding conditions or heavy biosynthetic load of disulfide-rich proteins cause unproductive and repeated cycles of protein oxidation and reduction, thereby increasing production of H_2O_2. Furthermore, buildup of improperly folded or hard-to-fold proteins inside the ER lumen leads to ER stress, which is associated with elevated H_2O_2 production. In an attempt to correctly fold this accumulating protein load, the cell activates a set of adaptive signaling cascades, cumulatively defined as the unfolded protein response (UPR). Normally, excess of H_2O_2 is efficiently neutralized by reducing enzymes such as glutathione peroxidases or peroxiredoxin-4 (Kakihana, Nagata, & Sitia, 2012). However, under pathological conditions, imbalance between generation and neutralization of H_2O_2 can lead to development of oxidative stress, which is manifested through accumulation of various oxidized products, damage of cellular constituents, and induction of antioxidant response mechanisms (Kregel & Zhang, 2007). Alternatively, the mitochondrial electron transport chain constantly produces superoxide anion that is further converted to H_2O_2 by the action of mitochondrial superoxide dismutase (SOD) (Feissner, Skalska, Gaum, & Sheu, 2009). If not resolved, UPR can lead to calcium leak into the cytosol and stimulate mitochondria to generate more hydrogen peroxide. Thus, ER stress is involved in the production of hydrogen peroxide both directly via oxidative protein folding activity and indirectly through modulation of mitochondrial oxidative phosphorylation. In recent years, the role of ER stress in accumulation of oxidative damage has gained interest (Malhotra & Kaufman, 2007), and this

chapter will provide examples of the methods used to evaluate markers of oxidative damage associated with the UPR.

1.1. Oxidative protein folding

In addition to being the major calcium storage compartment, the ER is the primary site of membrane and secretory protein folding, a multistep process ensuring that the newly synthesized polypeptides attain the native conformation. This is accomplished with the assistance of various enzymes and chaperone proteins acting as folding catalysts, facilitating the production and assembly of proteins before they exit the ER and reach the Golgi compartment (Hartl & Hayer-Hartl, 2009). One of the major steps in protein folding is the formation of disulfide bonds between two cysteine residues in polypeptide chains, which is required for protein maturation or function. This reaction is favored due to the ~10 times more oxidizing environment of the ER lumen with a higher ratio of oxidized to reduced glutathione (GSSG/GSH) (Hwang, Sinskey, & Lodish, 1992). In eukaryotes, disulfide bond formation is catalyzed by a family of ER oxidoreductases, including protein disulfide isomerase (PDI), ERp57, and ERp72. The transfer of a pair of electrons from the cysteine residues of the nascent chains to the active disulfide site of PDI initiates the oxidative folding of the protein and generates the reduced form of PDI (Freedman, Hirst, & Tuite, 1994). Reoxidation of PDI is catalyzed by enzymes including ER oxidoreductin 1 (ERO1, see below) that transfer electrons to oxygen as the final electron acceptor (Sevier & Kaiser, 2008; Wajih, Hutson, & Wallin, 2007). Other enzymes that have been implicated in the oxidative protein folding process include yeast essential for respiration and vegetative growth (Erv2p), quiescin sulfhydryl (SH) oxidase, vitamin K epoxide reductase, peroxiredoxin 4, and dehydroascorbate reductase. ERO1 is a membrane-associated flavoprotein, which transfers electrons from PDI to molecular oxygen and generates H_2O_2 as a by-product. It has been estimated that about 25% of the normal hydrogen peroxide production in the cell is generated by ERO1 (Tu & Weissman, 2004), and this percentage may be significantly higher if misfolded proteins accumulate under pathological conditions or following exposure to toxic agents.

1.2. Unfolded protein response

Proteins entering the ER are subject to numerous posttranslational modifications that are highly sensitive to changes in the luminal environment.

Hence, environmental insults, gene mutations, amino acid modifications, or elevated protein production can lead to accumulation of misfolded proteins and initiate a series of signaling cascades collectively known as the UPR (Patil & Walter, 2001; Schroder & Kaufman, 2005). In metazoans, three proteins residing on the ER membrane act as the major sensors that transmit UPR signals to the cytosol and the nucleus to relieve the cell from stress. Protein kinases PERK (double-stranded RNA-activated protein kinase-like ER kinase) (Harding, Zhang, Bertolotti, Zeng, & Ron, 2000) and IRE1 (inositol requiring protein 1) (Yoshida, Matsui, Yamamoto, Okada, & Mori, 2001), and the transcription factor ATF6 (Yoshida et al., 2000) constitutively bind the protein chaperone GRP78/BiP via their luminal domains. Concomitant with the accumulation of the misfolded proteins in the ER, BiP dissociates from PERK, IRE1, and ATF6 in order to chaperone folding of the nascent chains. Release of BiP allows PERK and IRE1 to homodimerize and activate signaling cascades on the cytosolic face of the ER. Unlike the aforementioned kinases, dissociation of ATF6 from BiP allows it to translocate to the Golgi compartment, where it is proteolytically cleaved to yield an active transcription factor (Haze, Yoshida, Yanagi, Yura, & Mori, 1999; Malhotra & Kaufman, 2007; Rutkowski et al., 2006). Each signal transducer activates an overlapping yet distinct transcriptional and translational program that is aimed at remedying the stress condition. As protein misfolding promotes accumulation of H_2O_2, the cell initiates PERK cascade to activate the expression of the antioxidant response genes including glutathione *S*-transferase (GST) and NAD(P)H:quinone oxidoreductase (NQO1). On the other hand, the same cascade activates expression of ERO1 that would eventually lead to elevated production of hydrogen peroxide (Marciniak, 2004). Accordingly, the survival decision is directed by the ability of the cell to resolve the protein folding defect, as chronic activation of the UPR will lead to apoptotic (programmed cell death) response (Malhotra & Kaufman, 2007; Rutkowski et al., 2006).

1.3. ER–mitochondria cross talk

Along with ATP production, mitochondria serve as a significant source for H_2O_2, perform calcium buffering functions, and orchestrate cellular Ca^{2+} signaling (Herrington, Park, Babcock, & Hille, 1996). Calcium signaling plays a central role in mitochondrial function, and as the ER is the central Ca^{2+} storage compartment, the functional linkage between the two organelles is essential for efficient mitochondrial metabolism. The close contacts

discovered between the mitochondria and the ER led to the model that ER–mitochondrial communication involves a direct traffic rather than vesicular transport and includes mitochondria-associated membranes (Raturi & Simmen, 2013). These connections are modulated by the dynamin-like GTPase Mitofusin 2, which is involved in mitochondrial fusion (de Brito & Scorrano, 2008). Physiological increases in cytosolic calcium levels stimulate Ca^{2+} uptake by the mitochondria via several mechanisms, including the mitochondrial calcium uniporters, the "rapid mode," and ryanodine receptors (Feissner et al., 2009). Inside the mitochondria, Ca^{2+} acts as a signal for activation of multiple mitochondrial enzymes, leading to stimulation of oxidative phosphorylation. However, both ER stress and oxidative stress lead to increased Ca^{2+} leakage from the ER (Berridge, Bootman, & Roderick, 2003; Gorlach, Klappa, & Kietzmann, 2006). Under ER stress conditions, calcium leak and its uptake by the mitochondria stimulate production of hydrogen peroxide due to inhibition of complexes I, III, and IV of the mitochondrial electron transport chain (Brookes, Yoon, Robotham, Anders, & Sheu, 2004; Kudin, Bimpong-Buta, Vielhaber, Elger, & Kunz, 2004). In addition, Ca^{2+} leak stimulates the TCA cycle, thereby increasing consumption of oxygen and leading to generation of more H_2O_2. Upon severe stress, Ca^{2+} leakage leads to mitochondrial membrane depolarization and promotes an opening of the mitochondrial permeability transition pore (mPTP). This, in turn, leads to loss of matrix solutes (including GSH) and release of cytochrome *c*, thereby blocking the respiratory chain at complex III (Feissner et al., 2009; Malhotra & Kaufman, 2007). Moreover, elevated levels of mitochondria-generated hydrogen peroxide facilitate Ca^{2+} release from the ER, further enhancing Ca^{2+}-stimulated oxidative stress (Fig. 14.1). Thus, the impaired Ca^{2+}-mediated communication between the ER and mitochondria provides additional basis for alteration in redox state of the cell and generation of oxidative damage.

2. UPR-INDUCED OXIDATIVE DAMAGE

As ER stress leads to the production of H_2O_2 and associated reactive oxygen species (ROS), the most direct method to measure changes in redox status is to use specific sensors to monitor real-time ROS production (Belousov et al., 2006; Malinouski, Zhou, Belousov, Hatfield, & Gladyshev, 2011; Wu, Ma, Liu, & Terada, 2010). However, these sensors have limited dynamic range and the methods are difficult to apply in

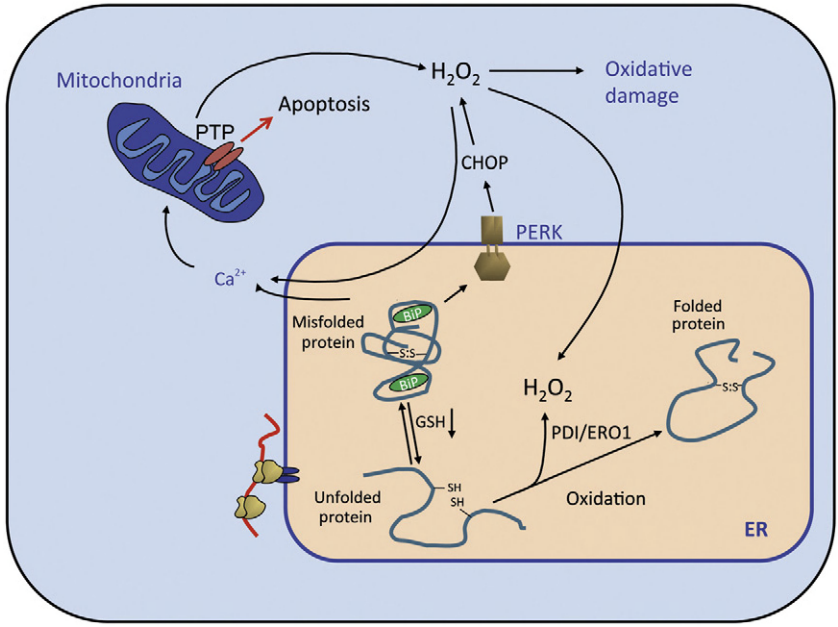

Figure 14.1 ER stress induced by accumulation of misfolded proteins perturbs the cross talk between the ER and the mitochondria and contributes to elevated levels of H_2O_2. Hydrogen peroxide is generated as a natural by-product of mitochondrial respiration and oxidative protein folding in the ER. In the process of protein folding, PDI-executed oxidation of cysteine residues promotes disulfide bond formation, while reduction of PDI is achieved via ERO1-mediated electron transfer to yield H_2O_2. Misfolded proteins cause repetitive cycles of oxidation/reduction reactions and thus deplete cellular reducing equivalents in the form of glutathione. Induction of ER stress by accumulation of misfolded proteins elicits Ca^{2+} leakage and uptake into the mitochondrial matrix, which perturbs mitochondrial activity and leads to production of reactive oxygen species (ROS). In addition, activation of the PERK arm of the UPR leads to induction of the transcription factor CHOP that increases expression of ERO1. If unresolved, ER stress leads to further Ca^{2+} leakage, which promotes mitochondrial membrane depolarization, opening of the PTP, and eventually results in apoptosis.

mammalian tissues. Although transcriptional activation of antioxidant response gene products including GST, NQO1, or HO-1 has been used as a surrogate for oxidative stress, their expression does not actually reflect the presence of ROS. In addition, the induction of the antioxidant response is not specific to ER stress. Hence, the most reliable methodology used to evaluate the extent of oxidative stress is based on assessment of the terminal or "stable" damage of biomolecules caused by free radicals. In addition,

levels or activity of several antioxidant defense system elements, such as glutathione or SOD, can provide complementary information on the redox balance of the cell. We and others have previously shown that ER stress results in accumulation of oxidative damage in the form of lipid peroxidation, oxidative protein modifications, changes in cellular glutathione levels, and perturbed mitochondrial function (Arduino et al., 2009; Back et al., 2009; Kim et al., 2009; Malhotra et al., 2008; Song, Scheuner, Ron, Pennathur, & Kaufman, 2008). Alterations in UPR signaling and accumulation of misfolded protein have been shown to play important role in etiology of numerous disease states, especially related to specified secretory cells like pancreatic β-cells, hepatocytes, and plasma cells. These advancements in understanding the interrelation between the ER stress and oxidative stress further suggest the causative role of UPR in accumulation of oxidative damage. Consequently, the levels of oxidative damage markers can correlate with the severity of ER stress. Several commercially available ER stress inducers including thapsigargin, tunicamycin, brefeldin A, or DTT are frequently used as activators of UPR. Incubation times and concentrations should be determined experimentally, while keeping in mind that prolonged treatments or higher concentrations are toxic and usually lead to induction of apoptotic cell death. Here, we provide several protocols used in our laboratory to measure oxidative damage associated with ER stress.

2.1. Protein carbonyls

Assessment of protein carbonylation as a marker for oxidative damage stems from the studies on bacterial glutamine synthetase, which is targeted for proteolytic degradation upon oxidation of its amino acid side chains (Stadtman, 2001). Studies on aging animals revealed similar effects of carbonyl modifications on protein activity and removal (Levine, 2002). In addition, carbonylation is associated with diseases such as Parkinson's, Alzheimer's, diabetes, and cancer (Dalle-Donne, Rossi, Giustarini, Milzani, & Colombo, 2003). Recent results from our group indicated that development of ER stress in pancreatic β-cells of diabetic mice and overexpression of misfolding-prone proteins in murine livers are associated with accumulation of protein carbonyls (Back et al., 2009; Malhotra et al., 2008). Carbonyl derivatives form by a metal-catalyzed oxidative attack on the side chains of amino acids, such as threonine, lysine, proline, and arginine, but several other amino acids can also be modified (Nystrom, 2005). This is the most common oxidative

protein modification, and the central feature of protein carbonylation is that this modification is irreversible and cells must get rid of the affected proteins (Dalle-Donne et al., 2003). Detection of carbonylated proteins is commonly achieved through 2,4-dinitrophenol hydrazine (DNP) derivatization of the carbonyl groups and subsequent colorimetric or immunologic assays.

2.1.1 Buffers and solutions

Homogenization buffer is 10 m*M* HEPES, pH 7.4, containing 150 m*M* NaCl, 4.6 m*M* KCl, 1.1 m*M* KH_2PO_4, 0.6 m*M* $MgSO_4$, 100 μ*M* diethylenetriaminepentaacetic acid (DTPA), 50 μ*M* butylated hydroxytoluene [BHT, stock solution made in absolute ethanol (v/v)], and protease inhibitor cocktail (Sigma). DTPA chelates metal cations and prevents free radical-mediated *ex vivo* oxidation whereas BHT is an organic antioxidant. The buffer should be prepared fresh.

2.1.2 Isolation of protein from cultured cells

Cells are harvested with 0.05% Trypsin–EDTA solution, neutralized with growth medium containing 10% FBS and centrifuged for 2 min at $600 \times g$. The resulting cell pellet is resuspended in 200–300 μl of ice-cold homogenization buffer. The cells are homogenized by sonication on ice and clarified by centrifugation at $10{,}000 \times g$ for 10 min at 4 °C.

2.1.3 Isolation of protein from tissue samples

For best results, animals should be perfused with the homogenization buffer prior to the isolation of tissues. This step removes the red blood cells and preserves the tissues from *ex vivo* oxidation. After perfusion, the tissue is extracted, washed in homogenization buffer, and either embedded in mounting solution for subsequent cryosectioning or immediately frozen in liquid nitrogen and stored at −80 °C. If frozen, the samples should be thawed on ice, washed in freshly prepared ice-cold homogenization buffer, and used for protein isolation. The amount of tissue sample required is estimated empirically; about 100 mg of liver tissue is used for the current experiment. Tissues are homogenized on ice using a Dounce homogenizer avoiding bubbling. Clarified lysates obtained after centrifugation at $10{,}000 \times g$ for 10 min at 4 °C are used in the subsequent steps.

2.1.4 Detection of protein carbonyls with ELISA

The principle of the assay is to derivatize the protein side chain carbonyls with 2,4-dinitrophenyl hydrazine (DNP) and detect using a biotinylated

anti-DNP antibody. For quantitation of the signal, the samples are incubated with streptavidin-conjugated horseradish peroxidase. As avidin–biotin binding affinity is much stronger than that of antibodies, this method provides superior detection sensitivity. We have found that the carbonyl enzyme immune assay kit from Biocell Corporation, NZ, gives reproducible results, and the protocol described here closely follows the manufacturer's instructions with only slight modifications. This kit can be used for determination of carbonylated protein content in cells, tissues, plasma, and other body fluids. Total protein concentration in clarified lysates was determined using DC Protein Assay kit (Bio-Rad, CA, USA). Briefly, DNP solution (200 μl) is aliquoted into prelabeled tubes and mixed with diluted standards or carbonyl control. Carbonyl control is used as an internal standard and should always provide a fixed value as an indicator of assay's reliability. About 20–30 μg of total protein (made up to 50 μl with assay dilution buffer) is added to the DNP aliquots and incubated for 45 min at room temperature (RT) to derivatize protein carbonyls. Next, 50 μl of the derivatized protein is mixed with 1 ml of assay dilution buffer and used for ELISA. When ready, 200 μl of each standard or sample is incubated in the ELISA plate overnight at 4 °C. Subsequently, the plate is washed three times with 200 μl of the provided wash buffer and incubated with blocking solution for 30 min at RT. After blocking, the plate is washed three times and incubated with biotinylated anti-DNP antibody for 1 h at 37 °C. Unbound antibody is washed off using the wash buffer, followed by incubation with streptavidin-conjugated HRP for 1 h at RT. Following three final washes, the wells are treated with 200 μl of chromatin reagent for 15 min at RT. The reaction is stopped by addition of 100 μl of stopping reagent and the absorbance is measured at 450 nm. Protein carbonyl concentrations are calculated from the standard curve and usually expressed in pmol/mg of total protein.

2.2. Glutathione levels

Glutathione (γ-L-glutamyl-L-cysteinylglycine, GSH) is a tripeptide synthesized in the cytosol and is the principal component of the cellular redox buffering system. Having the SH group of the cysteine residue, glutathione is a very potent antioxidant (Appenzeller-Herzog, 2011). The cell contains up to 10 m*M* of GSH maintained in a reduced form through an NADPH-dependent reaction catalyzed by glutathione reductase. Glutathione serves as a major redox buffer and the ratio between its reduced to oxidized form (GSH:GSSG) is used as an index of the redox state of the cell (Hwang et al.,

1992). Disulfide bond formation inside the ER requires an oxidizing environment and this is largely preserved due to maintenance of difference in ratios between the two forms of glutathione. As induction of ER stress leads to accumulation of oxidative damage, intracellular GSH status appears to be a sensitive indicator of cellular ability to resist toxicity challenge (Dickhout et al., 2012; Malhotra et al., 2008). The protocol described below is based on the oxidation of GSH by 5,5′-dithiobis(2-nitrobenzoic acid) (DTNB) resulting in GSSG and 5-thio-2-nitrobenzoic acid (TNB). Then GSSG is reduced back to GSH by highly specific action of glutathione reductase and NADPH. The assay enables detection of the total glutathione levels, while the oxidized form can be measured upon small modification of the protocol.

2.2.1 Cell culture sample preparation

Cells are rinsed with ice-cold PBS and collected with a rubber policeman on ice using 50 m*M* phosphate buffer (pH 7.4). Cells are centrifuged at 600 × *g* for 2 min at 4 °C, resuspended in 200 μl of phosphate buffer, and either homogenized with Dounce homogenizer or sonicated three times for 5 s with 10-s intervals and kept constantly on ice. Cell lysates are then centrifuged at 10,000 × *g* for 10 min at 4 °C and the supernatants are collected for the analysis. The samples are then deproteinated to avoid interference from protein SH groups (see below).

2.2.2 Tissue sample preparation

Extracted tissue is rinsed in PBS to remove residual red blood cells and immediately homogenized in 200–500 μl of ice-cold phosphate buffer and centrifuged at 10,000 × *g* for 10 min at 4 °C. Supernatant is used for deproteination.

2.2.3 Sample deproteination

This step is necessary to avoid artifacts due to the presence of protein SHs in the lysate. An equal volume of a freshly prepared 10% metaphosphoric acid solution (Sigma) is added to each sample and mixed for 1 min by vortexing. The samples are incubated at RT for 5 min followed by centrifugation at 3000 × *g* for 5 min. Supernatants are carefully separated from the pellet and mixed with 4 *M* triethanolamine solution such that 50 μl of triethanolamine is added per 1 ml of the supernatant. The samples are vortexed and taken for the analysis.

2.2.4 Sample preparation for measurement of oxidized glutathione (GSSG)

To separately quantify the levels of GSSG, GSH has to be first derivatized with 2-vinylpyridine (2VP), which masks the initial reduced glutathione

in the sample. Thus, it is essential to treat the standards with 2VP as well (5 μl of 2VP solution per every standard), meaning that the experiment has to be repeated once for total GSH and once for the oxidized. Solution of 1 *M* of 2VP is prepared in absolute ethanol and 10 μl is added per 1 μl of deproteinated sample, mixed by vortexing for 1 min and incubated at RT for 1 h. This part is applicable to both cell culture and tissue samples.

2.2.5 Reductase assay for GSH and GSSG

The rate of TNB formation is proportional to the concentration of GSH in the sample. The described protocol utilizes the glutathione assay kit 703002 from Cayman Chemical Company, Ann Arbor, MI. Briefly, the MES buffer is prepared by mixing 0.2 *M* 2-(*N*-morpholino)ethanesulfonic acid, 50 m*M* phosphate buffer, and 2 m*M* EDTA (pH 6.0). Then all the reagents provided in the kit (GSSG standard, cofactor, reductase enzyme, and DTNB) are reconstituted based on manufacturer's instructions. When all the mixtures are ready, 50 μl of GSSG standards or samples is added to microtiter plate and the plate is closed with a lid. At this point, the Assay Cocktail is prepared according to the number of samples and standards by mixing MES buffer, cofactor, DTNB, and reductase enzyme mixtures. The lid is removed and 150 μl of the cocktail is added to each well. The plate is covered and incubated in the dark for 25 min and the absorbance is measured at 405 nm. GSH concentration is usually measured by the "end point" method, but if high levels of cysteine or other thiols compared to GSH are expected, the kinetic method should be used (see manufacturer's protocol for instructions).

2.3. Lipid peroxidation

Lipid peroxidation is probably one of the most frequent forms of oxidative damages associated with human disease (Halliwell & Chirico, 1993). This process involves oxidative modification of fatty acids that occurs *in vivo* either by an enzymatic or a free radical-mediated reaction and has been implicated in a wide range of pathological conditions including atherosclerosis, stroke, diabetes, and aging (Dalle-Donne, Rossi, Colombo, Giustarini, & Milzani, 2006). In the nonenzymatic mode, it proceeds via a chain reaction that is initiated by the removal of hydrogen radical from the methylene group of polyunsaturated fatty acids (Fig. 14.2). Molecular rearrangement of the lipid radicals generates conjugated dienes, which react with oxygen to generate lipid peroxy radicals. It is these peroxy radicals that sustain the chain reaction by generating more lipid radicals and hydroperoxides from unmodified

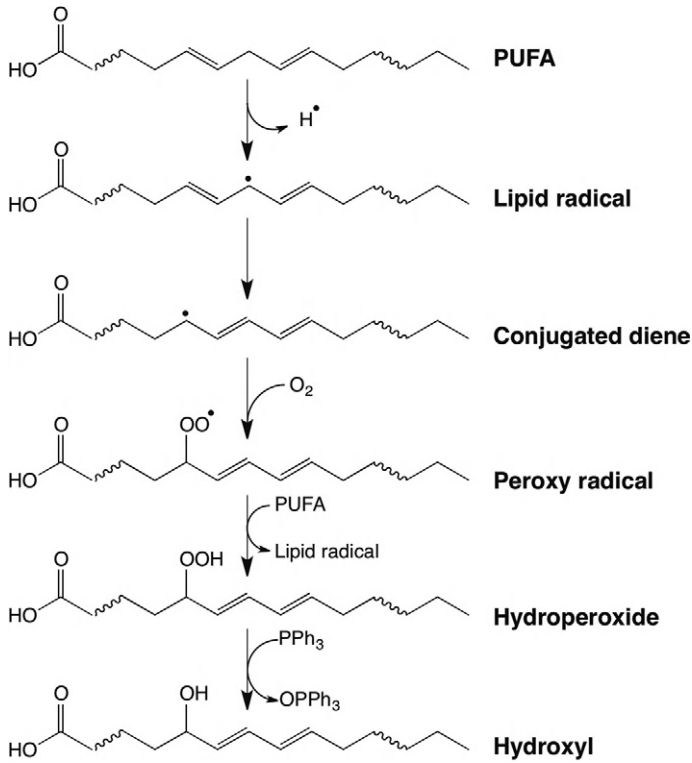

Figure 14.2 Nonenzymatic lipid peroxidation of a PUFA. For the sake of simplicity, only one possible isomer after the second step is represented. Free radical-mediated removal of a methylene hydrogen generates lipid radicals that rearrange to form conjugated dienes, which then react with molecular oxygen to form peroxy radicals. Peroxy radicals react with an unmodified PUFA to generate hydroperoxide dienoic acids that are reduced to hydroxy dienoic acids by triphenyl phosphine (PPh3) during the assay.

PUFAs (Fig. 14.2). In the case of linoleic acid—the most abundant PUFA *in vivo*—lipid peroxidation yields isomers of hydroperoxy lipids known as hydroperoxyoctadecadienoic acids (HPODEs). Hydroxyoctadecadienoic acids (HODEs) are the reduction products of HPODEs that have been described to be good biomarkers of lipid peroxidation (Yoshida & Niki, 2006). Oxidation of lipids has been successfully used as one of the oxidative stress markers and was found to be correlated with induction of ER stress. Importantly, treatments leading to amelioration of ER stress were able to reduce oxidized lipid products in mammalian cells (Back et al., 2009; Kim et al., 2009; Liu et al., 1997; Malhotra et al., 2008; Song et al., 2008). The most commonly assessed lipid peroxidation products include the HODEs,

4-hydroxynonenal, and malondialdehyde (MDA) (Esterbauer & Cheeseman, 1990). Below, we describe methods to detect HODEs and MDA.

2.3.1 Cell culture sample preparation

Cell pellets from 10×10^6 cells are washed with PBS and resuspended in the antioxidant buffer (100 μ*M* DTPA, 50 μ*M* BHT, 1% (v/v) ethanol, 10 m*M* 3-amino-1,2,4-triazole, 50 m*M* sodium phosphate buffer, pH 7.4), lyzed by three repeating cycles of flash-freezing in liquid nitrogen and thawing in a 37 °C water bath, and stored at −80 °C until the lipid extraction step.

2.3.2 Tissue sample preparation

Immediately after harvesting, the tissues are submerged in ice-cold antioxidant buffer and flash-frozen in liquid nitrogen. The frozen samples are stored at −80 °C until the lipid extraction.

2.3.3 Isolation of lipids

The procedure for isolation of lipids is derived from Dole and Meinertz (1960). All reagents must be of HPLC grade. Tissue samples are homogenized in ice-cold antioxidant buffer (0.3 ml) followed by the addition of 1 ml of a 40:10:1 (v/v/v) mixture of isopropanol, heptane, and 2 N acetic acid. Phase separation is achieved by the addition of 0.4 ml of water and 1.25 ml of heptane containing 40 μ*M* BHT and 1.2 m*M* triphenylphosphine (TPP) followed by a brief centrifugation at $2000 \times g$. The heptane phase is isolated and concentrated to dryness under nitrogen gas. Free fatty acids are extracted from this material by gentle base hydrolysis in a 4:1 (v/v) mixture of methanol and 5 N potassium hydroxide at 60 °C for 20 min. The samples are immediately cooled on ice and acidified using 0.2 volumes of 5 N acetic acid to terminate the hydrolysis reaction.

2.3.4 HPLC separation and quantitation of HODEs

Separation of HODEs is achieved by reverse-phase HPLC using an Ultrasphere ODS column (250 mm × 4.6 mm, 5 μ*M* particle size). The hydrolyzed fatty acid sample is passed through a 0.2-μm filter and loaded onto the column. Hydroxy fatty acids are eluted using a solvent phase of methanol:water:acetic acid (85:15:0.1, v/v/v) at a flow rate of 1 ml/min and detected by measuring absorbance at 234 nm. HODE standards are prepared by treating linoleic acid with soybean lipoxygenase followed by reduction with TPP, applied to the column in a similar fashion and used to assess

the retention time. HODEs are usually reported as pmol of oxidation product per mg of LDL protein.

2.3.5 Malondialdehyde

MDA is another frequently assessed marker of oxidative damage. Being a highly reactive dialdehyde produced upon the breakdown of peroxidated PUFAs, MDA readily interacts with functional groups of proteins, lipoproteins, DNA, and RNA (Esterbauer & Cheeseman, 1990). The toxicity of MDA stems from its ability to form Michael adducts with thiol groups, facilitate protein cross-linking, and cause mutagenesis (Esterbauer, Schaur, & Zollner, 1991). It was previously implicated in pathogenesis of diabetes mellitus, aging, brain ischemia, and other neurodegenerative diseases (Love, 1999; Lovell & Markesbery, 2007; Mutlu-Turkoglu et al., 2003; Slatter, Bolton, & Bailey, 2000). In addition, accumulation of MDA was demonstrated in cells experiencing ER stress (Kim et al., 2009; Lakshmanan et al., 2011; Malhotra et al., 2008). Detection of MDA is usually based on its reactivity with thiobarbituric acid (TBA), where one molecule of MDA reacts with two molecules of TBA with the production of a pink pigment having absorption at 532 nm. Here, we describe a modified version of such an assay where MDA is measured using a TBARS assay kit (10009055) manufactured by Cayman Chemical Company, Ann Arbor, MI.

2.3.6 Cell culture sample preparation

A good starting point for the assay is $1.5–2 \times 10^7$ cells. Cells are centrifuged for 2 min at $600 \times g$ and reconstituted in 1 ml of growth medium or PBS solution and transferred to Eppendorf tubes. The cells are kept on ice and sonicated three times for 5 s with 30-s intervals. No centrifugation is required at this point.

2.3.7 Tissue sample preparation

Tissue is extracted, rinsed in PBS, and 25–40 mg is transferred to an Eppendorf tube. Then the tissue is lyzed in 250 μl RIPA buffer (50 m*M* Tris–HCl, pH = 8, 150 m*M* KCl, 1.0% Nonidet P-40 (IGEPAL), 0.5% sodium deoxycholate, 0.1% SDS and protease inhibitors) on ice for 20 min and sonicated for 5 s with 10-s intervals. The tubes are centrifuged at $2000 \times g$ for 10 min at 4 °C, supernatant isolated for the analysis, and kept on ice.

2.3.8 Quantification of MDA by TBARS assay

Thiobarbituric acid reactive substances (TBARS) are a common way to measure lipid peroxidation products in cells, tissues, and body fluids, which

can complement a more specific assay such as HPLC. The assay is performed in the common microtiter format utilizing MDA standards as reference. Briefly, upon reconstitution of the reagents and solutions provided in the kit, 100 μl of colorimetric MDA standards or samples are added to 15-ml tubes, supplemented with 100 μl of the provided SDS solution, and diluted with 4 ml of the reconstituted color reagent. Color reagent solution contains TBA dissolved in a mixture of acetic acid and sodium hydroxide. The samples are mixed, placed in a rack, and boiled for 1 h. When the boiling is over, the samples should be quickly cooled in ice for at least 10 min to terminate the reaction and centrifuged at $1600 \times g$ for 10 min at 4 °C. At this point, the samples should be left at RT for 20 min and then 150 μl of either standards or samples are loaded to the microtiter plate to read the absorbance at 530 nm. When the mean absorbance of each sample is calculated, the absorbance of the "0" standard is subtracted from itself and all other samples and standards to give the corrected absorbance. The obtained values of standards are plotted as a function of the known MDA concentration (expressed in μmol/mg protein units) and the results are calculated from the standard curve equation.

2.4. Mitochondrial markers

Approximately 1–3% of the electrons passing through the mitochondrial respiratory chain leak out and absorbed by oxygen, leading to its partial reduction to the highly reactive superoxide anion (O_2^-). High concentrations of manganese SOD in the mitochondrial matrix catalyze the dismutation of (O_2^-) to H_2O_2, but elevated levels of superoxide can be detected by oxidation of a modified derivative of hydroethidine (HE). This modification makes HE positively charged and lipophilic and specifically targets it to the mitochondria, where it binds to mitochondrial DNA upon oxidation (Robinson, Janes, & Beckman, 2008). Binding to DNA makes HE highly fluorescent and enables its efficient detection by microscopy or flow cytometry. Another important parameter of mitochondrial function is an electrical potential difference ($\Delta\Psi$) across the mitochondrial inner membrane. Depolarization of mitochondria membrane leads to an opening of mPTP and eventually results in the activation of apoptosis. Mitochondrial depolarization can be detected using another group of lipophilic fluorescent dyes, such as rhodamine 123 and tetramethylrhodamine ethyl (TMRE) or methyl (TMRM) esters. These dyes accumulate at the inner mitochondrial membrane of normal cells and diffuse into the cytosol upon loss of

membrane potential, leading to reduction in signal intensity. It was previously shown that one of the sources for mitochondrial dysfunction is activation of the UPR and leakage of ER luminal calcium, making measurements of mitochondrial parameters a valuable tool in assessment of oxidative damage induced by ER stress (Arduino et al., 2009; Kim et al., 2008). Here, we describe two methods used to assess mitochondrial function in living cells applying confocal microscopy.

2.4.1 Preparation of cells for imaging

Subconfluent adherent cells are grown in 24-well culture plates. For cells growing in suspension, a culture plate should be preincubated overnight with 0.1% poly-L-lysine solution. Desired cell number should be diluted in 0.5 ml medium and adhered to wells by centrifugation of the plate at $600 \times g$ for 5 min.

2.4.2 Preparation of MitoSOX and TMRM

The MitoSOX Red (Life Technologies, NY, USA) is provided as 10 vials of 50 μg. Dissolve in 13.5 μl of DMSO to prepare 5 m*M* (×1000) working solution just before the experiment. Work in a reduced light environment and protect from light with a foil. The working solution of TMRM is 600 μ*M* dissolved in DMSO. Similarly, the reagent should be protected from light.

2.4.3 Analysis of superoxide and inner membrane potential with confocal microscopy

To assess mitochondrial function upon induction of ER stress, cells can be incubated with one of the common inducers of ER stress, such as thapsigargin (1 μ*M*) or tunicamycin (1 μg/ml). Times of incubation should be determined empirically, but usually would vary between 4 and 24 h. In our experimental system, CHO-K1 cells were engineered to produce human recombinant coagulation factor VIII, a naturally hard-to-fold protein, whose induced expression leads to acute ER stress (Malhotra et al., 2008). For detection of superoxide, cells are loaded with 5 μ*M* MitoSOX Red dye and incubated for 30 min at 37 °C in an incubator. The cells are washed twice with warm PBS solution and the medium is changed to a warm serum-free medium with 1% BSA. For detection of mitochondrial membrane potential, cells are loaded with 600 n*M* TMRM and incubated for 20 min at 37 °C. To maintain the equilibrium distribution of the fluorophore, the cells are washed twice with warm PBS and kept in warm

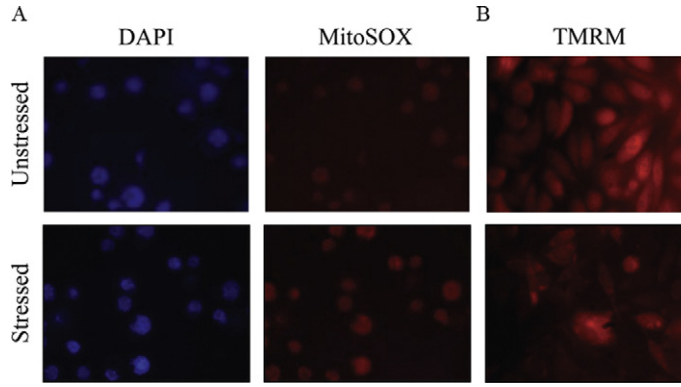

Figure 14.3 Measurement of mitochondrial markers of oxidative stress in CHO-K1 cells expressing human coagulation factor VIII. Expression of FVIII is inducible by sodium butyrate and leads to ER stress and activation of UPR. (A) Production of superoxide was monitored by incubating cells with MitoSOX red. Nuclei were stained with DAPI fluorescent dye. (B) Mitochondrial membrane potential was measured by changes in intensity of TMRM fluorescence.

serum-free medium with 1% BSA and 100 n*M* TMRM. Importantly, concentration of MitoSOX should be kept below 10 μ*M* and that of TMRM below 1 μ*M* to avoid toxicity. To monitor basal levels of TMRM fluorescence, an uncoupler of oxidative phosphorylation and electron transport (such as 1 μ*M* of FCCP) can be used. The plate should be positioned and fixed on a temperature-controlled stage of an appropriate confocal imaging system equipped with a Kr/Ar ion laser source with excitation at 568 nm for MitoSOX Red or TMRM and 405 nm for detection of DAPI nuclear staining (Fig. 14.3). Red fluorescence should be analyzed within 30 min of dye removal. Record images every 30 s. Data analysis can be done using any image processing software such as CellProfiler.

3. SUMMARY

Exposure of biological systems to oxidative stress leads to various age-dependent and pathological increases in the levels of oxidatively modified macromolecules, and the contribution of ER stress to these processes becomes more apparent. Accumulating data suggest that mitochondrial dysfunction plays a central role in ER stress-induced accumulation of ROS. Thus, parameters of mitochondrial activity are especially important in evaluating oxidative damage upon induction of ER stress. We have described

several methods that have been successfully implemented to monitor the redox status of the cell and evaluate markers of oxidative damage under the conditions of ER stress. Importantly, to avoid artifacts and evaluate the extent of oxidative damage, it is advised to analyze several oxidative markers and perform time course experiments to detect the most significant changes in the evaluated parameters.

REFERENCES

Appenzeller-Herzog, C. (2011). Glutathione- and non-glutathione-based oxidant control in the endoplasmic reticulum. *Journal of Cell Science*, *124*(Pt. 6), 847–855.

Arduino, D. M., Esteves, A. R., Domingues, A. F., Pereira, C. M., Cardoso, S. M., & Oliveira, C. R. (2009). ER-mediated stress induces mitochondrial-dependent caspases activation in NT2 neuron-like cells. *BMB Reports*, *42*(11), 719–724.

Back, S. H., Scheuner, D., Han, J., Song, B., Ribick, M., Wang, J., et al. (2009). Translation attenuation through eIF2alpha phosphorylation prevents oxidative stress and maintains the differentiated state in beta cells. *Cell Metabolism*, *10*(1), 13–26.

Belousov, V. V., Fradkov, A. F., Lukyanov, K. A., Staroverov, D. B., Shakhbazov, K. S., Terskikh, A. V., et al. (2006). Genetically encoded fluorescent indicator for intracellular hydrogen peroxide. *Nature Methods*, *3*(4), 281–286.

Berridge, M. J., Bootman, M. D., & Roderick, H. L. (2003). Calcium signalling: Dynamics, homeostasis and remodelling. *Nature Reviews. Molecular Cell Biology*, *4*(7), 517–529.

Brookes, P. S., Yoon, Y., Robotham, J. L., Anders, M. W., & Sheu, S. S. (2004). Calcium, ATP, and ROS: A mitochondrial love-hate triangle. *American Journal of Physiology. Cell Physiology*, *287*(4), C817–C833.

Brown, G. C., & Borutaite, V. (2012). There is no evidence that mitochondria are the main source of reactive oxygen species in mammalian cells. *Mitochondrion*, *12*(1), 1–4.

Dalle-Donne, I., Rossi, R., Colombo, R., Giustarini, D., & Milzani, A. (2006). Biomarkers of oxidative damage in human disease. *Clinical Chemistry*, *52*(4), 601–623.

Dalle-Donne, I., Rossi, R., Giustarini, D., Milzani, A., & Colombo, R. (2003). Protein carbonyl groups as biomarkers of oxidative stress. *Clinica Chimica Acta*, *329*(1–2), 23–38.

de Brito, O. M., & Scorrano, L. (2008). Mitofusin 2 tethers endoplasmic reticulum to mitochondria. *Nature*, *456*(7222), 605–610.

Dickhout, J. G., Carlisle, R. E., Jerome, D. E., Mohammed-Ali, Z., Jiang, H., Yang, G., et al. (2012). Integrated stress response modulates cellular redox state via induction of cystathionine gamma-lyase: Cross-talk between integrated stress response and thiol metabolism. *Journal of Biological Chemistry*, *287*(10), 7603–7614.

Dole, V. P., & Meinertz, H. (1960). Microdetermination of long-chain fatty acids in plasma and tissues. *Journal of Biological Chemistry*, *235*, 2595–2599.

Esterbauer, H., & Cheeseman, K. H. (1990). Determination of aldehydic lipid peroxidation products: Malonaldehyde and 4-hydroxynonenal. *Methods in Enzymology*, *186*, 407–421.

Esterbauer, H., Schaur, R. J., & Zollner, H. (1991). Chemistry and biochemistry of 4-hydroxynonenal, malonaldehyde and related aldehydes. *Free Radical Biology & Medicine*, *11*(1), 81–128.

Feissner, R. F., Skalska, J., Gaum, W. E., & Sheu, S. S. (2009). Crosstalk signaling between mitochondrial Ca^{2+} and ROS. *Frontiers in Bioscience*, *14*, 1197–1218.

Freedman, R. B., Hirst, T. R., & Tuite, M. F. (1994). Protein disulphide isomerase: Building bridges in protein folding. *Trends in Biochemical Sciences*, *19*(8), 331–336.

Go, Y. M., & Jones, D. P. (2008). Redox compartmentalization in eukaryotic cells. *Biochimica et Biophysica Acta*, *1780*(11), 1273–1290.

Gorlach, A., Klappa, P., & Kietzmann, T. (2006). The endoplasmic reticulum: Folding, calcium homeostasis, signaling, and redox control. *Antioxidants & Redox Signaling*, *8*(9–10), 1391–1418.

Halliwell, B., & Chirico, S. (1993). Lipid peroxidation: Its mechanism, measurement, and significance. *American Journal of Clinical Nutrition*, *57*(Suppl. 5), 715S–724S discussion 724S–725S.

Harding, H. P., Zhang, Y., Bertolotti, A., Zeng, H., & Ron, D. (2000). Perk is essential for translational regulation and cell survival during the unfolded protein response. *Molecular Cell*, *5*(5), 897–904.

Hartl, F. U., & Hayer-Hartl, M. (2009). Converging concepts of protein folding in vitro and in vivo. *Nature Structural & Molecular Biology*, *16*(6), 574–581.

Haze, K., Yoshida, H., Yanagi, H., Yura, T., & Mori, K. (1999). Mammalian transcription factor ATF6 is synthesized as a transmembrane protein and activated by proteolysis in response to endoplasmic reticulum stress. *Molecular Biology of the Cell*, *10*(11), 3787–3799.

Herrington, J., Park, Y. B., Babcock, D. F., & Hille, B. (1996). Dominant role of mitochondria in clearance of large Ca^{2+} loads from rat adrenal chromaffin cells. *Neuron*, *16*(1), 219–228.

Hwang, C., Sinskey, A. J., & Lodish, H. F. (1992). Oxidized redox state of glutathione in the endoplasmic reticulum. *Science*, *257*(5076), 1496–1502.

Kakihana, T., Nagata, K., & Sitia, R. (2012). Peroxides and peroxidases in the endoplasmic reticulum: Integrating redox homeostasis and oxidative folding. *Antioxidants & Redox Signaling*, *16*(8), 763–771.

Kim, J., Choi, T. G., Ding, Y., Kim, Y., Ha, K. S., Lee, K. H., et al. (2008). Overexpressed cyclophilin B suppresses apoptosis associated with ROS and Ca^{2+} homeostasis after ER stress. *Journal of Cell Science*, *121*(Pt. 21), 3636–3648.

Kim, H. R., Lee, G. H., Cho, E. Y., Chae, S. W., Ahn, T., & Chae, H. J. (2009). Bax inhibitor 1 regulates ER-stress-induced ROS accumulation through the regulation of cytochrome P450 2E1. *Journal of Cell Science*, *122*(Pt. 8), 1126–1133.

Kregel, K. C., & Zhang, H. J. (2007). An integrated view of oxidative stress in aging: Basic mechanisms, functional effects, and pathological considerations. *American Journal of Physiology. Regulatory, Integrative and Comparative Physiology*, *292*(1), R18–R36.

Kudin, A. P., Bimpong-Buta, N. Y., Vielhaber, S., Elger, C. E., & Kunz, W. S. (2004). Characterization of superoxide-producing sites in isolated brain mitochondria. *Journal of Biological Chemistry*, *279*(6), 4127–4135.

Lakshmanan, A. P., Thandavarayan, R. A., Palaniyandi, S. S., Sari, F. R., Meilei, H., Giridharan, V. V., et al. (2011). Modulation of AT-1R/CHOP-JNK-Caspase12 pathway by olmesartan treatment attenuates ER stress-induced renal apoptosis in streptozotocin-induced diabetic mice. *European Journal of Pharmaceutical Sciences*, *44*(5), 627–634.

Levine, R. L. (2002). Carbonyl modified proteins in cellular regulation, aging, and disease. *Free Radical Biology & Medicine*, *32*(9), 790–796.

Liu, H., Bowes, R. C., 3rd., van de Water, B., Sillence, C., Nagelkerke, J. F., & Stevens, J. L. (1997). Endoplasmic reticulum chaperones GRP78 and calreticulin prevent oxidative stress, Ca^{2+} disturbances, and cell death in renal epithelial cells. *The Journal of Biological Chemistry*, *272*(35), 21751–21759.

Love, S. (1999). Oxidative stress in brain ischemia. *Brain Pathology*, *9*(1), 119–131.

Lovell, M. A., & Markesbery, W. R. (2007). Oxidative damage in mild cognitive impairment and early Alzheimer's disease. *Journal of Neuroscience Research*, *85*(14), 3036–3040.

Malhotra, J. D., & Kaufman, R. J. (2007). Endoplasmic reticulum stress and oxidative stress: A vicious cycle or a double-edged sword? *Antioxidants & Redox Signaling*, *9*(12), 2277–2293.

Malhotra, J. D., Miao, H., Zhang, K., Wolfson, A., Pennathur, S., Pipe, S. W., et al. (2008). Antioxidants reduce endoplasmic reticulum stress and improve protein secretion. *Proceedings of the National Academy of Sciences of the United States of America*, *105*(47), 18525–18530.

Malinouski, M., Zhou, Y., Belousov, V. V., Hatfield, D. L., & Gladyshev, V. N. (2011). Hydrogen peroxide probes directed to different cellular compartments. *PLoS One*, *6*(1), e14564.

Marciniak, S. J., Yun, C. Y., Oyadomari, S., Novoa, I., Zhang, Y., Jungreis, R., et al. (2004). CHOP induces death by promoting protein synthesis and oxidation in the stressed endoplasmic reticulum. *Genes and Development*, *18*(24), 3066–3077.

Mutlu-Turkoglu, U., Ilhan, E., Oztezcan, S., Kuru, A., Aykaç-Toker, G., & Uysal, M. (2003). Age-related increases in plasma malondialdehyde and protein carbonyl levels and lymphocyte DNA damage in elderly subjects. *Clinical Biochemistry*, *36*(5), 397–400.

Nystrom, T. (2005). Role of oxidative carbonylation in protein quality control and senescence. *EMBO Journal*, *24*(7), 1311–1317.

Patil, C., & Walter, P. (2001). Intracellular signaling from the endoplasmic reticulum to the nucleus: The unfolded protein response in yeast and mammals. *Current Opinion in Cell Biology*, *13*(3), 349–355.

Raturi, A., & Simmen, T. (2013). Where the endoplasmic reticulum and the mitochondrion tie the knot: The mitochondria-associated membrane (MAM). *Biochimica et Biophysica Acta*, *1833*(1), 213–224.

Robinson, K. M., Janes, M. S., & Beckman, J. S. (2008). The selective detection of mitochondrial superoxide by live cell imaging. *Nature Protocols*, *3*(6), 941–947.

Rutkowski, D. T., Arnold, S. M., Miller, C. N., Wu, J., Li, J., Gunnison, K. M., et al. (2006). Adaptation to ER stress is mediated by differential stabilities of pro-survival and pro-apoptotic mRNAs and proteins. *PLoS Biology*, *4*(11), e374.

Schroder, M., & Kaufman, R. J. (2005). The mammalian unfolded protein response. *Annual Review of Biochemistry*, *74*, 739–789.

Sevier, C. S., & Kaiser, C. A. (2008). Ero1 and redox homeostasis in the endoplasmic reticulum. *Biochimica et Biophysica Acta*, *1783*(4), 549–556.

Slatter, D. A., Bolton, C. H., & Bailey, A. J. (2000). The importance of lipid-derived malondialdehyde in diabetes mellitus. *Diabetologia*, *43*(5), 550–557.

Song, B., Scheuner, D., Ron, D., Pennathur, S., & Kaufman, R. J. (2008). Chop deletion reduces oxidative stress, improves beta cell function, and promotes cell survival in multiple mouse models of diabetes. *The Journal of Clinical Investigation*, *118*(10), 3378–3389.

Stadtman, E. R. (2001). The story of glutamine synthetase regulation. *Journal of Biological Chemistry*, *276*(48), 44357–44364.

Tu, B. P., & Weissman, J. S. (2004). Oxidative protein folding in eukaryotes: Mechanisms and consequences. *The Journal of Cell Biology*, *164*(3), 341–346.

Veal, E. A., Day, A. M., & Morgan, B. A. (2007). Hydrogen peroxide sensing and signaling. *Molecular Cell*, *26*(1), 1–14.

Wajih, N., Hutson, S. M., & Wallin, R. (2007). Disulfide-dependent protein folding is linked to operation of the vitamin K cycle in the endoplasmic reticulum. A protein disulfide isomerase-VKORC1 redox enzyme complex appears to be responsible for vitamin K1 2,3-epoxide reduction. *Journal of Biological Chemistry*, *282*(4), 2626–2635.

Wu, R. F., Ma, Z., Liu, Z., & Terada, L. S. (2010). Nox4-derived H_2O_2 mediates endoplasmic reticulum signaling through local Ras activation. *Molecular and Cellular Biology*, *30*(14), 3553–3568.

Yoshida, H., Matsui, T., Yamamoto, A., Okada, T., & Mori, K. (2001). XBP1 mRNA is induced by ATF6 and spliced by IRE1 in response to ER stress to produce a highly active transcription factor. *Cell*, *107*(7), 881–891.

Yoshida, Y., & Niki, E. (2006). Bio-markers of lipid peroxidation in vivo: Hydroxyoctadecadienoic acid and hydroxycholesterol. *Biofactors*, *27*(1–4), 195–202.

Yoshida, H., Okada, T., Haze, K., Yanagi, H., Yura, T., Negishi, M., et al. (2000). ATF6 activated by proteolysis binds in the presence of NF-Y (CBF) directly to the cis-acting element responsible for the mammalian unfolded protein response. *Molecular and Cellular Biology*, *20*(18), 6755–6767.

AUTHOR INDEX

Note: Page numbers followed by "*f*" indicate figures.

A

Abdul-Ghani, M. A., 194
Abo, M., 85–86, 98
Ackrell, B. A., 190–191, 198–200, 203, 204–205, 212*f*
Adamus, J., 14–15, 146–149, 151–153, 154–155
Adam-Vizi, V., 201–202, 207–208
Adamzig, H., 114–115
Adeyoju, O., 137
Aeberhard, E., 85
Affourtit, C. L., 198–200
Afonso, C. A. M., 87–88
Ahmad, I. M., 85
Ahn, K. H., 23–25
Ahn, T., 235–237, 241–243, 244
Akerboom, J., 63
Albers, A. E., 22–23
Albrecht, S. C., 23–25, 63
Alderton, W. K., 84–85
Alexandre, J., 220, 227–228
Alvarez, I. S., 170–171
Amatore, C., 113–114, 124
Amino, H., 203
Anders, M. W., 234–235
Andersen, J. N., 176–177
Andreyev, A., 201
Ansenberger-Fricano, K., 10–12
Antonello, J., 193
Antunes, F., 160, 161, 163–164, 165–166, 171–172
Appenzeller-Herzog, C., 239–240
Arbault, S., 113–114, 124
Archer, S. L., 14
Arduino, D. M., 235–237, 245–246
Armour, A. G., 21
Armstrong, J. S., 14–15
Arnold, S. M., 233–234
Aviram, M., 117–118
Awano, M., 203
Ayala-Peña, S., 20
Aykaç-Toker, G., 244

B

Babcock, D. F., 234–235
Back, S. H., 235–238, 241–243
Bae, Y. S., 46
Baggiolini, M., 193
Bai, Y., 85, 92–93
Bailey, A. J., 244
Ballikaya, S., 62, 80
Balvers, W. G., 15
Bannai, S., 163–164, 169–170
Barata, A. G., 23–25, 63, 79–80
Barbouti, A., 84
Barrault, M.-B., 79–80
Bartolucci, S., 160
Bashan, N., 84–85, 92–93
Bashford, C. L., 206
Batandier, C., 132–133
Beal, M. F., 20, 84
Beckman, J. S., 100–101, 245–246
Bedard, K., 20–21, 46
Beija, M., 87–88
Beinert, H., 209
Bell, E. L., 124, 206
Bell, S., 170–171
Bellmunt, M. J., 140
Belousov, V. V., 23–25, 47–48, 62, 176–177, 184–185, 220–221, 235–237
Bentley, W. E., 110–111
Berridge, M. J., 234–235
Bertolotti, A., 233–234
Bertolotti, S. G., 2, 12–13
Bertozzi, C. R., 27
Beuster, G., 191
Beyerle, A., 9
Bhattacharya, A., 14–15, 194
Bilan, D. S., 23–25
Bimpong-Buta, N. Y., 234–235
Birringer, M., 191
Boada, J., 140
Bobrow, M. N., 137–138
Boden, M. J., 191
Boersma, M. G., 15

Bogdanova, E. A., 47–48, 176, 184–185
Bolton, C. H., 244
Bonini, M. G., 47
Bonner, W. D. Jr., 206
Bootman, M. D., 234–235
Boren, S. A., 137
Borquez-Ojeda, O., 15
Borutaite, V., 232–233
Bouton, C., 124
Boveris, A., 160, 163–164, 191–192, 193, 206
Bowes, R. C. III., 241–243
Bowman, M. K., 206
Brach, T., 63
Branco, M. R., 163–164, 171–172
Brand, M. D., 190–191, 193–194, 197–202, 199*f*, 200*f*, 203, 204–205, 206–209, 210–212, 212*f*
Brandon, A. E., 191
Brandt, U., 206
Brázdilová, P., 141–142
Brigelius-Flohé, R., 171–172
Britigan, B. E., 2, 3
Brookes, P. S., 124, 234–235
Brotea, G. P., 194
Brown, G. C., 200, 232–233
Browne, S. E., 14–15, 211
Bruce, D., 124
Buckingham, J. A., 193–194
Buckley, D. A., 176–177
Budinger, G. R. S., 124, 206
Bueno, C., 2, 12–13
Budworth, H., 20
Buettner, G. R., 197
Bunik, V. I., 190–191, 211
Burns, C. P., 2, 3

C

Cabrera, J. A., 14
Cadenas, E., 160, 163–164, 165–166, 206, 220–221
Cai, C. X., 114–115, 117–118
Cai, L., 220–221
Callera, G. E., 46
Calvin, S. A., 48, 51
Campian, J. L., 14
Canali, R., 197–198
Cao, Y., 85–86
Cao, Z., 86–87
Caporaso, N., 84
Carcamo, J. M., 15
Cardoso, S. M., 235–237, 245–246
Carlisle, R. E., 239–240
Carriulo, J. C., 25
Carroll, K. S., 20–21
Cary, S. P. L., 84–85
Cates, S., 51, 180
Chae, H. J., 85, 235–237, 241–243, 244
Chae, S. W., 85, 235–237, 241–243, 244
Chan, J. S. D., 23–25, 85
Chance, B., 160, 163–164, 191–192
Chandel, N. S., 206
Chang, C. J., 20, 21, 22–25, 27, 32, 47, 85–86, 89, 98, 176
Chang, M. C. Y., 21, 23, 26*f*, 35*f*
Chang, T. S., 108–109
Chang, Z., 22–23
Chatterjee, S., 10–12
Chaube, S. K., 84–85, 92–93
Chaudhuri, G., 85
Chaudhury, N. K., 110–111
Cheah, L. T., 114–115
Cheeseman, K. H., 241–243, 244
Chen, B., 86–87, 100–101
Chen, C., 85
Chen, F., 99–100
Chen, H. Y., 86–87, 100–101, 111–112, 114–115
Chen, J., 111–112
Chen, R.-K., 176–177
Chen, X., 87–88
Chen, Y.-Y., 113–114, 176–177
Chen, Z., 99–100, 137–138
Chignell, C. F., 47
Chinopoulos, C., 14–15, 201–202, 211
Chirico, S., 241–243
Chitambar, C. R., 85, 92–93
Chiu, D. T., 222
Cho, D. G., 23–25
Cho, E. Y., 235–237, 241–243, 244
Choi, D., 111
Choi, I. S., 222
Choi, J., 85
Choi, T. G., 245–246
Chowdhury, S. K., 207–208
Chung, K., 221, 222, 223

Clarke, W. L., 137
Clément, M.-V., 170–171
Cliffel, D. E., 111–112
Cobeño, L., 100–101
Codreanu, S. G., 20–21
Cogolludo, A., 100–101
Cohen, G., 108
Colombo, R., 237–238, 241–243
Colvin, K. E., 48, 51
Cooke, M. S., 84
Cooper, C. E., 84–85
Cooper, P. H., 193
Covas, G., 171
Covian, R., 206–207
Crofts, A. R., 205–206
Crooks, R. M., 113–114
Crow, J. P., 47
Crozatier, C., 113–114
Cubitt, A. B., 48, 180
Cyrne, L., 160, 161, 163–164, 165–166, 171–172
Czarnik, A. W., 23–25

D

Dagand, E., 85
Dai, Z., 111–112
Dalby, B., 51, 180
Dallas, S., 10–12
Dalle-Donne, I., 237–238, 241–243
Darley-Usmar, V., 220–221
Dasari, M., 99–100
Dasgupta, P. K., 140
D'Autréaux, B., 20, 46, 220
Davies, K. J., 220–221
Dawson, K., 160
Day, A. M., 20, 108, 232–233
de Brito, O. M., 234–235
de Groot, H., 85, 92–93
De Oliveira-Marques, V., 160
de Vries, H. E., 191
Debski, D., 148, 154–155
Delaunay, A., 79–80
Demaurex, N., 63
Demers, L. M., 99–100
Dencher, N. A., 132–133
Dennery, P. A., 220–221
Dequaire, M., 111–112
Deravi, L. F., 111–112
Derbyshire, E. R., 84–85
Derrickson, B., 141
Dertinger, S. K. W., 222
DeYulia, G. J. Jr., 15
Diaz-Bérrio, J., 161
Dick, T. P., 23–25, 62, 63–64, 79–80
Dickhout, J. G., 239–240
Dickinson, B. C., 20, 22–23, 26*f*, 27, 32, 35*f*, 85–86, 89, 98, 176
Dickinson, D. A., 85
Dickson, R. M., 48, 180
Dikalov, S., 14–15
Ding, H., 85, 92–93
Ding, Y., 245–246
Diwu, Z., 2, 137, 140, 193–194
Dizdaroglu, M., 84
Dodani, S. C., 23–25
Dole, V. P., 243
Domaille, D. W., 22–23, 85–86, 89, 98
Domingues, A. F., 235–237, 245–246
Domínguez-Arroyo, J. A., 170–171
Dou, Y. H., 114–115
Drahota, Z., 207–208
Dranka, B. P., 146–149, 151–153
Drapier, J. C., 124
Drews, M., 84–85
Dröge, W., 46
Drose, S., 206
Du, J., 23–25
Dubikovskaya, E. A., 27
Ducrocq, C., 84–85, 92–93
Durst, R. A., 115
Dutton, D. R., 15
Dutton, P. L., 206
Dybala-Defratyka, A., 146–148, 154–155
Dyer, C. E., 114–115
Dykstra, P. H., 110–111

E

Eaton, J. W., 14
Eaton, S., 210
Eguchi, H., 85, 92–93
Eichele, E., 163–164
Eisenbart, J., 124, 206
El-Agnaf, O. M., 108
Elger, C. E., 234–235
Elowitz, M. B., 221
Encinas, M. V., 2, 12–13

Enomoto, J., 110–111, 112–113, 114–115, 117–118
Erecinska, M., 206
Ermakova, Y. G., 23–25
Esterbauer, H., 241–243, 244
Esteves, A. R., 235–237, 245–246
Etzioni, A., 117–118
Euler, G., 46
Evans, M. D., 84
Exner, N., 20

F

Fahn, S., 108
Fales, H. M., 146–148
Fan, J., 23–25
Fann, Y. C., 47
Farias-Eisner, R., 85
Feissner, R. F., 232–233, 234–235
Feng, Y., 86–87
Feng, Z., 136–137
Fernandes, E., 47, 84, 124
Ferrans, V. J., 191
Figeys, D., 109
Filep, J. G., 85
Findlay, V. J., 160
Finkel, T., 191
Finn, O. J., 108
Fiorentino, G., 160
Firestein, G. S., 227–228
Fisher, A. B., 220–221
Fiskum, G., 14–15, 132–133, 197–198, 201, 211
Fleischman, A. J., 113–114
Flohé, L., 163–164, 171–172
Floryk, D., 207–208
Fluxà, V. S., 87–88
Folz, R. J., 20
Fontaine, E., 132–133
Forman, H. J., 46, 85, 220–221
Fradkov, A. F., 23–25, 47–48, 62, 176–177, 220–221, 235–237
Frazziano, G., 100–101
Freedman, R. B., 233
Freeman, B. A., 100–101
Frenzel, M., 132–133
Frerman, F. E., 209
Freyer, D., 85
Fricker, M. D., 63
Fridovich, I., 10–12, 191–192
Frisard, M., 20
Frisell, W. R., 209
Fujiwara, N., 85, 92–93
Fukada, T., 176–177
Fukuto, J. M., 85
Fung, Y. K., 100–101

G

Gabe, Y., 85–86, 89
Gadella, T. W. J., 23–25
Gage, F. H., 36
Galaris, D., 84
Galic, S., 176–177
Ganini, D., 10–12
Gao, W., 86–87, 100–101
Gao, X., 85–86, 89
Gaum, W. E., 232–233, 234–235
Gaydos, L. J., 99–100
Gelperin, A., 85–86, 98
Gendreizig, S., 22–23
Gerencser, A. A., 190–191, 198–200, 206–207, 212*f*
German, M. J., 108
Geurts, J. J., 191
Ghandour, H., 124
Ghatpande, A., 85–86, 98
Giorgio, M., 20
Giridharan, V. V., 244
Giustarini, D., 237–238, 241–243
Gladyshev, V. N., 176, 235–237
Go, Y. M., 232–233
Gogvadze, V., 124
Golde, D. W., 15
Golden, T., 191
Gomes, A., 47, 84, 124
Gomes, C. M., 209
Gong, X., 99–100
Gong, Z. N., 114–115, 117–118
González- Carrera, E., 170–171
Goodman, S. I., 209
Gorlach, A., 234–235
Gorokhovatsky, A. Y., 23–25
Goswami, P., 109–110, 111
Green, D. R., 227–228
Greenamyre, J. T., 14–15
Grisham, M. B., 85, 92–93, 220–221
Grivennikova, V. G., 200–201

Gronemeyer, T., 22–23
Gross, A. J., 137–138
Grosshans, J., 23–25, 63
Groth, M., 191
Guardiola, J., 14
Guilbe, M. M. R., 63
Gülden, M., 163–164
Gunasingham, H., 110–111
Gunnison, K. M., 233–234
Gunzler, A., 163–164
Guo, P., 85–86
Gupta, R., 110–111
Gutscher, M., 62, 80

H

Ha, K. S., 245–246
Haas, A. L., 85, 92–93
Haass, C., 20
Hagen, T. M., 146–148, 220–221
Hall, C. L., 209
Haller, M., 84
Halliwell, B., 20, 170–171, 241–243
Hampton, M. B., 160
Han, D., 197–198
Han, J., 235–238, 241–243
Han, S., 111–112
Hanaoka, K., 85–86, 98
Hansford, R. G., 201
Harder, D. R., 153
Harding, H. P., 233–234
Hardy, M., 14–15, 146–149, 151–153
Harman, D., 191
Harpe, J. D., 140
Harris, A., 51, 180
Harris, T. D., 137–138
Harry, R. S., 111–112
Hartl, F. U., 233
Haswell, S. J., 114–115
Hatfield, D. L., 176, 235–237
Haugland, R. P., 2, 137, 140, 193–194
Hayashi, Y., 108
Hayer-Hartl, M., 233
Haze, K., 233–234
He, J.-M., 85–86
He, L., 86–87, 100–101
He, X., 137–138
He, Y., 46
Hegedus, V., 207–208
Heger, J., 46
Heinze, K. G., 136–137
Heo, J., 113–114
Hermann, M., 84
Hernandez, H. H., 63
Herrero, E., 160
Herrington, J., 234–235
Hiatt, L. A., 111–112
High, K., 193
Hikosaka, K., 99–100
Hille, B., 234–235
Hinks, J. A., 176–177
Hirose, K., 23
Hirst, J., 190–191, 200–201
Hirst, T. R., 233
Hoffman, D. L., 124
Hoffman, P. S., 170–171
Hoffmann, O., 85
Hogue, B. A., 201
Holmgren, A., 20
Hopman, A. H. N., 137–138
Horsefield, R., 203
Hou, J., 85
Hsu, S.-F., 176–177
Hu, M., 23–25
Hu, X., 85, 92–93
Hu, Y., 137, 140
Huang, P., 220, 227–228
Huang, S.-T., 87–88
Huang, Y., 20
Huo, X., 203
Hur, K. C., 46
Hurt, D., 46
Husain, M., 209
Hutson, S. M., 233
Huynh, C., 22–23, 85–86, 89, 98
Hwang, C., 233, 239–240
Hwang, H., 140
Hyslop, P. A., 193

I

Iavarone, A. T., 22–23
Ikeda, Y., 209
Ilhan, E., 244
Imlay, J. A., 203
Ioannidis, I., 85, 92–93
Irani, K., 191
Isacoff, E. Y., 21, 22–23, 47, 176

Ishii, M., 85, 92–93
Ito, E., 136–137
Iwasaki, M., 85, 92–93
Iwuoha, E. I., 137

J

Jacobsen, L. B., 48, 51
Jaffe, J. S., 2, 3, 193–194
Janes, M. S., 146–148, 220–221, 245–246
Jang, Y. C., 194
Jencks, W. P., 25
Jeon, N. L., 222
Jeong, W., 108–109
Jerome, D. E., 239–240
Jess, A., 163–164
Ji, G. E., 99–100
Jiang, H., 239–240
Jiang, J., 2–3, 13, 13, 15
Jiang, M., 85, 92–93
Johnsson, K., 22–23
Jones, D. P., 220, 232–233
Jones, N., 160
Joo, C. U., 85
Joosen, L., 23–25
Jordan, M., 51
Jordan, W., 191–192
Joseph, J., 14–15, 25–27, 85, 92–93, 146–149, 151–153
Jové, M., 140
Ju, H., 111–112
Juhaszova, M., 132–133
Juillerat, A., 22–23
Jun, M. E., 23–25
Jung, H. K., 99–100
Jungreis, R., 233–234

K

Kachko, I., 84–85, 92–93
Kaiser, C. A., 233
Kakihana, T., 232–233
Kakinuma, K., 32–34
Kalcher, K., 141–142
Kalivendi, S., 146–148
Kalousova, M., 108
Kalwa, H., 85–86, 92–93, 176–177
Kalyanaraman, B., 20, 25–27, 146–149, 151–153, 220–221
Kamiya, M., 23
Kammann, J., 163–164
Kanda, K., 23
Kang, D., 108–109
Kaplowitz, N., 197–198
Kaufman, R. J., 232–237, 241–243
Kazlauskas, A., 46
Kehrer, I., 84
Kemp, M. L., 221, 222, 223
Keppler, A., 22–23
Keszler, A., 85, 92–93
Keys, K. B., 110–111
Khaja, S., 99–100
Khoo, K.-H., 176–177
Kietzmann, T., 234–235
Kikuchi, K., 85–86, 87–88, 89
Kim, H. J., 87–88
Kim, H. N., 87–88
Kim, H. R., 85, 235–237, 241–243, 244
Kim, J. J., 209, 245–246
Kim, J. S., 23–25, 87–88
Kim, O. S., 46
Kim, S. A., 136–137
Kim, S. R., 176–177
Kim, Y. J., 46, 245–246
Kindermann, M., 22–23
Kinjo, M., 136–137
Kishino, T., 85
Kita, K., 203
Kitao, T., 85
Klappa, P., 234–235
Klimova, T. A., 124, 206
Klingenberg, M., 207
Klomsiri, C., 20–21
Knowles, R. G., 84–85
Ko, J. K., 85
Ko, Y. T., 99–100
Koev, S. T., 110–111
Koge, K., 99–100
Koh, A. C., 124
Koh, W. G., 111, 112–113
Kojima, H., 85–86, 89
Komatsu, T., 85–86, 98
Komminoth, P., 137–138
Koppenol, W. H., 160
Korge, P., 14
Korshunov, S. S., 132, 201–202
Kotamraju, S., 85, 92–93, 153
Kotzian, P., 141–142

Kovsan, J., 84–85, 92–93
Koyama, Y., 99–100
Kozlov, A. V., 84
Kramer, D. M., 206
Krause, K.-H., 20–21, 46
Kregel, K. C., 232–233
Krohn, K., 84, 85
Krylov, A. V., 114–115
Kudin, A. P., 234–235
Kuhlow, D., 191
Kuhn, D. C., 99–100
Kuivila, H. G., 21, 27
Kunz, W. S., 234–235
Kurth, E., 114–115
Kuru, A., 244
Kushnareva, Y., 201
Kussmaul, L., 190–191, 200–201
Kutschy, P., 220–221, 224–225
Kuznetsov, A. V., 84
Kwak, Y. G., 85
Kwon, K. S., 176–177

L

Lachance, S., 85
Lai, Y. H., 110–111
Laketa, V., 46, 176–177, 179, 181
Lakshmanan, A. P., 244
Lambert, A. J., 198–200, 201–202
Lambeth, J. D., 20–21, 209
Lange, S., 46
Lapierre, C., 85
Lardy, H. A., 208
Larsson, N.-G., 20
Lazur, G. J., 112–113
Lee, C.-L., 176–177
Lee, D., 99–100
Lee, G. H., 235–237, 241–243, 244
Lee, K. H., 245–246
Lee, M. H., 87–88
Lee, S. R., 176–177
Lee, S.-J., 99–100
Lee, W., 111
Lee, Y.-H., 87–88
Leger, C., 203
Lenich, A. C., 209
Leto, T. L., 46
Leverve, X., 132–133
Levine, A. J., 221
Levine, R. L., 146–148, 237–238
Levy, R., 117–118
Li, C. Y., 114–115, 117–118
Li, C. Z., 110–111
Li, H., 99–100, 111–112
Li, J.-H., 85, 92–93, 233–234
Li, Q., 99–100
Li, T., 85, 92–93
Li, Y. M., 110–111
Li, Y. S., 137, 140
Li, Z., 111, 117–118
Liang, H., 14–15, 137–138
Liebler, D. C., 20–21
Lim, J., 20
Lim, K.-T., 99–100
Lima, J. L. F. C., 47, 84, 124
Limoges, B., 111–112
Lin, C.-M., 87–88
Lin, H.-F., 85, 92–93
Lin, M. T., 20, 84
Lin, V. S., 32
Lin, W., 86–87, 90*f*, 91*f*, 93*f*, 95*f*, 97*f*, 100–101, 100*f*, 101*f*
Liochev, S. I., 10–12
Lippard, S. J., 85–86, 92–93, 98, 176–177
Lippert, A. R., 21
Litt, G. J., 137–138
Liu, H. H., 110–111, 241–243
Liu, S., 111–112
Liu, X., 100–101, 111–112
Liu, Y.-Q., 14–15, 85, 92–93, 194, 197–198
Liu, Z., 137, 140, 235–237
Lochel, B., 114–115
Lodi, F., 100–101
Lodish, H. F., 233, 239–240
Logan, D. C., 63
Long, L. H., 86–87, 170–171
Lopez, M., 25–27, 146–148
Lorenzo, B. J., 14–15, 211
Loschen, G., 163–164
Lou, Y.-W., 176–177
Love, S., 244
Lovell, M. A., 244
Lowe, G., 85–86, 98
Lowman, A. M., 110–111
Lu, H., 221, 222, 223
Lü, P., 85, 92–93
Lu, Z. H., 111–112, 114–115

Luan, S. R., 110–111
Lubeck, E., 220–221
Lukyanov, K. A., 23–25, 47–48, 62, 176–177, 220–221, 235–237
Lukyanov, S., 47–48, 176, 184–185
Luna-Chavez, C., 203
Lunec, J., 84
Luo, J., 110–111
Luo, W., 137, 140
Luo, X., 110–111
Lustgarten, M. S., 194
Lutz, A. K., 20

M

Ma, J., 85–86, 98
Ma, Z., 235–237
Mackenzie, C. G., 209
Maeda, S., 85
Mahrhofer, C., 85
Maier, J., 84, 85
Maillard, N., 87–88
Majima, H. J., 32–34
Makino, N., 163–164
Malavé, E. C. A., 63
Malhotra, J. D., 232–238, 239–240, 244, 246–247
Malinouski, M., 176, 235–237
Malinski, T., 84–85
Mao, M., 10–12
Marcaccio, M., 124, 126–127, 128, 130
Marchesi, E., 47
Marcinek, A., 146–148
Marciniak, S. J., 233–234
Marcu, R., 124, 126–127, 128, 130
Mariani, T. J., 20
Marinho, H. S., 160, 161, 163–164, 165–166, 171–172
Markakis, E. A., 36
Markesbery, W. R., 244
Markvicheva, K. N., 46, 47–48, 176–177, 179, 181, 184–185
Marletta, M. A., 84–85
Martinho, J. M. G., 87–88
Martino, E., 193
Martín-Romero, F. J., 170–171
Marty, L., 63
Maser, E., 163–164
Mason, R. P., 2–3, 4*f*, 5–8, 5*f*, 7*f*, 9*f*, 10–13, 11*f*, 14, 15, 47
Mata, A., 113–114
Matharu, Z., 110–111, 112–113, 114–115
Matias, A. C., 160
Matsui, T., 233–234
Mattson, M. P., 20
Mayer, B., 84–85
McCord, J. M., 191–192
McDonald, J. F., 220–221, 224–225
McKenzie, J. R., 111–112
McQuade, L. E., 85–86, 98
Mehta, J. P., 14
Meilei, H., 244
Meinertz, H., 243
Melov, S., 191
Meng, T.-C., 176–177
Meng, Y., 193
Messner, K. R., 203
Meves, A., 9
Meyer, A. J., 62, 63–64, 80
Mezencev, R., 220–221, 224–225
Miao, H., 235–238, 239–240, 244, 246–247
Miao, Y. Q., 110–111
Michalowski, B., 148, 154–155
Michalski, R., 146–148
Michel, T., 85–86, 92–93, 176–177
Michelakis, E. D., 14
Migliaccio, E., 20
Miguel-Lasobras, E. M., 170–171
Mildaziene, V., 201
Millar, J. B. A., 160
Miller, C. N., 233–234
Miller, E. W., 22–23, 27, 47, 85–86, 89, 98, 176
Milligan, S. A., 85, 92–93
Millonig, G., 79–80
Milzani, A., 237–238, 241–243
Minor, R. L., 100–101
Minteer, S. D., 109–110, 111
Mishina, N. M., 46, 176–177, 179, 181
Mitchell, P., 205–207
Miura, T., 137
Miwa, S., 201–202, 207–208
Miyata, Y., 206
Miyoshi, H., 203
Mochizuki, Y., 163–164
Moerner, W. E., 48, 180

Mohammed-Ali, Z., 239–240
Mohanty, J. G., 2, 3, 193–194
Moiroux, J., 111–112
Monceau, L., 79–80
Monette, J. S., 146–148, 220–221
Moraes, C. T., 124, 206
Morand, S., 46
Moreno, L., 100–101
Morgan, B. A., 20, 64, 108, 160, 232–233
Mori, A., 85
Mori, K., 233–234
Morikawa, M., 137
Motobu, M., 99–100
Mracek, T., 207–208
Mucke, L., 20
Mueller, S., 79–80
Müller, C., 63
Muller, F. L., 14–15, 194, 206
Murphy, A. N., 201
Murphy, M. P., 20, 124, 206
Mutlu-Turkoglu, U., 244
Muto, H., 136–137
Myers, M. P., 176–177

N

Nagano, T., 23, 32–34, 85–86, 87–88, 89, 98
Nagaraja, P., 137, 140
Nagata, K., 232–233
Nagelkerke, J. F., 241–243
Nakamura, K., 99–100
Nakamura, T., 136–137
Nam, C. I., 22–23
Nathan, C. F., 140
Negishi, M., 233–234
Nelson, K. J., 20–21
Neumann, M. G., 2, 12–13
Neuzil, J., 191
Nichols, J. H., 137
Niki, E., 241–243
Nithipatikom, K., 146–148
Niu, W., 111–112
Nohl, H., 191–192, 193
Nomura, Y., 136–137
Novak, J., 63
Novoa, I., 233–234
Nunomura, A., 227–228
Nystrom, T., 237–238

O

O'Brien, T., 9
Ochs, R. S., 208
Ohki, E. C., 51, 180
Ohkura, Y., 137–138, 140
Ohnishi, S. T., 200–201
Ohnishi, T., 200–201
Ohta, K., 200–201
Okada, R., 137
Okada, T., 233–234
Okreglak, V. S., 22–23
Oliveira, C. R., 235–237, 245–246
Oliveira-Marques, V., 171
Orr, A. L., 190–191, 198–200, 199*f*, 203, 204–205, 206–209, 210–212, 212*f*
Orrenius, S., 124
Oshino, N., 191–192
Ostman, A., 46
Oswald, B., 2, 3
Ouari, O., 146–149, 151–153
Ovadia, H., 84–85, 92–93
Owens, M. W., 85, 92–93
Oyadomari, S., 233–234
Oztezcan, S., 244

P

Pahan, K., 100–101
Palaniyandi, S. S., 244
Paleologou, K. E., 108
Palmer, T. D., 36
Pamplona, R., 140
Panchuk-Voloshina, N., 2, 137, 140, 193–194
Pandey, A. N., 84–85, 92–93
Pang, D. W., 110–111
Panov, A., 14–15
Paranagama, M. P., 203
Park, J., 111
Park, S. Y., 99–100
Park, Y. B., 234–235
Parkinson, A., 15
Partridge, L., 201–202, 207–208
Paschke, R., 84, 85
Pase, L., 23–25
Patel, M. S., 14–15, 211
Patil, C., 233–234
Paulsen, C. E., 20–21

Payne, G. F., 110–111
Pedone, E., 160
Pedrosa, V. A., 110–111, 112–113, 117–118
Pehar, M., 146–148, 220–221
Pelicci, P. G., 20, 124, 126–127, 128, 130
Peltier, J., 27
Peng, X., 23–25
Pennathur, S., 235–238, 239–240, 241–243, 244, 246–247
Peppas, N. A., 110–111
Pereira, C. M., 235–237, 245–246
Perevoshchikova, I. V., 190–191, 198–200, 199*f*, 203, 204–205, 206–209, 210–212, 212*f*
Perry, G., 227–228
Pestka, J. J., 99–100
Petros, J., 99–100
Peus, D., 9
Peyrot, F., 84–85, 92–93
Pflieger, D., 79–80
Pick, H., 22–23
Pine, L., 170–171
Ping, P., 14
Pinto, D., 109
Pipe, S. W., 235–238, 239–240, 244, 246–247
Piper, H. M., 46
Pishko, M. V., 111, 112–113
Pittelkow, M. R., 9
Pluth, M. D., 85–86, 92–93, 176–177
Poburko, D., 63
Pohanka, M., 108–109
Poole, L. B., 79–80
Portero-Otín, M., 140
Pott, M., 9
Pradhan, T., 87–88
Pralle, A., 21, 22–23
Pravda, M., 137
PremKumar, K. V., 84–85, 92–93
Preston, E., 191
Previtali, C. M., 2, 12–13
Price, P. J., 51, 180
Priebe, S., 191
Prince, R. C., 206
Pryde, K. R., 200–201
Pulz, O., 114–115

Q

Qian, L., 109–110, 111–112
Quang, D. T., 23–25
Quinlan, C. L., 190–191, 197–201, 199*f*, 202, 203, 204–205, 206–209, 210–212, 212*f*
Quinn, J., 160

R

Rada, B., 46
Raible, D. G., 2, 3, 193–194
Raina, A. K., 227–228
Ralph, S. J., 191
Ramalingam, J., 170–171
Ramsay, R. R., 209
Ranguelova, K., 2–3, 13, 13, 15
Rapino, S., 124, 126–127, 128, 130
Raturi, A., 234–235
Rauchova, H., 207–208
Rauen, U., 85, 92–93
Ravussin, E., 20
Redl, H., 84
Reed, G. A., 15
Ren, C., 111, 117–118
Ren, Y., 25
Repine, J. E., 100–101
Repovská, M., 220–221, 224–225
Reszka, K. J., 2, 3
Reth, M., 84
Rettori, D., 197–198
Revzin, A., 110–111, 112–113, 114–115, 117–118
Reymond, J.-L., 87–88
Reynolds, I. J., 13, 15, 124, 201–202
Rhee, S. G., 20, 84, 108–109, 176–177
Ribick, M., 235–238, 241–243
Rich, P. R., 206–207
Ridnour, L. A., 85
Rietjens, I. M., 15
Ristow, M., 191
Rivera-Sánchez, S., 20
Rivet, C. A., 221, 222, 223
Roberts, A. G., 206
Robin Harris, J., 79–80
Robinson, K. M., 146–148, 220–221, 245–246
Robotham, J. L., 234–235

Roderick, H. L., 234–235
Rodrigues, J. V., 209
Roebuck, S. J., 193–194
Rogers, L. C., 20–21
Rommelspacher, H., 132–133
Ron, D., 233–234, 235–237, 241–243
Rosen, G. M., 100–101
Rosenblat, M., 117–118
Ross, M. F., 146–148, 220–221
Rossi, R., 237–238, 241–243
Rota, C., 47
Rottenberg, H., 206–207
Rottkamp, C. A., 227–228
Roy, A., 100–101
Roy, B., 23–25
Roy, S., 113–114
Rubloff, G. W., 110–111
Ruch, W., 193
Rudich, A., 84–85, 92–93
Rutkowski, D. T., 233–234
Ruzicka, F. J., 209
Rydstrom, J., 210–211

S

Sabia, M., 14–15
Sadamoto, H., 136–137
Safar, F., 36
Saito, K., 136–137
Sakamoto, K., 203
Sakamoto, Y., 137
Sakiyama, H., 85, 92–93
Salmeen, A., 176–177
Salter, J. D., 124
Samstag, Y., 62, 80
Santo-Domingo, J., 63
Sarasin, A., 124
Sari, F. R., 244
Sarma, A. K., 109–110, 111
Sartoretto, J. L., 85–86, 92–93, 176–177
Sauer, H., 46
Saveant, J. M., 111–112
Schafer, F. Q., 197
Schaffer, D. V., 27
Schagger, H., 132–133
Schaur, R. J., 244
Scheuner, D., 235–238, 241–243
Schiffrin, E. L., 46
Schmeisser, S., 191
Schmidt, U., 79–80
Schmielau, J., 108
Schonfeld, P., 132–133
Schröder, E., 79–80
Schroder, M., 233–234
Schubert, D., 197–198
Schulman, E. S., 2, 3, 193–194
Schulz, T. J., 191
Schumacker, P. T., 14
Schwarzländer, M., 63
Schwille, P., 136–137
Scorrano, L., 234–235
Seibert, H., 163–164
Serrano, J., 140
Sessler, J. L., 23–25
Setsukinai, K., 32–34
Sevier, C. S., 233
Seymour, A. M., 114–115
Shakhbazov, K. S., 23–25, 47–48, 62, 176–177, 220–221, 235–237
Shalbuyeva, N., 14–15
Shang, G.-Q., 85–86, 89
Shaughnessy, K. J., 137–138
She, X.-P., 85–86
Shelton, C. C., 15
Shen, H., 137–138
Sherer, T., 14–15
Sheu, S. S., 232–233, 234–235
Shi, L., 111–112
Shimizu, S., 85, 92–93
Shinzawa-Itoh, K., 200–201
Shiota, K., 85, 92–93
Shivakumar, A., 137, 140
Shrestha, A. K., 137, 140
Shrivastav, T. G., 84–85, 92–93
Sies, H., 160, 163–164
Sievers, C., 190–191, 211
Siggia, E. D., 221
Sikora, A., 14–15, 25–27, 146–149, 151–153, 154–155
Sillence, C., 241–243
Sim, J. E., 85
Simmen, T., 234–235
Simonian, A. L., 110–111, 112–113, 117–118
Singer, O., 48, 180
Sinskey, A. J., 233, 239–240
Sirkar, K., 111

Sitia, R., 232–233
Sizer, I. W., 137–138
Skalska, J., 232–233, 234–235
Skiada, V., 84
Skladai, P., 108–109
Sklar, L. A., 193
Skoda, E. M., 20
Skulachev, V. P., 132, 201–202
Slatter, D. A., 244
Smith, M. A., 227–228
Smith, S. H., 85
Smyth, M. R., 137
Sobotta, M. C., 62, 64, 80
Soito, L., 20–21
Sojic, N., 124
Sokoloski, E. A., 146–148
Sollott, S. J., 132–133
Soneja, A., 84–85
Song, B., 235–238, 241–243
Song, J., 86–87
Song, W., 14–15
Song, X.-G., 85–86
Song, Y., 111, 117–118
Sousa-Lopes, A., 161
Speel, E. J. M., 137–138
Squillace, K., 9
Srikun, D., 22–23, 85–86, 89, 98
Srinivasan, S., 146–148
Stadtman, E. R., 237–238
Staniek, K., 193
Starkov, A. A., 14–15, 132–133, 201–202, 211
Staroverov, D. B., 23–25, 47–48, 62, 176–177, 184–185, 220–221, 235–237
Steenkamp, D. J., 209
Stevens, J. L., 241–243
Stone, D., 27
Stone, J. R., 20, 124
Stoppani, A. O. M., 193
St-Pierre, J., 193–194, 201–202, 207–208
Stroock, A. D., 222
Stuart, E., 191
Su, D., 203
Sugawa, M. D., 132–133
Sugita, Y., 163–164
Summers, F. A., 2–3, 4*f*, 5–8, 5*f*, 7*f*, 9*f*, 10–11, 12–13, 12, 14
Sun, C., 99–100
Sun, F., 203
Sundaresan, M., 191
Sung, J. Y., 46
Suzuki, K., 85, 92–93
Swain, P. S., 221
Sweetlove, L. J., 63

T

Tabet, F., 46
Tabner, B. J., 108
Tacnet, F., 79–80
Tak, P. P., 227–228
Takacs, K., 207–208
Takakusa, H., 87–88
Takamiya, K. I., 206
Tampo, Y., 85, 92–93
Tan, S. G., 110–111
Tan, S. N., 110–111
Tan, W., 86–87
Tanaka, K., 209
Tang, B., 137–138
Tang, H., 137, 140
Tang, Y., 22–23
Tapsoba, I., 113–114
Taylor, G., 14–15
Teleman, A. A., 23–25, 63
Teng, C.-J., 87–88
Teo, P. Y. T., 110–111
Terada, L. S., 235–237
Terai, T., 85–86, 98
Terskikh, A. V., 23–25, 47–48, 62, 176–177, 220–221, 235–237
Thandavarayan, R. A., 244
Thebaud, B., 14
Thevenot, D. R., 115
Thibert, R. J., 194
Thomas, S., 153
Tian, L., 63
Tid-Ang, J. D., 191
Tiganis, T., 176–177
Tilkins, M. L., 51, 180
Tiscornia, G., 48, 180
Tkachuk, V. A., 46, 176–177, 179, 181
Toledano, M. B., 20, 46, 79–80, 220
Tomasi, A., 47
Tonks, N. K., 176–177
Tonyushkina, K., 137
Tornroth, S., 203
Torres, M., 46
Torres-Lugo, M., 110–111

Tortora, G. J., 141
Toth, K., 115
Towne, V., 2, 3
Trachootham, D., 220, 227–228
Treberg, J. R., 190–191, 197–202, 199*f*, 200*f*, 203, 204–205, 206–207, 211–212, 212*f*
Tretter, L., 207–208
Trinei, M., 20, 124, 126–127, 128, 130
Tripathi, A., 84–85, 92–93
Trumpower, B. L., 205–207
Tsien, R. Y., 27, 48, 180
Tsukeda, H., 169–170
Tu, B. P., 232–233
Tuite, M. F., 233
Tulyathan, O., 22–23, 47, 176
Turnbull, S., 108
Tyurin-Kuzmin, P. A., 46, 176–177, 179, 181

U

Ueno, T., 23
Ueyama, T., 46
Updegrove, T., 220–221, 224–225
Urano, Y., 23, 32–34, 85–86, 89, 98
Urban, N., 191
Ustunol, Z., 99–100
Uysal, M., 244

V

Valenti, G., 124, 126–127, 128, 130
Van de Bittner, G. C., 21, 27
van de Water, B., 241–243
Van den Berg, W. H., 206
van der Valk, P., 191
vanHorsen, J., 191
Vasa, R. A., 9
Vasquez-Vivar, J., 146–148
Vatsyayan, P., 109–110, 111
Veal, E. A., 20, 108, 232–233
Vélez Rivera, J. D., 63
Velasquez-Castano, J. C., 99–100
Verma, I. M., 48, 180
Vervoort, J., 15
Vielhaber, S., 234–235
Villamor, E., 100–101
Villegas, M. L., 2, 12–13
Vinh, J., 79–80
Vinogradov, A. D., 200–201
Vogel, H., 22–23
Voigt, A., 191
Vorotnikov, A. V., 46, 176–177, 179, 181
Vos, J. G., 137
Votyakova, T. V., 13, 15, 124, 201–202
Vuillaume, M., 124
Vytřas, K., 137, 141–142

W

Wabnitz, G. H., 62, 80
Wadhawan, J. D., 114–115
Wagner, B. A., 2, 3
Wajih, N., 233
Wallace, D. C., 124
Wallin, R., 233
Walter, A. D., 114–115
Walter, P., 233–234
Wang, A., 203
Wang, F., 87–88
Wang, G., 111–112, 114–115
Wang, J., 110–111, 235–238, 241–243
Wang, K.-L., 87–88
Wang, X.-C., 85, 92–93, 99–100
Wang, Y., 137–138
Wardman, P., 47
Wartenberg, M., 46
Washabaugh, M. W., 193
Watabe, S., 137
Watmough, N. J., 209
Waypa, G. B., 14
Wei, T., 85
Weir, E. K., 14
Weiss, J. N., 14
Weissman, J. S., 232–233
Wernette, M. E., 208
West, I. C., 206–207
White, C. W., 100–101
Whiteman, M., 14–15
Whitesides, G. M., 222
Wiles, R. A., 21
Wilhelm, J., 207–208
Wilks, D., 191
Will, M., 2, 3
Willhoite, A. R., 36
Wilson, D. F., 206
Wilson, G. S., 115
Winger, J. A., 84–85
Winklhofer, K. F., 20
Winterbourn, C. C., 20, 46, 79–80, 84, 160

Witte, M. E., 191
Wittig, I., 132–133
Wojtczak, L., 132–133
Wolfson, A., 235–238, 239–240, 244, 246–247
Wood, Z. A., 79–80
Wright, D. W., 111–112
Wright, G., 110–111
Wright, M., 48, 51
Wu, J.-Y., 87–88, 233–234
Wu, P., 114–115, 117–118
Wu, R. F., 235–237
Wurm, F., 51

X

Xie, Y., 86–87, 100–101
Xin, W., 85
Xu, G. L., 114–115, 117–118
Xu, J., 203
Xu, J. J., 111–112, 114–115
Xu, J.-G., 85–86, 89
Xu, K., 99–100
Xu, S., 85, 92–93
Xu, Y., 85–86
Xun, Z., 20

Y

Yadavalli, V. K., 112–113
Yamada, M., 99–100
Yamamoto, A., 233–234
Yamamoto, S., 85, 92–93
Yamamoto, T., 85, 92–93
Yamamuro, A., 85
Yamataka, H., 25
Yan, J., 110–111, 112–113, 117–118
Yanagi, H., 233–234
Yang, G., 239–240
Yang, S.-Y., 20, 85–86, 89, 124
Yang, X. L., 109–112
Yang, Y., 86–87, 100–101, 110–111
Yankovskaya, V., 203
Yao, G., 46
Yoon, J., 87–88
Yoon, Y., 234–235
Yoshida, H., 233–234
Yoshida, Y., 241–243
Yoshihara, D., 85, 92–93
Yoshikawa, S., 200–201
Yoshioka, Y., 85
Yu, C. A., 203
Yu, L., 203
Yu, Z. X., 191
Yuan, J., 137, 140
Yuan, L., 86–87, 90*f*, 91*f*, 93*f*, 95*f*, 97*f*, 100–101, 100*f*, 101*f*
Yun, C. Y., 233–234
Yura, T., 233–234

Z

Zaitsu, K., 137–138, 140
Zarse, K., 191
Zelko, I. N., 20
Zeng, H., 233–234
Zhai, Y., 203
Zhang, A., 85, 92–93
Zhang, H. J., 114–115, 117–118, 146–148, 232–233
Zhang, J., 85, 92–93, 209
Zhang, K., 235–238, 239–240, 244, 246–247
Zhang, L., 203
Zhang, S., 110–111
Zhang, Y., 233–234
Zhang, Z., 137, 140
Zhao, B., 2–3, 4*f*, 5–8, 5*f*, 7*f*, 9*f*, 10–11, 12–13, 12, 13, 14, 15, 85–86
Zhao, H., 146–148
Zhao, Q., 2, 3, 193
Zhao, S., 86–87, 100–101
Zheng, H., 85–86, 89
Zhivotovsky, B., 124
Zhou, K. F., 110–111
Zhou, M., 2, 137, 140, 193–194
Zhou, Y., 176, 235–237
Zhu, G., 111, 117–118
Zhu, L., 137, 140
Zhu, S., 86–87, 100–101
Zhu, Y. H., 110–111
Zielonka, J., 14–15, 25–27, 146–149, 151–153, 154–155
Zielonka, M., 14–15, 146–149, 151–153
Zima, T., 108
Zollner, H., 244
Zorov, D. B., 132–133
Zvaifler, N. J., 227–228
Zweigner, J., 85

SUBJECT INDEX

Note: Page numbers followed by "*f*" indicate figures, and "*t*" indicate tables.

A

Amplex Red Assay
  catalyze, resorufin, 5
  confocal microscopy, 15
  description, 2
  ESR and DMPO, 6
  fluorescence, 8
  HaCaT keratinocytes, 9–10, 9*f*
  H_2O_2 measurement, 3
  HRP, 6
  instrumental light, 3–5, 5*f*
  MnSOD, 10–12
  oxygen consumption experiments, 6–8
  photobleached oxidation product, 3
  photochemical mechanism, 12–13
  photo-induced oxidation, 3, 4*f*
  photoreaction, 13
  resorufin, 2–3
  room light effect, 6–8, 7*f*
  SOD, 5–6
  spectrofluorometer, 3–5
  standard curve, 8
  UV light, 9
Amplex Red-based *vs.* FCS-based method
  glucose concentrations, buffer and human blood plasma, 141
  H_2O_2 concentrations, 140–141
Amplex UltraRed, 195

B

Boronate oxidation, 21

C

Catalase, 164
CBA. *See* Coumarin boronic acid (CBA)
Cellular response
  HeLa cells imaging, 96–97
  materials and instrumentation, 94–96
Confocal microscopy
  description, 66
  living larvae imaging, 69–71
Coumarin boronic acid (CBA)
  H_2O_2 formation, 151–153
  oxidation products, 151–153, 152*f*
Cytochrome bc_1 complex, complex III
  cytochrome b_{566} and b_{562}, 206–207
  description, 205–206
  presence, antimycin A, 206
  Q-cycle, 205–206
  superoxide production, site $IIIQ_o$, 206–207

D

Data analysis, H_2O_2 amperometric measurements
  electrode response tests, 126–127, 127*f*
  equilibration phase, 126–127
  mitochondrial respiration, 127–128
  surface modification, electrode, 127
Dihydrolipoamide (DL)-containing enzyme complexes, 211

E

Electrochemical biosensors, on-chip detection
  calibrating enzyme sensor methods, 115–116
  fabrication, hydrogel microstructures, 112–113
  HRP-sensing electrodes, microfluidic channels, 113–115
  matrices, biomolecule encapsulation, 110–111
  monitoring ROS production, electrochemistry, 117–118
  pre-polymer enzyme hydrogel solution, 111–112
  substrate preparation, photolithography, 109–110
Electron transfer chain (ETC), 124
Electron-transferring flavoprotein-ETF ubiquinone oxidoreductase (ETF-ETFQOR)
  carnitine, 210
  FAD and Fe–S, 209

Electron-transferring flavoprotein-ETF ubiquinone oxidoreductase (ETF-ETFQOR) (*Continued*)
H_2O_2 production, 210–211
β-oxidation and branched-chain amino acid metabolic pathway, 209
ROS production, fatty acid oxidation, 210
ETC. *See* Electron transfer chain (ETC)
ETF-ETFQOR. *See* Electron-transferring flavoprotein-ETF ubiquinone oxidoreductase (ETF-ETFQOR)

F

FCS. *See* Fluorescence correlation spectroscopy (FCS)
Fluorescence correlation spectroscopy (FCS)
vs. Amplex-Red based method, 140–141
biological applications, 136–137
blood alcohol concentration, 142
detection volume, 136–137, 136*f*
diffusion time, 138–139
enzymatic reaction, H_2O_2 and glucose detection, 137–138, 138*f*
fluorescence intensity fluctuations, 136–137, 136*f*
focused laser beam, 136–137
glucose concentrations, 139
glucose, human blood plasma, 140
GOD-catalyzed oxidation, glucose, 141–142
industrial quality control, 137
limit value, detection and minimum value, determination, 139
treatment, diabetes, 137
Fluorescent probes
boronate oxidation, 21
cellular environments, 86
coumarin–rhodamine, 88–89
data processing and analysis, 29
flow cytometry, 21
H_2O_2 and NO, 85
hydrogen peroxide, 21
in vitro time course assays, 29
intensity, 93–94
NADPH oxidases, 20–21
organic, 86–87
oxidative pathways, 92–93
phenylenediamine group, 90–92
PO1 used for fluorometry, 28–29
RAW 264.7 macrophages cells, 98
rhodamine acceptor, 87–88
RNS, 84–85
ROS, 20, 84
selectivity, 94
sensing scheme, 87–89
spectroscopic properties, 89–94
spectroscopy, 28–29
transduction and oxidative pathways, 85–86

G

Global profiling approach, 148
Glucose oxidase (GO)
activity determination, 161–162, 167*f*
amino acid, 161
cell culture, 161–162
cellular antioxidants, 161–162
determination, H_2O_2 production, 166
enzymatic system, 161–162
H_2O_2 concentration profiles, 162–163
oxygen electrode, 161–162, 167*f*
steady-state assay, 168–169
Glutathione (GSH)
cell culture sample preparation, 240
cellular redox buffering system, 239–240
reductase assay, 241
sample deproteination, 240
sample preparation, oxidized measurement, 240–241
tissue sample preparation, 240
GO. *See* Glucose oxidase (GO)
Growth factor stimulation
cell culture, dye loading, stimulation and imaging, 36–37
confocal fluorescence imaging, 37
materials and instrumentation, 36

H

High-performance liquid chromatography (HPLC)
CBA-derived products, 151–153
DAF-2-derived products, 153, 154*f*
HE-derived products, 148–150
o-mito-PhB$(OH)_2$, 154–155, 155*f*

H_2O_2 consumption
aerobic cells, 160
biological effects, 160
bolus addition, 161
calibration curve, 165
cellular antioxidants, 160
data handling, 166–169
delivery methods, 161, 162*f*
dynamics, 163–164
exposure, cells, 171–172
first order rate constant, 167, 168*f*
GO, 161–163
kinetics, cells, 166
nitric oxide research, 171–172
oxygen electrode, 166
plasma membrane permeability, 171–172
reagents, 164
steady state implementation, 169–170
transition metals, 160
HODEs. *See* Hydroxyoctadecadienoic acids (HODEs)
H_2O_2 electrochemical detection
ATP synthase activation, 132–133
cellular metabolism, 124
data analysis, amperometric measurements, 126–128
electrochemical instrumentation, 124–125, 125*f*
electrochemical measurement of O2, 125
ETC, 124
fluorescent probes, 124
mitochondrial suspension, 130–131
and O_2 calibration tests, 128–129
OMEA, 124–125
platinized carbon fiber microelectrode, 126
preparation, isolated mitochondria, 129–130
H_2O_2 fluorescent probes
controls utilizing inhibitors, 38–39
dual-imaging experiments, 32–34
hydrogen peroxide-dependent, 32–34
H_2O_2 microdomains
cytoplasmic surface, endoplasmic reticulum membrane, 185*f*, 186
description, 176
EGFR-HyPer construct, 184–185, 184*f*
EGFR-HyPer-expressing HeLa-Kyoto cells, 184–185, 184*f*
experimental design
cell lines and stimuli, 176
for image acquisition, 177
image processing and quantification, 177
immobilizing HyPer within cell, 176–177
HyPer fusion proteins, 179–180
materials, 178–179
profile, HyPer ratio change, 184–185, 184*f*
transfection (*see* Transfection, hydrogen peroxide (H_2O_2) microdomains)
H_2O_2 probes
boronate-based, 22–23
chemodosimeters, 23–25
design, 22–23
fluorescent boronate-based, 23–25
fluorophore sensitive, 25
molecular structures, 22–23, 22*f*
oxidizing species, 25–27
PET, 23
selection, 27
spectroscopic properties and applications, 23
use and storage, 28
H_2O_2 production
Drosophila
confocal microscopy, 66
dynamic measurements, 62
fixed tissues preparation, 65–66
fly husbandry and larvae collection, 64
fly husbandry, larvae and adult synchronization, 66–67
generation, ratio images, 71–73
genetically encoded probes, 62–63
HyPer, 63
intact larvae preparation, 67
living larvae, preparation, 64–65
metazoan physiology and pathology, 62
raw data analysis, 74–78
reduced and oxidized tissue samples, 68
roGFP2-Orp1 transgenic flies, 63–64
measurements
antioxidant system, 197–198

H_2O_2 production (*Continued*)
correction and calibration curve, 194–195
in situ ROS production, 191–192
membrane permeability, 191–192
mitochondrial release, 193–194
platereader- *vs.* cuvette-based assays, 195–197
Horseradish peroxidase (HRP)-sensing electrodes
amperometric measurements, 114–115
enzyme- based electrochemical biosensors, 114–115
microfluidic devices, 113–114
PDMS, 113–114
HPLC. *See* High-performance liquid chromatography (HPLC)
Human blood plasma
Amplex Red-based *vs.* FCS-based method, 141
detection, glucose, 140
Hydroethidine (HE)-derived products
"cell-free" model system, 150
oxidation products, 150, 151*f*
peroxynitrite generation, 148–149, 149*f*
Hydrogel microstructures
fabrication, patterned substrates, 112–113
free radical polymerization, 112
UV exposure, 111
Hydrogen peroxide (H_2O_2)
amperometry and CV techniques, 117–118
biosensors, 108–109
calibration curve, 115–116
cellular signaling, 108
detection, oxidative stress, 111–112
ethanol-stimulated hepatocytes, 114–115
fluorescence and electrochemistry, 108–109
quantification, cells, 118
Hydroxyoctadecadienoic acids (HODEs), 243–244
HyPer
creating, fusion proteins, 179–180
description, 176
FuGene6 transfection reagent, 180
immobilizing, within cell, 176–177
mercury/xenon arc lamps, 179
HyPer-Mito. *See* Mitochondrial hydrogen peroxide production

I

Imaging. *See* H_2O_2 microdomains
Intracellular hydrogen peroxide
cell starvation and imaging medium, 50
chemical probes, 47–48
confocal microscope, 55
dyes, 47
fluorescence microscope, 51
HyPer time-lapse imaging, 54
light, laser/lamp, 49
oxygen radicals, 46
parameter selection, image acquisition, 48–49
reagents, 49–51
ROS, 46
transfected cells preparation, 52
transfection, 48, 51
visualization, 53
wide-field fluorescent microscope, 55–56
zymosan particle ingestion, 57–58
*i*PLS regression*see* Interval partial least-squares (*i*PLS) regression

L

Lipid peroxidation
cell culture sample preparation, 243
HODEs, 243–244
isolation, 243
malondialdehyde, 244
TBARS, 244–245
tissue sample preparation, 243
Live single-cell mitochondrial ROS imaging
cellular processes, 220
device operation and image analysis, 228
electron transport chain, mitochondria, 220
fluorescent indicators, 220–221
imaging, MitoSOX and HyPer-Mito, 228–229
Matlab (MathWorks) scripts, image analysis, 223–224
microfluidic (*see* Microfluidic systems)
microscope setup, 223, 224*f*
mitochondrial

hydrogen peroxide production, 226–227
superoxide production, 224–226
multicolor live imaging microscopy, 221–222
production, 220–221, 221*f*
recombinant protein, HyPer, 220–221
stochastic fluctuations, 221

M

Macrophages cells
culture and imaging, 98–99
fluorescence, 99–100
materials and instrumentation, 98
PMA, 99–100
Matrices, biomolecule encapsulation
carbon nanotubes, 111
cellulose, 110–111
electrode surface, 110–111
gold and silver nanoparticles, 111
hydrogels, 110–111
synthetic sol–gel glass, 110–111
mGPDH. *See* Mitochondrial glycerol 3-phosphate dehydrogenase (mGPDH)
Microfluidic systems
densely arrayed single-cell trapping device, 222
device preparation, 223
Mitochondrial glycerol 3-phosphate dehydrogenase (mGPDH)
cytosol-facing orientation, 207–208
description, 207
factors, 208–209
ROS production, 208
Mitochondrial hydrogen peroxide production
HyPer-Mito into Jurkat cell line, 226
live cell imaging, HyPer-Mito, 226–227
Mitochondrial markers
cell preparation, imaging, 246
DNA binding, 245–246
preparation, MitoSOX and TMRM, 246
superoxide and inner membrane, confocal microscopy, 246–247
Mitochondrial reactive oxygen species (ROS) production
behavior and capacity, 198–200
complex III, cytochrome bc_1 complex, 205–207
complex II, succinate:ubiquinone oxidoreductase, 203–205
complex I, NADH-ubiquinone oxidoreductase, 200–203
description, 190–191
DL-containing enzyme complexes, 211
ETF–ETFQOR (*see* Electron-transferring flavoprotein-ETF ubiquinone oxidoreductase (ETF-ETFQOR))
H_2O_2 production measurements, 191–198
maximum rates, superoxide/H_2O_2 production, 211–212, 212*f*
mGPDH (*see* Mitochondrial glycerol 3-phosphate dehydrogenase (mGPDH))
mitochondrial superoxide/H_2O_2 production, 191, 192*f*
OGDH and ETF-ETFQOR, 198–200
physiological and pathological events, 191
supplier, cellular ATP, 190
Mitochondrial superoxide production
live cell imaging, MitoSOX Red, 225–226, 225*f*, 227*f*
treating cells, MitoSOX, 224–225
MitoSOX Red. *See* Mitochondrial superoxide production
MnSOD
fluorescence, 11–12
peroxidase activity, 10
resorufin, 10–11
spectrophotometer, 11–12

N

NADH-ubiquinone oxidoreductase, complex I
ATP hydrolysis, 202
flavins, 201
NADH pool, 201
production, superoxide, 200–201
rate, I_Q superoxide production, 201–202
reaction, 200
reduction potentials, redox centers, 200, 200*f*
"reverse electron transfer", 201–202
Rotenone (4 μM), 202–203

O

OGDH. *See* Oxoglutarate dehydrogenase (OGDH) complex
OLS regression. *see* Ordinary least squares (OLS) regression
O_2 metabolism electrochemical analyzser (OMEA)
  aerobic metabolism, 132
  ATP synthase activation, 132–133
  detection, mitochondrial H_2O, 132, 133*f*
  H_2O_2 signal measurement, 130
  reduction, concentration, 132
Oxidative damage, ER stress
  –mitochondria, 234–235
  protein folding, 233
  SOD, 232–233
  uncontrolled production and/or accumulation, 232–233
  UPR (*see* Unfolded protein response (UPR))
Oxoglutarate dehydrogenase (OGDH) complex
  and ETF-ETFQOR, 198–200
  and PDH, 211
  proline and dihydroorotate, 190–191
  ROS production, 201

P

PDMS. *See* Poly dimethyl siloxane (PDMS)
PET. *See* Photoinduced electron transfer (PET)
Photoinduced electron transfer (PET), 23
Photolithography
  biomedical applications, 109
  gold electrode chips preparation, 109–110
  on-chip electrochemical biosensors, 109–110
  photoresist, 109
  semiconductor and microelectronics industries, 109
Platereader- *vs*. cuvette-based assays
  advantages, 195–196
  Amplex UltraRed/HRP detection system, 196–197
  protocols, 196
  Shimadzu RF5301-PC spectrofluorimeter, 195
Platinized carbon fibrer microelectrode, 126
Poly dimethyl siloxane (PDMS), 113–114
Protein carbonylation
  bacterial glutamine synthetase, 237–238
  buffers and solutions, 238
  colorimetric/immunologic assay, 237–238
  detection, ELISA, 238–239
  isolation
    cultured cells, 238
    tissue samples, 238

R

Raw data analysis, 74–78
Reactive nitrogen species (RNS), 84–85
Reactive oxygen species (ROS), 20, 84
Real-time monitoring, ROS and RNS
  assay plate layout, 148
  automated liquid-handling systems, 156
  cell-free and cell systems, 148
  enzymatic and cellular systems, 146–148
  fluorescence intensity, 146
  HPLC analyses (*see* High-performance liquid chromatography (HPLC))
  structures, chemical probes, 146
Receptor tyrosine kinases (RTK). *See* H_2O_2 microdomains
RNS. *See* Reactive nitrogen species (RNS)
roGFP2-Orp1 transgenic flies
  fruit fly, 63
  larvae, 63
  redox state, 63–64
ROS. *See* Reactive oxygen species (ROS)
ROS production, electrochemistry
  H_2O_2 concentration, cells, 118
  injured cells, 117–118
  seeding of cells, sensing device, 117

S

Signaling. *See* H_2O_2 microdomains
SOD. *See* Superoxide dismutase (SOD)
Succinate:ubiquinone oxidoreductase, complex II
  enzyme isolation, *Escherichia coli*, 203
  glycerol 3-phosphate, 205
  mitochondria, electron transport chain inhibitors, 204–205

oxygen consumption and ROS generation, 203–204
peak H_2O_2 production, 203–204
Q-binding sites, 204–205
SDH, 203
succinate, 203–204
Superoxide dismutase (SOD), 5–6, 111–112

T

Targeted MitoPY1
cell culture, 32
dye loading, imaging and data analysis, 32
instrumentation and materials, 31
TBARS. *See* Thiobarbituric acid reactive substances (TBARS)
Tetramethyl rodamine, 137–138
Thiobarbituric acid reactive substances (TBARS), 244–245
Transfection, hydrogen peroxide (H_2O_2) microdomains
cell culturing, 180
cells, glass-bottom dishes, 180
FuGene6 transfection reagent, 180
images processing and quantification, 182–184
imaging settings, 181–182, 182*t*
preparation, 180–181
primary visualization, 181
Trappable PF6-AM
cell culture, dye loading, stimulation and flow cytometry, 30–31
data processing and results, 31
instrumentation and materials, 30
Tyramide
2,2'-dihydroxydiphenyl derivatives, 137–138
fluorescent probes, 137–138

U

Unfolded protein response (UPR)
antioxidant response genes, 233–234
glutathione levels, 239–241
oxidative damage markers, 235–237
posttranslational modifications, 233–234
protein carbonyls, 237–239
real-time ROS production, 235–237
UPR. *See* Unfolded protein response (UPR)

W

Wide-field fluorescent microscope, 55–56